Enhanced Performance of Optical Sources in III-V Materials Using Photonic Crystals

by

Alexei Andrew Erchak

B.A., Mathematics and Physics, Skidmore College, 1997
S.M., Materials Science and Engineering, Massachusetts Institute of Technology, 1999

SUBMITTED TO THE DEPARTMENT OF MATERIALS SCIENCE AND ENGINEERING IN PARTIAL FULFILLMENT OF THE REQUIREMENTS FOR THE DEGREE OF

DOCTOR OF PHILOSOPHY IN ELECTRONIC, PHOTONIC, AND MAGNETIC MATERIALS AT THE MASSACHUSETTS INSTITUTE OF TECHNOLOGY

JUNE 2002

© 2002 Massachusetts Institute of Technology

All rights reserved.

Signature of Author: ______________________________

Department of Materials Science and Engineering
May 10, 2002

Certified by: ______________________________

Leslie A. Kolodziejski
Professor of Electrical Engineering
Thesis Supervisor

Certified by: ______________________________

Lionel C. Kimerling
Thomas Lord Professor of Materials Science and Engineering
Thesis Supervisor

Accepted by: ______________________________

Harry L. Tuller
Professor of Ceramics and Electronic Materials
Chair, Departmental Committee on Graduate Students

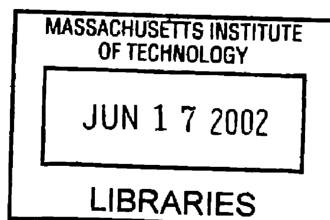
MASSACHUSETTS INSTITUTE OF TECHNOLOGY
JUN 1 7 2002
LIBRARIES

ARCHIVES

Enhanced Performance of Optical Sources in III-V Materials Using Photonic Crystals

by

Alexei Andrew Erchak

Submitted to the Department of Materials Science and Engineering on May 10, 2002
in Partial Fulfillment of the Requirements for the Degree of Doctor of Philosophy in
Electronic, Photonic, and Magnetic Materials

Abstract

This thesis applies the unique properties of photonic crystals to enhance the performance of several III-V optical sources. Emphasis is placed on the primary limitation of using photonic crystals for III-V optical sources: nonradiative recombination pathways introduced at the high dielectric contrast interfaces of the photonic crystal. Chapter 1 begins the thesis by providing a theoretical and historical framework for photonic crystals, and lays the foundation for the design of the novel optical sources presented in the later chapters. Chapter 2 develops a framework for improving the external efficiency of a semiconductor LED using photonic crystals. The design, fabrication, and testing of a novel high-efficiency semiconductor LED is described in detail. To improve coupling to radiation modes without introducing nonradiative surface recombination pathways, a triangular lattice photonic crystal in two-dimensions is etched into the top layer of an asymmetric InGaP/InGaAs quantum well structure emitting at 980 nm. Enhanced injection and external efficiency of the LED is demonstrated. Chapter 3 develops methods of laterally steam oxidizing AlAs into Al_2O_3 to form large-area wide stop-band one-dimensional Al_2O_3/GaAs photonic crystals. The mechanical stability of the high-dielectric contrast interface determines the quality of the photonic crystal and is therefore explored in detail by examining the AlAs steam oxidation process. The Al_2O_3/GaAs photonic crystal is integrated with an InP/InGaAs absorber region and used to self-start ultra-short 35 femtosecond pulses in a Cr^{4+}:YAG laser. Chapter 4 develops the design, fabrication, and testing of a novel low-threshold microcavity laser. Feedback in the microlaser is provided by a one-dimensional photonic crystal embedded in a ridge-waveguide containing an InGaP/InGaAs quantum well structure emitting at 980 nm. The rate equations are solved for the microlaser and several models are developed that identify the key role of nonradiative recombination on the threshold properties of the microlaser. Chapter 5 concludes the thesis and presents several potential pathways for future work.

Thesis Supervisor: Leslie A. Kolodziejski
Title: Professor of Electrical Engineering

Acknowledgements

During my doctoral work I was privileged to work with and learn from many talented individuals. These are the type of people I hope I can work with in the future and these are the people that need to be thanked for their individual important contributions towards my dissertation.

First and foremost, I'd like to start with thanking my thesis advisor, Dr. Leslie Kolodziejski, who made my experience at MIT more enjoyable than it may have been. Although graduate school at MIT can be a fight, it was nice to know that she was always in my corner looking out for me. Leslie's door was always open for me and that kind of support is extremely important in a graduate student's career.

Next, I'd like to thank all the members of the CBE group at MIT. In particular, thanks to Dr. Gale Petrich for performing the MBE growth of the complex materials structures required in this thesis. In addition to being the "fix-it" guy in the CBE lab, Gale provided excellent feedback to all the crazy ideas I would bounce off him daily. Special thanks is needed to my office-mate Solomon ("Sol") for brewing the world's strongest coffee each morning and for the many enlightening discussions. I regret the day I played a "group-initiation" trick on Solomon when he first joined our group, and I paid the price in the years to come with his never ending onslaught of practical jokes. Thanks to Aleksandra Markina, Reggie Bryant, Ryan Williams, and Sheila Tandon for always asking the right questions that forced me to derive better answers.

Thanks are also due to the past members of the CBE group (Elisabeth Koontz, Steve Patterson, and Ed Lim) all of which were a pleasure to work with and taught me a lot. In

particular, special thanks to Ed for taking the time to give a crash course in fabrication to someone who had never set foot in a cleanroom, and for answering my infinite list of questions when I first joined the group.

To the people I have collaborated with during my dissertation I express my deepest appreciation for all their efforts. In particular, thanks to Dr. Dan Ripin and Peter Rakich for persevering through the often difficult experiments and never losing enthusiasm. Thanks to Dr. Shanhui Fan for providing the simulations necessary to complete this work. Shanhui embodies the brightest and rarest type of scientist, one who also makes the effort to understand engineering. Thanks to Prof. Ippen and Prof. Joannopoulos, for the many useful discussions and for always doing their best to take time from their busy schedules and attend those pesky meetings I would constantly schedule.

I'd also like to thank Prof. Smith and all the members of the nanostructures laboratory who provided a massive fabrication knowledge and experience database from which I could draw expertise. Thanks especially to Mark Mondol for operating the electron beam lithography system and for somehow always managing to pencil me in at the top of the queue. I'd also like to extend special thanks to Jim Daley who was always willing to drop whatever he was doing if I needed a hand. Jim is one of the most valuable assets I discovered early on at MIT.

Thanks to all of my friends for being supportive and helping me relax during the often stressful times of my graduate work. In particular, thanks to Brett Smith, Andy Waldrop, Sajan Saini, Gianni Taraschi, Dan Cipperly, Adrian Salvetti, John May, Chris Tuohy, and Jim Vanderveer.

A special thanks to Lauren Massingham for pushing me when I needed it most, listening when I needed to vent, and helping me decide that the time had come to move on from MIT.

Finally, I want to thank all of my family for their love and support. I dedicate this thesis to them. Thanks especially to my older bro Ivan, for making choices different than my own and being someone I can respect and look up to. Thanks Dad, for inspiring me ever since I was young, even all those years ago watching you receive your Ph.D. up the street at Harvard. And thanks especially to my Mom, who gave me the strength, taught me the patience, and gave me the perspective I needed to accomplish this goal.

Table of Contents

Abstract iii

Acknowledgements v

Table of Contents ix

List of Figures xvii

Chapter 1. Photonic Crystals from III-V Materials 23

1.1 Introduction 23

1.2 Introduction to Photonic Crystals 24

1.2.1 Photonic Band Structure 24
1.2.2 The Master Equation 25
1.2.3 Symmetries of Photonic Crystals 27
1.2.4 Frequency Domain Calculations 28
1.2.5 Time-Domain Calculations 30
1.2.6 Scaling PCs 30
1.2.7 One, Two, and Three Dimensional PCs 31
1.2.8 Physical Origin of PBG 32
1.2.9 Defect Modes 33

1.3 History of PCs 34

1.3.1 Early Development 34
1.3.2 Recent Progress 35
1.3.3 Future Trends 35

1.4 Enhanced Optical Sources Using PCs 36

Chapter 2. The Two-Dimensional PC Semiconductor Light Emitting Diode... 37

2.1 Semiconductor LED Efficiency 37

2.1.1 Injection Efficiency 38
2.1.2 Radiative Efficiency 39
2.1.3 Extraction Efficiency 40
2.1.4 LED Figure of Merit 41
2.1.5 Semiconductor LED Design 42
2.1.6 Previous Attempted Solutions 45

2.2 PCs for Semiconductor LEDs 46

2.2.1 Radiation States and Guided States 47
2.2.2 Elimination of Guided Modes with PBG 49
2.2.3 Elimination of Guided Modes at High Frequencies 50
2.2.4 Extraction through PC Resonant States 51

2.3 Two-Dimensional Slab PCs 52
2.3.1 The Triangular Lattice PC 53
2.3.2 Mirror Symmetry: TE-like and TM-like Solutions 56
2.4 Materials Design 57
2.4.1 Generic High-Efficiency PC LED Structure 58
2.4.2 Nonradiative Surface Recombination 59
2.4.3 Advantages of Asymmetric Active Region 59
2.4.4 Active Region 60
2.4.5 Spacer Layer: Thermal Oxidation of AlGaAs 60
2.4.6 The Distributed Bragg Reflector 60
2.4.7 Material Growth and Characterization 62
2.5 Photonic Crystal Design 66
2.5.1 PBG-Enhanced Structure 66
2.5.2 Resonance-Enhanced Structure 68
2.6 Device Fabrication 70
2.6.1 Sample Layout 70
2.6.2 Process Overview 73
2.6.3 Evaporative Deposition of SiO_2 73
2.6.4 Direct Write Electron Beam Lithography 75
2.6.5 Transfer of PC Pattern to SiO_2 77
2.6.6 Transfer of PC Pattern to InGaP 77
2.6.7 Photolithography to Define LED Mesas 78
2.6.8 Mesa Etching 79
2.6.9 Wet Thermal Oxidation 80
2.7 Optical Characterization 83
2.8 Optical Characterization: Resonance-Enhanced PC LED 84
2.8.1 Initial Observations 85
2.8.2 Resonance-Pump Coupling 87
2.8.3 Literature Review 89
2.8.4 Quantifying the Resonance Enhancement 90
2.8.5 Resonance External Efficiency Enhancement 93
2.9 PBG-Enhanced PC LED Results 100
2.9.1 Initial Observations 100
2.9.2 Quantum Well Damage 101
2.9.3 Literature Review 103
2.9.4 Reducing Quantum Well Damage 103
2.9.5 Pump-Coupling to PBG Structures 104
2.9.6 Upper Frequency Cutoff 106
2.10 Conclusions: PCs for High-Efficiency Semiconductor LEDs 107
Chapter 3. Large Scale Oxidation of AlAs Layers for Broadband Saturable Bragg Reflectors 109
3.1 Motivation: Ultrashort Optical Pulse Generation 109
3.2 Saturable Bragg Reflector Design 112

3.2.1 Mirror Design 112
3.2.2 Absorber Design 114
3.2.3 Epitaxial Growth of the Absorber Region 116
3.2.4 Additional Growth Observations 118

3.3 Large Scale Oxidation of GaAs/Al_2O_3 Mirrors 118
3.3.1 Fabrication 119
3.3.2 Delamination of AlAs layers at High Temperature 119
3.3.3 Literature Review: GaAs/AlAs Mirror Oxidation 120
3.3.4 Alternative SBR Designs 121
3.3.5 $Al_xGa_{1-x}As$ Oxidation Process 122
3.3.6 Al_2O_3 Microstructure 126
3.3.7 Oxide/Semiconductor Interface 126
3.3.8 Literature Review: Mechanical Instability of GaAs/AlAs mirrors 127
3.3.9 Delamination of the SBR 129
3.3.10 Oxidation Rate Dependencies 130

3.4 Stabilizing the SBR Structure 131
3.4.1 Stabilization of SBR at Reduced Oxidation Temperature 131
3.4.2 Alternative High-Reflectivity GaAs/Al_2O_3 Mirror 135
3.4.3 Buffer Layer at GaAs/Al_2O_3 Interface 140
3.4.4 AlGaAs/Al_2O_3 SBR Structure 143

3.5 Self-Starting Cr^{4+}:YAG Laser 146
3.5.1 Reducing Two-Photon Absorption 149

3.6 Conclusions 153

Chapter 4. The Monorail Microcavity Laser 155

4.1 Optical Sources for Integrated Optoelectronics 155

4.2 Literature Review: Low-Threshold Semiconductor Lasers 157

4.3 Integrated Waveguide Microcavities 161

4.4 The Monorail Microcavity Laser 164
4.4.1 Materials System 165
4.4.2 Design of the Lasing Cavity 167

4.5 Rate Equation Analysis 168
4.5.1 Estimation of Spontaneous Emission Factor 171
4.5.2 The Effects of Nonradiative Recombination 173
4.5.3 Alternative Model of Monorail Microcavity Laser 175

4.6 Device Fabrication 178
4.6.1 Materials Growth and Characterization 180
4.6.2 Device Patterning 180
4.6.3 Reactive-Ion Etching and Oxidation 181

4.7 Device Characterization 181

4.8 Conclusions 184

Chapter V. Conclusions and Future Directions 187
5.1 Introduction 187
5.2 Future Work: The High-Efficiency Semiconductor PC LED 187
5.3 Future Work: Saturable Bragg Reflectors 192
5.4 Future Work: The Microcavity Laser 193
5.5 The Potential of Photonic Crystal Optical Sources 194

Appendix A: MATLAB Scripts 195
A.1 SBR Transmission Matrix Reflectivity Calculation 195
A.2 Monorail Microlaser Rate Equations Model 1 197
A.3 VCSEL Transmission Model for Monorail Microlaser 201
A.4 Monorail Microlaser Rate Equations Model 2 202

References 205

List of Figures

Figure 1-1. (from [2]) The allowed electronic states of a crystal such as silicon (a) are displayed in a band diagram (b) that may contain an electronic bandgap (shaded). Analogously, a PC is a periodic arrangement of dielectric (c) that may create a PBG (shaded in (d)), a range of frequencies in which light cannot propagate through the structure. 25

Figure 1-2. Example of a PC slab (a) with a dielectric periodicity in two-directions and index contrast confines light in the third (z) direction. Example of a 1D PC where index contrast confines light in the other two (x,z) directions. 31

Figure 1-3. a) Schematic demonstrating how two orthogonal eigenstates with wavevector distribute their electric field intensity differently in a 1D periodic dielectric structure. b) Photonic band diagram (from [2]) showing PBG in allowed energies for structure in (a). 33

Figure 1-4. (from [2]) A defect introduced into the periodicity of a PC creates states within the PBG. Adding or removing dielectric determines the symmetry of the state. The size of the defect determines the frequency of the state.. 34

Figure 2-1. a) Total internal reflection causes reabsorption of emitted light. b) Periodicity in the dielectric constant increases LED efficiency. 38

Figure 2-2. Past improvements on semiconductor LED external efficiency. For sake of comparison, the numbers plotted are "bare" external efficiencies which do not include any form of lens encapsulant....45

Figure 2-3. a) Dispersion relation along any direction in a dielectric slab. b) The effect of a periodicity in the dielectric constant on the disperison relation. 47

Figure 2-4. (from [2]) a) A square lattice of discrete dielectric posts allows for PBGs for TM polarizations but not for TE polarizations. b) A connected square weave pattern allows for PBGs for TE polarizations but not for TM polarizations. 54

Figure 2-5. (from [2]) a) Generic PC consisting of a triangular lattice of air holes in high-dielectric semiconductor. b) Calculated photonic band diagram for PC in (a) extruded infinitely in the z-direction with r=0.35a (inset: the Brillouin zone and reduced Brillouin zone (shaded) along with the real space orientation of the triangular PC. 55

Figure 2-6. a) High-Efficiency PC LED generic design 58

Figure 2-7. a) Asymmetric active region used in high-efficiency PC LED structure 59

Figure 2-8. a) Reflectivity (calculated) of a 6 period AlAs/GaAs DBR (dotted line) as compared to a 6 period Al_2O_3/GaAs DBR (solid line). 61

Figure 2-9. a) Riber 32P molecular beam epitaxy system and other interconnected ultrahigh vacuum chambers ...63

Figure 2-10. X-ray diffraction measurement of PC LED materials structure grown by GSMBE. 64

Figure 2-11. a) PL experimental set-up. b) Room temperature PL from InGaP/InGaAs quantum well. 64

Figure 2-12. a) PBG-enhanced LED structure (a) used for calculation of photonic band diagram (b). A PBG is created surrounding the quantum well emission and overlapping the DBR stopband. 67

Figure 2-13. a) top view and b) side view of electric field intensity calculation of a photonic crystal slab when a dipole is excited that emits a frequency within the PBG. 68

Figure 2-14. Schematic of diffraction-enhanced LED structure (a) and corresponding calculated photonic band diagram (b). The solid line indicates a band that is folded at the edges of the Brillouin zone to create a guided resonance at the Γ-point that lies within the emission spectrum of the LED (dark-shaded region). 69

Figure 2-15. Calculated enhancement from leaky-resonance high-efficiency LED structure. 70

Figure 2-16. a) Each PC LED sample contains an array of LED mesas. The lattice constant is changed along one direction while the hole radius is changed along the other direction yielding a wide range of (r/a) ratios. b) The array is surrounded by a border of LED mesas that do not contain a PC. 71

Figure 2-17. Overview of fabrication process for high-efficiency semiconductor PC LED. 74

Figure 2-18. a) SEM of PC pattern in PMMA following development (100k magnification). The CAD pattern files have square holes but following development the holes are circular b) Close-up view of a hole in another PC pattern (200k magnification). 77

Figure 2-19. a) Top view and b) side view of PC holes etched in InGaP. The etch depth is stopped approximately 10 nm short of the InGaAs quantum well. 78

Figure 2-20. a) Mesas defined in photoresist cover the PC patterns. 79

Figure 2-21. a) Oxidation set-up used to convert high Al-containing AlGaAs ternary compounds into low-dielectric Al_2O_3. 80

Figure 2-22. a) Cross-sectional SEM of cleaved mesa showing oxidized layers. b) SEM of a single DBR period showing the strong contrast between Al_2O_3 and AlAs. c) Completed high-efficiency PC LED structure. 81

Figure 2-23. High-efficiency semiconductor PC LED measurement (setup #1) 83

Figure 2-24. a) Calculated photonic band diagram. b) PL from PC LED mesa containing PC featured in (a). Localized PL from regions internal and external to the PC (c) 86

Figure 2-25. PL with various chromatic filters. The pump laser is positioned on the portion of the LED mesa external to the PC region. 87

Figure 2-26. a) Calculated photonic band diagram. b) Composite image of enhanced optical pumping occurring outside the edge of the PC region when the pump light is focused just inside the edge of the PC region...88

Figure 2-27. White-light reflectivity spectrum for PC structure featured in Figure 2-24. 89

Figure 2-28. High-efficiency semiconductor PC LED measurement (setup #2) 90

Figure 2-29. a) Calculated band structure near the G point for inset PC. b) Narrow collection angle reflectivity spectrum matches well with spectral and integrated enhancement pumping on and off resonance. c) PL spectra taken at 6 mW pumping on and off resonance and compared to an unpatterned reference LED mesa. d) Finite-difference time-domain calculation of enhancement relative to an arbitrary reference. 95

Figure 2-30. a) Measured PL spectra for PC LED mesa compared to an unpatterned LED mesa for several different pump powers. b) Integrated PL/pump power as a function of pump power. The ratio of the two plots is equivalent to an enhancement in external efficiency. 96

Figure 2-31. a) Reflectivity spectrum and PL enhancement spectrum for a PC structure where two-doubly degenerate resonances overlap a large portion of the quantum well emission. b) A 6-fold enhancement in external efficiency is observed and attributed to the large resonance overlap in (a). 99

Figure 2-32. a) PC LED mesa with quantum well damage. The center PC region is designed for PBG-enhancement. b) PL spectra from PC structure before and after oxidation. c) Dependence of quantum well damage on air filling factor. 102

Figure 2-33. Reflectivity and PL emission from a PC structure that may contain a PBG. PL is observed when the pump wavelength is tuned to a resonance near 740 nm. 106

Figure 3-1. Absorption fraction of transmission in a saturable absorbing material (from [76]). 111

Figure 3-2. Optical power spectrum of a Cr^{4+}:YAG pulse (from [76]). 112

Figure 3-3. Calculated reflectivity for a GaAs/AlAs Bragg mirror (dotted line) and high-index contrast GaAs/Al_2O_3 Bragg mirror (solid line). 113

Figure 3-4. Calculated GDD for a 7 pair GaAs/Al_2O_3 Bragg mirror (from [75]). 114

Figure 3-5. SBR design using λ=1440 nm includes an InGaAs/InP quantum well and a 7 pair GaAs/Al_2O_3 Bragg mirror. 115

Figure 3-6. Calculated reflectivity spectrum of high-index contrast GaAs/Al_2O_3 Bragg mirror for a 20% range of error in thickness of the low-index Al_2O_3 layer. 116

Figure 3-7. PL emission from the absorber region of a broadband SBR. 117

Figure 3-8. a) Top down SEM of mesa structure oxidized at 435°C for 4 hours. b) Cross-sectional view showing delamination. 120

Figure 3-9. a) Schematic showing transition from linear to parabolic regimes for extended steam oxidations 125

Figure 3-10. a) Oxidation front progressing in AlAs [108] b) Oxidation front progressing in $Al_{0.92}Ga_{.08}As$ [108] 126

Figure 3-11. a) Cross-sectional SEM of unoxidized/as-grown layers in SBR. b) Optical micrograph of oxidation front progressing in SBR mesa oxidized at 400°C c) Cross-sectional SEM of SBR with oxidized low-index layers. d) Comparison between measured (solid-line) and simulated (dotted line) reflectivity. 133

Figure 3-12. Reflectivity of a 7 period quarter-wave Bragg mirror (dashed line) and thinner oxide Bragg mirror (solid line). The thinner oxide mirror has a >99.5% reflectivity from 1280 to 1730 nm. 136

Figure 3-13. a) Cross-sectional SEM of unoxidized/as-grown layers in SBR. b) Optical micrograph of oxidation of SBR material containing thinner Al_2O_3 layers in the Bragg mirror. c) Obstructed oxidation due to dense As_2O_3-containing layer at oxide terminus causes uneven oxidation fronts to develop. d) Cross-sectional SEM of SBR structure with oxidized low-index layers and the top absorber layer removed. e) Comparison between FTIR measured reflectivity from the mesa edge and unoxidized mesa (solid lines), the mesa center (dashed-dotted line), and calculated (dotted line) reflectivities 137

Figure 3-14. Optical micrograph of a partially oxidized SBR mesa containing SBR material (1 hr. at 435°C). b) Close-up SEM of interface separated during sample preparation revealing an oxidized interfacial buffer layer. b) Cross-sectional SEM of SBR with oxidized low-index layers. d) Comparison between measured (solid line) and calculated (dotted line) reflectivity. 142

Figure 3-15. Reflectivity of a 7 period $GaAs/Al_2O_3$ Bragg mirror (dashed line) and a 7 period $Al_{0.7}Ga_{0.3}As/Al_2O_3$ Bragg mirror (solid line). The $Al_{0.7}Ga_{0.3}As/Al_2O_3$ mirror has a >99.5% reflectivity from 1260 to 1680 nm. 144

Figure 3-16. a) Cross-sectional SEM of unoxidized/as-grown layers in SBR containing $GaAs/Al_{0.7}Ga_{0.3}As$ layers. b) Optical micrograph of partially-oxidized SBR mesa (1 hr. at 435°C) containing SBR material in (a). An oxidation time of 2 hrs. completes the mesa oxidation. c) Cross-sectional SEM of SBR with oxidized low-index layers taken from the center of a 500 mm mesa and 50 mm from the edge (d). 145

Figure 3-17. Measured data from the Cr^{4+}:YAG laser cavity modelocked using the oxidized SBR from growth R885 in combination with KLM. Results show a) Tunability from 1400 to 1525 nm. b) Pulse spectrum c) Interferometric auto-correlation. 148

Figure 3-18. a) Original SBR structure oxidized at 375°C for 2 hrs. b) Original SBR structure oxidized at 375°C for 10 hrs. c) Continued oxidation of structure in (b) at 375°C for 2 hrs. causes delamination at the oxide terminus. d) Cross-sectional SEM of delaminated layer originating at oxide terminus in SBR structure oxidized at 435°C for 45 mins. 150

Figure 3-19. 500 mm SBR mesas with top absorbing layer removed, each oxidized for 3.5 hrs.at 435°C: Thinner-oxide (a), buffered-interface (b) $AlGaAs/Al_2O_3$ (c) and standard quarter-wave stack (d). e) FTIR-measured reflectivity for structures (a)-(c). 151

Figure 4-1. (from [123]) The cost per interconnection decreases dramatically as optical networking becomes more integrated. 156

Figure 4-2. (from [126]) Low-threshold lasing is obtainable by limiting the available optical and electrical density of states in a semiconductor laser. 158

Figure 4-3. (from [126]) Properties of several microcavity lasers 160

Figure 4-4. a) (from [147]) Photonic band diagram along the x-direction for a waveguide (n=3.37) surrounded by air (n=1) containing air holes separated by a lattice constant a, with a waveguide width 1.2a, waveguide

thickness 0.4a, and hole diameter 0.6a. b) Vector plot of electric field distributions for air-band, dielectric band, and a defect state with hole separation of 1.5a....162

Figure 4-5. (from [155]) a) SEM of several passive monorail microcavity structures in the $GaAs/Al_2O_3$ materials system b) Measured transmission spectra for several different monorail microcavity structures....164

Figure 4-6. Generic monorail microcavity laser....165

Figure 4-7. Monorail microcavity laser materials system....167

Figure 4-8. Simulated transmission through a monorail microcavity (schematic of simulated structure is inset)..168

Figure 4-9. Calculated power output from monorail microcavity laser with simulated transmission from Figure 4-8 for a wide range of b values....171

Figure 4-10. The effects of surface recombination on the power output from a monorail microcavity laser (parameters are inset)....174

Figure 4-11. The effects of Auger recombination on the power output from a monorail microcavity laser (parameters are inset)....175

Figure 4-12. Comparison between monorail microcavity laser models. The first model (dotted line) uses the rate-equations in EQ. 83 and EQ. 84 and defines threshold as the stimulated emission rate equaling the cavity loss rate. The second mode (solid line) uses EQ. 87 and EQ. 88 and determines the threshold gain by maximizing transmission through a VCSEL structure analogous to the monorail microcavity....177

Figure 4-13. Monorail microlaser fabrication process....179

Figure 4-14. Monorail microlaser materials system characterization. a) Comparison between simulated and measured x-ray diffraction spectra. b) Room-temperature PL spectra....180

Figure 4-15. a) A sample consisting of various size structures is used to measure the effects of surface recombination. b) Normalized PL as a function of sample size....183

Figure 5-1. Generic design for electrically activated high-efficiency PC LED structure....189

Figure 5-2. SEMs of LED structures consisting of two separate PC regions. a) The center PC region contains a resonance that overlaps the pump wavelength at 810 nm and therefore provides enhanced optical pumping of the surrounding PC region. The surrounding PC contains a resonance that overlaps the emission linewidth. b) The inverse of the structure shown in (a) at higher magnification....191

Figure 5-3. A PC LED structure that contains resonances used to enhance external efficiency is pumped above threshold. A lasing peak is observed at 1005 nm....192

Figure 5-4. Generic design for electrically activated low-threshold monorail microcavity laser....193

Chapter 1. Photonic Crystals from III-V Materials

1.1 Introduction

Photonic devices at telecommunication wavelengths (1.3-1.55 μm) require micron size features (microphotonics). The use of traditional index confinement is useful for certain aspects of microphotonics, but cannot support the growing diversity of integrated photonic devices required to generate, sort, filter, combine, detect, and guide optical signals on a chip. Photonic crystals provide an attractive alternative for microphotonics because they give unique control otherwise unachievable from conventional index confinement.

In particular, photonic crystals (PCs) constructed from semiconductor materials provide: 1) a large dielectric contrast, with air or various oxides, enabling small footprints for microphotonic devices and 2) the ability to integrate electrical devices with microphotonic devices on the same chip. Furthermore, the use of III-V semiconductor materials provides the ability to integrate optical sources with passive microphotonic devices on the same chip. It is therefore worthwhile to explore the enhanced performance of optical sources in III-V materials using PCs.

1.2 Introduction to Photonic Crystals

This section discusses the origin of the various properties of PCs. A deep understanding of the condensed matter theoretical framework of PCs becomes crucial in the design, fabrication, and testing of the III-V semiconductor devices described in this thesis.

1.2.1 Photonic Band Structure

Electromagnetic radiation interacts with a material through the dielectric constant of the material. For instance, waveguiding of light is achieved by surrounding a high-dielectric material with a lower dielectric material, creating total internal reflection at the dielectric interface. The high-dielectric material effectively forms a frequency-dependent potential well for the photon in an analogous fashion to an electron confined in an electronic potential well (a quantum well). The minimum energy eigenstate of each system confines the majority of its wavefunction inside the potential well. It is well known from solid-state physics [1] that a periodic variation in the electronic "potential wells", as established by the atoms in a crystal lattice (Figure 1-1a), creates bands of allowed and forbidden electronic states within a material (Figure 1-1b). The eigenstates are Bloch waves and are solutions to the Schrodinger equation resulting from the coherent scattering of an electron from the periodic electronic potential. Analogously, a PC repeats the optical potential (the dielectric constant) periodically throughout a material (Figure 1-1c). The coherent scattering of light from the periodic dielectric contrast interfaces creates new types of optical modes and forbidden frequency ranges or photonic band gaps (PBGs) [Figure 1-1d].

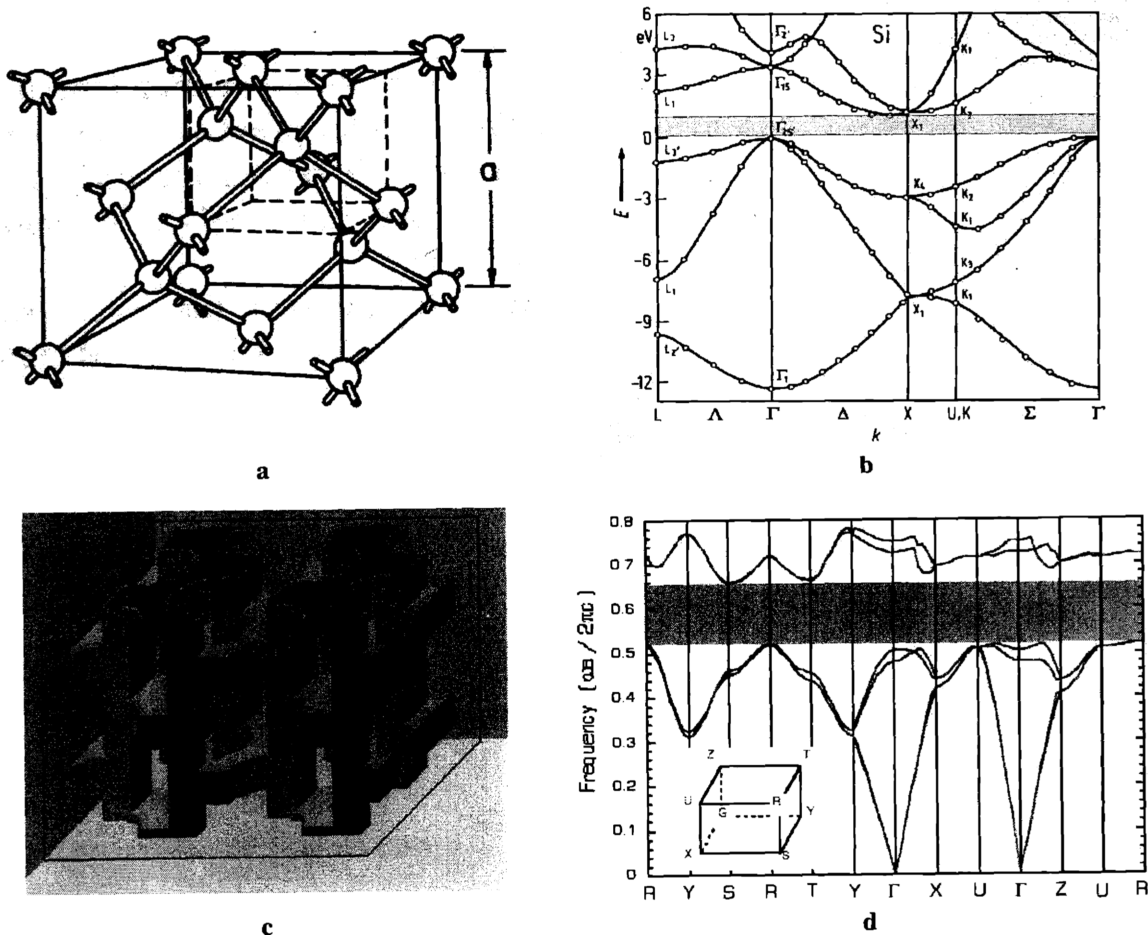

Figure 1-1. (from [2]) The allowed electronic states of a crystal such as silicon (a) are displayed in a band diagram (b) that may contain an electronic bandgap (shaded). Analogously, a PC is a periodic arrangement of dielectric (c) that may create a PBG (shaded in (d)), a range of frequencies in which light cannot propagate through the structure.

1.2.2 The Master Equation

The behavior of electromagnetic radiation in macroscopic media is summarized by Maxwell's equations:

$$\nabla \bullet \mathbf{D} = 4\pi\rho \quad \text{(EQ 1)} \qquad \nabla \bullet \mathbf{B} = 0 \quad \text{(EQ 2)}$$

$$\nabla \times \mathbf{H} - \frac{1}{c}\frac{\partial \mathbf{D}}{\partial t} = \frac{4\pi}{c}\mathrm{J} \quad \text{(EQ 3)} \qquad \nabla \times \mathbf{E} + \frac{1}{c}\frac{\partial \mathbf{B}}{\partial t} = 0 \quad \text{(EQ 4)}$$

Assuming a linear, isotropic, and macroscopic material, the displacement field is related to the electric field by a scalar dielectric constant

$$\mathbf{D}(\mathbf{r}, \omega) = \varepsilon(\mathbf{r}, \omega)\mathbf{E}(\mathbf{r}, \omega). \quad \text{(EQ 5)}$$

Provided the material is lossless and disregarding any frequency dependence of the dielectric constant[1], EQ. 5 becomes

$$\mathbf{D}(\mathbf{r}) = \varepsilon(\mathbf{r})\mathbf{E}(\mathbf{r}). \quad \text{(EQ 6)}$$

The semiconducting materials discussed hereafter are nonmagnetic so that the magnetic induction field (**B**) is equal to the magnetic field (**H**). Further assuming no free charges or currents $\rho = J = 0$, Maxwell's equations can now be rewritten in the following simplified form:

$$\nabla \bullet \varepsilon(\mathbf{r})\mathbf{E}(\mathbf{r}, t) = 0 \quad \text{(EQ 7)} \qquad \nabla \bullet \mathbf{H}(\mathbf{r}, t) = 0 \quad \text{(EQ 8)}$$

$$\nabla \times \mathbf{H}(\mathbf{r}, t) - \frac{\varepsilon(\mathbf{r})}{c}\frac{\partial \mathbf{E}(\mathbf{r}, t)}{\partial t} = 0 \quad \text{(EQ 9)} \qquad \nabla \times \mathbf{E}(\mathbf{r}, t) + \frac{1}{c}\frac{\partial \mathbf{H}(\mathbf{r}, t)}{\partial t} = 0 \quad \text{(EQ 10)}$$

Any solution to Maxwell's equations may be formulated from a linear combination of harmonic modes each with the general form:

$$\mathbf{E}(\mathbf{r}, t) = \mathbf{E}(\mathbf{r})e^{i\omega t} \quad \text{(EQ 11)}$$

$$(\mathbf{r}, t) = \mathbf{H}(\mathbf{r})e^{i\omega t} \quad \text{(EQ 12)}$$

Substituting EQ. 11 and EQ. 12 into EQ. 7-EQ. 10 eliminates the explicit time dependence:

$$\nabla \bullet \varepsilon(\mathbf{r})\mathbf{E}(\mathbf{r}) = 0 \quad \text{(EQ 13)} \qquad \nabla \bullet \mathbf{H}(\mathbf{r}) = 0 \quad \text{(EQ 14)}$$

$$\nabla \times \frac{\mathbf{H}(\mathbf{r})}{\varepsilon(\mathbf{r})} - \frac{i\omega}{c}(\mathbf{E}(\mathbf{r})) = 0 \quad \text{(EQ 15)} \qquad \nabla \times \mathbf{E}(\mathbf{r}) + \frac{i\omega}{c}\mathbf{H}(\mathbf{r}) = 0 \quad \text{(EQ 16)}$$

EQ. 13 and EQ. 14 maintain that the direction of propagation of the electromagnetic waves is transverse to the polarization of both the displacement and the magnetic fields. Taking the curl of EQ. 15 and substituting EQ. 16 yields a master equation in **H**(**r**):

1. a reasonable assumption for the optical wavelengths in semiconductors of concern in this thesis

$$\nabla\times\left(\frac{1}{\varepsilon(\mathbf{r})}\nabla\times\mathbf{H}(\mathbf{r})\right) = \left(\frac{\omega}{c}\right)^2\mathbf{H}(\mathbf{r}) \qquad \text{(EQ 17)}$$

EQ. 17 is in many ways similar to the Schrodinger equation in quantum mechanics [1] since the operator

$$\Theta = \nabla\times\frac{1}{\varepsilon(\mathbf{r})}\nabla\times \qquad \text{(EQ 18)}$$

is both linear and Hermitian. The difference is that $\mathbf{H}(\mathbf{r})$ is a vector whereas $\Psi(\mathbf{r})$ in the Schrodinger equation is a scalar. Directly analogous to quantum mechanics, however, the eigenvalues are real while the orthogonal, normalizable, eigenfunctions may be obtained by a variational principle and catalogued according to their symmetry properties [2].

1.2.3 Symmetries of Photonic Crystals

The solutions to EQ. 17 must be Bloch waves since the commutator of Θ and the translation operator is zero [3]:

$$\begin{aligned} T_{\mathbf{R}}f(\mathbf{r}) &= f(\mathbf{r}-\mathbf{R}) \\ [\Theta, T_{\mathbf{R}}] &= 0 \end{aligned} \qquad \text{(EQ 19)}$$

Bloch wave solutions may be indexed by a wavevector $\mathbf{k}=(k_x,k_y,k_z)$ and written:

$$\begin{aligned} \mathbf{H}_{\mathbf{k}}(\mathbf{r}) &= e^{i(\mathbf{k}\cdot\mathbf{r})}\mathbf{h}_{\mathbf{k}}(\mathbf{r}) \\ \mathbf{h}_{\mathbf{k}}(\mathbf{r}) &= \mathbf{h}_{\mathbf{k}}(\mathbf{r}+\mathbf{R}) \qquad \forall\mathbf{R} \end{aligned} \qquad \text{(EQ 20)}$$

The master equation, EQ. 17, may now be reduced even further by eliminating the plane wave component from the Bloch form in EQ. 20:

$$\begin{aligned} (i\mathbf{k}+\nabla)\times\frac{1}{\varepsilon(\mathbf{r})}(i\mathbf{k}+\nabla)\times\mathbf{h}_{\mathbf{k}}(\mathbf{r}) &= \left(\frac{\omega(\mathbf{k})}{c}\right)^2\mathbf{h}_{\mathbf{k}}(\mathbf{r}) \\ \Theta_{\mathbf{k}}\mathbf{h}_{\mathbf{k}}(\mathbf{r}) &= \left(\frac{\omega(\mathbf{k})}{c}\right)^2\mathbf{h}_{\mathbf{k}}(\mathbf{r}) \end{aligned} \qquad \text{(EQ 21)}$$

EQ. 21 shows that all the information about each mode is given by the wavevector **k** and the periodic function $\mathbf{h}_{\mathbf{k}}(\mathbf{r})$. The periodic boundary condition given in EQ. 20 allows a restriction of the eigenvalue problem in EQ. 21 to a single unit cell of the PC. A family of discrete eigenvalues is thereby created for each wavevector **k** and indexed with a band number n. The band number indicates that unique solutions for the PC exist only within the 1st Brillouin zone.

The number of unique solutions is further reduced by examining other symmetries of the PC besides translational symmetry. If A is a symmetry besides a translation (that is A commutes with Θ) and τ is a translation that is not a symmetry of the PC then

$$\omega_n(\mathbf{k}) = \omega_n(A\mathbf{k}). \quad \text{(EQ 22)}$$

Invariance under time-reversal yields one final symmetry [2]:

$$\omega_n(\mathbf{k}) = \omega_n(-\mathbf{k}). \quad \text{(EQ 23)}$$

EQ. 22 and EQ. 23 enable use of a reduced Brillouin zone to describe the band structure [the $\omega_n(\mathbf{k})$] for the PC (e.g. Figure 1-1d).

1.2.4 Frequency Domain Calculations

EQ. 17 describes the propagation of light in a material and since Maxwell's equations are exact, it is the starting point for calculating the allowed states of a PC. The non-interaction of photons greatly simplifies the calculation of allowed states in a PC as compared to the allowed electronic states in a periodic electronic potential. The method for calculating the allowed states of the various PCs presented in this work is done *ab-initio* (from first principles). No prior knowledge of the electromagnetic field distribution is necessary to calculate the bandstructure. In essence, EQ. 21 is a standard eigenvalue equation and the eigenvalues may be solved for by diagonalizing $\Theta_{\mathbf{k}}$ for each wavevector **k.** Indeed, the calculation need only be performed over wavevectors **k** in the reduced Brillouin zone, thanks to the symmetries of EQ. 22 and EQ. 23. Since the magnetic field must be transverse (EQ. 14), it is appropriate to expand the $\mathbf{h}_{n\mathbf{k}}$ in a basis of transverse plane-waves: $\mathbf{e}_\lambda e^{i(\mathbf{k}+\mathbf{G})\cdot\mathbf{r}}$, where $\mathbf{e}_\lambda$ are unit vectors perpendicular to the

wavevectors $\mathbf{k} + \mathbf{G}$. Plane-waves form a particularly useful basis because they are complete, can be systematically improved upon, in addition to allowing calculation *ab-initio*. The dielectric function is periodic and therefore may also be expanded in a basis of plane-waves. The photonic band structure may then be readily calculated by substituting both plane-wave expansions into EQ. 21 and using one of many techniques available for solving Hermitian eigenvalue problems [4]. Since a PC is periodic, the computational cell itself need only be the size of the structure's unit cell, further simplifying the calculation. It is possible to even further simplify the diagonalization of the operator $\Theta_{\mathbf{k}}$ by exploiting representation theory [3].

The number of plane waves (N) used in the expansion of $\mathbf{h}_{n\mathbf{k}}$ per polarization must be at least as great as the number of grid points used in the computational cell [4]. The computation time required to diagonalize the operator $\Theta_{\mathbf{k}}$ by storing every element of the $N \times N$ matrix, can therefore be substantial especially for large computational cells. A straight-forward diagonalization is therefore unrealistic for nonperiodic structures where the computational cell must be larger than just a unit cell (such as for defects in PCs). Instead, a variational approach is used where each eigenvalue is computed separately by minimizing the functional

$$\langle \mathbf{h}_{n\mathbf{k}} | \Theta_{\mathbf{k}} | \mathbf{h}_{n\mathbf{k}} \rangle . \qquad \text{(EQ 24)}$$

The minimum is found by using a conjugate gradient method with preconditioning, the details of which are presented in more detail in [4]. Briefly, each eigenvalue is calculated individually while remaining orthogonal to any previously calculated eigenvalues. The conjugate gradient method allows for storage of each of the N matrix elements individually, dramatically reducing the number of iterations until convergence and hence saves computing time. The band structures of PCs with defects can then be calculated by imposing an artificial periodicity, that is, choosing a "super-cell" that is repeated in space [5]. The piece-wise continuity of the dielectric function also requires smoothing algorithms to improve the accuracy of the conjugate gradient method [4].

To summarize, frequency domain calculations allow one to determine the photonic band structure for any given PC. In particular, the conjugate gradient plane-wave method pro-

vides a fast means of determining band structure, even for PCs containing defects. In addition to the band structure, the polarization, symmetry, and electromagnetic field distributions of each eigenstate of the PC are determined using the conjugate gradient plane-wave method in the frequency-domain.

1.2.5 Time-Domain Calculations

The temporal response of a PC is determined by discretizing EQ. 9 and EQ. 10 on a simple cubic lattice so that space-time points are separated by fixed units of time and distance. The derivatives at each lattice point are calculated using a centered difference with the surrounding points, giving rise to standard finite-difference equations. Since the calculation domain is finite, particular care must be taken to the boundary conditions at the border of the calculation cell. For this thesis, the boundary conditions used in the calculations presented are either Berenger's Perfectly Matched Layer (PML) conditions for 2D calculations, or Mur's absorbing boundary conditions for 3D calculations [5]. The equations are then stepped-through in time to obtain the temporal response of the PC structure.

1.2.6 Scaling PCs

Consider scaling a PC by a factor s so that if $s > 1$ the PC contracts and if $s < 1$ the PC expands. EQ. 17 in becomes

$$\nabla\times\left(\frac{1}{\varepsilon\left(\frac{\mathbf{r}'}{s}\right)}\nabla\times\mathbf{H}\left(\frac{\mathbf{r}'}{s}\right)\right) = \left(\frac{\omega}{c}\right)^2\mathbf{H}\left(\frac{\mathbf{r}'}{s}\right), \quad \text{(EQ 25)}$$

where the scaled coordinate system obeys the mapping $\mathbf{r} \rightarrow \frac{\mathbf{r}'}{s}$. Since $\nabla = s\nabla'$,

$$\nabla'\times\left(\frac{1}{\varepsilon\left(\frac{\mathbf{r}'}{s}\right)}\nabla'\times\left(\mathbf{H}\left(\frac{\mathbf{r}'}{s}\right)\right)\right) = \left(\frac{\omega/s}{c}\right)^2\mathbf{H}\left(\frac{\mathbf{r}'}{s}\right). \quad \text{(EQ 26)}$$

The eigenstates scale ($\mathbf{H}(\mathbf{r}) \rightarrow \mathbf{H}\left(\frac{\mathbf{r}'}{s}\right)$) along with the corresponding eigenvalues ($\omega \rightarrow \frac{\omega}{s}$). Therefore, the calculation of a photonic band diagram for a PC structure need only be done once on an arbitrary length scale; this is reflected in Figure 1-1, where the axes are labeled in units of an arbitrary lattice constant (a) Scalability to any desired wavelength of operation helps make PCs attractive for microphotonic applications.

1.2.7 One, Two, and Three Dimensional PCs

One-dimensional (1D) PCs are fairly common. A good example of a 1D PC is the quarter-wavelength dielectric stacks used as high-reflectivity mirrors in vertical cavity surface-emitting lasers (VCSELs). Although the index contrast is less than is typical for a PC, distributed feedback lasers (DFBs) use quarter wavelength gratings to achieve narrow linewidth single mode lasing [6]. Two-dimensional (2D) PCs consist of a periodicity in the dielectric constant in two dimensions. Dielectric contrast in the third dimension may be used to confine light within the two-dimensional periodicity yielding a PC slab (Figure 1-2a). Dielectric confinement may also

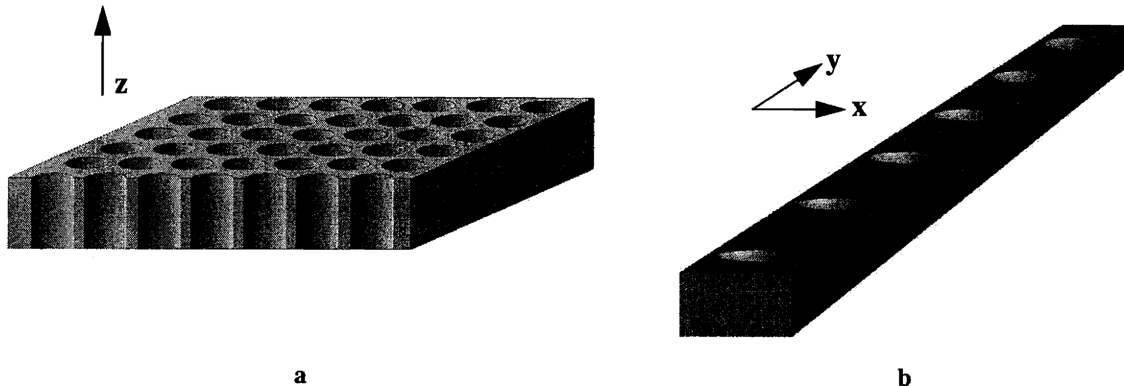

Figure 1-2. Example of a PC slab (a) with a dielectric periodicity in two-directions and index contrast confines light in the third (z) direction. Example of a 1D PC where index contrast confines light in the other two (x,z) directions.

be used in two directions to obtain a 1D PC waveguide structure (Figure 1-2b). The structures shown in Figure 1-2 are planar and thus are feasible using modern fabrication techniques developed for microelectronic chip fabrication (reactive-ion etching, film deposition, optical lithography, etc.). Three dimensional PCs (Figure 1-1c), however, are much more difficult to fabricate and therefore have less potential for low-cost semiconductor-based photonic devices.

1.2.8 Physical Origin of PBG

A physical understanding of the origin of the PBG may be obtained by considering a simple 1D periodicity in the dielectric constant as depicted in Figure 1-3a. The structure is assumed to be uniform and infinite in the two (x,y) directions orthogonal to the 1D periodicity. The 1st Brillouin zone for such a structure has a boundary[2] at $k = \frac{\pi}{a}$, where a is the lattice constant of the PC. At the boundary of the 1st Brillouin zone, a PBG may appear (given a finite dielectric contrast) within which electromagnetic radiation is forbidden from propagating (Figure 1-3b). A PBG occurs because there exist two unique electric field distributions that match the symmetry of the structure's unit cell about its center. The two field distributions correspond to the lowest energy state in the upper band and highest energy state in the lower band, located at the edge of the 1st Brillouin zone. The two field distributions must be orthogonal and to be eigenstates of the system they must minimize the energy functional:

$$E_f = \frac{1}{2(\mathbf{H}, \mathbf{H})} \int \frac{1}{\varepsilon(\mathbf{r})} \left| \frac{\omega}{c} \mathbf{D} \right|^2 d\mathbf{r}^{3} \qquad \text{(EQ 27)}$$

To minimize its variational energy then, inspection of EQ. 27 shows that the lower band (lower frequency) eigenstates concentrate their electric field intensity in the high-dielectric region; for this reason the lowest band is sometimes termed the "dielectric band". The upper band (high frequency) eigenstates, however, have a significant amount of electric field intensity in the low-dielectric region. Since the low-dielectric is often air, it is sometimes referred to as the "air band". Higher order PBGs will also occur at the edges of the 1st Brillouin zone as more complex field distributions attempt to minimize the energy functional while simultaneously remaining orthogonal to lower energy eigenstates. For higher dimensionality PCs (Figure 1-1b) the same rules apply creating PBGs such as that shown in Figure 1-1d.

2. From time-reversal symmetry the eigenmodes at -k are identical up to a phase shift.

3. Minimizing the energy functional directly relates to minimizing the functional in EQ. 24 [2] and therefore corresponds to an eigenstate of the system.

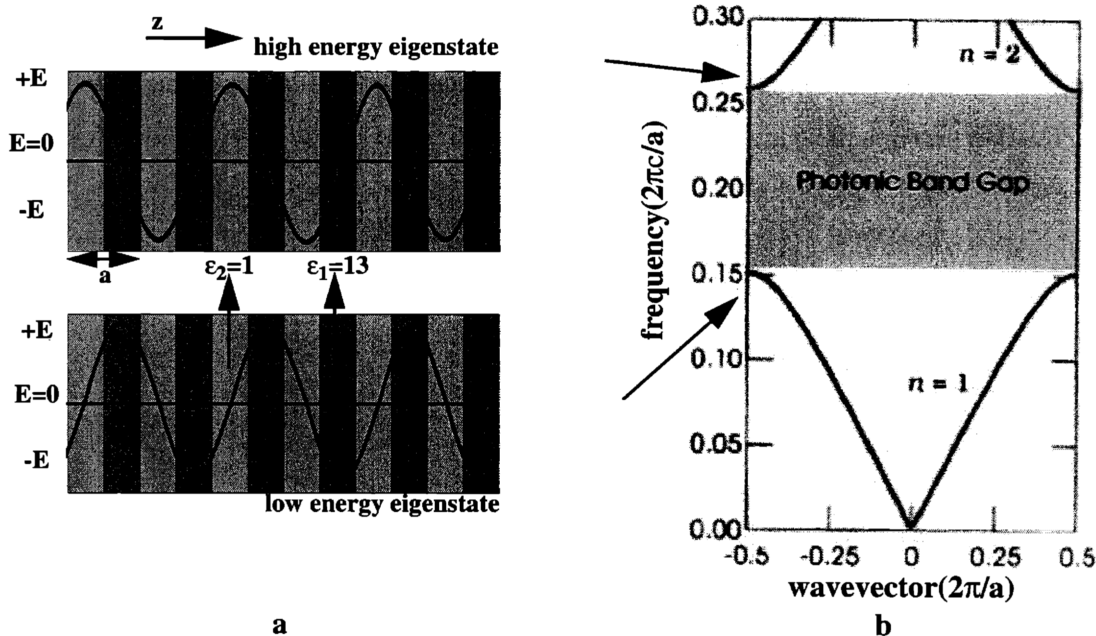

Figure 1-3. a) Schematic demonstrating how two orthogonal eigenstates with wavevector $k = \frac{\pi}{a}$ distribute their electric field intensity differently in a 1D periodic dielectric structure. b) Photonic band diagram (from [2]) showing PBG in allowed energies for structure in (a).

1.2.9 Defect Modes

Perhaps the most interesting applications of PCs arise by breaking the translational symmetry of the crystal lattice. Analogous to localized electronic states created by defects in semiconductor crystal material, localized optical states may be introduced into PCs by creating a defect in the periodicity [7,8]. For instance, consider a two-dimensional PC consisting of infinitely long dielectric rods surrounded by a lower dielectric material and the corresponding photonic band diagram (Figure 1-4). As the radius of a single dielectric rod decreases (an air defect), a localized optical state is created within the PBG. The defect state emerges from the top of the dielectric band because as the rod diameter is reduced some of the electric field intensity that was within the rod is forced to coincide in the lower dielectric material. Therefore, the energy of the optical state is slightly higher than the eigenstate at the top of the dielectric band. As the diameter

of the dielectric rod is reduced even further the defect state sweeps across the PBG. A similar pattern is observed as the dielectric radius is increased (a dielectric defect). An isolated defect state emerges from the bottom of the air band and sweeps across the PBG towards lower frequencies as the radius of the rod decreases and more and more of the electric field intensity near the defect is forced to overlap the high dielectric.

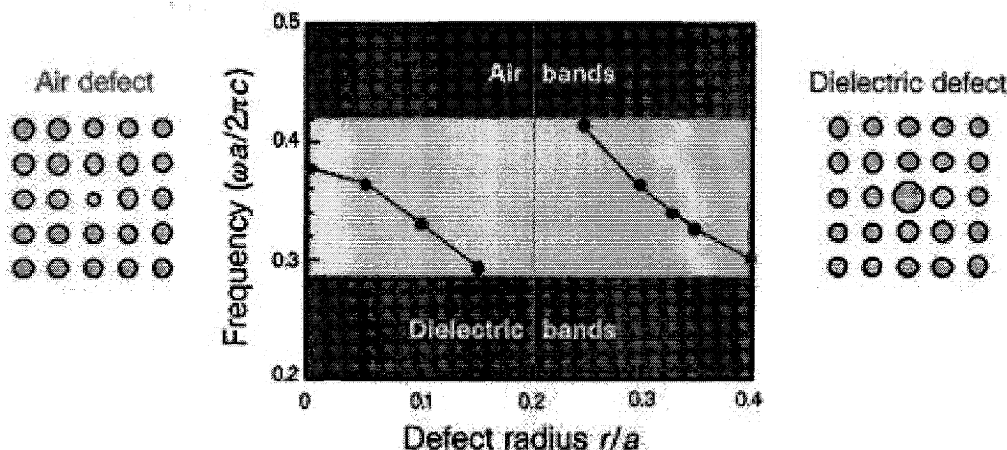

Figure 1-4. (from [2]) A defect introduced into the periodicity of a PC creates states within the PBG. Adding or removing dielectric determines the symmetry of the state. The size of the defect determines the frequency of the state.

1.3 History of PCs

1.3.1 Early Development

The idea that a material containing a dielectric periodicity in three dimensions may yield a complete PBG that forbids the propagation of certain frequency light in any direction was first proposed in 1987 [9,10]. It was believed that such a structure could be useful for semiconductor lasers, solar cells, or even heterojunction bipolar transistors where spontaneous emission into unwanted optical modes limits device performance; the dielectric periodicity could be designed so that the unwanted optical modes are eliminated within a certain range of frequencies corresponding to the PBG.

Ever since the work of Purcell [11] it has been realized that the rate of spontaneous emission can be controlled by modifying the radiation field surrounding an optical source (such as

an atom), thereby altering the atom-field coupling or the density of allowed optical states. Indeed, work with microwave cavities experimentally demonstrated inhibited spontaneous emission [12]. It was well established that a dielectric stack consisting of alternating layers of high and low dielectric material with quarter-wavelength thicknesses creates "stop-bands" for light at normal or near normal incidence within certain frequency ranges, a concept used for DFB semiconductor lasers, VCSELs, and various interference coatings. Analogously, it was believed that there may exist a 3D periodic structure with a lattice constant on the order of half the wavelength of light in the material that opens a complete 3D PBG. An optical source whose emission frequency lies within the PBG should then experience inhibited spontaneous emission because of the reduced density of allowed optical states.

Initial work involved searching both experimentally and theoretically for 3D structures possessing a stop band [13-15] in all directions and climaxed with the first discovery of a PC with a complete PBG [16]. Many papers were subsequently published in the past decade detailing new 3D PBG structures and corresponding fabrication techniques. The minimum feature size of each PC is on the order of half the wavelength of light. Therefore, most of the initial experimental work on 3D PCs was performed at microwave frequencies for ease of fabrication.

1.3.2 Recent Progress

The use of 3D PCs for integrated optical devices at telecommunication wavelengths (1.3-1.55 μm) requires minimum features sizes on the order of hundreds of nanometers; the construction of a 3D PC with such feature sizes has proven difficult and therefore the more interesting applications of PCs are in one and two dimensions. Recent work at telecommunication wavelengths has explored PC waveguides created by introducing line defects in 2D PCs [17-20], 2D PC lasers [21,22], microcavity filters [23], PC fibers[24-26], and 2D add-drop multiplexers\demultiplexers [27].

1.3.3 Future Trends

An extensive amount of theoretical and experimental work has been performed throughout the past decade exploring novel 3D PC structures that possess a complete 3D PBG and

corresponding fabrication techniques [28-30]. Until difficulties in fabricating 3D PC devices are overcome, the next generation of PC research will focus on device applications and implementation of microphotonics devices using 1D and 2D PCs. The continuous symmetry in one or more directions for lower dimensionality PCs introduces complications to device design otherwise absent in a perfect 3D PC. It is the interaction of a PC with its surroundings (in particular radiation modes that propagate away from the PC) that has become more important in terms of functionality than the specific design of the PC itself. For example, it is now well-established that linear defect waveguides may exist in a PC, but efficient input and output coupling of light from the waveguides has proven extremely challenging [31].

1.4 Enhanced Optical Sources Using PCs

Most of the work over the past decade on PCs has dealt with passive devices such as waveguides and filters. This thesis explores the use of PCs in enhancing the performance of light-sources based in III-V semiconductor materials. In particular, a PC (Figure 1-2a) is used to enhance the brightness of a light-emitting diode (LED). A large area PC is developed as part of a saturable Bragg reflector (SBR). Finally, a PC embedded in a waveguide (Figure 1-4b) is explored for use as an integrated ultra-low threshold microcavity laser with potential application to high-speed on-chip interconnection.

The goal of this thesis is to design, fabricate, and characterize the high-brightness LED, the large area SBR, and the microcavity laser; to do this more general problems concerning the use of PCs with active material are explained. For instance, the competition between radiative and nonradiative processes such as surface recombination is of central importance to the fabrication of any PC light source. Throughout the exploration of the PC devices presented in this work, several additional applications of PCs to microphotonics are discovered and investigated.

Chapter 2. The Two-Dimensional PC Semiconductor Light Emitting Diode

2.1 Semiconductor LED Efficiency

The total conversion efficiency of a light-emitting diode (LED) is given by the expression:

$$\eta = \eta_i \eta_r \eta_e , \qquad \text{(EQ 28)}$$

where η_i is the injection efficiency, η_r is the radiative efficiency, and η_e is the extraction efficiency. Semiconductor LEDs have the potential to be low-cost and long-lifetime solid-state lighting sources for applications as varied as room lighting to flat panel displays [32]. LEDs are also used in short-range telecommunication systems and may be desirable for optical interconnects in future optoelectronic systems [33, 123]. The interest in *semiconductor* LEDs as light sources stems in large part from their high injection and radiative efficiencies. That is, most of the current injected in a semiconductor LED generates photons rather than, for instance, generating heat

which unnecessarily wastes power. Unfortunately, most of the light emitted from a semiconductor LED is lost to planar guided modes propagating within the high dielectric material, where it may be reabsorbed, resulting in a low external efficiency (Figure 2-1a). The goal of Chapter 2 is to explore all methods of using a 2D PC to enhance light extraction from a semiconductor LED (Figure 2-1b) [34].

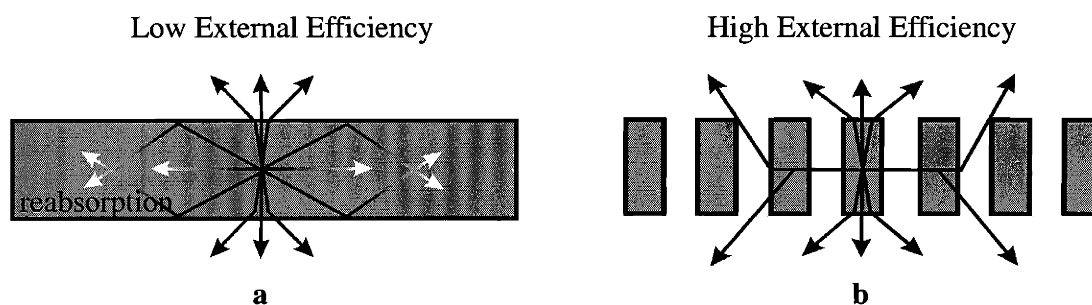

Figure 2-1. a) Total internal reflection causes reabsorption of emitted light. b) Periodicity in the dielectric constant increases LED efficiency.

2.1.1 Injection Efficiency

The injection efficiency for an electrically-pumped LED is the number of carriers that recombine in the active region relative to the total number of carriers injected into the device. Testing of LED designs often utilizes optical pumping of the active material to avoid lossy electrical contacts that may absorb significant amounts of the emission. For an optically-pumped LED, the injection efficiency is the number of photons that generate carriers relative to the total number of photons incident on the device. Different semiconductor LED designs may have different injection efficiencies. Therefore, in measuring LED performance by optical pumping it is important to account for effects on the injection efficiency. Since efficient electrical injection of carriers is typically used for LED devices in practice, the effect on η_i should be normalized out when exploring novel LED designs by optical pumping.

2.1.2 Radiative Efficiency

The radiative efficiency may be written in terms of the radiative and nonradiative recombination rates:

$$\eta_r = \frac{\frac{1}{\tau_r}}{\frac{1}{\tau_r} + \frac{1}{\tau_{nr}}} \quad \text{(EQ 29)}$$

where τ_r and τ_{nr} are the characteristic radiative and nonradiative recombination times that may each be subdivided into several different mechanisms. For the context of an LED, the component of $\frac{1}{\tau_r}$ due to stimulated emission is negligible and emission into all modes may be considered spontaneous. The irreversible spontaneous emission rate at a position $\mathbf{r}$ in a weakly-interacting system is given by Fermi's Golden Rule [35]:

$$\Gamma(\mathbf{r}) = \frac{2\pi}{h}\langle(\mathbf{d}\cdot\mathbf{E}(\mathbf{r}))\rangle^2\rho(\omega) \quad \text{(EQ 30)}$$

where $\mathbf{d}$ is the electric dipole moment of the transition, $\mathbf{E}(\mathbf{r})$ is the local zero-point rms electric field, and $\rho(\omega)$ is the density of electromagnetic modes. Inspection of EQ. 30 shows that emission may be inhibited/enhanced by minimizing/maximizing the dipole matrix element $\langle(\mathbf{d}\cdot\mathbf{E}(\mathbf{r}))\rangle$ or by decreasing/increasing the density of available optical states $[\rho(\omega)]$.

The spontaneous emission rate may be modified when emitting into a resonant optical mode, such as an optical cavity. Indeed, the maximum possible emission rate enhancement over that of bulk material is [35]:

$$\frac{\Gamma}{\Gamma_o} = \frac{3Q(\lambda/n)^3}{4\pi^2 n^3 V} \quad \text{(EQ 31)}$$

where $Q = \omega_o/(\Delta\omega)$ is the quality factor of the resonance, n is the index of refraction of the semiconductor, and V is the effective volume of the mode. EQ. 31 is called the Purcell enhance-

ment [11], and is particularly useful for enhancing emission from narrow linewidth emitters in microcavities. However, even semiconductors with high-quality quantum wells have broad emission linewidths at room-temperature and therefore the Q in EQ. 31 needs to be replaced by the material quality factor Q_m, which is typically much smaller. The exact value of the Purcell enhancement for a semiconductor quantum well is [36]:

$$\frac{\Gamma_s}{\Gamma_o} = \frac{3gQ_m(\lambda/n)^3}{16\pi n^3 V} \qquad \text{(EQ 32)}$$

where g is the degeneracy of the resonant optical mode. Therefore, the potential Purcell enhancement of η_r is typically small for a semiconductor LED. Even considering the smallest possible semiconductor cavity ($V = 2(\lambda/2n)^3$) and $_m = 10$ for an InGaAs quantum well, the enhancement is only ~2.5 (5 if both degenerate polarizations are included) [37].

2.1.3 Extraction Efficiency

The extraction efficiency is the number of photons that escape from the semiconductor LED into radiation modes relative to the total number of photons generated. Recall, that the primary reason for poor extraction efficiency in a semiconductor LED is reabsorption of the emitted light due to total internal reflection at the dielectric interfaces (Figure 2-1a). Reabsorption may not always translate to loss, however, as it may generate additional electron-hole pairs that recombine radiatively, a process called "photon-recycling." In theory then, if the radiative efficiency is equal to unity and no other parasitic absorption exists, then all photons are recycled and eventually extracted from the LED, no matter how poor the extraction efficiency. In most semiconductor LEDs, however, a finite nonradiative recombination rate exists. Even semiconductor LEDs fabricated from the highest-quality material, that intentionally use "photon-recycling" to achieve conversion efficiencies of 72%, are very susceptible to parasitic losses such as free carrier absorption [38].

2.1.4 LED Figure of Merit

Clearly, neither the radiative nor the extraction efficiency by itself is sufficient to fully measure the performance of a semiconductor LED. Rather, a more appropriate figure of merit is to couple the two together and define an external efficiency,

$$\eta_{ext} = \sum_N \eta i_r \eta i_e, \quad \text{(EQ 33)}$$

where N is the number of modes available to the emitting active region, ηi_r is the partial radiative efficiency into the ith mode, and ηi_e is the extraction efficiency of the ith mode.

To fully characterize a semiconductor LED then, the relative rates of electron-hole recombination, photon extraction, and photon reabsorption must be compared. An electron-hole pair generated in a semiconductor LED that recombines radiatively may either emit a photon directly into a free space mode or emit a photon into any other available mode in the high-dielectric semiconductor material. The former are extracted from the LED as useful light output, while the latter may either be extracted, recycled, or lost to any parasitic absorption mechanism, such as free carrier absorption. It is helpful then to rewrite EQ. 33 in terms of free and non-free space modes, so that the external efficiency for a LED becomes:

$$\eta_{ext} = \frac{\frac{1}{\tau_{fr}} + \sum \frac{1}{\tau_i} P_i}{\frac{1}{\tau_{fr}} + \sum \frac{1}{\tau_i}\left(P_i + A'_i\right) + \frac{1}{\tau_{nr}}} \quad \text{(EQ 34)}$$

where $\frac{1}{\tau_{fr}}$ is the emission rate into free-space modes, $\frac{1}{\tau_i}$ is the emission rate into the ith non-free space mode, $\frac{1}{\tau_{nr}}$ is the nonradiative recombination rate, and P_i and A'_i are the probabilities of extraction and parasitic absorption, respectively. The extraction efficiency of free space modes is assumed to be unity even though a small percentage of light is reflected at the interface between the dielectric and the free space. Even with such reflections, eventually, light emitted into free space modes is extracted and very little is absorbed. Notice that a photon-recycling rate term does not appear in the denominator since its *net* contribution to electron-hole recombination is zero.[1]

Since it is often the case that a single dominant non-free space mode (such as a guided mode) limits its external efficiency, EQ. 34 is rewritten for sake of clarity as

$$\eta_{ext} = \frac{\frac{1}{\tau_{fr}} \times 1}{\frac{1}{\tau_{fr}} + \frac{1}{\tau_{non}}(P + A') + \frac{1}{\tau_{nr}}} + \frac{\frac{1}{\tau_{non}} \times P}{\frac{1}{\tau_{fr}} + \frac{1}{\tau_{non}}(P + A') + \frac{1}{\tau_{nr}}} = \eta_r^{fr}\eta_e^{fr} + \eta_r^{non}\eta_e^{non}; \quad \text{(EQ 35)}$$

EQ. 34 can easily be extended for multiple non-free space modes.

2.1.5 Semiconductor LED Design

As stated in Section 2.1.2, the Purcell enhancement of the emission rate is small for semiconductor LEDs because of the broad emission linewidth of quantum wells at room temperature. However, the emission rate into a non-free space mode may be much higher than the emission rate into free space. For instance, for the standard dielectric-slab semiconductor LED shown in Figure 2-1a, the majority of radiative recombination emits into guided modes for which the extraction efficiencies are all zero because of total internal reflection. Therefore, in designing a high-efficiency semiconductor LED it is important to maximize the extraction efficiency η_e^{non} of the dominant non-free space mode. If the η_r^{non} into multiple non-free space modes are comparable, all the η_e^{non} should be maximized.

The leakage rate of the dominant non-free space mode in EQ. 35 into free space modes is $\frac{2\pi\nu}{Q}$, where ν is the photon frequency and Q is the modal quality factor. The absorption rate is $v_g\Gamma(\alpha + \alpha')$, where $v_g = c/n_g$ is the group velocity, n_g is the group index of the modes [6], c is the speed of light in vacuum, Γ is the overlap of the non-free space mode with the active region, α is the band-to-band absorption coefficient per unit centimeter, and α' is the total

1. Photon recycling actually lowers the probabilities of both extraction and parasitic absorption.

parasitic absorption coefficient per unit centimeter. Using EQ. 35 then, the extraction efficiency for any non-free space mode may be written using the relative rates of extraction and absorption:

Extraction Efficiency: Non-Free Space Mode

$$\eta_e^{non} = \frac{\frac{2\pi\nu}{Q}}{\frac{2\pi\nu}{Q} + v_g\Gamma(\alpha + \alpha')} \qquad \text{(EQ 36)}$$

If non-free space modes are available in the semiconductor LED, a high-efficiency design attempts to maximize the extraction efficiency through EQ. 36 by reducing the modal Q to satisfy the condition:

$$\frac{v_g Q V_a}{2V\pi\nu}(\alpha + \alpha') \ll 1 \qquad \text{(EQ 37)}$$

where the modal overlap is approximated as $\Gamma = \frac{V_a}{V}$ where V_a and V are the active and modal volumes, respectively. If the modal Q drops below the material Q, however, a reduced emission rate into the non-free space mode results (EQ. 32) in a lower external efficiency. EQ. 36 also states that a high-efficiency semiconductor LED minimizes the overlap between the non-free space modes and the active material to prevent reabsorption.[2] Minimizing Γ, however, will also reduce the dipole matrix element in Fermi's golden rule (EQ. 30). Therefore, a high-efficiency semiconductor LED design compromises emission rate and photon reabsorption. Calculations have been performed that lead to the conclusion of an optimal Q of [39]:

$$Q \sim Q_{material}, \qquad \text{(EQ 38)}$$

where $Q_{material} = \frac{\omega_o}{\Delta\omega}$ and ω_o and $\Delta\omega$ are the center frequency and full-width half-maximum of the emitter respectively. A maximum Q is desirable for narrow linewidth emitters (e.g Er^{3+}emitters [40]) and a maximum Γ if photon reabsorption is weak (e.g. certain organic emitters [39]). However, a semiconductor LED needs to be designed more carefully using EQ. 37 and EQ.

2. Situations do arise in which a maximum overlap with the active region is desired, an example of which is the low-threshold microcavity laser to be discussed in Chapter 4. Indeed, a high-Q is also desirable for the low-threshold microcavity laser to maximize the spontaneous emission rate and potentially increase the modulation rate.

38. Creating a high extraction efficiency non-free space mode using PCs will be explored in Section 2.2.4.

Another method of maximizing the external efficiency is to eliminate the existence of any non-free space modes (i.e. $\eta_r^{non} = 0$). In this case, the primary figure of merit to consider is the radiative efficiency η_r^{fr}.

Figure of Merit: Only Free Space Modes

$$\eta_r = \frac{\frac{1}{\tau_r}}{\frac{1}{\tau_r} + \frac{1}{\tau_{nr}}} \quad \text{(EQ 39)}$$

Elimination of non-free space modes using PCs will be explored in Section 2.2.2 and Section 2.2.3.

2.1.6 Previous Attempted Solutions

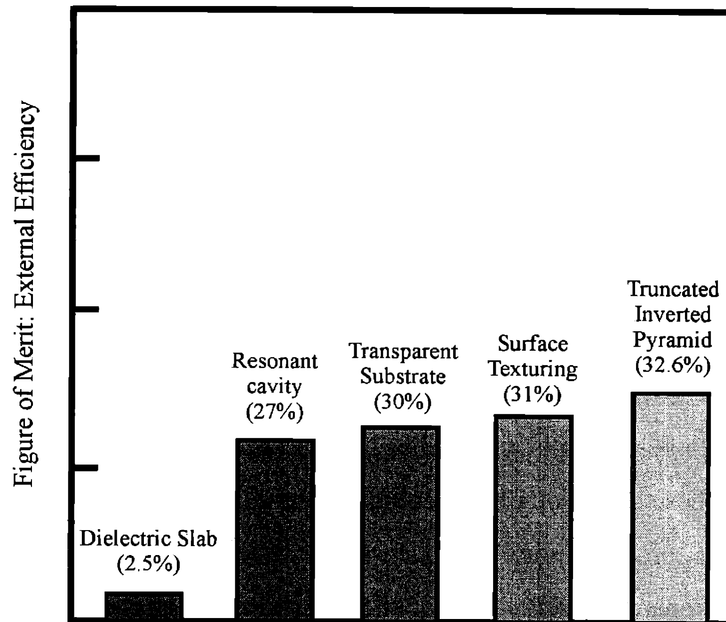

Figure 2-2. Past improvements on semiconductor LED external efficiency. For sake of comparison, the numbers plotted are "bare" external efficiencies which do not include any form of lens encapsulant.

Ever since the first demonstration of a practical semiconductor LED [41], several improvements have been made to enhance the external efficiency as summarized in Figure 2-2. By placing the emitter inside a microcavity, the number of optical modes may be limited to a set of resonant modes that couple light out of the device with maximum reported external efficiencies of 27% [41]. Microcavities are high-Q devices, however, and that limits the achievable extraction efficiency for semiconductor LEDs. In addition, the enhanced frequencies are limited to only the cavity resonances [43]. Semiconductor LEDs employing thick (albeit costly) transparent semiconductor layers have been optimized to gain external efficiencies as high as 30% [44]. Surface texturing is a promising technique for infrared semiconductor LEDs, with 31% demonstrated external efficiency. But surface texturing requires a relatively long free path before photons escape, which may be a problem for shorter wavelength visible LEDs that have more significant photon reabsorption [45]. Another costly approach used since the 1960s is to use chip-shaping technology (such as semiconductor domes [46, 49] and other shapes [48]) that help direct the emitted light out of the semiconductor. Recently, a more cost-effective approach using a trun-

cated-inverted-pyramid produced an external efficiency of 32.6% [49]. In addition, several groups have considered surface-plasmon-enhanced LEDs using periodically patterned metallic contacts, although no external efficiency data has been reported [50,51].

During the author's doctoral work, several other research groups began to simultaneously explore PCs as a method of increasing the external efficiency of semiconductor LEDs [36, 52-55]. In general, most groups report an "enhancement factor" by comparing the photoluminescence (PL) from an unpatterned device to that of a patterned device. In [52], a 10 times enhancement is reported from a 2D array of semiconductor microcolumns. In [53], a 6.25 enhancement is reported by using separate photon generation and PC light extraction regions. In [54], an enhancement factor of 4.5 is reported using a hexagonal pattern of holes as the PC. However, it is not clear if these observed enhancement factors directly correspond to an enhancement of external efficiencies. To determine the exact effect of the PC on external efficiency, it is not sufficient to simply compare the PL of the unpatterned reference structure to that of the PC structure. The PC LED and the unpatterned reference LED structures may have different injection efficiencies in addition to different radiative and extraction efficiencies.

In this work, the contributions of each injection and radiative efficiency are carefully separated from EQ. 28 while testing the devices in order to extract the true external efficiency of the semiconductor PC LED. Only then may a comparison be made to the alternative methods presented in Figure 2-2.

2.2 PCs for Semiconductor LEDs

PCs are used to design high-efficiency LEDs according to the guiding design principles presented in Section 2.1.5. PC LEDs have several additional important advantages that are worth considering especially from a cost-effective manufacturing point of view. First and foremost, the design may be scaled to any wavelength of operation simply using the scaling principles discussed in Section 1.2.6. In principle, the photonic band diagram only needs to be calculated once and may be applied to any wavelength of LED operation. The only limitation to the wavelength of operation is technological constraints on the fabrication at smaller wavelength dimensions. PCs also enable control over the directionality of the LED output, a useful characteristic for

interconnecting the PC LED with other optical components or directional display technology. PC LEDs may also enable rate-enhancement when using narrow-bandwidth emitters and therefore may operate at fast-modulation speeds. Finally, PCs are cost-effective in that they may be incorporated into any planar semiconductor LED design without dramatically increasing the cost of manufacturing.

2.2.1 Radiation States and Guided States

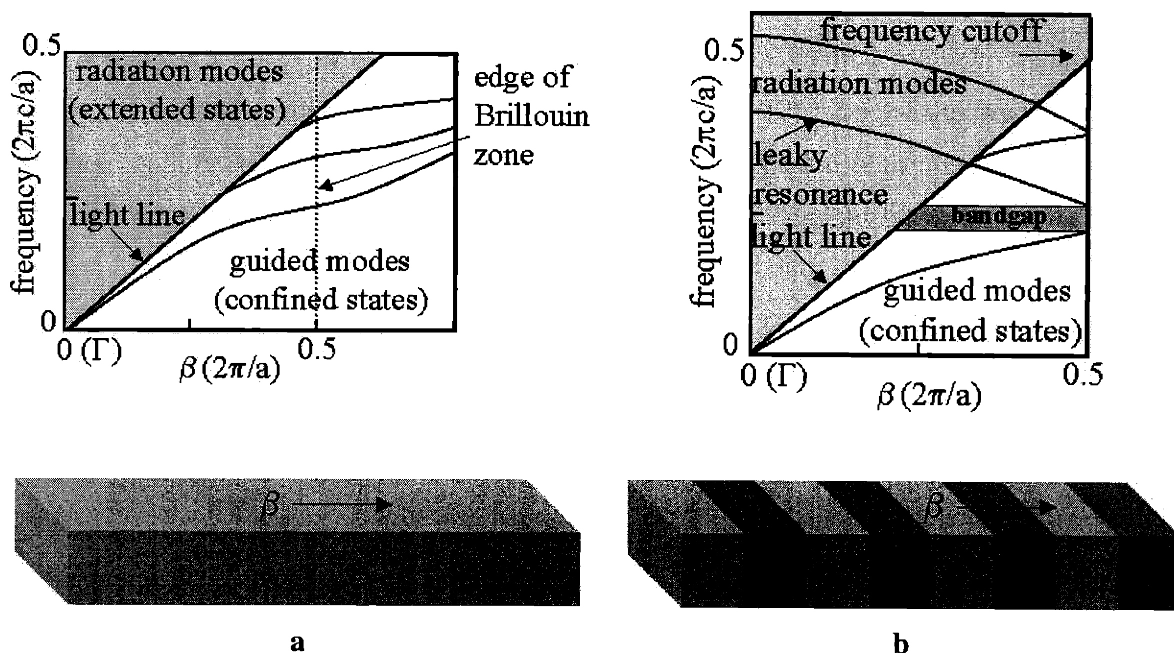

Figure 2-3. a) Dispersion relation along any direction in a dielectric slab. b) The effect of a periodicity in the dielectric constant on the disperison relation.

Semiconductor LEDs typically consist of a slab of high-dielectric semiconducting material such as AlGaAs or InGaAsP sometimes embedded with several quantum wells. A PC modifies the dispersion relation for a slab of dielectric material by opening several pathways to improve light extraction from an LED. Figure 2-3a shows light propagating in any direction in a slab of dielectric material[3] surrounded by some medium of lower dielectric constant (e.g air or oxide). The corresponding dispersion relation is also plotted in Figure 2-3a in units of $\frac{1}{a}$, where a is the unit cell repeat distance, or lattice constant, for the structure to be discussed in reference

3. A 1D scenario is presented for sake of clarity, but the conclusions drawn carry over easily into higher dimensionality.

to Figure 2-3b. For the simple slab scenario, there exist two types of optical modes, guided modes and radiation modes, separated by the "light-line:"

$$\omega = ck_0\sqrt{\varepsilon_1}, \qquad \text{(EQ 40)}$$

where k_0 is the wavevector of light in vacuum with frequency ω and ε_1 is the low-dielectric medium surrounding the LED slab.

The system has mirror symmetry about the plane parallel to the center of the dielectric slab. Therefore, there exist two irreducible representations of the eigenstates corresponding to transverse electric (TE) and transverse magnetic (TM) modes; TE/TM modes have their electric/magnetic field polarized in the plane of the dielectric slab. The guided modes are solutions to the transcendental equations:

TE Modes

$$\tan(k_\perp d) = \frac{2k_\perp\sqrt{(\beta^2-\varepsilon_1 k_0^2)}}{k_\perp^2-(\beta^2-\varepsilon_1 k_0^2)} \qquad \text{(EQ 41)}$$

TM Modes

$$\tan(k_\perp d) = \frac{2k_\perp\left(\frac{\varepsilon_2}{\varepsilon_1}\right)\sqrt{(\beta^2-\varepsilon_1 k_0^2)}}{k_\perp^2-\left(\frac{\varepsilon_2}{\varepsilon_1}\right)(\beta^2-\varepsilon_1 k_0^2)}, \qquad \text{(EQ 42)}$$

where β is the in-plane propagation wavevector of the guided mode, ε_1 is the dielectric constant of the surrounding medium, ε_2 is the dielectric constant of the slab, and $k_\perp$ is the wavevector perpendicular to the plane of the slab. Again, the solutions are eigenstates of the system that minimize the variational energy by confining their energy within the high-dielectric region while remaining orthogonal to lower energy eigenstates (see Section 1.2.4).

The solutions to EQ. 41 and EQ. 42 become imaginary when for a given frequency $\beta < k_0\sqrt{\varepsilon_1} = \frac{\omega}{c}$, which corresponds to the light line of the surrounding medium (EQ. 40). Thus, above the light line there are no guided modes but rather a continuum of radiation states. The radiation states cannot couple to guided states because of a phase mismatch; the tangential wavevector must be equal across the interface between the slab and the surrounding medium [56]. As a result, only light at a given frequency emitted in directions within the light line (or light cone for all directions in the 2D slab) will escape from the dielectric slab.

Therefore, using EQ. 34 and ignoring photon recycling so that all guided light is assumed to be parasitically absorbed ($A' = 1$), a lower limit on the external efficiency of the semiconductor slab may be written:

$$\eta_{ext} = \frac{1}{1 + \frac{\tau_g}{\tau_{fr}}}, \qquad \text{(EQ 43)}$$

where $1/\tau_g$ is the emission rate into guided states, and the active material is assumed to be of high-quality so that non-radiative recombination may be neglected. The relative fraction τ_g/τ_{fr} of the partial radiative emission rates is given by the fraction of emission into 4π steradians that falls within the light cone, $1/(2(n_1/n_2)^2)$, where here both sides of the slab are being included in the external efficiency. For an index of refraction of $n_1 = 3.5$ (typical for a semiconductor), and a surrounding medium of air ($n_2 = 1$), the external efficiency of the semiconductor slab is only about 4%. The low external efficiency of the slab is due to the large partial emission rate into guided slab modes relative to radiation states. If one were to include photon recycling the external efficiency would rise slightly and the parasitic absorption probability would be less than one.

A PC may be used to enhance the extraction of light from a semiconductor slab LED by: 1) eliminating guided modes in the plane of the dielectric slab with a PBG, 2) diffracting light into the radiation continuum, or 3) creating phase-matched (or "leaky") resonant states in the plane of the dielectric slab. A PC may also be used to create a cavity where a resonant mode efficiently couples light to radiation. The high Q cavity, however, results in a low figure of merit according to EQ. 36 and is therefore not an attractive use of PCs for high-efficiency semiconductor LEDs.

2.2.2 Elimination of Guided Modes with PBG

The folding of the dispersion relation for guided modes at the edge of the 1st Brillouin zone (Figure 2-3b) due to the PC may create a PBG for guided modes (see Section 1.2.8). By designing the PC such that the lattice constant (a) is on the order of the wavelength of light

emitted from the LED, the PBG may be made to overlap the emission spectrum. Since no guided modes are available within the PBG, emitted light is forced to couple to radiation states potentially leading to higher external efficiencies [34].[4] Photon recycling and parasitic absorption need not be considered for the case of the PBG provided the thickness of the slab is greater than their respective absorption lengths. An examination of EQ. 34, leads to a conclusion of 100% external efficiency when the emission spectrum lies within the PBG. However, the external efficiency is limited by nonradiative recombination. As discussed in Section 2.1.5, the figure of merit for the PBG LED should be the radiative efficiency, which for only free-space modes is equivalent to the external efficiency

$$\eta_{ext} = \frac{1}{1 + \frac{\tau_{fr}}{\tau_{nr}}}. \qquad \text{(EQ 44)}$$

The external efficiency is therefore entirely determined by the competition between radiative and nonradiative processes. The expected enhancement relative to a dielectric slab is given by the ratio of the corresponding extraction efficiencies (EQ. 43 and EQ. 44):

Photonic Band Gap Enhancement

$$E = \frac{1 + \frac{\tau_{fr}}{\tau_g}}{1 + \frac{\tau_{fr}}{\tau_{nr}}} \qquad \text{(EQ 45)}$$

2.2.3 Elimination of Guided Modes at High Frequencies

As was seen in Section 2.2.1, by calculating the dielectric modes of a semiconductor slab, the coupling of guided states to radiation states is forbidden due to a phase mismatch of the tangential wavevector at the interface between the dielectric slab and the surrounding low-

4. Here it is implied that a sufficient overlap exists between the zero-point field intensity of the radiation states above the light-cone and the active material so that the dipole matrix element in EQ. 30 is non-zero. Otherwise, no modes are available and emission will be completely suppressed.

dielectric medium. However, large wavevector photons emitted in the plane of the PC are Bragg scattered into the continuum of radiation modes by satisfying the phase-matching condition

$$(\vec{\beta} - \mathbf{k}') = \mathbf{G} \quad \text{(EQ 46)}$$

where $\mathbf{k}'$ is the component of $\mathbf{k_0}$ parallel to the plane of the dielectric slab and $\mathbf{G}$ is a reciprocal lattice vector. EQ. 46 amounts to a folding of the light cone at the edge of the 1st Brillouin zone (Figure 2-3b), creating a frequency cutoff above which only radiation states exist. Since only radiation modes exist, the external efficiency for a PC LED with an emission spectrum above the frequency cutoff is given by

$$\eta_{ext} = \frac{1}{1 + \frac{\tau_{fr}}{\tau_{nr}}} \quad \text{(EQ 47)}$$

where as in the case for the emission spectrum of the LED in the PBG, the external efficiency is determined entirely by the radiative efficiency. The enhancement in external efficiency is then again given by:

Enhancement Above Upper Frequency cutoff

$$E = \frac{1 + \frac{\tau_{fr}}{\tau_g}}{1 + \frac{\tau_{fr}}{\tau_{nr}}} \quad \text{(EQ 48)}$$

2.2.4 Extraction through PC Resonant States

The diffraction condition (EQ. 46) is also satisfied by folding guided modes at the edge of the 1st Brillouin zone (Figure 2-3b) to create resonances that exist above the light line. The resonant states may be "leaky" (finite Q) depending on the symmetry of the state. In general, the amount of light coupling between the resonant state in the slab which may be written as $\mathbf{E}_\beta(\mathbf{r}) = \hat{\mathbf{e}}|E_\beta(\mathbf{r})|e^{i(\beta \cdot \mathbf{r})}$, and the free space modes $\mathbf{E}(\mathbf{r})_{fr} = \hat{\mathbf{e}}_{fr}|\mathbf{E}_{fr}|e^{i(\mathbf{k} \cdot \mathbf{r})}$, is proportional to:

$$\int_V \mathbf{E}^*_{\beta}(\mathbf{r}) \cdot \mathbf{E}(\mathbf{r})_{fr} dV \quad \text{(EQ 49)}$$

where $\hat{\mathbf{e}}$ is a unit vector that gives the polarization, and V is the volume over which the modes are coupling. Note that if β does not equal $\mathbf{k}$, then the integral in EQ. 49 goes to zero and coupling cannot occur; the periodicity in the PC enables such phase-matching (EQ. 46). The integral also goes to zero if the resonant states do not have the same irreducible representation (the same symmetry) as that of the radiation states [57, 58]. A particularly useful case to consider is the enhancement of light extracted into the vertical direction through a guided resonance at the Γ-point in the 1st Brillouin zone [59].

The external efficiency when the material emission overlaps a leaky resonant state (denoted by the subscript "lr") is given by:

$$\eta_{ext} = \frac{1 + \frac{\tau_{fr}}{\tau_{lr}} \eta_e^{lr}}{1 + \frac{\tau_{fr}}{\tau_{lr}}\left(\eta_e^{lr} + A'\right) + \frac{\tau_{fr}}{\tau_{nr}}}. \quad \text{(EQ 50)}$$

where η_e^{lr} is the extraction efficiency of the leaky mode (EQ. 36). The enhancement factor relative to the unpatterned dielectric slab becomes:

Enhancement From Leaky Resonant Modes

$$E = \frac{\left(1 + \frac{\tau_{fr}}{\tau_{lr}} \eta_e^{lr}\right) \cdot \left(1 + \frac{\tau_{fr}}{\tau_g}\right)}{1 + \frac{\tau_{fr}}{\tau_{lr}}\left(\eta_e^{lr} + A'\right) + \frac{\tau_{fr}}{\tau_{nr}}} \quad \text{(EQ 51)}$$

2.3 Two-Dimensional Slab PCs

Any periodic dielectric contrast may be used to improve the extraction efficiency from a semiconductor dielectric slab LED. In general, 2D periodicities are preferred because of simplicity in fabrication relative to 3D structures and the higher order of symmetry relative to 1D

lattices. There is a large number of potential 2D lattices that may be chosen. This section describes the reasoning behind using a triangular lattice PC for a high-efficiency semiconductor LED.

2.3.1 The Triangular Lattice PC

Discrete periodicities, such as a square lattice of dielectric posts, yield PBGs only for transverse magnetic (TM) polarizations (Figure 2-4a); the physical reason being that the lowest energy band of optical states (the dielectric band) for the TE polarization has a low filling factor defined as

$$f = \frac{\int_{V_\varepsilon} \mathbf{E}(\mathbf{r}) \cdot \mathbf{D}(\mathbf{r}) d^3\mathbf{r}}{\int_{V} \mathbf{E}(\mathbf{r}) \cdot \mathbf{D}(\mathbf{r}) d^3\mathbf{r}}. \quad \text{(EQ 52)}$$

The filling factor describes the extent that the displacement field is concentrated inside the high-dielectric regions and hence, from EQ. 27, determines the energy of the optical state. For a square lattice of discrete dielectric posts, the transverse electric (TE) displacement field lines must be continuous and are forced to intersect the low-dielectric medium separating the posts, thereby reducing f and increasing the energy and the frequency of the dielectric band. The air-band concentrates itself in the lower dielectric region (low value of f) as well. Therefore, the two bands are too close to each other in energy to allow a PBG for the TE polarization. For the TM polarization, however, a PBG is possible with a discrete structure because of a large difference in f between the dielectric band and the air band. Conversely, connecting the posts to form a square weave pattern (Figure 2-4b) allows the displacement field lines to be continuous within the high-dielectric inside

the plane of periodicity. A PBG for the TE polarization is therefore possible with a connected structure.

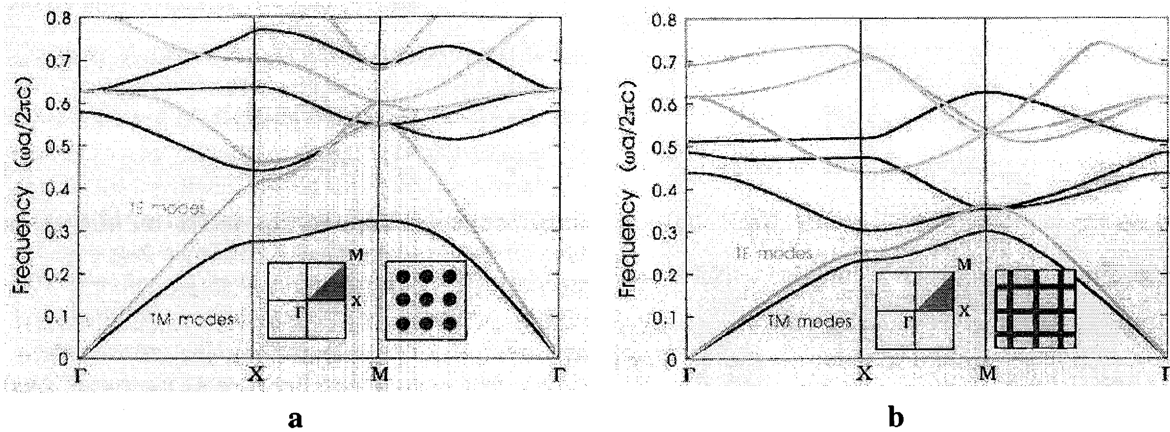

Figure 2-4. (from [2]) a) A square lattice of discrete dielectric posts allows for PBGs for TM polarizations but not for TE polarizations. b) A connected square weave pattern allows for PBGs for TE polarizations but not for TM polarizations.

By compromising the ratio of the lattice constant to the hole radius $\left(\frac{r}{a}\right)$, the hexagonal PC lattice (Figure 2-5a) can exhibit some extent of both connectivity and discreteness yielding a complete PBG for both polarizations (Figure 2-5b). The generic PC used consists of a triangular lattice of air holes of diameter (d) and hole spacing or lattice constant (a), embedded within a high-dielectric semiconductor. Air holes are used rather than rods to allow for more active material within the semiconductor slab per unit area.

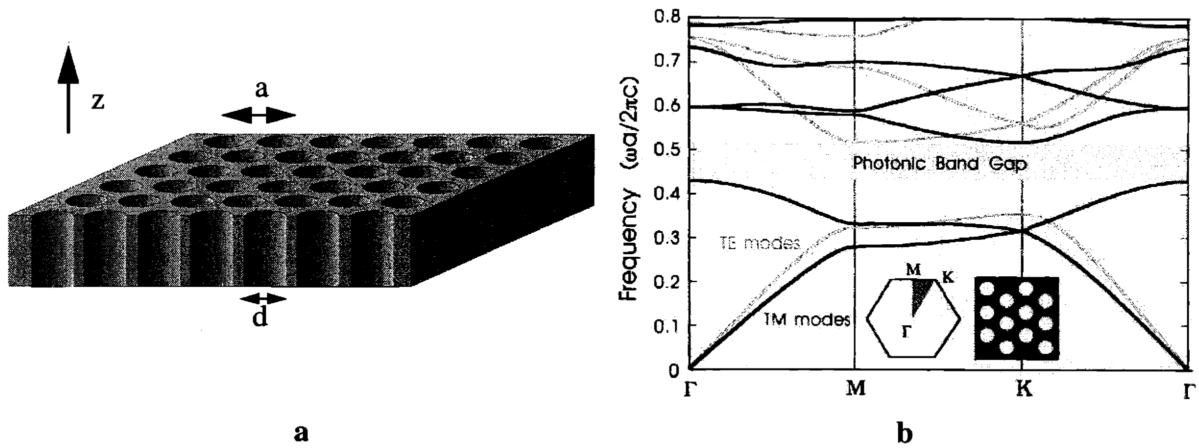

Figure 2-5. (from [2]) a) Generic PC consisting of a triangular lattice of air holes in high-dielectric semiconductor. b) Calculated photonic band diagram for PC in (a) extruded infinitely in the z-direction with r=0.35a (inset: the Brillouin zone and reduced Brillouin zone (shaded) along with the real space orientation of the triangular PC.

The second reason for using triangular lattice PCs for high-efficiency semiconductor LEDs stems from the high order of rotational symmetry in the system leading to: 1) an increased density of resonant optical states available for diffracting light out of the plane of symmetry and a subsequent increase in the partial rate of emission into those leaky resonant states, and 2) an increased directionality in the emission. The density of states is inversely proportional to $1/(\nabla_{\mathbf{k}}\omega(\mathbf{k}))$. The slope of each band of optical states approaches zero near points of high symmetry in the 1st Brillouin zone, such as the Γ-point, corresponding to the vertical direction (normal to the plane of periodicity). Therefore, as the number of optical bands folded back to the Γ-point that overlap the emission spectrum increases, the density of states increases. The higher the order of rotational symmetry, the more points in the 1st Brillouin zone at which optical bands are folded back to the Γ-point. Therefore, a triangular lattice is used in the LED design rather than a square lattice such as that shown in Figure 2-4a.[5]

5. An even higher density of states may be possible using quasicrystalline structures. However, the emission rate is still limited by the broad material quality factor for semiconductors (see Section 2.1.2).

2.3.2 Mirror Symmetry: TE-like and TM-like Solutions

When the generic 2D PC shown in Figure 2-5 is truncated to form a semiconductor slab of finite height in the z-direction, a light-line is introduced separating guided states from radiation states (see Section 2.2). The LED slab must be relatively thin so that higher-order guided modes are not introduced that result in additional pathways through which light may be parasitically absorbed. However, the slab must be thick enough to provide sufficient electron confinement in the active material (typically a quantum well located at the center of the semiconductor slab). A thickness on the order of $\frac{\lambda}{2n}$ is optimal which for a semiconductor LED and for optical fiber telecommunication wavelengths is approximately 200 nm. Since the slab LED is so thin, it must be placed on a thicker substrate for physical strength. The introduction of a substrate, however, removes the mirror symmetry from the LED slab. Therefore, the optical modes may no longer be classified in a strict formalism as purely TE (TM), but rather TE-like (TM-like), in the sense that the majority (above some predetermined threshold) of the electric (magnetic) field is polarized in the plane of the LED slab.

2.4 Materials Design

A III-V semiconductor material system is chosen for the high-efficiency PC LED to maximize the radiative efficiency of the active region. The active material needs to be epitaxially-grown and lattice-matched to a high-dielectric III-V substrate (GaAs or InP) for sufficiently high radiative efficiency. If the thin generic PC slab shown in Figure 2-5 were to be placed directly on the high-dielectric substrate, then the majority of emitted light would be lost to guided modes in the substrate. Therefore, a lower dielectric material is required to separate the active region from the substrate. Since radiation modes exist in both the air above the PC slab and in the underlying low-dielectric, a low loss mirror would be beneficial to reflect downward propagating light into the forward direction for maximum brightness. One possibility is to separately grow the active region and the low loss mirror and then wafer bond them together. However, wafer bonding may degrade the quality of the active region leading to poorer radiative efficiency. Therefore, a more attractive solution is to epitaxially grow and process the entire structure without the need for wafer bonding.

2.4.1 Generic High-Efficiency PC LED Structure

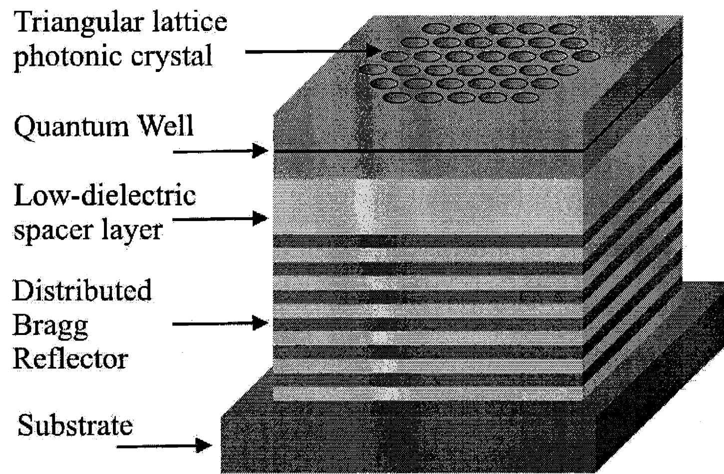

Figure 2-6. a) High-Efficiency PC LED generic design

The chosen generic PC LED structure (Figure 2-6) consists of a quantum well active region, a low-dielectric spacer layer, a low-loss distributed bragg reflector (DBR), and a substrate. A quantum well is chosen because it emits primarily TE radiation [6]. The TM-like PBG closes because of the low-dielectric spacer layer and the absence of mirror symmetry. The TE-like PBG remains large enough however to eliminate guided TE-like modes (see Section 2.3.1). The entire LED structure lies on top of a high-dielectric substrate. A DBR consisting of alternating high and low dielectric layers of quarter-wavelength thickness is placed beneath the active region to avoid loss of emitted light to the substrate. The DBR is in essence a PC in 1D with a PBG encompassing the emission spectrum. DBRs are commonly used for VCSELs and strongly reflect light at normal or near-normal incidence [6]. The DBR is separated from the active region of the LED structure by a low-dielectric spacer layer. The purpose of the low-dielectric spacer layer is to avoid loss of emitted light to the high-dielectric layers within the DBR.

2.4.2 Nonradiative Surface Recombination

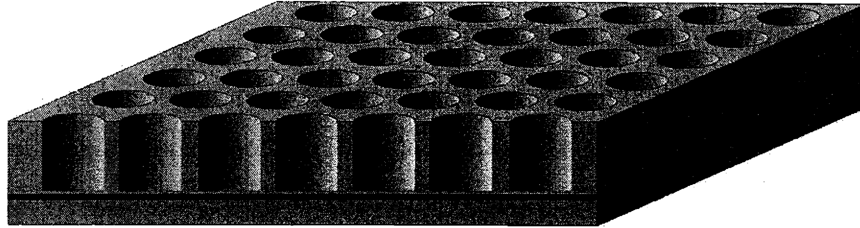

Figure 2-7. a) Asymmetric active region used in high-efficiency PC LED structure

One of the major concerns of using PCs in active devices, such as an LED, is the presence of surfaces near the active material. Surface states provide pathways for nonradiative recombination reducing the external efficiency of the device (see EQ. 44, EQ. 47, and EQ. 50). One method of avoiding surface recombination is explored in [53], where the active (light-emitting) region is separated from the PC (light-extracting) region. A more compact design, however, is to place the active material directly below the PC region (Figure 2-7).[1] Therefore, electron-hole pairs that are confined in the quantum well cannot recombine non-radiatively at the surfaces of the air holes. By making the active region asymmetric, the relative depth of the holes may be made deep enough to strongly scatter the light in the dielectric slab and obtain the high-efficiency benefits of the PC.

2.4.3 Advantages of Asymmetric Active Region

There are several advantages to the asymmetric active region in addition to compactness. For the PBG-enhanced structure, where nonradiative recombination directly competes with radiative emission into free space modes, it is important to not have any exposed surfaces in the quantum well. For the leaky resonance-enhanced structures, the asymmetric active region skews the leaky resonant mode profile towards the top air-interface thereby decreasing Γ and the rate of reabsorption before the light can escape.

1. Compactness is crucial for III-V semiconductor LED manufacturing since the cost per unit area is much higher than in silicon.

2.4.4 Active Region

The active region consists of an InGaP/InGaAs quantum well structure emitting at a wavelength of 980 nm. InGaAs is a fairly common material for semiconductor lasers because 980 nm is the wavelength that pumps erbium-doped optical amplifiers [60,61]. A high-efficiency LED emitting at 980 nm may become useful for optical interconnection. InGaP is chosen as the barrier layer for the quantum well because it can be easily lattice-matched to GaAs. Also, the surface recombination of InGaP is an order of magnitude lower than that of GaAs [62-64].

2.4.5 Spacer Layer: Thermal Oxidation of AlGaAs

The spacer layer must be a low-dielectric material compatible with the other materials in the high-efficiency PC LED structure. One option is to deposit a low-dielectric material directly; but since the spacer layer is buried, the deposition would need to occur prior to the deposition of the active region. The active region is a crystalline material and hence must be grown epitaxially along with the rest of the structure. Various semiconductor materials are available for epitaxial growth, but the dielectric contrast is very small.

Another option is to convert a semiconductor material into a lower dielectric material after it has been grown epitaxially. AlAs may be grown epitaxially and lattice-matched to the GaAs substrate. Throughout the past decade, thermal oxidation has been used in various applications to convert high Al-containing layers of AlGaAs into a low-dielectric Al_2O_3 material [66]. Therefore, Al_2O_3 is chosen as the material for the spacer layer. The thickness of the spacer layer is 0.5 μm (thick enough ($>\frac{\lambda}{2n}$) to reduce loss of emitted light to the high-dielectric layers in the DBR). Since the spacer layer is relatively thick it is grown epitaxially as $Al_{0.98}Ga_{0.02}As$, where 2% Ga has been added to reduce the amount of interfacial strain upon oxidation (see Section 3.3).

2.4.6 The Distributed Bragg Reflector

To obtain the high-dielectric contrast necessary for a DBR with a wide stop-band, each period is chosen to consist of the bilayer period $GaAs/Al_2O_3$. Figure 2-8 shows the calculated reflectivity spectrum of a 6-period oxidized $GaAs/Al_2O_3$ mirror and compares it to the

unoxidized 6-period GaAs/AlAs mirror. Transmission matrices are used in the calculation and the MATLAB code may be found in Appendix A.1. It is possible to simply use a GaAs/AlAs mirror for high-reflectivity, as is commonly done for VCSELs, but the very small index contrast between GaAs and AlAs ($\Delta n \approx 0.4$) usually requires nearly 30 pairs for sufficient reflectivity. The low-dielectric Al_2O_3 ($n = 1.6$), however, requires less layers in the DBR as compared to AlAs ($n= 2.91$), creates a wide stop band from 800-1300 nm, and uses the same thermal oxidation process step as is already necessary for the conversion of the spacer layer. Maximum reflectivity at $\lambda \approx 980\,\text{nm}$ is obtained when the thickness of each layer is given by a quarter-wave ($t = \frac{980}{4n_{layer}}$), where n_{layer} is the index of refraction of the corresponding layer.

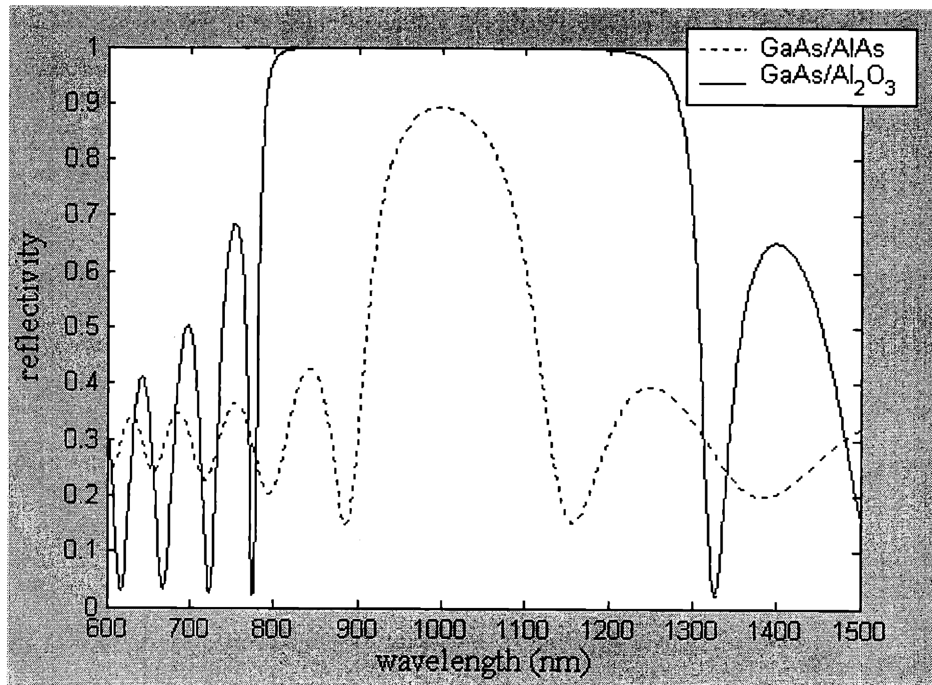

Figure 2-8. a) Reflectivity (calculated) of a 6 period AlAs/GaAs DBR (dotted line) as compared to a 6 period Al_2O_3/GaAs DBR (solid line).

2.4.7 Material Growth and Characterization

The material system for the PC LED is grown using gas-source molecular beam epitaxy (GSMBE) in a Riber 32P system (Figure 2-9). GSMBE provides the thickness and compositional control necessary for the high-efficiency PC semiconductor LED structure. The group III elements (Al, Ga, In) are evaporated from solid sources while the group V elements are cracked from gas sources (AsH_3 and PH_3). The material composition and layer thicknesses are verified by x-ray diffraction. A typical x-ray diffraction spectrum taken from the PC LED material structure (as-grown but not oxidized), is compared to the simulated structure in Figure 2-10. Matching the positions of the experimental peaks to the calculated peaks determines the composition of the grown structures. Matching the widths of the peaks determines the thicknesses of the as-grown structure (see [67] for more detail on the x-ray analysis). The oxide does contract upon oxidation so that thicker AlAs layers may need to be grown. However, the DBR layers are typi-

cally still grown as quarter-wave Al_2O_3 thicknesses because of the wide stop-band of the DBR (see Section 3.2.2).

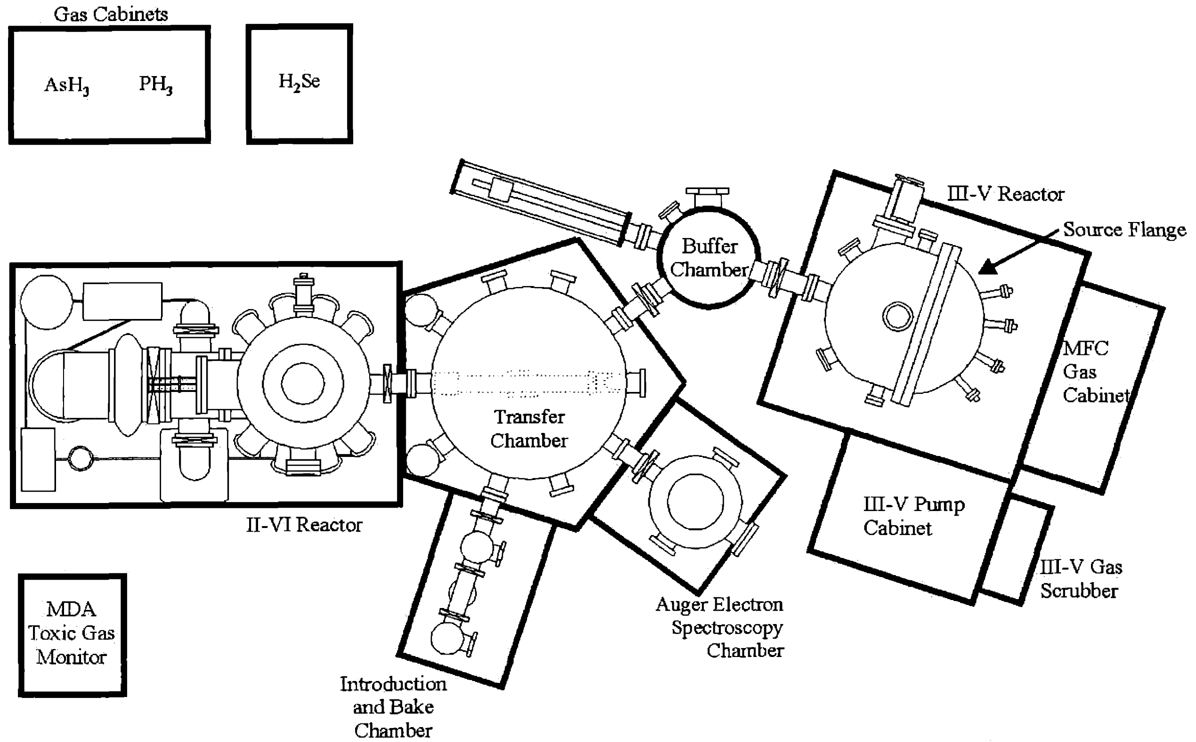

Figure 2-9. a) Riber 32P molecular beam epitaxy system and other interconnected ultrahigh vacuum chambers

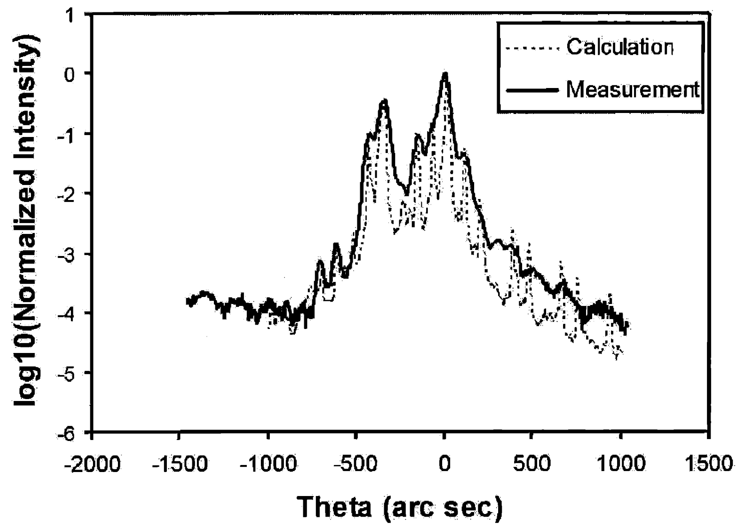

Figure 2-10. X-ray diffraction measurement of PC LED materials structure grown by GSMBE.

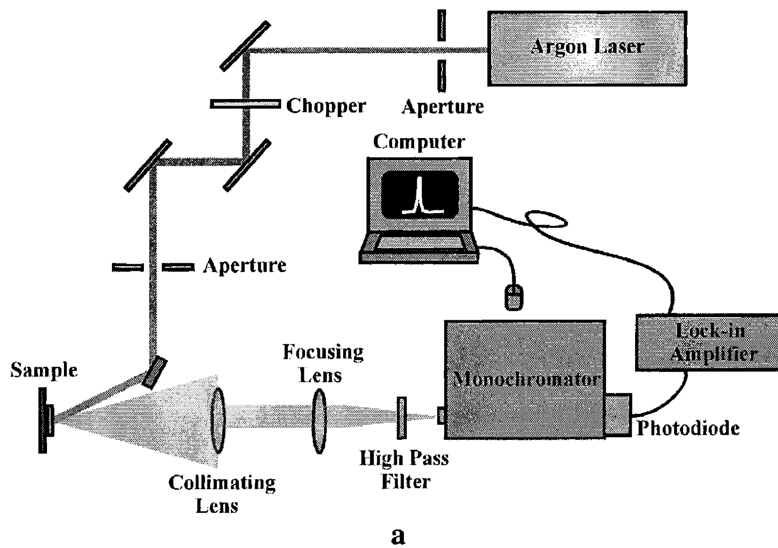

Figure 2-11. a) PL experimental set-up. b) Room temperature PL from InGaP/InGaAs quantum well.

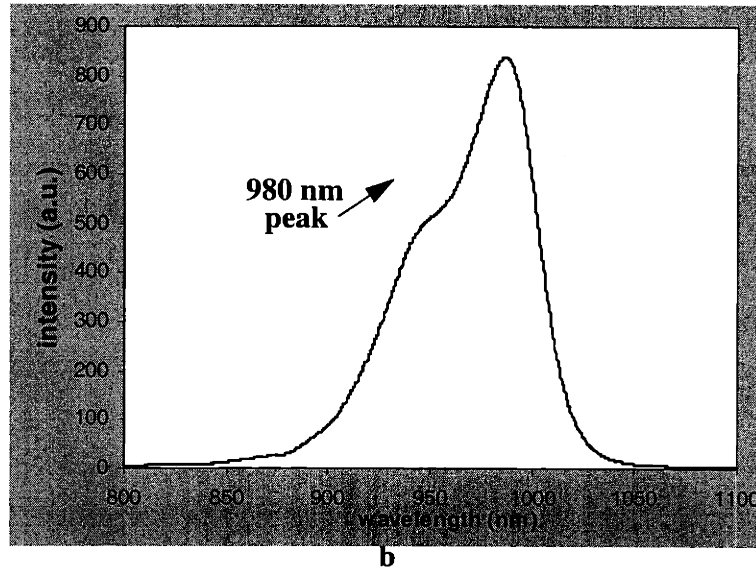

Figure 2-11. a) PL experimental set-up. b) Room temperature PL from InGaP/InGaAs quantum well.

The emission spectrum of the quantum well is measured using room-temperature photoluminescence (PL) [Figure 2-11a]. The sample is pumped using an argon laser emitting at a wavelength of $\lambda = 514$ nm. Light is focused into a spectrometer and the intensity is measured with a lock-in amplifier (see [67] for more detail on the PL measurement). A typical emission spectrum for an 8 nm $In_{0.20}Ga_{0.8}As$ quantum well with $In_{0.51}Ga_{0.49}P$ barrier layers lattice-matched to GaAs, is shown in Figure 2-11b. The emission peak is at $\lambda = 980$ nm, the desired wavelength for the high-efficiency PC LED. The high-frequency feature in the spectrum corresponds to a higher order transition in the quantum well and can be removed at lower pump powers.

2.5 Photonic Crystal Design

Various parameters of the PC such as hole radius, lattice constant, and index contrast determine the photonic band structure. In this section, PC designs are presented that yield PBG-enhanced structures (Section 2.2.2) and structures that contain leaky resonances (Section 2.2.4). A large majority of the emission from the leaky resonant structures is above the upper-frequency cutoff (Section 2.2.3) so that the emission rate into radiation modes and the leaky modes may be compared.

2.5.1 PBG-Enhanced Structure

To enhance extraction from the LED by eliminating guided modes (section 2.2.2), the PC depicted in Figure 2-12a is inserted in the active region of the generic high-efficiency PC LED structure (Figure 2-5). The PC creates a PBG (shown in white in Figure 2-12c) that overlaps both the GaAs/Al_2O_3 DBR stop-band and the InGaAs quantum well emission peak.

The photonic band diagram (Figure 2-12b) is calculated using the methods described in Section 1.2.4. Even though the calculation is performed without the presence of the DBR, it is accurate since the Al_2O_3 thickness is large enough (500 nm) to optically isolate the modes in the active region from the high-dielectric layers in the DBR. For $\lambda = 980$ nm, the dielectric constant of Al_2O_3 is $\varepsilon = 2.75$ [69] and the dielectric constant of the entire active region is assumed to be $\varepsilon = 10.43$ for InGaP. The change in the dielectric constant of the active region due to the InGaAs quantum well is neglected because of its small thickness (8 nm) relative

to the entire active region (134 nm). Finally, to center the PBG at $\lambda = 980\,nm$, the lattice constant is set at $a = 319\,nm$.

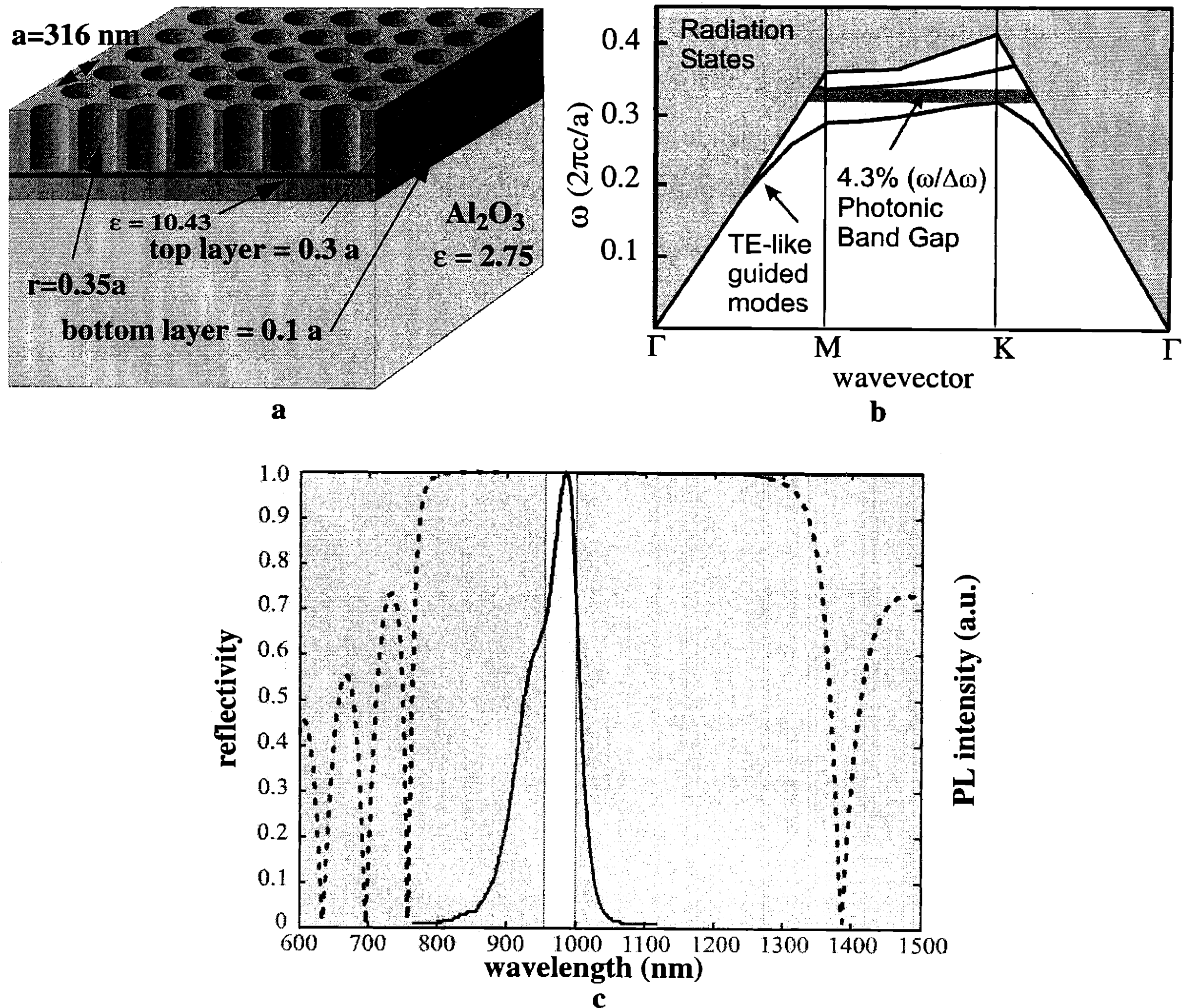

Figure 2-12. a) PBG-enhanced LED structure (a) used for calculation of photonic band diagram (b). A PBG is created surrounding the quantum well emission and overlapping the DBR stopband.

Figure 2-13 is a plot of the electric field intensity when a dipole is excited inside a slab, embedded with the PC from Figure 2-12a, at a frequency that lies inside the PBG. The absence of guided modes at that frequency within the PC slab forces light to emit into radiation states that propagate away from the structure. For the PBG-enhanced structure in Figure 2-12a, 30% of the total amount of emitted light is expected to emerge from the active region when con-

sidering both sides of the slab. The calculated enhancement assumes the absence of nonradiative recombination which according to EQ. 44 should yield an external efficiency of 100%. The reason for the difference in values is due to the asymmetry of the structure in Figure 2-12a. Since the modes are not entirely TE, but rather are TE-like as discussed in Section 2.3.2, the PBG must be thought of as a pseudo-gap. Some of the emitted TE-radiation may couple to TM-like guided modes that do exist in the TE-like pseudo-gap shown in Figure 2-12b. Still, a 30% external efficiency is a vast improvement over the unpatterned semiconductor dielectric slab ($\eta_{ext} \sim 2.5\,\%$), and is competitive with the past designs described in Figure 2-2.

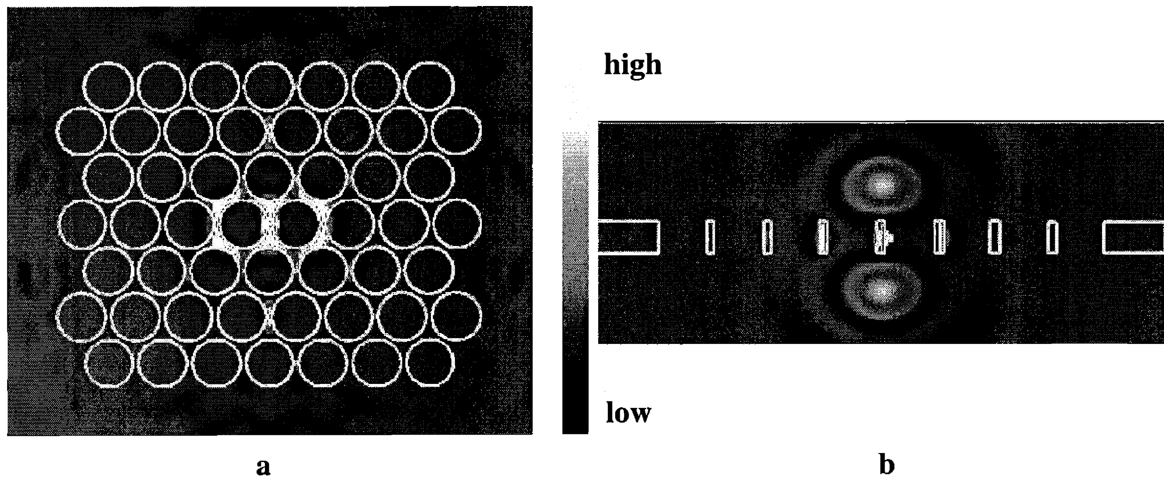

Figure 2-13. a) top view and b) side view of electric field intensity calculation of a photonic crystal slab when a dipole is excited that emits a frequency within the PBG.

2.5.2 Resonance-Enhanced Structure

A leaky resonance-enhanced structure contains smaller air holes (Figure 2-14a) and a thicker active region relative to the PC used to create a PBG (Figure 2-12a). A portion of the photonic band diagram is shown in Figure 2-14b. A comparison to Figure 2-14b shows that the smaller holes (r=.15a) and thicker active region (198 nm) decrease the energy of the bands as prescribed by EQ. 27. Figure 2-14b is plotted for a lattice constant of $a = 380\,\text{nm}$. The guided resonances at the Γ-point overlap the emission spectrum of the quantum well leading to higher

extraction from the LED. As in Figure 2-12c, the emission spectrum overlaps the wide stop-band of the DBR

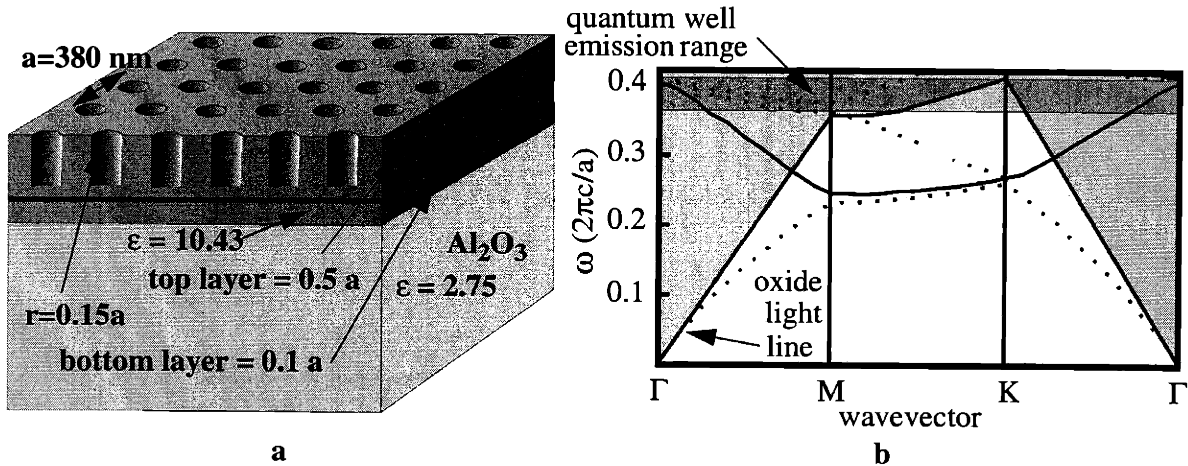

Figure 2-14. Schematic of diffraction-enhanced LED structure (a) and corresponding calculated photonic band diagram (b). The solid line indicates a band that is folded at the edges of the Brillouin zone to create a guided resonance at the Γ-point that lies within the emission spectrum of the LED (dark-shaded region).

Figure 2-15 is a plot of the enhancement from the structure in Figure 2-14a as compared to an arbitrary reference. The various spikes in the enhancement spectrum are attributed to the high partial emission rate into leaky-resonance modes as compared to free-space radiation modes, both of which overlap the quantum well emission spectrum (Figure 2-14b). It is assumed in the simulation that no nonradiative recombination exists. The total external efficiency

expected from such a structure is over 90% [34] provided: 1) that nonradiative recombination does not exist and 2) that all light reflected by the DBR is collected.

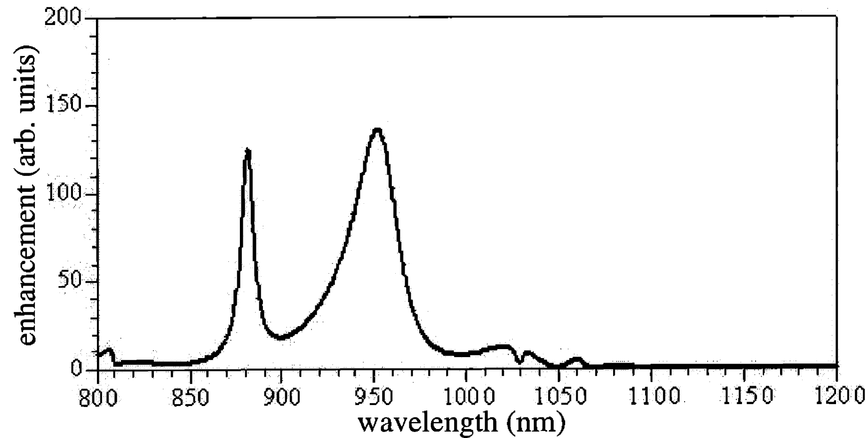

Figure 2-15. Calculated enhancement from leaky-resonance high-efficiency LED structure.

2.6 Device Fabrication

Fabrication of the high-efficiency semiconductor PC LED is non-trivial for two primary reasons. First and foremost, the minimum feature size [lattice constant (*a*)-hole diameter (*d*)] is on the order of 100 nm requiring sophisticated lithographic techniques. Secondly, the diverse III-V materials system used contains both In-based and Ga-based ternary compounds which each require different etch chemistries.

2.6.1 Sample Layout

In order to understand light extraction as a function of the ratio of lattice constant to the hole radius for the PC LEDs and to compare measured enhancements to predicted enhancements, each sample contains an array of PC LED mesas (Figure 2-16a). The array of LED mesas

is surrounded by a border of LED mesas that do not contain PCs (Figure 2-16b); the purpose of the border is a reference for comparison while testing the PC LED mesas.

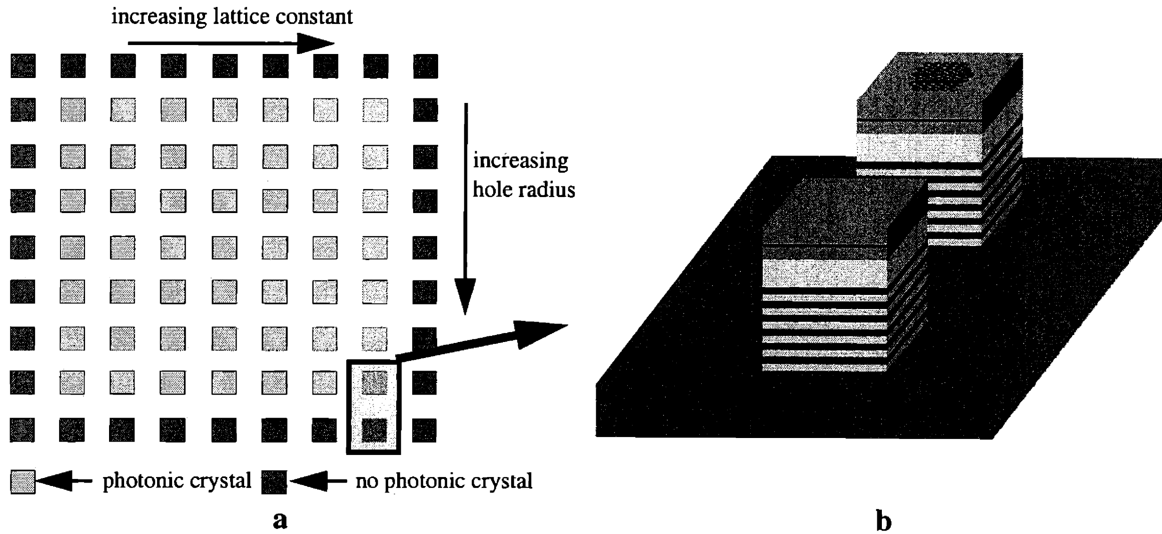

Figure 2-16. a) Each PC LED sample contains an array of LED mesas. The lattice constant is changed along one direction while the hole radius is changed along the other direction yielding a wide range of (r/a) ratios. b) The array is surrounded by a border of LED mesas that do not contain a PC.

2.6.2 Process Overview

The PC LED mesas are fabricated using various lithography, deposition, oxidation, and etching techniques as presented in Figure 2-17. The epitaxial growth of the PC LED material structure is described in Section 2.4.6. The epitaxial growth is performed on a 2 inch GaAs wafer substrate. Following epitaxy, each wafer is cleaved into approximately .25 cm^2 samples each of which is taken through the fabrication process. The fabrication process is closely monitored using primarily scanning electron microscopy (SEM) and optical microscopy.

2.6.3 Evaporative Deposition of SiO_2

The first step for each PC LED sample is the electron beam deposition of 50 nm of SiO_2 that is used as an etch mask for transferring the PC pattern into the active region. Although in theory the PMMA electron beam resist itself may be used as an etch mask, SiO_2 provides a better etch mask during transfer of the PC pattern into the active region. SiO_2 is also chosen as the etch mask because it may be stripped using CHF_3, a non-destructive etchant gas; metal masks require etchants that attack parts of the diverse materials system used in the PC LED materials system. Typically, a quarter of the 2 inch wafer is coated with SiO_2 prior to cleaving individual samples.

Several samples (typically 4) are processed in parallel and shall hereafter be referred to as the "batch." Processing a batch of samples: 1) saves time in the event that errors occur during processing of one of the samples in the batch and 2) provides parallel-processed monitor samples that may be Au-coated and examined with the SEM at any point in the fabrication process.

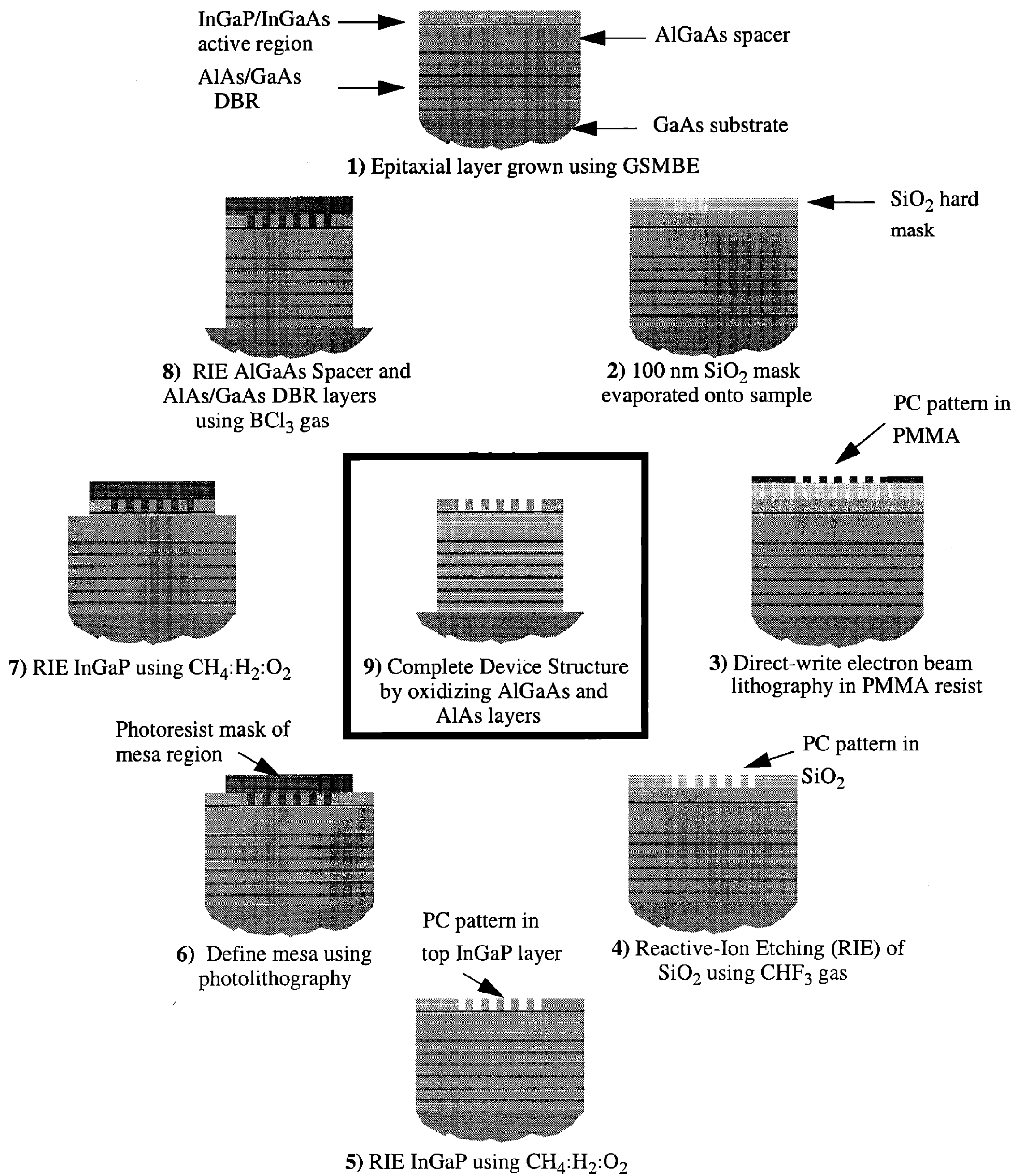

Figure 2-17. Overview of fabrication process for high-efficiency semiconductor PC LED.

2.6.4 Direct Write Electron Beam Lithography

The minimum feature size for the PC [lattice constant (*a*) - hole radius(*d*)] used in the PC LED is below the resolution limit for conventional photolithography. Available higher resolution lithographic techniques include inteferometric lithography, deep ultra-violet (UV) photolithography, x-ray lithography, and electron beam lithography. Interferometric lithography that provides a uniform periodic pattern across a large area is inappropriate for the PC LEDs because of the different PC patterns desired on each sample. X-ray and deep UV lithography require the construction of a hard mask. Therefore, anytime the PC patterns need to be altered a new hard mask must be constructed, a tedious process. Therefore, direct-write electron beam lithography (EBL) is deemed the most appropriate form of lithography for the PC LED. New PC patterns may be generated simply by changing the parameters of a computer-aided design (CAD) file input into the EBL system. In addition, various PC patterns (of different lattice constant and hole sizes) are easily included in the same pattern file.

In direct-write EBL, an electron beam is focused onto an electron beam resist, in this case a 3% solution of polymethylmethacrylate (PMMA) in chlorobenzene; the resist is positive so that areas exposed to the electron beam are removed during a development process that follows the exposure. The electron beam translates in an x-y coordinate system by 6.1 nm steps. Each step is represented by a pixel in the CAD file. Thus, the CAD file for the PC patterns contains selected pixels in the regions of the holes. The PC patterns are created using a CAD program developed at MIT specifically for compatibility with the .vsx file format used by the direct-write EBL system in the nanostructures laboratory (NSL) at MIT.

It was initially believed that the circular electron beam profile may itself be utilized to generate holes of the correct size for the PC by simply having one pixel per hole arranged in a triangular array. Each dose (related to the amount of time the electron beam remains focused on each pixel) then corresponds to a particular hole size. The dose was changed by varying the clock-speed on the EBL system. The hole sizes, however, were too small using only a single pixel per hole. The holes of the PCs are therefore instead written as multiple pixel square boxes that subsequently become circular due to the finite electron beam width (~60 nm). The side of

each square box is approximated by the diameter of the desired hole minus the beam width. Further details on the electron beam dosing for the PCs are found in [67].

The coating of the electron beam resist proceeds as follows: first each sample is placed on a vacuum spinner and sprayed with a N_2 gun to remove any dust particles that may lead to a non-uniform coating. An RCA-cleaned glass dropper is used to place a small drop of 3% PMMA in chlorobenzene on the center of each sample. Each sample is then spun at 3.6k rpm for 1 min. If the uniformity of the coating is non-satisfactory, the PMMA is stripped in acetone, rinsed with isopropanol, and the coating process is repeated. The samples are then baked at 180°C for 1 hour to further improve surface uniformity of the PMMA. The pyrex carrier boat used to bake the sample is placed inside the oven ahead of time to help maintain a constant temperature throughout the entire hour. The final layer thickness of the PMMA is 200 nm.

Following electron beam exposure each sample is developed in 300 mL of a 1:2 solution of methyl-isobutyl-ketone (MIBK): isopropanol (IPA) in the clean-room of NSL. The components of the solution are carefully measured in a graduated cylinder (a new batch for each sample). The solution is hand-warmed to 20°C (slightly above room temperature) and the sample is submerged for 90 seconds, followed by a 1 minute rinse in IPA to dissolve the MIBK. The sample is then dried with a N_2 gun and the development is verified using an optical microscope with a 100x objective. A typical scanning electron micrograph (SEM) of holes in PMMA is

shown in Figure 2-18. The sample shown is Au-coated to provide a higher-quality image of the PMMA (a poor conductor).

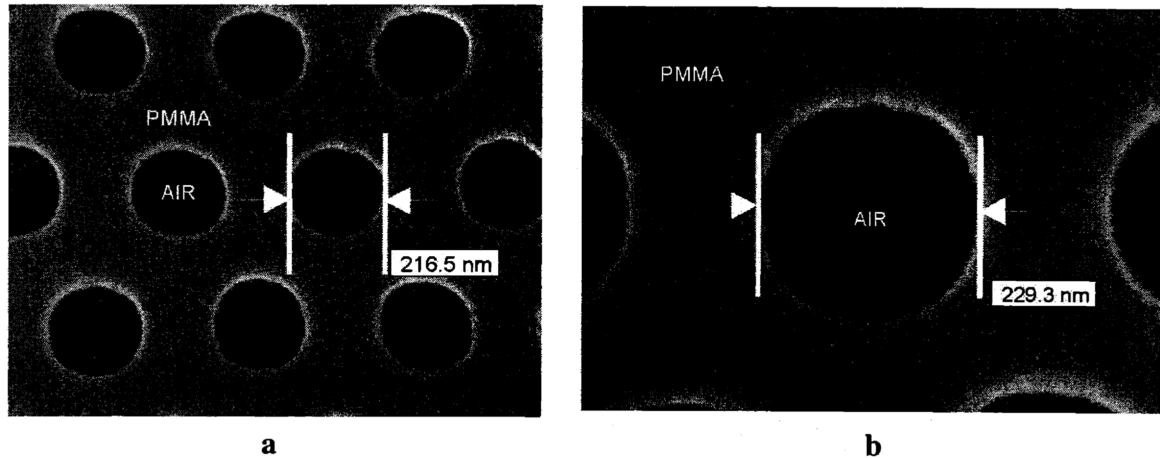

Figure 2-18. a) SEM of PC pattern in PMMA following development (100k magnification). The CAD pattern files have square holes but following development the holes are circular b) Close-up view of a hole in another PC pattern (200k magnification).

2.6.5 Transfer of PC Pattern to SiO_2

Transfer of the PC pattern to the hard mask layer requires an anisotropic etching technique that selectively removes SiO_2 relative to the PMMA mask. Reactive-Ion Etching (RIE) in a CHF_3 plasma is a well-developed process that generates smooth, straight sidewalls in the SiO_2 mask layer. Following etching, the PMMA is removed by placing each sample in acetone for 5 mins followed by 1 min. in IPA and then drying with an N_2 gun. The samples are then ashed in an O_2 plasma for 5 mins to clear any residual PMMA. The complete removal of the PMMA is verified with an optical microscope for each sample.

2.6.6 Transfer of PC Pattern to InGaP

The SiO_2 is used as a hard mask to transfer the PC pattern to the top InGaP layer of the active region using RIE in a CH_4:H_2:O_2 gas mixture. Large features located on each sample next to the array of PC patterns are used to obtain a course estimate of the etch rate using a profileometer. Once the etch rate is determined, etching is continued until a depth 10 nm above the InGaAs quantum well is achieved, providing a thick enough overlayer to prevent carrier tunneling

out of the quantum well to the etched surface and nonradiative recombination. Each of the remaining samples in the batch is etched using the established etch rate. Figure 2-19 shows a top view and a cross-sectional SEM of the PC holes etched into the top InGaP layer. It is interesting to note the hexagonal pattern easily distinguished by the absence of every other hole etched in the cross-sectional view. Once the desired etch depth has been reached, the SiO_2 mask is removed using RIE with the CHF_3 etchant gas.

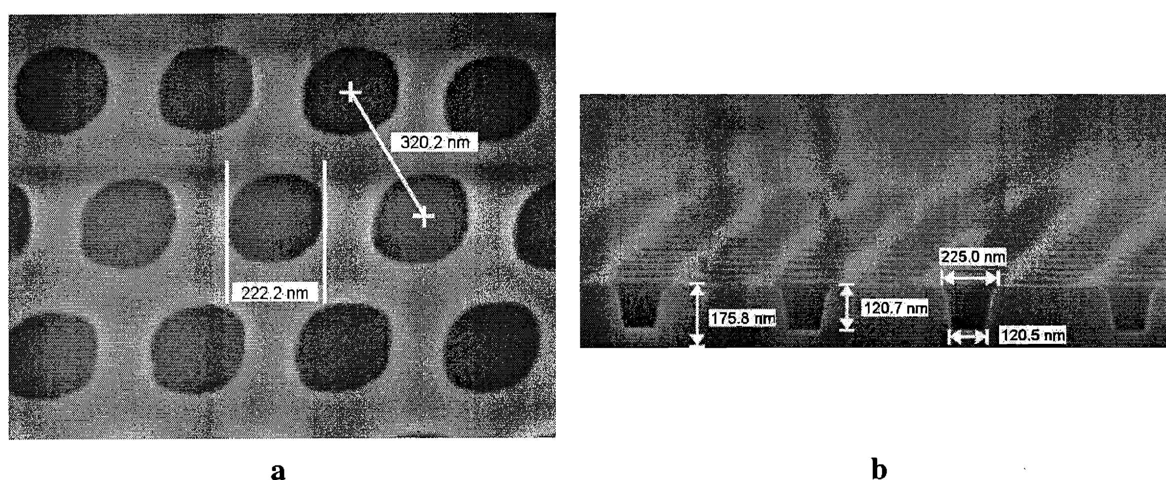

Figure 2-19. a) Top view and b) side view of PC holes etched in InGaP. The etch depth is stopped approximately 10 nm short of the InGaAs quantum well.

2.6.7 Photolithography to Define LED Mesas

After successful pattern transfer into the top InGaP layer of the active region, mesas are defined surrounding each PC using contact photolithography in the Technology Research Laboratory (TRL) at MIT. Samples are first dehydrated in an oven set at 130 degrees for 30 mins. to improve photoresist adhesion. Each sample is next placed on a vacuum spinner and simultaneously spun and sprayed with a N_2 gun to remove any dust particles that may lead to a non-uniform coating. Using a dropper, a single drop of Shipley 1813 (a positive photoresist that works well as an etch mask) is placed at the center of each sample. The sample is then spun for 30 seconds at 4k rpm. If the uniformity of the coating is non-satisfactory, the photoresist is stripped in acetone, rinsed with IPA, and the coating process is repeated starting with the dehydra-

tion bake. The resulting thickness of the photoresist following the coating process is 1.3 μm. The samples are next soft baked at 90°C for 30 mins to further increase surface uniformity of the photoresist.

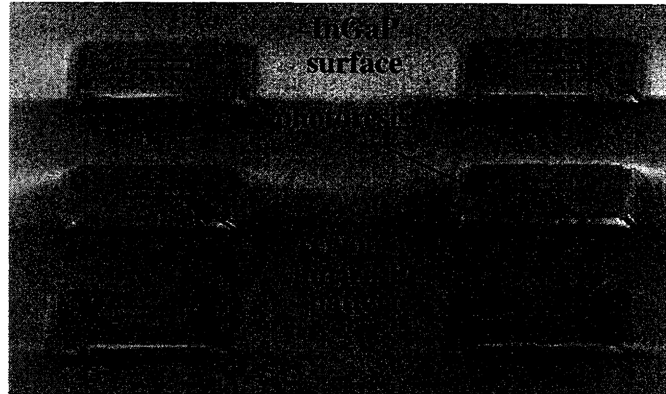

Figure 2-20. a) Mesas defined in photoresist cover the PC patterns.

The LED mesa mask consists of 9 x 9 arrays of chrome squares or circles that mask the 7 x 7 PC pattern region during the exposure (the array on the chrome mask is larger than the PC array to form a border of blank PCs as depicted in Figure 2-16). The size of the mesas ranges from 50 μm to 250 μm in width. Using a Karl Suss contact aligner in vacuum contact mode, each sample is exposed for 210 seconds. After exposure, each sample is submerged in MF-319 developer for 60 seconds followed by a 60 second deionized (DI) H_2O rinse. Satisfactory mesa pattern definition is verified using an optical microscope with a 100x objective. Figure 2-20 shows an SEM of several mesas defined in photoresist. The final step in preparation for etching of the mesas is to hard-bake the samples in an oven at 130°C for 30 mins.

2.6.8 Mesa Etching

Using the photoresist as an etch mask, the mesas are etched into the active region using an AZTeX PlasmaQuest Series III Electron Cyclotron Resonance (ECR) RIE located in TRL, with a CH_4:H_2:O_2 gas mixture (appendix A.4.2). The reason for performing the active region etch in the PlasmaQuest is that the ECR generates a high-density He:BCl_3:Cl_2 plasma that quickly etches the AlAs/GaAs/AlGaAs layers, avoiding burning of the relatively soft photoresist

mask. Sufficient etch depth of the mesas is verified using an optical microscope, by first focusing on the PC region (covered in photoresist) and then comparing that focal plane to that of the etched surface; this is a coarse approximation of the etch depth but the exact depth is not crucial as long as the etching has progressed completely through the underlying DBR. Following etching the photoresist mesa mask is removed in NSL by placing each sample in acetone for 5 mins followed by 1 minute in IPA and then drying with an N_2 gun. The samples are then ashed in an O_2 plasma for 5 mins. to clear any residual photoresist. The complete removal of the photoresist from each sample is verified using an optical microscope at 100x magnification.

2.6.9 Wet Thermal Oxidation

The final step in the fabrication of the PC LEDs is a wet thermal oxidation process (Figure 2-21), used to convert the $Al_{0.98}Ga_{.02}As$ spacer layer and the AlAs DBR layers into the low dielectric Al_2O_3. A N_2 gas flows over a DI H_2O bubbler heated to 90°C and carries H_2O vapor through a quartz tube inside an oxidation furnace maintained at 435°C. The temperature of the furnace is monitored by two separate thermocouples. The sample is placed on a quartz boat that is positioned inside the quartz tube at the center of the oxidation furnace. The positions of the thermocouples, the relative position of the sample on the quartz boat, and the position of the quartz boat inside the furnace are kept constant for each oxidation. The quartz boat is heated inside the furnace until the temperature stabilizes. The quartz boat is then removed from the furnace and replaced with the sample on the boat. The N_2 is kept constant at 1.5 liters/min.

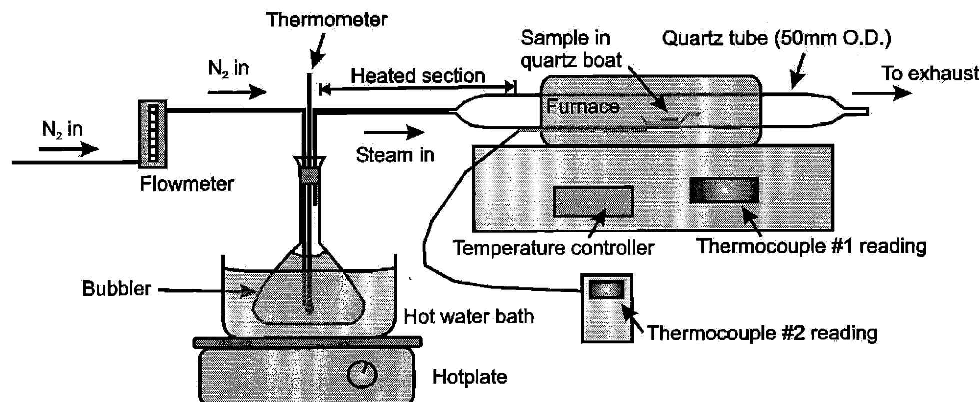

Figure 2-21 a) Oxidation set-up used to convert high Al-containing AlGaAs ternary compounds into low-dielectric Al_2O_3.

Samples containing 50 μm LED mesas are oxidized for 6 hrs. Samples containing 100 μm LED mesas are oxidized for up to 24 hrs. The oxidation time is limited by the oxidation rate of the Ga-containing spacer layer since the oxidation rate drops off significantly as the Al content decreases [66]. The measured initial oxidation rate for pure AlAs is 0.5 μm/min. and is determined by examining the progression of oxidation fronts into the LED mesa using both optical microscopy and SEM. The oxidation rate is non-linear as described in further detail in Chapter 3. SEM gives high-contrast micrographs of the entire oxidized DBR stack and spacer layer (Figure 2-22a) along with a close-up view of a partially oxidized test DBR structure (Figure 2-22b); note the high contrast between AlAs and Al_2O_3[1]. Figure 2-22c shows a SEM of a completed high-efficiency semiconductor PC LED mesa structure.

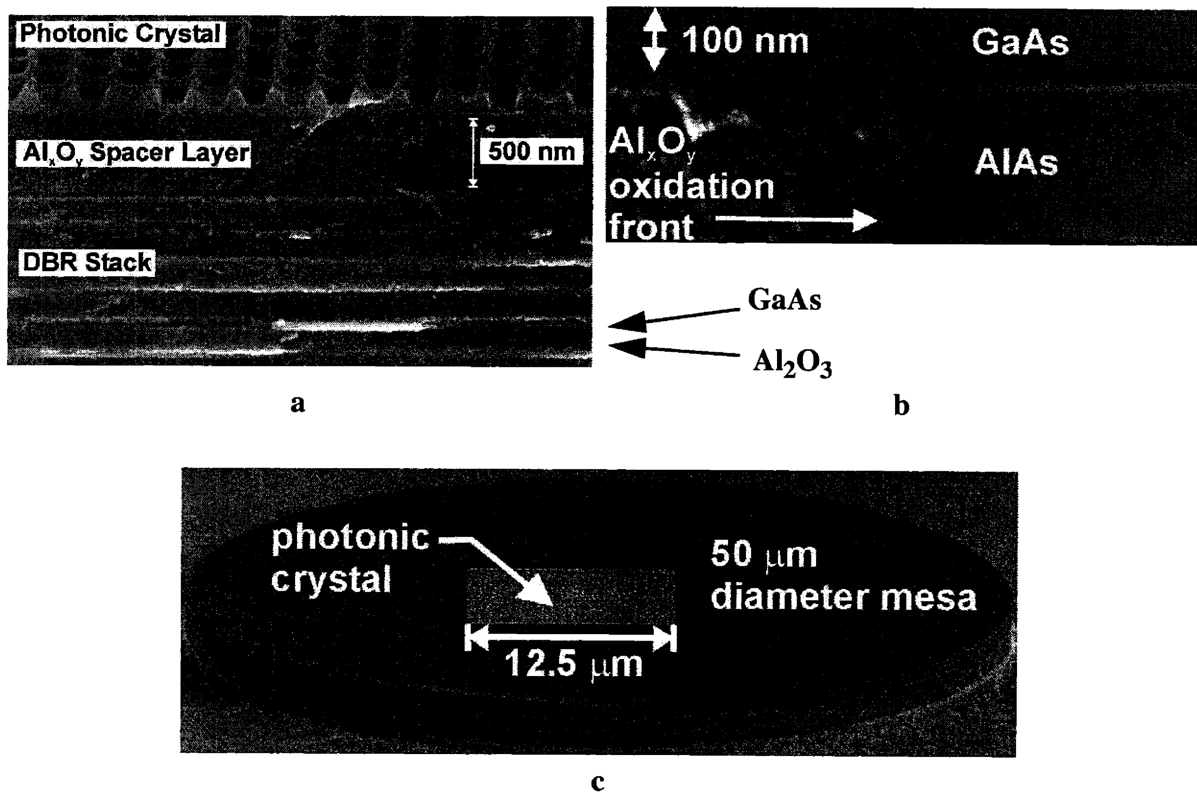

Figure 2-22. a) Cross-sectional SEM of cleaved mesa showing oxidized layers. b) SEM of a single DBR period showing the strong contrast between Al_2O_3 and AlAs. c) Completed high-efficiency PC LED structure.

1. The oxide phases is labelled Al_xO_y sometimes since several intermdiate phases exist as the oxide front progresses, as described in detail in Chapter 3.

2.7 Optical Characterization

Initial optical characterization of the high-efficiency semiconductor PC LED samples was performed using the room-temperature PL setup depicted in Figure 2-23. A Ti:Sapphire pump laser emitting at a wavelength of 810 nm is focused onto the sample through a microscope objective with a numerical aperture of 0.25, collecting light up to 15 degrees off-axis with the normal direction. The 810 nm pump light generates carriers in the InGaAs quantum well but is not absorbed by the surrounding InGaP barrier layers. The pump light is reflected by the wide-stop band of the DBR and is also absorbed in the GaAs layers. LED light is collected and imaged onto a charge-coupled device (CCD) camera through various chromatic filters. By replacing a flip-mirror, the LED light may also be directed into an optical spectrum analyzer (OSA).

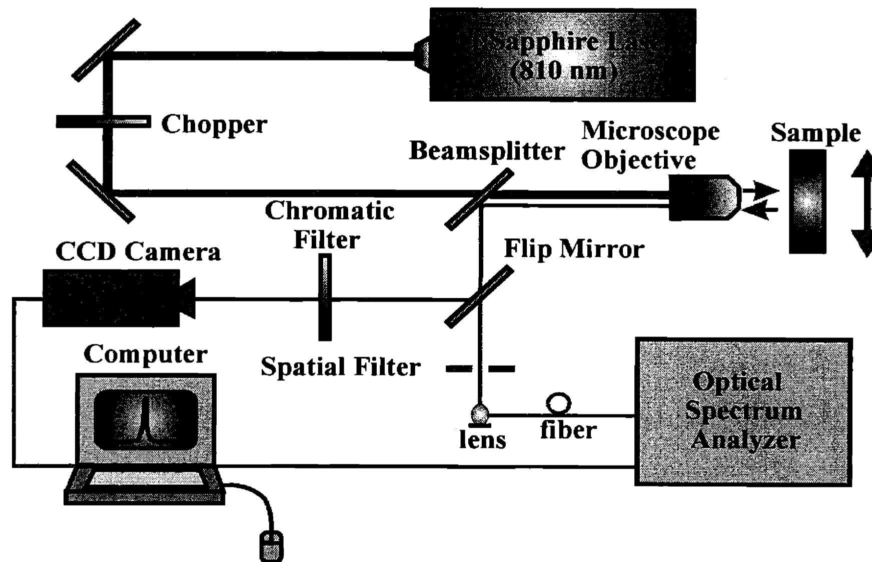

Figure 2-23. High-efficiency semiconductor PC LED measurement (setup #1)

The measured PL is related to the input pump power by:

$$PL = \eta \times Pump \quad \text{(EQ 53)}$$

where PL and Pump are the measured PL and input pump power respectively measured in watts, and $\eta = \eta_i \eta_{ext} \eta_c$ is the total (injection, external, and collection) efficiency. A collection efficiency has been added to the original expression for η given in EQ. 28 where it was assumed for

simplicity that $\eta_c = 1$. When measuring the PL of the LED devices, however, $\eta_c \neq 1$ in general so that it must be written explicitly. In addition, the radiative and extraction efficiencies are combined as was done in Section 2.1.3 to define an external efficiency. Physically, if every input photon generates an electron-hole pair that recombines radiatively and is subsequently collected by the detector, then the total efficiency of the optically-pumped LED is equal to one. PL is measured on the LED mesa inside the PC region and either compared to PL outside the PC region or to a blank mesa containing no patterning. The ratio in total measured PL power is:

$$\frac{PL^{PC}}{PL^{ref}} = \frac{\eta^{PC}}{\eta^{ref}} = \frac{\eta_i^{PC}\eta_{ext}^{PC}\eta_c^{PC}}{\eta_i^{ref}\eta_{ext}^{ref}\eta_c^{ref}} \quad \text{(EQ 54)}$$

Since LED sources typically have Lambertian far-field spatial distributions [68], a $\cos\theta$ angular dependence is assumed for both the reference and the PC sample. It is also verified in [36], that the emission from similar PC LED samples is Lambertian. Therefore, provided identical collection angles are used and the same range of wavelengths are collected between the reference and PC samples, it is assumed that $\eta_c^{PC} = \eta_c^{ref}$. EQ. 53 then reduces to:

$$\frac{PL^{PC}}{PL^{ref}} = \frac{\eta_i^{PC}\eta_{ext}^{PC}}{\eta_i^{ref}\eta_{ext}^{ref}} \quad \text{(EQ 55)}$$

2.8 Optical Characterization: Resonance-Enhanced PC LED

The enhancement in external efficiency due to a leaky resonance in the PC is given by EQ. 51 which is repeated here for convenience:

$$E = \frac{\left(1 + \frac{\tau_{fr}}{\tau_{lr}}\eta_e^{lr}\right) \cdot \left(1 + \frac{\tau_{fr}}{\tau_g}\right)}{1 + \frac{\tau_{fr}}{\tau_{lr}}\left(\eta_e^{lr} + A'\right) + \frac{\tau_{fr}}{\tau_{nr}}}, \quad \text{(EQ 56)}$$

where the only assumption is high-quality epitaxial material so that there is no nonradiative recombination in the unpatterned LED. The extraction efficiency from the unpatterned region (or a blank LED mesa) is:

$$\eta_{ext}^{ref} = \frac{\frac{1}{\tau_{fr}}}{\frac{1}{\tau_{fr}} + \frac{1}{\tau_g}} = \frac{1}{4\left(\frac{n_f}{n_{ox}}\right)^2} + \frac{1}{4\left(\frac{n_f}{n_{air}}\right)^2} \qquad \text{(EQ 57)}$$

where emission directly into the air above the active region and reflections from the DBR below are accounted for explicitly. Using the known indices of refraction for the oxide and the active region at 980 nm, $n_{ox} = 1.66$ and $n_f = 3.23$, yields an extraction efficiency of $\eta_{ext} = 8.9\,\%$; EQ. 57 ignores photon recycling, so this is actually a lower limit on the extraction efficiency. The maximum obtainable enhancement in extraction efficiency (ignoring photon recycling) for the leaky resonance-enhanced PC LED structures is then:[1]

<u>Maximum obtainable enhancement from resonance-enhanced PC LEDs</u>

$$E = 1 + \frac{\tau_{fr}}{\tau_g} = \frac{1}{\eta_{ext}^{ref}} = 11.23\,, \qquad \text{(EQ 58)}$$

According to EQ. 55, a higher-extraction efficiency enhancement than the EQ. 57 threshold may be observed only if the injection efficiency for the PC region is greater than the injection efficiency for the reference.

2.8.1 Initial Observations

A portion of the calculated photonic band diagram for an instructive PC LED structure that will be examined in detail in this section with a lattice constant (*a*) of 380 nm, hole radius (*r*) of 56 nm, and hole depth (*d*) of 101 nm, having a 198 nm thick active region, is shown in Figure 2-24a. A close-up SEM of the PC is shown in the inset. Since the quantum well emits primarily TE-radiation, only modes with at least 80% of the electric field polarized in the plane of

1. It is reasonable to ignore photon recycling since the PC LED structures are low Q.

the active region are included; this requirement creates the shown band discontinuity. As an additional requirement, and in order to clearly identify leaky resonant modes, only bands above the light line with at least 80% of their power concentrated in the active region are plotted. A clear folding of the guided modes below the light line (white region) occurs at the points of high-symmetry in the 1st Brillouin zone (inset). A guided resonant state capable of coupling to vertical radiation is created at the Γ point at a frequency of $.4064\left(\frac{2\pi c}{a}\right)$ that corresponds to 935 nm.

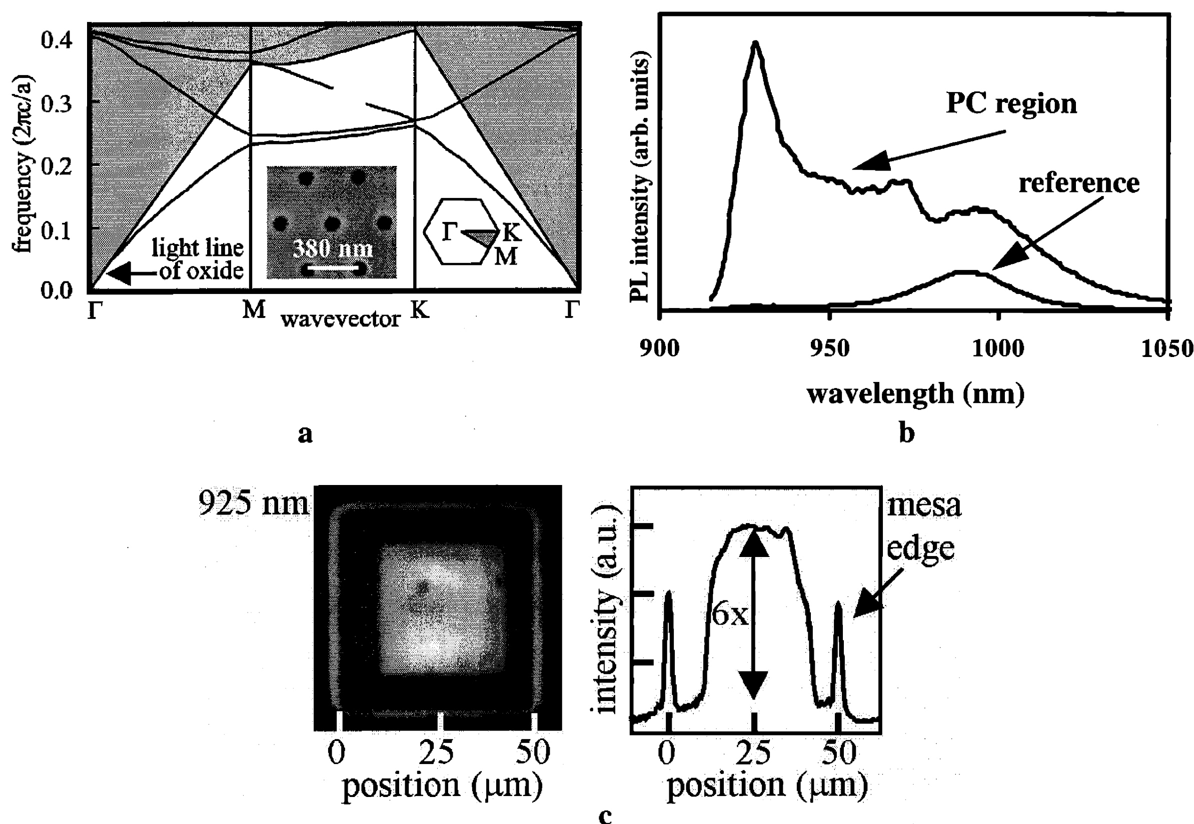

Figure 2-24. a) Calculated photonic band diagram. b) PL from PC LED mesa containing PC featured in (a). Localized PL from regions internal and external to the PC (c)

The PC LED mesa containing the PC featured in Figure 2-24a is optically excited using a broad spot, and the PL is passed through a 10 nm full-width at half-maximum (FWHM) filter centered at 925 nm before being imaged onto the CCD camera (Figure 2-24c). The region inside the PC appears approximately 6x brighter than the region of the LED mesa surrounding the PC (filters are used to avoid saturating the CCD camera, making the surrounding LED region

appear especially dark). The LED mesa is also pumped with a small 5 μm spot in each of the two regions with and without the PC pattern. The emitted light from each region is directed into the OSA producing the two spectra in Figure 2-24b. The sharp feature in the spectrum emitted from the PC region near 935 nm is attributed to leaky resonant mode at the Γ point.

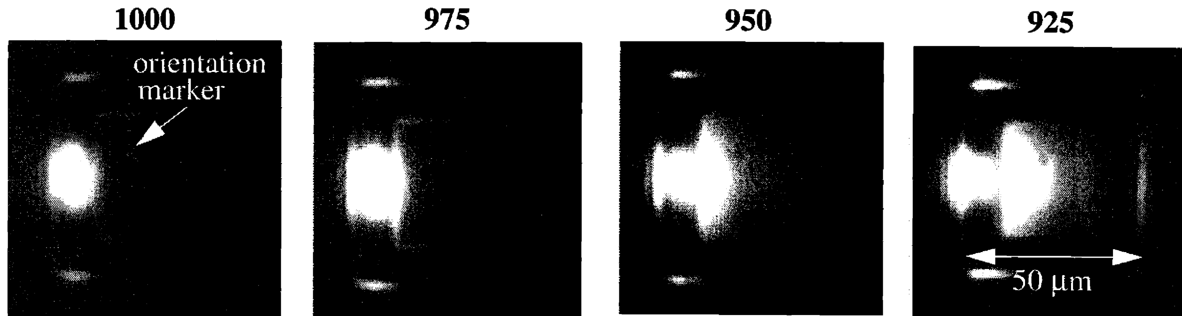

Figure 2-25. PL with various chromatic filters. The pump laser is positioned on the portion of the LED mesa external to the PC region.

To verify the wavelengths of the resonances, various chromatic filters are placed in front of the CCD camera and localized excitation of the quantum well is shown in Figure 2-25. Each filter transmits a spectral range FWHM of 10 nm centered around 925 nm, 950 nm, 975 nm, or 1000 nm. The pump light is focused down to a <5 μm spot just outside the edge of the PC region on the LED mesa.[1] By optically pumping a region external to the PC, light that is emitted from the quantum well is index guided in all lateral directions, with some of the light coupling to modes in the PC. Only wavelengths of the quantum well emission near the calculated resonance of 935 nm are efficiently extracted in the vertical direction. Therefore, the image taken with the 925 nm filter shows the most light extracted from the device.

2.8.2 Resonance-Pump Coupling

There exist higher-order resonances at energies above the emission frequency at the Γ point. Since optical pumping must also occur at a frequency higher than the emission frequency, it is important to consider the possibility that the pump wavelength also overlaps a higher energy resonance causing an enhanced injection efficiency into the PC structures as compared to the reference. Indeed, coupling of the pump light at 810 nm to a higher energy resonance was

1. The small feature in the upper-left hand corner of the PC region in each image was used to verify the orientation of the Brillouin zone with respect to the PC lattice.

observed on many PC LED structures. Figure 2-26a shows the photonic band diagram for one such PC with a=340 nm, r=104 nm, d=60 nm, having a 135 nm thick active region. A SEM of the PC is shown in the inset. The optical modes plotted are TE-like and satisfy the same criteria as the modes plotted in Figure 2-24a. A resonance at the Γ point is calculated to be near .4304 ($2\pi c/a$), which corresponds to 790 nm. Figure 2-26b shows a composite image of eight CCD images taken with a broad spectral filter that covers the entire quantum well emission spectrum. For each image, the pump light is focused down to a <5 μm spot size and excites a region inside the edge of the PC featured in Figure 2-26a. Strong optical pumping is observed outside the PC region. The collection angle of the focusing lens combined with inaccuracies of the SEM micrographs (~±5 nm) give some spread to the resonance at Γ.

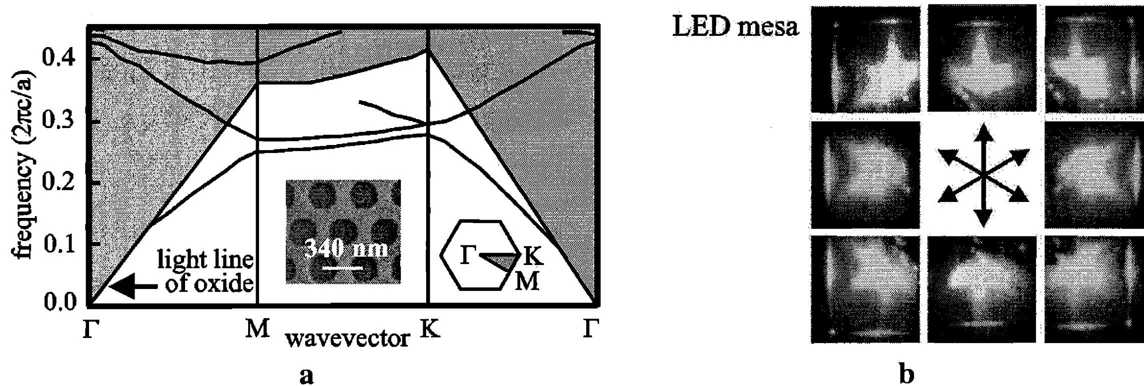

Figure 2-26. a) Calculated photonic band diagram. b) Composite image of enhanced optical pumping occurring outside the edge of the PC region when the pump light is focused just inside the edge of the PC region.

White-light reflection measurements were performed to directly detect higher order resonances that may overlap with the pump wavelength causing enhanced injection of the pump light into the PC structure featured in Figure 2-24a. The spectrum is plotted in Figure 2-27 and clearly shows a resonance at the pump wavelength of λ=810 nm. The reflectivity measurement was performed using the setup in Figure 2-28 except with a filter in place to avoid lasing in the source cavity. With the pump wavelength on resonance it may be the case that $\eta_i^{PC} \neq \eta_i^{ref}$, so that the enhancement in external efficiency may not be deduced directly from the PL measure-

ments shown in Figure 2-24c. By tuning the pump wavelength off resonance, however, the condition $\eta_i^{PC} \approx \eta_i^{ref}$ is satisfied and EQ. 53 reduces to:

$$\frac{PL^{PC}}{PL^{ref}} = \frac{\eta_{ext}^{PC}}{\eta_{ext}^{ref}} = E, \qquad \text{(EQ 59)}$$

enabling a direct measurement of the external efficiency enhancement due to the PC.

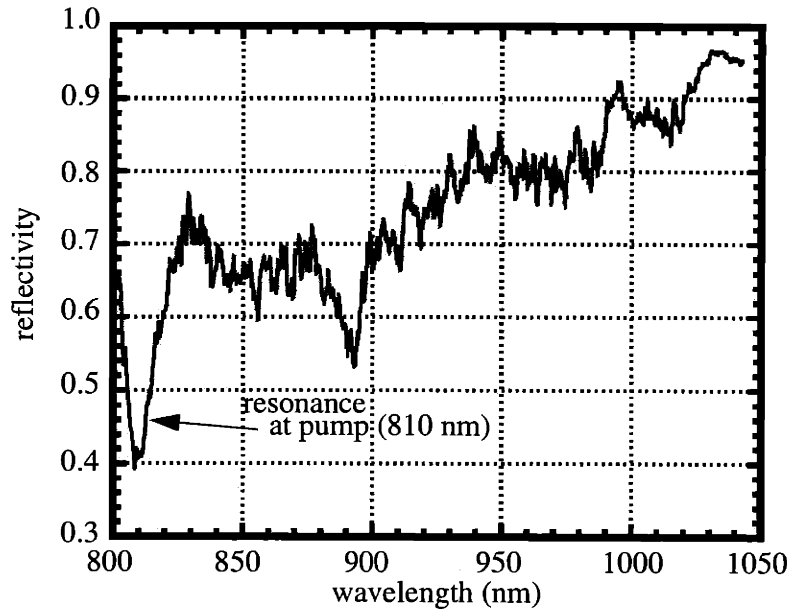

Figure 2-27. White-light reflectivity spectrum for PC structure featured in Figure 2-24.

2.8.3 Literature Review

From the input coupling observations it can be concluded that the same leaky resonances that help enhance emission may also have a significant effect on the optical pumping of each PC LED structure. That is, the injection efficiency may be enhanced significantly by the PC making it difficult to separate out a measured enhancement in external efficiency. Despite the importance of ensuring the condition $\eta_i^{PC} \approx \eta_i^{ref}$ when using EQ. 59, it is not described in any of the reports of optical testing of PC LED structures by other groups [36, 52-55]. Therefore, the

quoted enhancements in the literature presented in Section 2.1.6 may derive from enhanced optical pumping/injection efficiency, instead of enhanced external efficiency due to the PC.

2.8.4 Quantifying the Resonance Enhancement

Figure 2-28 depicts a schematic of a second high-efficiency PC semiconductor LED measurement apparatus, used to collect narrow angle PL spectra and to quantify the enhancement in external efficiency. Pump light from a tunable Ti:Sapphire source (730-950 nm) is focused down to a < 5 μm spot on the sample through a lens that also collects light up to 5° off-axis with the normal direction. Emitted light is either directed into a viewing CCD or into a cooled CCD spectrometer for spectral analysis.

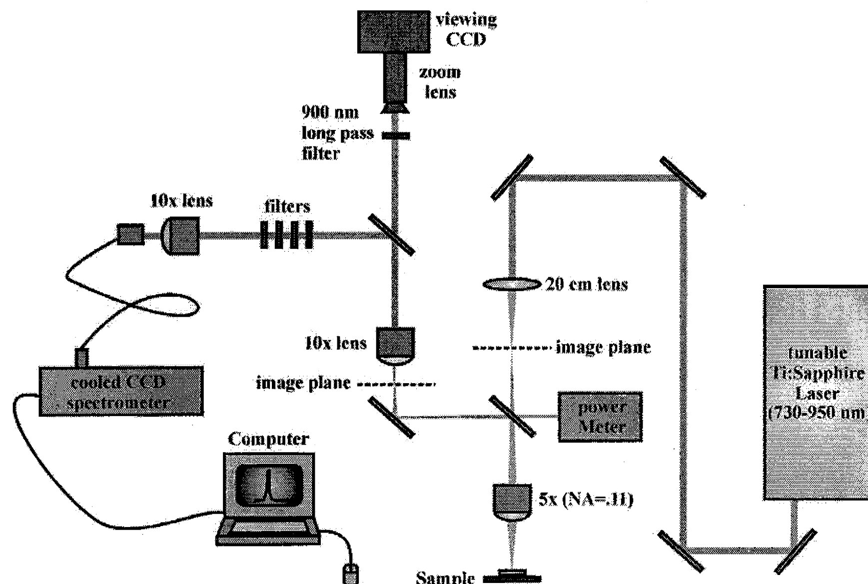

Figure 2-28. High-efficiency semiconductor PC LED measurement (setup #2)

It is important to justify the assumption that photon recycling may be ignored in the calculation of EQ. 58. The effect of photon recycling should be small if light is collected from a region significantly less than the reabsorption length of guided modes in the active region. Assuming an absorption coefficient in the InGaAs quantum well of $\alpha = 5 \times 10^{3} \text{cm}^{-1}$ [6] and a conservative estimation of the modal overlap of $\Gamma = \frac{V_a}{V}$, or 4%, with the 8 nm quantum well in the 198 nm active region, the average absorption length is about 50 μm. It is therefore unlikely

that recycled photons are being collected for the reference structures provided the pump spot is sufficiently less than the reabsorption length. Accordingly, a small 5 μm spot size is used in the measurements of the PL enhancement.

The leakage length for the resonance with quality factor Q is $\frac{Qc}{\omega n}$. For the observed $Q \sim 30$ at 935 nm in Figure 2-24c, the leakage length is ~1.4 μm. Therefore, most of the light in leaky resonance modes escapes before being reabsorbed and possibly recycled. Indeed, the absorption length is larger than the entire PC region on each LED mesa so that any error in the PL measurement of the PC LED regions due to photon recycling should be negligible.

It is also reasonable to assume that parasitic reabsorption is playing a minor role within the small spot size of the measurement setup. Although the carrier density may be high in the quantum well depending on the pump power, the overlap of the leaky resonance mode is only 4% at maximum. The actual overlap is even less because of the asymmetry of the active region. For the average parasitic absorption length to be 5 μm, the parastic absorption coefficient needs to be $\alpha' = 5 \times 10^4 \mathrm{cm}^{-1}$, an order of magnitude greater than the reabsorption coefficient in the quantum well. As further justification, an examination of Figure 2-26b shows strong scattering at the edge of the PC mesa when the pump spot is at least 10 μm away. It is therefore unlikely that parasitic absorption is playing a significant role. Therefore, for the small spot size measurement, it is reasonable to assume that the extraction efficiency for leaky resonance modes is $\eta_e^{lr} = 1$. The measured enhancement in external efficiency for the small spot size then becomes:

$$E = \frac{\left(1 + \frac{\tau_{fr}}{\tau_{lr}}\right) \cdot \left(1 + \frac{\tau_{fr}}{\tau_g}\right)}{1 + \frac{\tau_{fr}}{\tau_{lr}} + \frac{\tau_{fr}}{\tau_{nr}}}. \qquad \text{(EQ 60)}$$

An additional advantage of a small spot size is the uniformity of the PC pattern being measured. Back-scattering of electrons from the semiconductor layers during EBL causes holes in the center of the PC pattern to receive a larger effective dose than holes on the edges of the PC. Therefore, holes in the center of the PC pattern develop larger than holes on the edge

(~10% variation in hole diameter from the center to the edge of a 30 μm PC area is measured using SEM). The effect is worsened for even larger pattern sizes.

The only unknowns in EQ. 60 are τ_{fr}/τ_{nr} and τ_{fr}/τ_{lr}. For a semiconductor, the radiative and nonradiative rates in EQ. 60 may be rewritten [6]:

$$E = \frac{\left(\frac{1}{\tau_{fr}} + \frac{1}{\tau_{lr}}\right) \cdot \left(1 + \frac{\tau_{fr}}{\tau_g}\right)}{\frac{1}{\tau_{fr}} + \frac{1}{\tau_{lr}} + \frac{1}{\tau_{nr}}} = \frac{BN^2 \cdot \left(1 + \frac{\tau_{fr}}{\tau_g}\right)}{BN^2 + \left(AN + CN^3\right)} \qquad \text{(EQ 61)}$$

The radiative recombination term requires both an electron and a hole, the densities of which are assumed to be equal under normal injection currents yielding the quadratic dependence. The coefficient B may be enhanced or suppressed according to Fermi's golden rule, as discussed in Section 2.1.2. The linear term represents nonradiative recombination through surface or defects states and the coefficient A depends on the nature of the recombination process; for instance, the surface recombination velocity and total exposed surface area. The cubic term represents Auger recombination that requires the presence of three carriers to support the energy transfer; therefore, this term only arises at extremely high carrier injection or high-temperatures.

2.8.5 Resonance External Efficiency Enhancement

Figure 2-29a shows the calculated photonic band diagram near the Γ point for a measured PC LED structure used to quantify external efficiency enhancement. A parabolic approximation to the bands near the Γ point was used with the same restrictions given in Section 2.8.1. The inset SEM shows a close-up of the PC structure itself. Band 1 intersects the Γ point at 920 nm, bands 2 and 3 at 896 nm, band 4 at 884 nm, and bands 5 and 6 at 860 nm. Bands 2 and 3, and bands 5 and 6, are degenerate at the Γ point; the six-fold symmetry requires two doubly-degenerate bands and two nondegenerate bands at the Γ point.

As discussed in Section 2.8.2, in order to compare the reference LED spectrum to that of the PC LED, the injection efficiencies for each need to be the same. Therefore, to accurately measure the PC enhancement, the pump wavelength used must not overlap a high-energy resonance in the PC structure. Figure 2-29b shows the white-light reflectivity spectrum for the structure in Figure 2-29a taken with a narrow collection angle of 5 degrees off-axis with the Γ point. A strong resonance appears near 787 nm. The greater than one reflectivity near 840 nm may be due to nonuniformity in the underlying DBR mirror. As the pump wavelength is tuned on and off the resonance, the integrated PL enhancement relative to the unpatterned mesa increases. The peak enhancement occurs at a pump wavelength that exactly matches the dip in reflectivity. The pump power incident on the sample for the spectra in Figure 2-29b is 3 mW.[1] It is concluded that an enhancement in injection efficiency is occurring in the PC region when the pump wavelength is aligned with the 787 nm resonance. The raw PL at 6 mW pump power pumping on and off resonance is also given in Figure 2-29b and compared to a reference unpatterned LED mesa. The effect of injection efficiency is dramatic and must be eliminated before measuring an enhancement in external efficiency due to the PC resonances.

The PL enhancement for the PC region at a pump wavelength of 831 nm (off-resonance with the pump wavelength) is also shown in Figure 2-29b. The pump power used in the measurement is 112 mW. Increases in the spectral enhancement correspond directly to dips in the

1. Higher pump powers can damage samples because of the large increase in power coupling from the pump into the PC resonance.

reflectivity spectrum and are attributed to the degenerate leaky resonant modes calculated in Figure 2-29a. Bands 2 and 3 correspond to the longer wavelength resonance at 910 nm while bands 5 and 6 correspond to the resonance near 875 nm. The SEM measurements were calibrated to the lattice constant with an error bar of approximately 5%. For instance, a conservative 2% underestimation of the lattice constant places the resonances at about 910 nm and 875 nm. Therefore, the match between the simulated and measured resonant peaks appears accurate. Indeed, the separation between the measured enhancement peaks is ~35 nm and matches well with the separation between the simulated peaks. Since the band structure scales with wavelength (as discussed in Section 1.2.6), it is the *separation* between the resonances rather than the *absolute* wavelength that should remain constant to first order to errors in the SEM-measurement of the lattice constant.

Spectral enhancement in the normal direction from leaky resonances in the PC structure is also calculated in the time-domain yielding supplemental information to the frequency domain calculation of the band structure. The spectral enhancement calculation from Figure 2-15 is reproduced for comparison to measurement in Figure 2-29c. The positions of the resonances are the most important information yielded by the calculation while the absolute magnitude of enhancement is arbitrary. Two strong resonances occur centered near 870 nm and 950 nm closely matching the measured structures. Some error arises from fabrication variations such as nonvertical etching of the holes. However, the higher frequency resonance is much sharper (higher Q) than the long-wavelength resonance in close agreement with the reflectivity spectrum in Figure 2-29b.

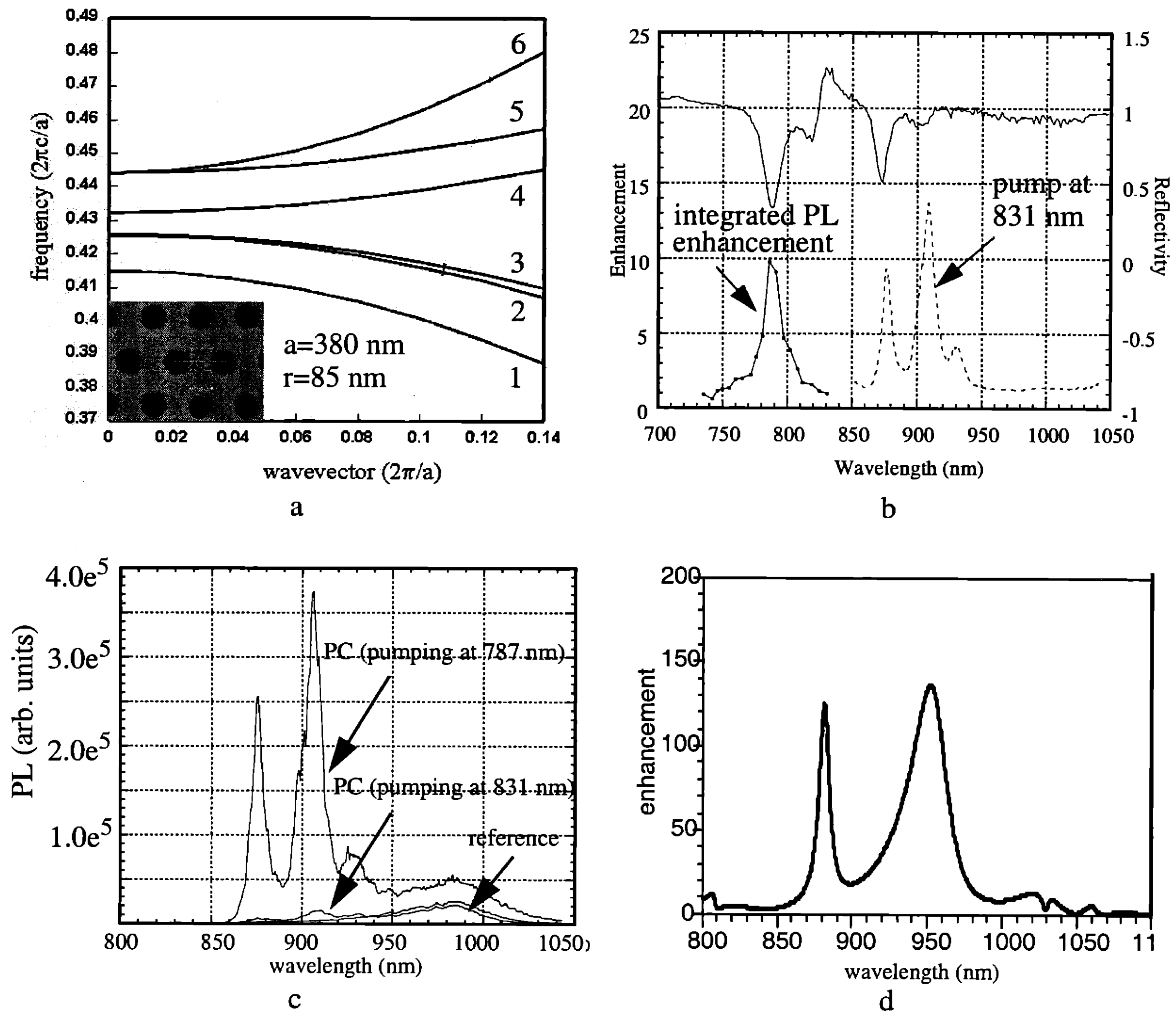

Figure 2-29. a) Calculated band structure near the Γ point for inset PC. b) Narrow collection angle reflectivity spectrum matches well with spectral and integrated enhancement pumping on and off resonance. c) PL spectra taken at 6 mW pumping on and off resonance and compared to an unpatterned reference LED mesa. d) Finite-difference time-domain calculation of enhancement relative to an arbitrary reference

From EQ. 53, the ratio of PL to pump power is equivalent to the total efficiency of the LED. According to EQ. 60, radiative recombination should dominate nonradiative recombination at intermediate carrier densities (or intermediate pumping powers) where Auger recombination is negligible. Therefore, intermediate-power measurements of PL should yield the highest levels of enhancement from the PC. Figure 2-30 shows the effect of the PC on the external effi-

ciency as a function of pump power. All of the plots are taken while exciting carriers off-resonance with the pump wavelength, so that injection efficiencies are approximately the same and the PL from the PC may be directly compared to the PL from the blank reference mesa. Very little resonance-enhancement is observed at low powers because there is little overlap between the material emission and the leaky resonances identified in Figure 2-29. In addition, Figure 2-30b shows that the peak intensity from the PC structure is approximately 40% less than the peak intensity from the reference structure, indicating the presence of nonradiative recombination that may be introduced during device processing. As the pump power is increased, however, the external efficiency increases as radiative recombination dominates nonradiative recombination and as higher-order transitions in the quantum well shift the spectrum to shorter wavelengths, thereby increasing the overlap with the leaky resonances.

Figure 2-30e plots the integrated PL from the PC LED mesa to that of the unpatterned mesa as a function of pump power. From EQ. 58, the ratio of the two plots in Figure 2-30e is equivalent to the enhancement in external efficiency. The enhancement in external efficiency due to the resonances in the PC saturates at high-pump powers. Since the external efficiency of the blank LED mesa is 8.9%, the observed factor of ~2 enhancement at high-pump powers translates to an external efficiency of 17.8% due to the leaky resonances of the PC.

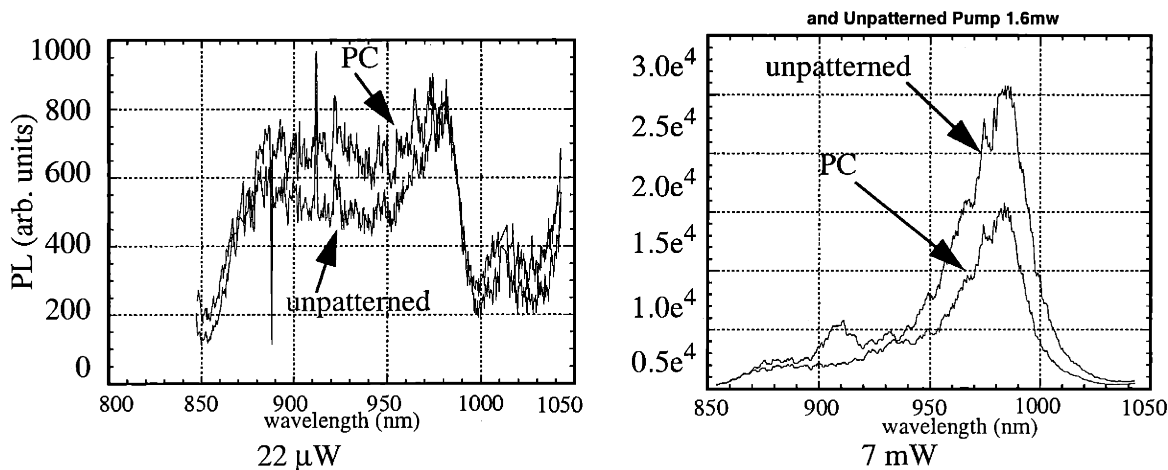

Figure 2-30. a) Measured PL spectra for PC LED mesa compared to an unpatterned LED mesa for several different pump powers. b) Integrated PL/pump power as a function of pump power. The ratio of the two plots is equivalent to an enhancement in external efficiency.

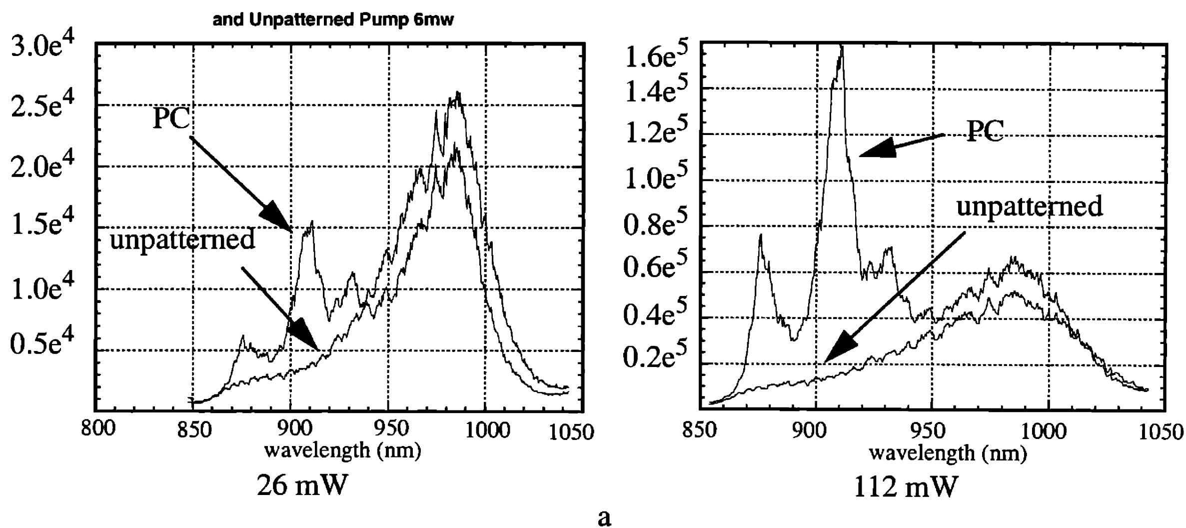

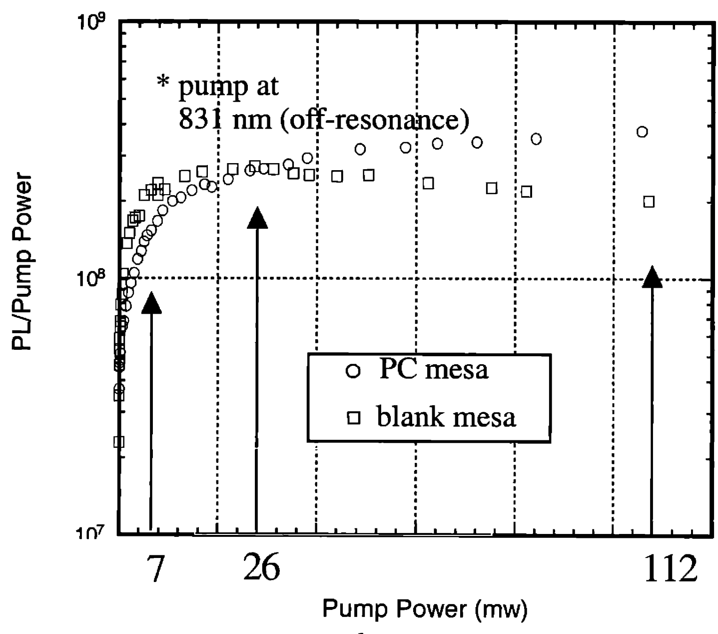

Figure 2-30. a) Measured PL spectra for PC LED mesa compared to an unpatterned LED mesa for several different pump powers. b) Integrated PL/pump power as a function of pump power. The ratio of the two plots is equivalent to an enhancement in external efficiency.

The external efficiency of 17.8% from the PC is actually a promising result since the measured structure is not optimized because the leaky resonance does not completely overlap the material emission peak. At high pump-powers, the material emission lineshape shifts to higher-energy quantum-well transitions, and a larger portion of the material emission linewidth

overlaps the PC resonances. In addition, the external efficiency given in EQ. 61 assumes emission into only free-space modes and resonances in the PC. For the structure described above, however, the longer-wavelength tail of the material emission may also overlap guided modes below the light line.

It is also desirable to limit nonradiative recombination pathways that may be introduced during the device processing and compete with the leaky resonant modes through EQ. 60. That is, the value of A in EQ. 61 is larger for the PC sample than for the reference sample as indicated by the less than unity enhancement factor of 0.6 at 7 mW of pump power in Figure 2-30e. Although the holes do not penetrate the active region so that surface recombination is unlikely, other nonradiative recombination pathways may have been introduced in the high-temperature device processing.[2] A less-invasive shallower hole structure may reduce the nonradiative recombination component introduced in the device processing.

To clarify each component of the external efficiency of the PC LED structure, it is helpful to rewrite the "ideal" PC resonance-enhancement (EQ. 61) as

$$E = \frac{\left(\frac{1}{\tau_{fr}} + \frac{1}{\tau_{lr}}\right) \Big/ \left(\frac{1}{\tau_{fr}} + \frac{1}{\tau_{lr}} + \frac{1}{\tau_{nr}} + \frac{1}{\tau_g'}\right)}{\frac{1}{\tau_{fr}} \Big/ \left(\frac{1}{\tau_{fr}} + \frac{1}{\tau_g}\right)} = \frac{B'N^2 \cdot \left(1 + \frac{\tau_{fr}}{\tau_{lr}}\right)}{BN^2 + AN}, \qquad \text{(EQ 62)}$$

where all possible partial emission rates have been explicitly written including partial emission for the PC into guided modes under the light cone $1/\tau_g'$. The possibility of slight Purcell enhancement has also been allowed in EQ. 62 ($B \neq B'$) and it is assumed that the pump powers are too low for Auger recombination to be important.[3] At low powers there are no available leaky resonant modes within the material emission and no possibility of Purcell enhancement so that EQ. 62 becomes:

2. The degradation of the radiative efficiency of the quantum well is even more pronounced when testing the PBG-enhanced structures as will be explained in the next section.

3. A slight roll-off in the PL is observed in Figure 2-30 at high-powers and may be due to the onset of Auger effects.

$$E_{low} = \frac{BN^2}{BN^2 + AN} = 0.6 \quad \text{(EQ 63)}$$

The enhancement at low powers is less than unity due to the presence of nonradiative recombination pathways. At high pump powers, the emission bandwidth shifts to higher-energies and overlap with leaky resonances in the PC occurs. It is unlikely that the overlap is enough to cause a large Purcell enhancement ($B = B'$), so that:

$$\tau_{fr} \approx \tau_{lr}. \quad \text{(EQ 64)}$$

EQ. 64 states that the partial emission rate into leaky resonant modes is about the same as the emission into free space modes; this is due to the relatively small overlap of the material emission with the PC resonances even at high pump powers. The external efficiency may be further optimized by maximizing the overlap between the material emission lineshape and the PC resonance so that emission into the leaky resonances dominates.

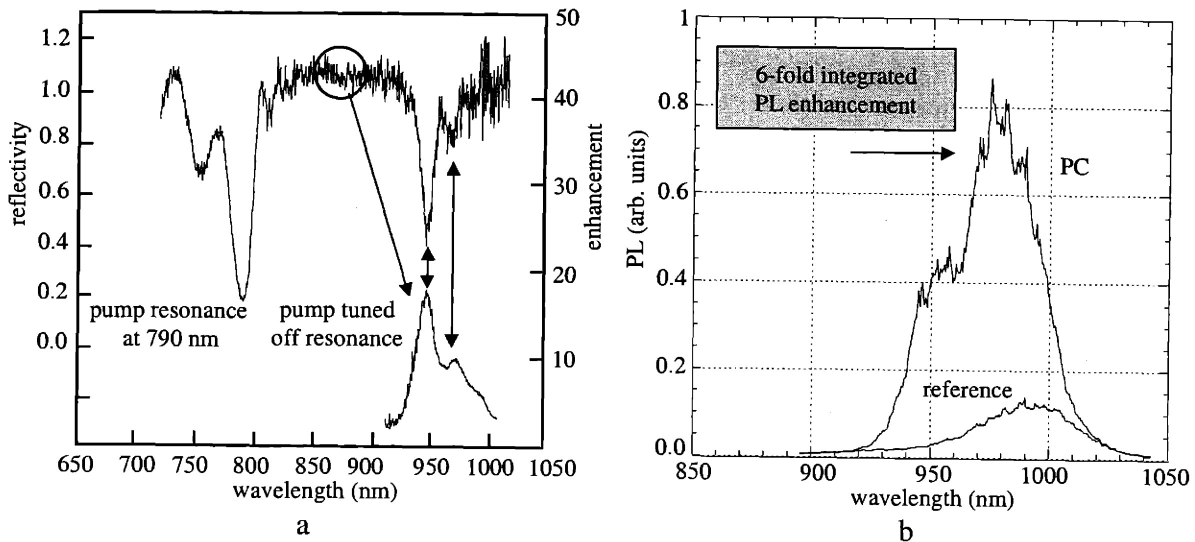

Figure 2-31. a) Reflectivity spectrum and PL enhancement spectrum for a PC structure where two-doubly degenerate resonances overlap a large portion of the quantum well emission. b) A 6-fold enhancement in external efficiency is observed and attributed to the large resonance overlap in (a).

Figure 2-31a shows the reflectivity spectrum for a PC LED structure designed for larger overlap with the material emission spectrum and shallower (less-invasive) holes. A pump resonance is revealed near 790 nm. When pumping off-resonance near 850 nm, strong spectral enhancement is observed near 950 nm and 970 nm indicating that the two doubly-degenerate resonances now have much stronger overlap with the material emission spectrum. Figure 2-31b shows a 6-fold enhancement in total integrated PL intensity from the PC LED structure as compared to the reference structure. The enhancement is observed at all pump-powers indicating little to no nonradiative recombination pathways. The 6-fold enhancement corresponds 5-times faster emission into leaky resonant states as compared to free space and a 54% external efficiency. The external efficiency from the optically-pumped resonance-enhanced structures is significantly larger than the best reported external efficiencies using alternative methods (Figure 2-2). The external efficiency may be further improved by ensuring that none of the material emission tail falls below the light-line at longer wavelengths. The ideal resonance-enhanced PC LED structure is achieved by perfectly overlapping the material emission lineshape with that of the PC resonances ($Q \sim Q_m$).

2.9 PBG-Enhanced PC LED Results

2.9.1 Initial Observations

The predicted 30% external efficiency from the PBG-enhanced structure (see Section 2.5.1) was not observed initially. The result, however, was not all that surprising since the PBG reduces the density of available optical states and therefore (see EQ. 30) suppresses emission to the point where nonradiative recombination may become more influential. The predicted enhancement does not account for nonradiative recombination. EQ. 44 and EQ. 45 state that the external efficiency will be significantly limited in the presence of strong nonradiative recombination pathways. Even though by design the holes of the PC do not penetrate the quantum well region, other nonradiative recombination pathways (defects, impurities) besides surface recombination may be introduced during the fabrication of the devices. Indeed, the only reported measurement in the literature of an observed enhancement in emission attributed to a PBG was performed at low-temperature where nonradiative recombination effects are reduced [55]. A low-

temperature PC LED however has no practical application besides being of theoretical interest. Therefore, attempts to observe low-temperature enhancement were not explored. Instead, the quantum well damage process was investigated. Since the holes do not penetrate the quantum well (no surface recombination), it should be possible to observe enhancement at room-temperature provided the active material can remain of high-quality throughout the fabrication process. Indeed, enhancement was observed in the resonance-enhanced PC LED structures where there is a higher available density of optical density of states. A nonradiative recombination component however was also discovered in the leaky resonance structures and needs to be investigated.

2.9.2 Quantum Well Damage

By carefully measuring the PL before and after each step in the fabrication process, it has been determined that the final wet thermal oxidation step in the fabrication process (Figure 2-17) causes damage to the quantum well enabling the characteristic nonradiative recombination time to become significantly shorter than the radiative recombination time. Figure 2-32 shows various PL measurements that verify the quantum well damage due to oxidation. The damage is first qualitatively observed in the CCD image shown in Figure 2-32a. The dark region inside the PC LED mesa corresponds to poor PL due to the wet thermal oxidation process. The damage is not observed, however, in the region external to the PC. Figure 2-32b is a plot of the PL before and after oxidation from a test PC LED structure. The fabrication process is identical to Figure 2-17 for the test structure except that a mesa is not defined prior to oxidation. Therefore, the effect of oxidation on the quality of the quantum well itself may be isolated without changing the structure's reflectivity by oxidizing the underlying AlGaAs spacer layer and AlAs DBR layers. Prior to oxidation, the PL for the PC region is approximately 40% of the GaAs signal, that primarily comes from the underlying substrate and acts as a reference in the measurement. After 30 mins of oxidation,[4] the PL drops to approximately 10% of the GaAs reference, a four-fold decrease in PL intensity due to the quantum well damage. It should be noted that any

4. In this context, oxidation refers to exposure in the steam oxidation furnace under normal oxidizing conditions even though a mesa has not been defined and sidewalls are not exposed for oxidation.

effects on emission due to the PC should remain constant before and after oxidation since the underlying layers are not being oxidized in the experiment.

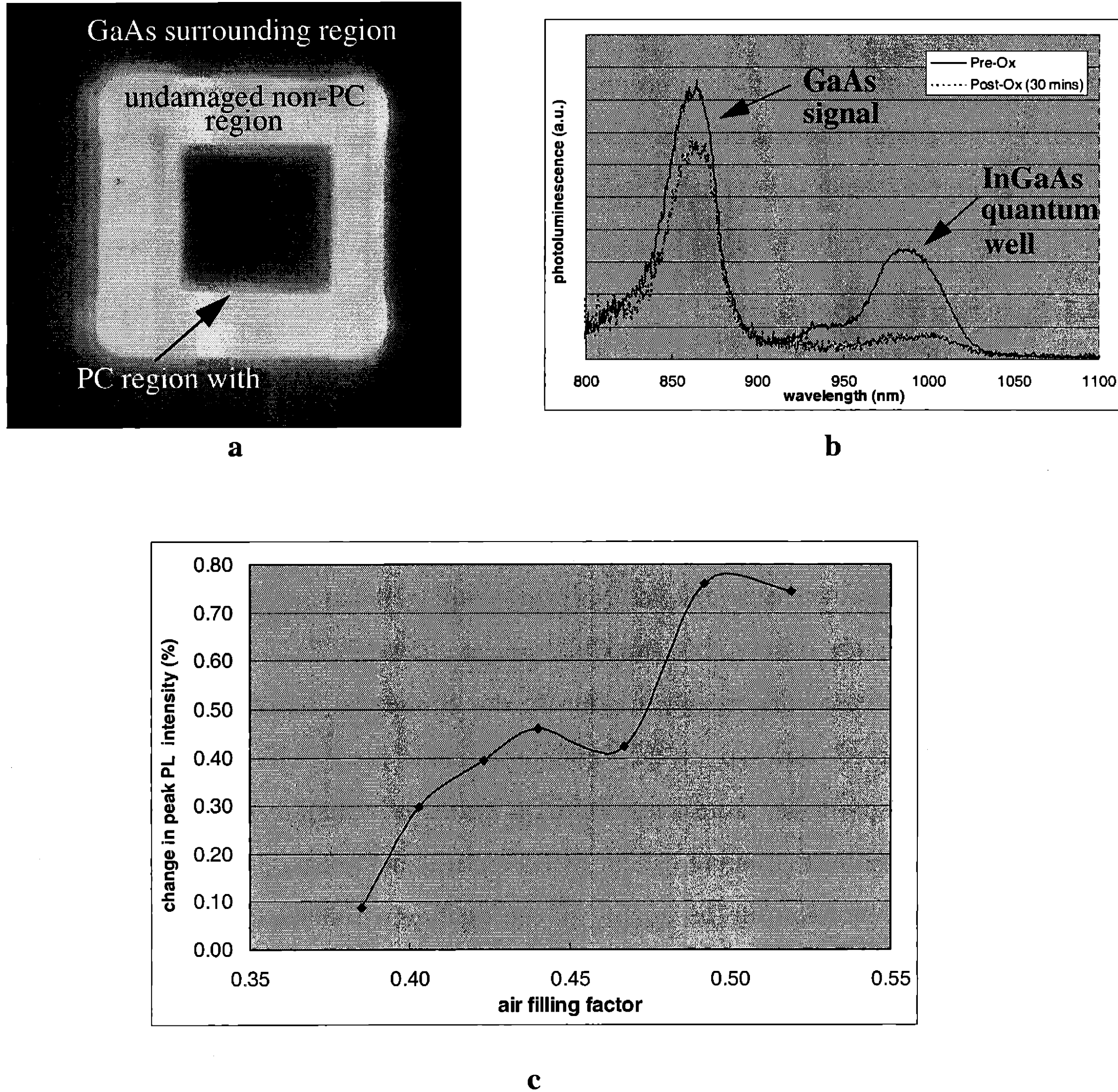

Figure 2-32. a) PC LED mesa with quantum well damage. The center PC region is designed for PBG-enhancement. b) PL spectra from PC structure before and after oxidation. c) Dependence of quantum well damage on air filling factor.

The drop in PL was also found to scale with the air filling factor ($1-\frac{2\pi}{\sqrt{3}}\left(\frac{r}{a}\right)^2$)of the PC. Figure 2-32c plots the fractional change in PL versus the filling factor for several different test PC LED structures. Lower air filling factors result in less degradation of the PL signal.

Moreover, the dependence on filling factor may partially explain the retained high-quality of the quantum wells in the resonance-enhanced structures where the air filling factor is significantly less (~.23) than the PBG-enhanced structures (~.45) and the range of test PC LED structures in Figure 2-32c. The required mesa oxidation time for the high-efficiency semiconductor PC LED is well above 30 mins (~ 6 hrs for a 50 μm wide mesa). Therefore, the quantum well damage will need to be eliminated to observe a room-temperature PBG-enhancement.

2.9.3 Literature Review

Although the oxidation process is common for optical sources such as VCSELs where one may expect such quantum well damage to appear, only one report was found that matched the quantum well damage results in Figure 2-32. The reason for few reports may be that the majority of the lasing action in a VCSEL occurs far away from the oxidation front. Indeed, a damaged quantum well region on the edges of a VCSEL mesa may even prove beneficial since gain is undesirable far from the center of the mesa. In [70], however, a 5-fold decrease in PL is observed from an $In_{.20}Ga_{.80}As$ quantum well near an oxidizing AlGaAs layer along with a corresponding increase in the radiative lifetime from 1 to 12 ns. Secondary ion mass spectroscopy was used to identify significant oxygen concentration in the degraded quantum well region. As reported, the oxygen diffused from the oxidizing layer through a 22.5 nm AlGaAs barrier layer and a 10 nm GaAs layer into the quantum well; these depths are even greater than the distance from the $In_{0.20}Ga_{0.80}As$ in the PC to the exposed surface. In addition, the dependence on air-filling factor (Figure 2-32c) is indicative of a diffusion dependent process. For lower air-filling factors, such as the resonance-enhanced PC LED structures, the percent of quantum well material containing significant oxygen defects is reduced as compared to the higher air-filling factor PBG-enhanced PC LED structures.

2.9.4 Reducing Quantum Well Damage

One potential method of preserving the high-quality of the $In_{0.20}Ga_{0.80}As$ quantum well is to deposit a protective overlayer prior to the oxidation process. To determine the benefits of a protective overlayer, a 500 nm thick SiO_2 layer was sputtered on a PC LED test sample (without mesas) before commencing oxidation. Unfortunately, similar quantum well damage was

observed when comparing PL before and after oxidation. Alternative protective overlayers such as Si_3N_4 and spin-on glass were deemed incompatible with the PC LED fabrication process and therefore were not pursued.

Since the drop in PL arises from the proximity of the quantum well to the surface in the etched PC holes, it is reasonable to consider etching the PC holes as the last step in the fabrication sequence (i.e. after the oxidation). Two methods were investigated for doing the PC etching after the oxidation process: 1) A dual-hard mask process and 2) an electron-beam alignment process. In the dual hard-mask process, a metal mask is defined using EBL and then left on during the mesa definition and the oxidation. The metal is used at the end of the process as a mask to etch the PC region. However, initial experiments with Ni, Ti, and W metal masks for the PC demonstrated poor adhesion during the high-temperature oxidation process. In addition, a lift-off step must be used for the metal mask process so all of the area surrounding the holes needs to be exposed in the EBL step. The inverted pattern requires a larger total written area than the process depicted in Figure 2-17, and therefore the uniformity in hole size across the PC pattern is more difficult to control due to the proximity effect. For these reasons, the dual-hard mask process is not suitable for the fabrication of the PC LED.

The second option is to define and oxidize the mesas first followed by definition of the PC pattern by aligning electron beam lithography system to the predefined mesas. The electron-beam alignment is not critical to the process and may easily be performed with $<5\ \mu m$ accuracy using alignment marks defined in the same step as the mesas. Therefore, performing the EBL on the predefined and pre-oxidized mesas is the most attractive solution for eliminating quantum well damage from the PC LED structures.

2.9.5 Pump-Coupling to PBG Structures

As was detailed in Section 2.8, coupling of the pump light to higher-order resonances in the PC LED can greatly enhance injection efficiency and therefore may prove useful in testing PBG-structures. According to EQ. 45, enhancements in external efficiency due to a PBG will only be observed if radiative emission into free-space modes (a relatively slow process as

evidenced by the poor external efficiency of plain slab LEDs) exceeds nonradiative recombination. Rewriting EQ. 45 for a semiconductor as

$$E=\frac{BN^2\left(1+\frac{\tau_{fr}}{\tau_g}\right)}{BN^2+\left(AN+CN^3\right)}, \quad \text{(EQ 65)}$$

shows explicitly the direct competition between radiative and nonradiative recombination. EQ. 65 is very similar to EQ. 61 except that the factor B is suppressed by the PBG.

To test these ideas, white light reflectivity is performed on a PC LED mesa with a lattice constant of 320 nm and a hole radius of 220 nm yielding an *r/a* ratio of about 0.35 and a PBG around the emission wavelength according to the calculated photonic band diagram shown in Figure 2-12. Figure 2-33a shows the white-light reflectivity for a PC (shown in the inset) that according to the calculated band diagram may contain a PBG. The peak in reflectivity is unphysical and must be due to a nonuniformity in the mirror or a Fabry-Perot effect due to the reduced effective index of the top layer from the holes of the PC. A resonance peak near 740 nm is used to pump the PBG LED structure that otherwise shows low PL. The PL spectra for the PC region is shown along with the reference emission from a blank mesa both taken while exciting with the pump laser tuned to 740 nm. Strong emission is observed near the material emission peak and it is speculated that the strong emission may be due at least in part to the presence of a PBG. The enhancement is mainly attributed, however, to the enhanced injection of carriers while pumping on resonance and therefore the enhancement in external efficiency due to the PBG cannot be directly extracted from this data. When tuned off resonance the PL emission from the PBG is

drastically reduced. A four-fold decrease in PL due to quantum well damage has been demonstrated in Section 2.9.2, making a room temperature measurement of the PBG difficult.

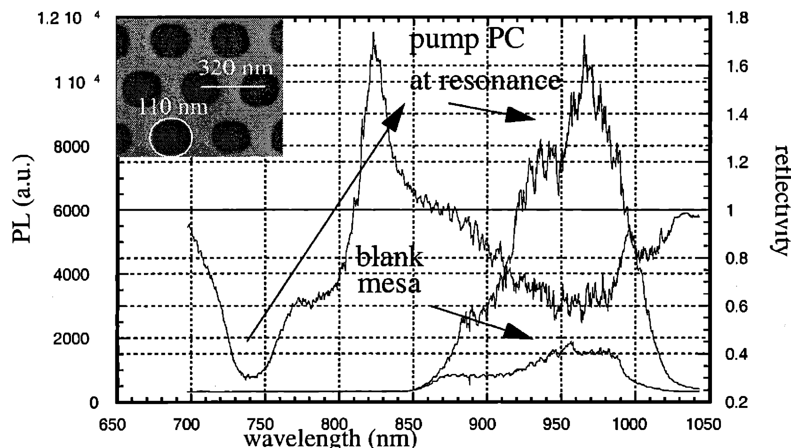

Figure 2-33. Reflectivity and PL emission from a PC structure that may contain a PBG. PL is observed when the pump wavelength is tuned to a resonance near 740 nm.

From the results, it is concluded that using a PC with a PBG surrounding the material emission is an interesting but impractical method of obtaining an enhancement in external efficiency. Suppression of radiative emission in the PBG constrains the device processing to extremely sensitive processes that do not introduce any nonradiative recombination pathways. The presence of oxygen in the PC LED quantum wells has created a nonradiative recombination mechanism that may be greatly magnified due to the presence of a PBG.

2.9.6 Upper Frequency Cutoff

The folding of the light-cone at the edges of the Brillouin zone creates an upper frequency cutoff above which only leaky resonances and free-space modes exist as discussed in Section 2.2.3. The external efficiency for such a structure is given by EQ. 48 and is identical to that for a PBG structure provided the emission rate into free space modes remains relatively constant between the two. Since the emission rate into free space is a relatively slow process in comparison to the emission into leaky resonance modes, the creation of an upper-frequency cutoff is a less promising PC LED design. For this reason, PC structures with an upper frequency cutoff

were not directly explored. However, emission into free-space modes does contribute a small amount to the 17.8% external efficiency reported in Section 2.8.4.

2.10 Conclusions: PCs for High-Efficiency Semiconductor LEDs

PCs have been examined in detail as potential candidates for high-efficiency semiconductor LEDs. Enhancement through leaky resonances in the PC was identified at the most promising method. Careful testing was performed allowing a direct measurement of a factor of 6 enhancement due to resonances in the PC. A large external efficiency of 54% is reported for a particularly noninvasive high-efficiency PC LED structure, a dramatic improvement over past attempts. Even larger enhancements in external efficiency are expected for devices that contain PC resonances with maximum overlap of the material emission ($Q \sim Q_m$). Many such structures have been fabricated and should be explored in the near future at MIT. A particularly important measurement that needs to be performed uses a wide-collection angle to ensure equal injection efficiencies between the PC structure and the reference structure as initially assumed in Section 2.7.

This chapter has also identified and quantified oxygen contamination of the quantum well during the oxidation process that introduces nonradiative recombination pathways. When considering the impact of nonradiative recombination, a PC structure containing a PBG or an upper-frequency cutoff is a less promising means of obtaining a practical high-efficiency semiconductor LED. However, a means of eliminating the oxygen contamination by reversing the fabrication process has been suggested.

This chapter has presented a framework for the implementation of PCs into any thin-film semiconductor LED. The generic designs given are especially attractive because they are noninvasive in that material is not removed in creating the PC and surface recombination may be potentially eliminated. The designs are more easily transferable into manufacturing than previously attempted solutions, even those using PCs. The challenges of making the high-efficiency PC LED presented in this chapter electrically-active need to be explored in the near future.

Chapter 3. Large Scale Oxidation of AlAs Layers for Broadband Saturable Bragg Reflectors

3.1 Motivation: Ultrashort Optical Pulse Generation

Time-division multiplexing (TDM) combines data in time from one or more optical sources for transmission through optical fibers. The generation of ultrafast optical pulses allows for higher bit transmission rates [74]. In general, narrowing of the pulse width is limited by the uncertainty principle

$$\Delta\upsilon\Delta\tau \geq \frac{1}{4\pi}. \qquad \text{(EQ 66)}$$

By increasing the spread in frequencies (and correspondingly the range in Fourier components that constitute the pulse), the pulse width may be shortened to only a few optical cycles; the lower limit being the natural time-scale of a single optical cycle:

$$\tau \sim \frac{\lambda}{c}, \qquad \text{(EQ 67)}$$

where λ is the wavelength of light used to generate the pulse and c is the speed of light in vacuum. For instance, for λ=1.55 μm (the minimum loss wavelength in standard optical fiber), the

minimum pulse width is 5 fs. The Cr^{4+}:YAG laser system provides a widely tunable range near 1.55 μm suitable for the generation of ultrafast laser pulses for telecommunications [75].

Optical pulses are generated in a laser cavity provided they experience higher gain than continuous wave (cw) light. To create this condition, periodically-spaced frequency domain laser cavity modes are phase-locked to each other to take advantage of the entire gain spectrum, a technique termed modelocking. In cw operation, the electric field energy is concentrated in only a few modes near the laser cavity gain peak. By phase-locking a large number of modes together, a much larger bandwidth is utilized and from EQ. 66 a shorter duration optical pulse is achievable. However, the control of large bandwidths of light is difficult and relies on broadband dispersion compensating and reflective optical elements. In addition, one must consider effects such as gain, loss, group delay dispersion, and self-phase modulation.

Modelocking is accomplished by creating a time-dependent optical loss within the laser cavity either by an optical modulator (active modelocking) or by nonlinear interactions within the laser cavity itself (passive modelocking). Active modelocking, while effective in rapidly compressing long pulses, is ineffective in further compressing already short pulses. In contrast, passive modelocking creates a time-dependent loss based on the intensity of the pulse itself, and shortens pulses further by a process called self amplitude modulation (SAM). A saturable absorber is an optical element that exhibits such an intensity-dependent loss mechanism; an example of a typical saturable absorbing material is shown in Figure 3-1. Low-intensity cw light is absorbed linearly, while high energy density short intense pulses experience less absorption. If the recovery time of the absorbing medium is fast enough, both the leading and trailing ends of the optical pulse experience significant loss leading to a shorter pulse. A fast saturable absorber in combination with large bandwidth reflective optical elements may generate pulses short enough to allow further reduction through self-phase modulation and group velocity dispersion; the balance of the two creates soliton-like pulse shaping effects. Fast-saturable absorbing materi-

als are also self-starting in that they require no external perturbation to initiate passive modelocking.

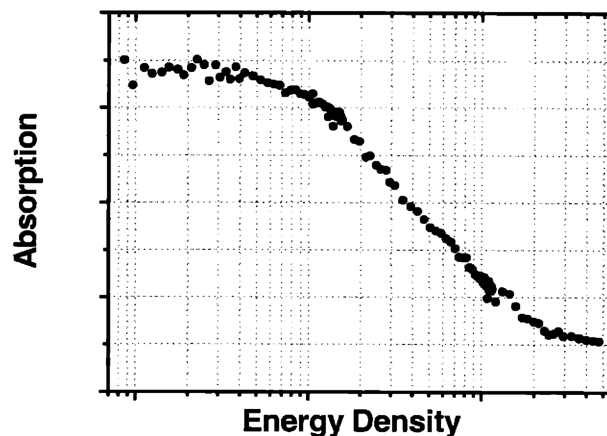

Figure 3-1. Absorption fraction of transmission in a saturable absorbing material (from [76]).

An elegant method of combining a broadband reflective optical element and a saturable absorbing material for use in an ultrashort pulse laser cavity is to epitaxially grow a semiconductor quantum well on a Bragg mirror to form a saturable Bragg reflector (SBR). The quantum well is the saturable absorbing medium while the Bragg mirror provides a broadband mirror that is also low-loss, an essential feature for the low gain of the Cr^{4+}:YAG laser. The recovery time of a semiconductor quantum well is on the order of 10 ns and is therefore not by itself capable of generating femtosecond pulse widths. However, the quantum well may be used to quickly self-start a nanosecond optical pulse that may be further compressed using Kerr-lens modelocking (KLM). KLM is a fast saturable absorber form of passive modelocking that relies on the optical Kerr effect which is an intensity-dependent index of refraction. In Kerr media, high-intensity pulses "self-focus" creating a different beam profile than low-intensity cw radiation in the laser cavity. Spatial filters may then be inserted in the laser cavity to preserve only the intense short pulses. By using KLM, the pulse width becomes primarily limited by the bandwidth of the Bragg mirror.

3.2 Saturable Bragg Reflector Design

To date, several groups have reported using SBRs for modelocking Cr^{4+}:YAG lasers [77-80] where the saturable absorbing material is typically an InGaAs quantum well (emitting near 1.55 μm) clad with either InP or InAlAs barrier layers, and the Bragg mirror consists of GaAs/AlAs pairs.

Figure 3-2 shows the optical power spectrum of a Cr^{4+}:YAG pulse. To take full advantage of the entire available bandwidth from the Cr^{4+}:YAG laser, the SBR mirror design should be centered near 1440 nm and should have a reflectivity greater than 99.5% spanning over 300 nm. Likewise, the saturable region of the SBR should absorb wavelengths above 1580 nm.

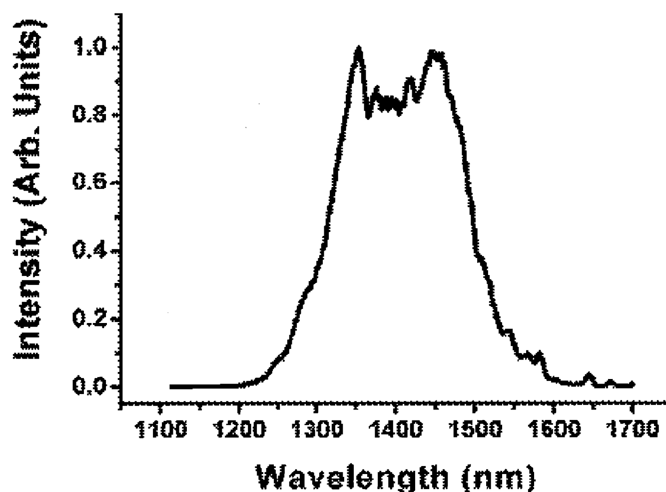

Figure 3-2. Optical power spectrum of a Cr^{4+}:YAG pulse (from [76]).

3.2.1 Mirror Design

Even with upward of 30 periods, the GaAs/AlAs mirror is limited to a useful bandwidth of ~100 nm, which limits the achievable pulsewidth to ~ 60 fs. The bandwidth of the mirror may be expanded significantly by instead using a GaAs/Al_2O_3 mirror, a 1D PC, with a much higher index contrast for each mirror period. Figure 3-3 compares the calculated reflectivity from a 30 pair GaAs/AlAs Bragg mirror to that of a 7 period GaAs/Al_2O_3 Bragg mirror. The indices of refraction of the GaAs, AlAs, and Al_2O_3 are 3.43, 2.87, and 1.66 respectively at 1440

nm. The thickness of each layer is equal to a quarter-wavelength in the respective material. A 10% volume contraction upon conversion to Al_2O_3 is accounted for in the design (the oxidation process is further detailed in Section 3.3.5). The number of periods is set at 7 to maximize the bandwidth while also limiting the nonsaturable loss in the mirror. The reflectivity is calculated using transmission matrices (see Appendix A.1). The mirrors are both centered at 1440 nm. The $GaAs/Al_2O_3$ mirror has a broadband reflectivity of >99.5% from 1250 nm to 1850 nm, where as the same threshold only spans from 1400 nm to 1550 nm for the GaAs/AlAs mirror. The high-index contrast of the $GaAs/Al_2O_3$ system offers the additional advantages of a smaller number of periods, short epitaxial growth times, and a relaxed requirement on the thickness control.

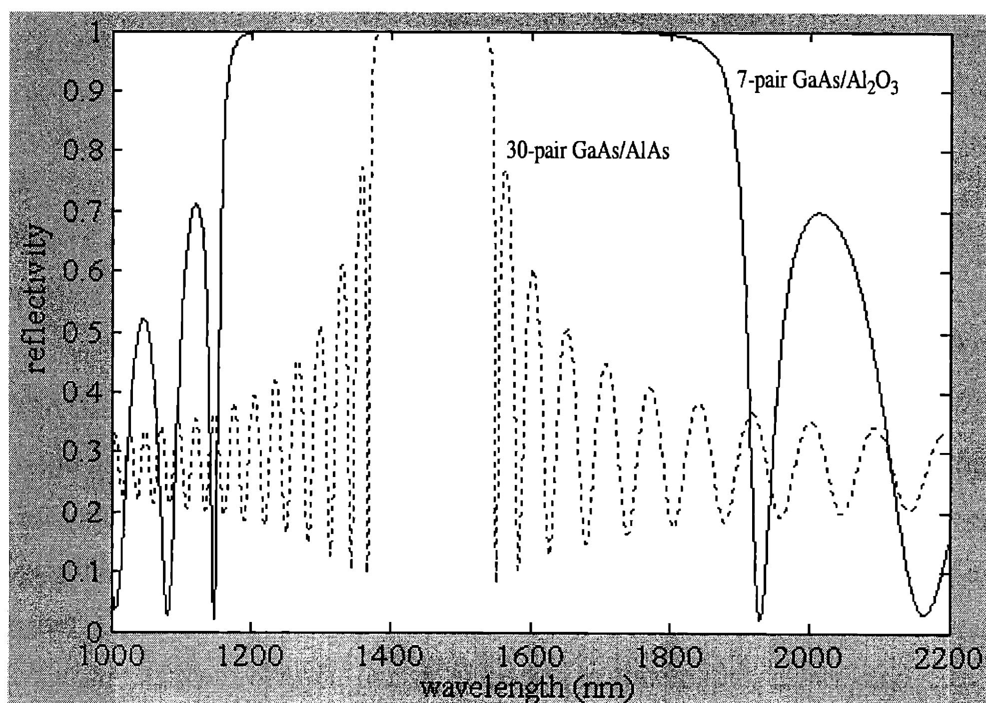

Figure 3-3. Calculated reflectivity for a GaAs/AlAs Bragg mirror (dotted line) and high-index contrast $GaAs/Al_2O_3$ Bragg mirror (solid line).

Group delay dispersion (GDD) describes the effect on radiation propagating through a medium with a frequency-dependent index of refraction. GDD must be carefully controlled or compensated for during generation of ultrashort optical pulses. Figure 3-4 shows a plot of the calculated GDD for a 7 layer $GaAs/Al_2O_3$ Bragg mirror. The dispersion is close to zero

from approximately 1200 nm to 1800 nm closely matching the broad stopband of the GaAs/Al_2O_3 Bragg mirror. Therefore, the GaAs/Al_2O_3 mirror itself does not cause significant dispersion. The broadband reflectivity, low loss, ease of epitaxial growth, and lack of dispersion motivate the use of a GaAs/Al_2O_3 mirror in the Cr^{4+}:YAG laser cavity.

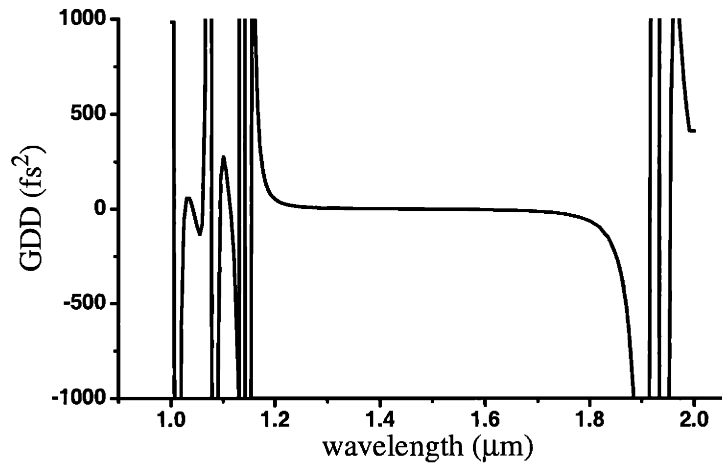

Figure 3-4. Calculated GDD for a 7 pair GaAs/Al_2O_3 Bragg mirror (from [75]).

3.2.2 Absorber Design

The absorber region, lying on top of the GaAs/Al_2O_3 mirror, consists of a quantum well comprised of a 10 nm $In_{0.52}Ga_{0.48}As$ layer centered within a half-wavelength thick InP layer and designed for a band-edge near 1580 nm (Figure 3-5). The center wavelength for the SBR structure is chosen to be 1440 nm, sufficiently below the band edge of the absorbing quantum well. A standing field pattern is created by the interference from the GaAs/Al_2O_3 mirror and the incident radiation. The quantum well is placed at an anti-node in the standing wave pattern, which lies at the center of the half-wavelength absorber region, to maximize the overlap with the local energy density. A more detailed analysis of the absorber region design may be found in [75].

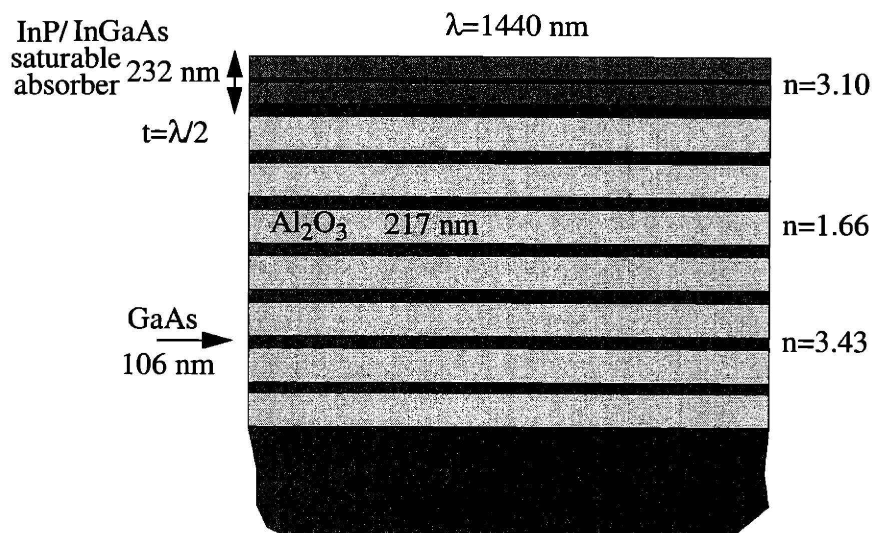

Figure 3-5. SBR design using λ=1440 nm includes an InGaAs/InP quantum well and a 7 pair GaAs/Al_2O_3 Bragg mirror.

The AlAs layer is grown approximately 10% thicker than the final thickness of the Al_2O_3. It has been reported that the AlAs layer shrinks by approximately 12% upon oxidation and this shrinkage is therefore accounted for in the epitaxial growth [113]. Actually, the large bandwidth of the mirror due to the high index contrast between Al_2O_3 and GaAs makes the performance of the mirror less sensitive to the exact thickness of the low-index layer. Figure 3-6 shows the reflectivity of the Bragg mirror for various thickness contractions upon oxidation. Considering a threshold of > 99.5% reflectivity for the SBR, a wide range from approximately 1250 to 1700 nm of usable bandwidth from the Cr^{4+}:YAG is still available over a 20% final Al_2O_3 thickness error range.

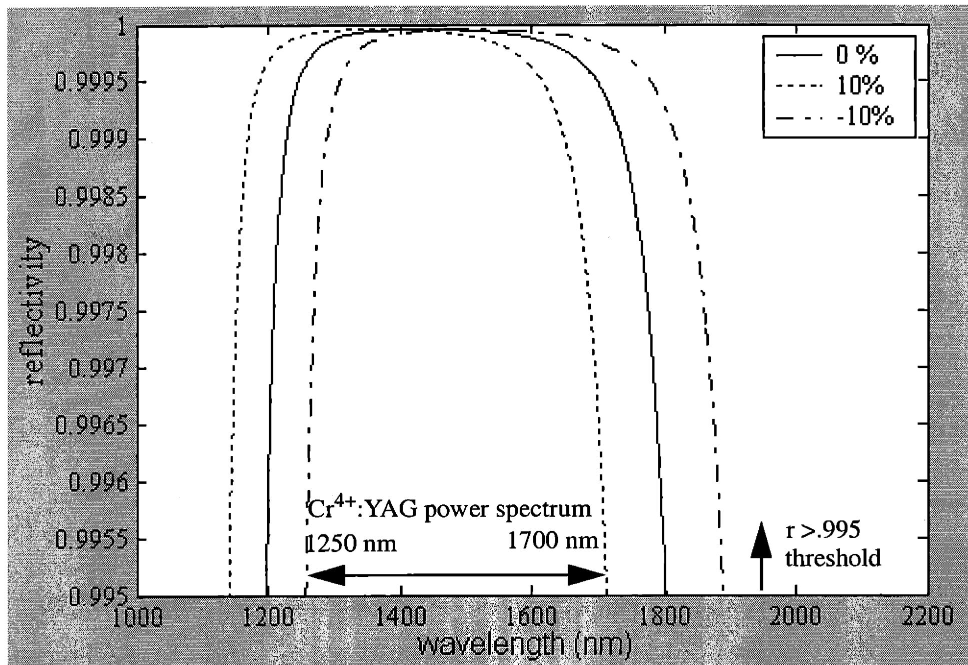

Figure 3-6. Calculated reflectivity spectrum of high-index contrast $GaAs/Al_2O_3$ Bragg mirror for a 20% range of error in thickness of the low-index Al_2O_3 layer.

3.2.3 Epitaxial Growth of the Absorber Region

Of particular interest is the quality of the absorber region grown by GSMBE on the Riber 32P system shown in Figure 2-9. Since the GaAs/AlAs mirror layers must be grown lattice-matched to a GaAs substrate, the InGaAs/InP absorber region is heavily strained due to the lattice mismatch between GaAs (a=5.65 Å) and InP (a=5.87 Å). The epitaxial growth process may therefore only progress pseudomorphically to some critical thickness at which point defects are introduced that limit the internal efficiency of the quantum well. The critical thickness at which a layer relaxes may be calculated by balancing the strain energy at the growth interface with the energy required to generate misfit dislocations as was done by Matthews and Blakeslee [81]. It is well known that the critical thickness is less than 100 Å for InP on GaAs. The index of refraction of InP near 1440 nm is approximately 3.1 so that the total required thickness of the absorber region is 232 nm (for half a wavelength in the material), well above the critical thickness. Indeed,

the lattice mismatch is so severe that separate islands of material form to minimize the surface energy of the growth interface. As a general rule of thumb, an interface that has greater than 1.5% lattice mismatch (~3.5% for InP on GaAs) will exhibit such island growth. Island growth yields a poor quality active material for most light-emitting applications where high internal efficiency is essential (e.g.the PC LED discussed in Chapter 2).

Room-temperature PL from the SBR material is plotted in Figure 3-7; this PL was taken using the setup detailed in Figure 2-11. The full-width at half-maximum is ~90 nm indicating the poor quality of the quantum well. However, the presence of defects in the quantum well may actually enhance the passive modelocking process by decreasing the carrier lifetime in the quantum well. The quality of the InP/InGaAs absorber region is therefore sufficient for use in the Cr^{4+}:YAG laser cavity, but must first be confirmed by pump-probe measurements as reported in [75].

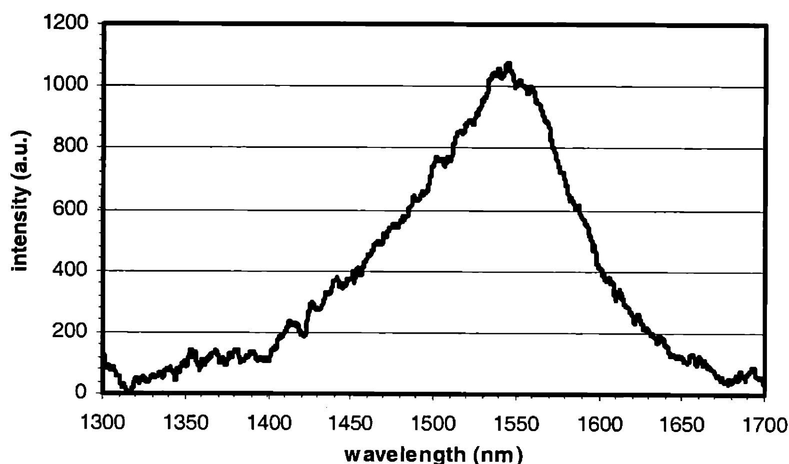

Figure 3-7. PL emission from the absorber region of a broadband SBR.

A potential alternative to growing a quantum well for the SBR in the Cr^{4+}:YAG laser is to instead grow InAs quantum dots that may demonstrate higher luminescence efficiency near 1.55 μm. Size nonuniformity, however, may increase the required saturation fluence of the absorbing region. In general, one wants the saturation fluence to be on the same order as the intracavity pulse intensity incident on the SBR.

3.2.4 Additional Growth Observations

The PL of the quantum well improves if a phosphine overpressure is applied before commencing the growth of the lower InP layer in the absorbing region [121]. The phosphine overpressure induces the growth of a thin monolayer of GaP (a=.545). The heavy lattice mismatch between the InP layers (a=5.87 Å) and the GaP monolayer (~7.1%) causes the interface to immediately relax generating defects. The defect density then decreases with distance from the relaxed interface. The quality of the quantum well is therefore slightly improved by inducing the surface relaxation immediately at the absorber region interface, rather than allowing pseudomorphic growth to progress up until the critical thickness (<10 nm). In the latter case, misfit dislocations are formed that extend into the quantum well itself further decreasing the radiative efficiency.

3.3 Large Scale Oxidation of GaAs/Al_2O_3 Mirrors

As described in Chapter 2, a steam oxidation process is used to convert the AlAs layers to Al_2O_3. For use in the ultrashort Cr^{4+}:YAG laser cavity, however, the size of the mirrors must be greater than approximately (200 μm)^2. The reason for the large mirror size is that a smaller mirror requires a smaller beam spot size incident on the SBR, translating to higher fluences. At high fluences two-photon absorption begins to limit the narrowing of the pulse width by acting as an inverse saturable absorber; this limiting effect may be observed using pump-probe spectroscopy [82]. Indeed, it is expected that a (500 μm)^2 mirror may eliminate the effects of two-photon absorption in the Cr^{4+}:YAG laser cavity [82]. The effect of two-photon absorption absorption is particular severe because the quantum well is placed at an anti-node in the standing wave pattern of the SBR. The large-scale oxidation of GaAs/AlAs pairs, however, can be problematic. AlAs layers contract to Al_2O_3 creating interfacial stress that results in the delamination of layers. The goal is then to successfully fabricate a large area GaAs/Al_2O_3 PC directly integrated with a saturable absorber for use in the Cr^{4+}:YAG laser cavity.

3.3.1 Fabrication

All SBR samples are oxidized using the setup in Figure 2-21. Careful attention is given to consistency between oxidation runs. The bubbler temperature is maintained at an average temperature of 90°C. The N_2 flow is set at 1.5 liter/min. for all oxidations, well above the saturation threshold at the temperatures of interest [72]. Therefore, the oxidation rate is at a maximum for any given oxidation temperature and independent of slight variations in the N_2 flow. Only the temperature and time are varied between oxidations. Samples are either prepared by cleaving a wafer to expose an edge facet, or by defining mesas using photolithography and acid wet-etching.

The photolithography is performed to define mesas in photoresist that act as masks for the wet-etching process. Wet-etching of the active region is accomplished using a (1:1) $HCl:H_3PO_4$ solution to remove the top and bottom InP layers (10 seconds each) and a (1:8:40) $H_2SO_4:H_2O_2:H_2O$ acid solution dip to remove the InGaAs quantum well. The $H_2SO_4:H_2O_2:H_2O$ acid solution also nonselectively etches the AlAs/GaAs material system. 3 mins is typically sufficient to penetrate the entire 7-period GaAs/AlAs stack. DI H_2O is used to rinse each sample and stop the etching process between each wet-etch step. Samples are each dried with an N_2 gun and examined under the microscope to verify removal of the various materials. Sufficient etch depth is also confirmed using the SEM.

3.3.2 Delamination of AlAs layers at High Temperature

Figure 3-8a shows a top down SEM of a circular SBR mesa, 500 μm in diameter, oxidized at 435°C for 2 hrs. The roughness of the GaAs substrate surrounding the SBR mesa is due to nonuniform wet-etching rates along defects on the surface. Several layers in the mesa structure have apparently buckled and delaminated during the oxidation process. Figure 3-8b verifies that the delaminated interfaces exist between the GaAs and the AlAs interfaces. The same SBR material system also showed severe delamination after only 45 mins of oxidation at 435°C. Clearly, the oxidation process itself is causing enough stress at the oxidation front to propagate

delamination throughout the mesa structure. Therefore, the oxidation process itself needs to be thoroughly investigated before large-scale SBR mirrors can be successfully fabricated.

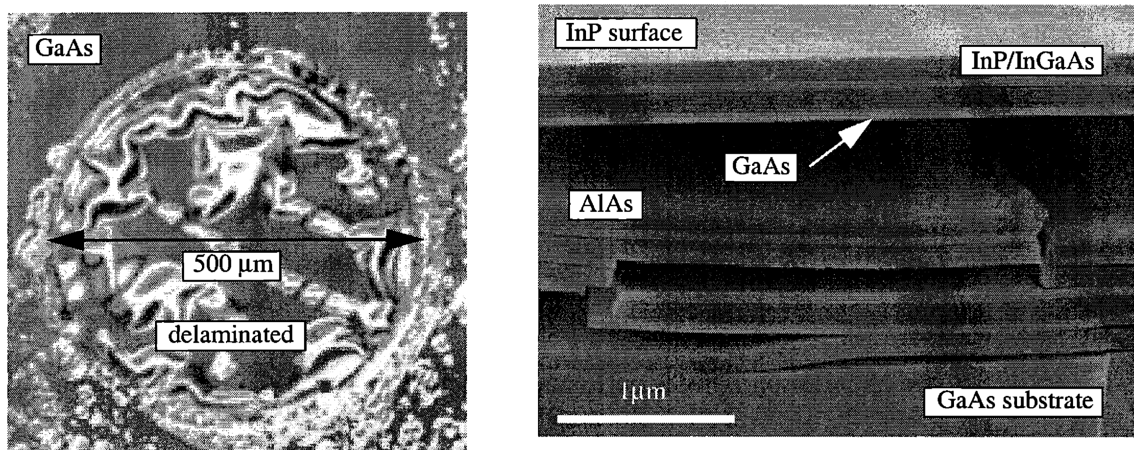

Figure 3-8. a) Top down SEM of mesa structure oxidized at 435°C for 4 hours. b) Cross-sectional view showing delamination.

3.3.3 Literature Review: GaAs/AlAs Mirror Oxidation

Some groups have met with success of oxidation of structures containing GaAs/AlAs mirrors, but all at smaller length-scales than the large-scale oxidation (>~(200 μm)^2) required for the SBRs. A particularly popular application of the GaAs/Al_2O_3 mirror is for vertical cavity surface-emitting lasers (VCSELs), but typically the mirror is of much smaller area than that required for the SBR [89]. In [90], a 57 μm wide ridge containing 3 GaAs/AlAs periods was oxidized successfully. However, the mirror is designed for a reflectivity centered around λ=1 μm, and therefore the pre-oxidation AlAs layers are thinner (162 nm) than for the SBR (240 nm) centered around λ=1.44 μm. In addition to the smaller length-scale of oxidation, the thinner layers and less periods should reduce delamination in such ridge mirror structures.

In [95], a 5 period GaAs/$Al_{0.95}Ga_{.05}As$ mirror centered at λ=1.55 μm is oxidized without report of delamination. The width of the mirrors are less than 40 μm, however, and the oxide is $(Al_xGa_{1-x})_2O_3$ rather than Al_2O_3. It is expected that the addition of Ga helps stabilize the structure (see Section 3.3.6), but reduces the oxidation rate dramatically, limiting the width of the

mirrors (40 μm or less). Indeed, in additional work by the same authors [94], $Al_xGa_{1-x}As$ with lower Al compositions (ranging form x=0.65 to x=0.8) are deliberately utilized to slow the oxidation rate and create stable mirror structures.

In [92], a Bragg mirror consisting of 2.5 periods of $Al_{0.1}Ga_{0.9}As/Al_2O_3$ is successfully constructed and even actuated to form a tunable filter. The stability of the mirror is attributed to the small number of periods used in the mirror and the added Al-content in the high-index layer of the mirror. In [93], an $AlGaAs/Al_2O_3$ mirror is constructed and no delamination is reported, again in large part due to the Al-content of the high-index layer. The small structures (50 μm) and relatively low temperature (400°C) for steam oxidation also contribute to the stability of the reported mirror.

In summary, the oxidation of AlAs/GaAs mirrors appears feasible over a small scale, provided sufficiently thin layers and a small number of periods are used. Recall that the PC LED structure presented in Chapter 2 does not suffer the same delamination problem as the SBR, primarily because of the thinner Al_2O_3 layers required for the Bragg mirror centered at λ=980 nm. Bragg mirrors in the PC LED structure as large as 250 μm in diameter have been successfully oxidized without delamination. The thickness of the mirror, however, and number of periods is dictated by the high-reflectivity necessary for the SBR centered at 1440 nm as described in Section 3.2.1. As demonstrated in the literature [92-93], the addition of Ga to the oxidizing layer helps stabilize certain mirror structures. But the Al-content of the oxidizing layer must remain close to unity, however, since large area oxidations in a reasonable time period are required for the SBR. Therefore, alternative methods must be pursued to stabilize a large area SBR mirror where the oxidizing layer is binary AlAs.

3.3.4 Alternative SBR Designs

Before undertaking the endeavor of stabilizing the SBR structure, one should consider alternative materials systems and processing schemes. Perhaps the most obvious solution to stabilizing the SBR structure is to utilize a different materials system that does not require oxidation for the mirror. However, the index contrast available using semiconductors is limited. For instance, GaAs-based GaAs/AlAs mirrors were shown in Section 3.2.1 to have insufficient index

contrast ($\Delta n=0.4$) and do not cover the entire Cr^{4+}:YAG gain spectrum. Sb-based AlAsSb/AlGaAsSb ($\Delta n=0.52$) [96] and InP-based InGaAs/InP ($\Delta n=0.31$) [95] mirrors also do not offer sufficiently high index contrast. Alternative materials such as (Al,Ga)-InP/AlAs have been investigated as Bragg mirrors [97], but oxidation for large area mirrors is expected to yield the same delamination problems for the SBR as the GaAs/AlAs materials system. Si/SiO_2 mirrors offer high-index contrast, but are not crystalline and therefore cannot be used as substrates for growth of reasonable quality absorber material using molecular beam epitaxy. It is possible, however, to sputter InAs quantum dots on Si/SiO_2 mirrors as described in [75]; this method is currently being explored in the ultrafast optics group at MIT.

An alternative process is to grow the active material on InP (where it is lattice matched), remove the substrate, and then wafer bond to a broadband mirror (Si/SiO_2 or GaAs/Al_2O_3). The wafer bonding process is not trivial but may be explored in the future in the CBE group at MIT. The oxidation of InAs/AlAs superlattices [98] and AlAs/GaAs digital alloys [99] also show promise for use in constructing broadband SBRs in the future.

3.3.5 $Al_xGa_{1-x}As$ Oxidation Process

In order to completely understand the nature of the Al_2O_3 interface delamination, the oxidation process itself must be considered in detail. The oxidation of $Al_xGa_{1-x}As$ to $(Al_xGa_{1-x})_2O_3$ involves three primary steps: transport of reactants from the bubbler (see Figure 2-21) to the oxide terminus, reaction at the oxide terminus to form Al_2O_3 or other reaction by-products, and the creation and transport of volatile by-products away from the oxide terminus. The entire oxidation process may be described by the Deal and Grove model [100]:

$$t = \frac{d^2}{k_{diff}} + \frac{d}{k_{rxn}} \qquad \text{(EQ 68)}$$

where the rate is either reaction- or diffusion-limited depending on the values of the reaction constants. Here, $\frac{1}{k_{diff}}$ and $\frac{1}{k_{rxn}}$ represent the sum of all diffusion and reaction rate constants, respectively, each dominated by the corresponding rate-limiting process. A reaction-limited regime is preferable because of the precise process control, but several authors have reported a parabolic

oxidation rate especially for long oxidation times [82,101-104]. For the SBR, long oxidation times (estimated >5 hrs. for oxidation temperatures less than the InP growth temperature) are necessary, and therefore the transfer from the linear regime to the parabolic regime needs to be examined. For large scale oxidations it is preferable to remain in the linear regime as long as possible so the overall oxidation time is reduced. The variation between the two regimes is best explained by examining the several phases present during the temporal evolution of the oxidation process.

In [105], the initial reacting species are determined using ultra-high vacuum conditions in conjunction with Auger electron spectroscopy (AES). The oxidation process begins with the molecular adsorption of water vapor on the reacting $Al_xGa_{1-x}As$ layer, that occurs anywhere above 100 K (steam oxidations are typically performed from 573-773 K). The adsorbed water vapor either desorbs or dissociates into various Al-O, Al-H, and As-H species on the $Al_xGa_{1-x}As$ surface. The As-H species are then observed to form arsine which readily desorbs.

Following [106] then, the initial stages of the oxidation process may be summarized by the equivalent molecular equations,

$$2AlAs + 3H_2O_{(g)} = Al_2O_3 + 2AsH_3 \qquad \Delta G = -451\frac{kJ}{mole} \qquad \textbf{(EQ 69)}$$

$$2AlAs + 4H_2O_{(g)} = 2AlO(OH) + 2AsH_3 \qquad \Delta G = -404\frac{kJ}{mole} \qquad \textbf{(EQ 70)}$$

where it is assumed that As-H dissociates directly into As-H_3. EQ. 69 and EQ. 70 are energetically favorable at 425°C, as evidenced by the corresponding change in Gibbs free energy (ΔG) associated with each reaction (ΔG is at 425°C, a temperature comparable to those used for oxidizing the SBRs). Although the AsH_3 may desorb above 200 K as reported in [105], it is not detected as a by-product in [106]. Using Raman spectroscopy, however, a constant *a*-As_2O_3 intensity is detected from the reaction:

$$2AsH_3 + 3H_2O_{(g)} = As_2O_{3(l)} + 6H_2 \qquad \Delta G = -22\frac{kJ}{mole} \qquad \textbf{(EQ 71)}$$

The relatively low change in Gibbs free energy at 425°C associated with EQ. 71 most likely explains why the formation of *a*-As_2O_3 was not observed in [105], where the measurements were performed at lower temperatures. A constant Raman intensity for As was also observed through-

out the temporal evolution of the oxide in [106]. Indeed, it is energetically favorable for the *a*-As_2O_3 species to further dissociate into elemental As:

$$As_2O_{3(l)} + 6H_2 = 2As + 3H_2 + 3H_2O_{(g)} \qquad \Delta G = -131\frac{kJ}{mole} \qquad \text{(EQ 72)}$$

Combining EQ. 71 and EQ. 72 shows that AsH_3 may also directly dissociate to form elemental As:

$$2AsH_3 = 2As + 3H_2 \qquad \Delta G = -153\frac{kJ}{mole} \qquad \text{(EQ 73)}$$

The resulting arsenic either diffuses from the film, resides in interstitial sites, or segregates to nearby interfaces, a problem shown to be detrimental to metal-insulator-semiconductor (MIS) devices based on the steam oxidation process [107]. The complete oxidation process is therefore described by combining EQ. 69 and EQ. 70 with EQ. 73:

$$2AlAs + 3H_2O_{(g)} = Al_2O_3 + 2As + 3H_2 \qquad \Delta G = -604\frac{kJ}{mole} \qquad \text{(EQ 74)}$$

$$2AlAs + 4H_2O_{(g)} = 2AlO(OH) + 2As + 3H_2 \qquad \Delta G = -557\frac{kJ}{mole} \qquad \text{(EQ 75)}$$

EQ. 74 and EQ. 75 show the possibility of two amorphous materials that may exist behind the *a*-As_2O_3-containing amorphous region at the oxidation front (AlO(OH) and Al_2O_3). Using elastic recoil detection (ERD), however, it has been shown that the hydrogen concentration is too small to support hydroxide phases in the oxidized layer [108].

The critical role of hydrogen in reducing the *a*-As_2O_3 has been demonstrated by using an O_2 carrier gas [109] as it consumes atomic hydrogen (inhibiting oxidation) to form water (ΔG=-1148 kJ/mole), and helps substantiate the intermediate oxidation steps given in EQ. 71 and EQ. 72. The existence of a thin (~10 nm) dense amorphous region at the oxidation front has also been observed [66]. The formation (EQ. 71) and reduction (EQ. 72) of *a*-As_2O_3 is critical in determining the regime of oxidation (linear or parabolic) as described by EQ. 68. Figure 3-9 is a schematic of the growth of the dense amorphous region at the oxidation front and the change from a linear (reaction-limited) to a parabolic regime (limited by diffusion through the dense amorphous region). An increased width of the dense amorphous region and the subsequent change to a parabolic time dependence is favored by increasing oxidation temperature and Al mole fraction

[106]. The overall effect on extended oxidations is to slow the oxidation rate, making large-scale oxidations difficult. It is speculated that the dense amorphous region containing a-As_2O_3 also contributes to the low reported rates of dry O_2 oxidation of AlGaAs [110]. It should be noted that the transport process through the oxide regions behind the dense amorphous region is not, at least initially, rate-limiting in the oxidation process since $k_{diff} \sim 8.5 \times k_{rxn}$ [111].

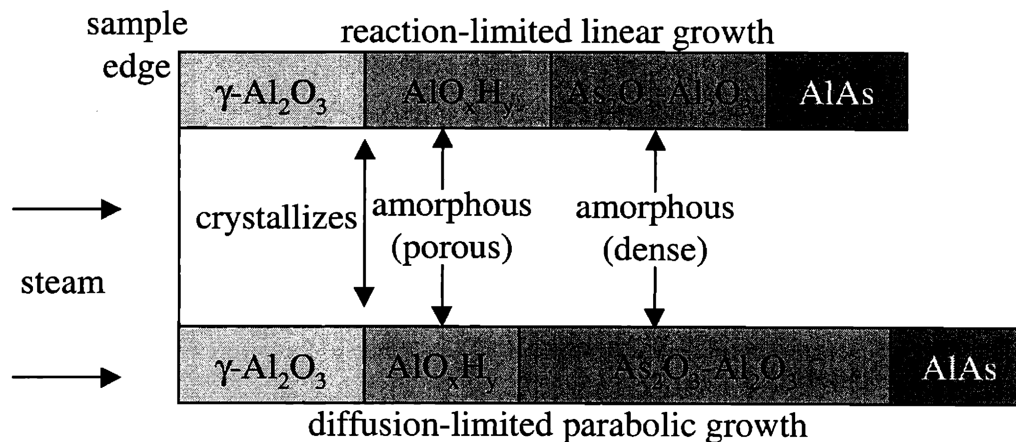

Figure 3-9. a) Schematic showing transition from linear to parabolic regimes for extended steam oxidations

Figure 3-10 shows transmission electron micrographs of oxidizing AlAs (a) and $Al_{0.92}Ga_{.08}As$ (b) layers. The oxidizing conditions are comparable to those used to oxidize the SBRs. The dense As_2O_3-containing amorphous region can be easily distinguished at the oxidation front in both micrographs.

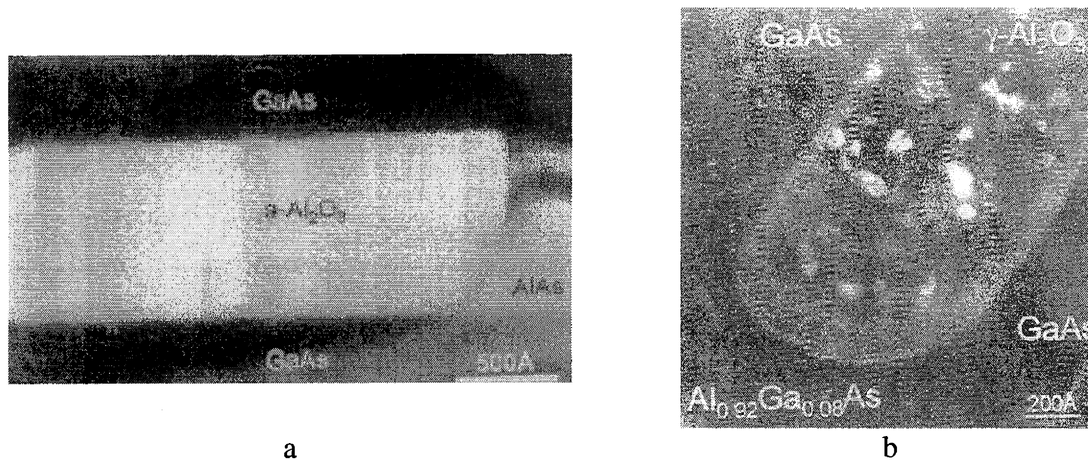

Figure 3-10. a) Oxidation front progressing in AlAs [108] b) Oxidation front progressing in $Al_{0.92}Ga_{.08}As$ [108]

3.3.6 Al_2O_3 Microstructure

The microstructure of the oxidizing film is determined primarily using electron diffraction. An amorphous solid solution of $(Al_xGa_{1-x})_2O_3$ (since nonstoichiometric alumina is uncommon), extends from behind the a-As_2O_3-containing layer to the edge facet of the exposed oxidizing layer [108]. Over time, and especially at higher temperatures, a small fraction of crystalline $(Al_xGa_{1-x})_2O_3$ may form along with grains ~10 nm in size of γ-$(Al_xGa_{1-x})_2O_3$ [112]. A complete transition from AlAs to crystalline γ-Al_2O_3 corresponds to a 20% linear contraction. Experimentally, a 12-13% contraction has been observed for AlAs steam oxidation [113] and a 6.7% contraction for $Al_{0.92}Ga_{.08}As$ [112]. The crystallization to γ-$(Al_xGa_{1-x})_2O_3$ grains may also be induced by electron beam exposure. By contrast, the a-As_2O_3-containing amorphous region at the oxidation front (Figure 3-10) is stable under electron beam exposure. In Figure 3-10a, the coarse γ-$(Al_xGa_{1-x})_2O_3$ grains behind the oxidation front can easily be distinguished. In Figure 3-10b, however, the amorphous Al_2O_3 has not yet begun to crystallize.

3.3.7 Oxide/Semiconductor Interface

A sharp interface has been reported between GaAs and the amorphous solid solution Al_2O_3 layer [108]. Void formation is reported to occur, however, because of electron beam-

induced crystallization during examination with TEM. Indeed, examination of SBR samples using SEM has routinely revealed void formation. At the oxide/GaAs interfaces a Ga_2O_3 layer has been observed to form [108]. The thickness of the Ga_2O_3 layer depends on the amount of time the porous oxide layer is exposed to the GaAs interface. Therefore, a thin but significant Ga_2O_3 layer should exist at the GaAs/oxide interfaces in the lengthy oxidations of the SBRs. The thickness of the Ga_2O_3 layer will depend on the proximity to the exposed facet where the oxidation process commenced.

3.3.8 Literature Review: Mechanical Instability of GaAs/AlAs mirrors

The mechanical instability of the interface between GaAs and Al_2O_3 has been noted by several groups [65, 84-88] although no systematic study has been performed to date and no data is available for large-scale (>100 μm) oxidation. In [65] and [85], the mechanical stability of mesas containing oxides formed from $Al_{0.98}Ga_{.02}As$ vs. AlAs are discussed following thermal annealing. The $(Al_{0.98}Ga_{.02})_2O_3$ is found to be more stable than the Al_2O_3. GaAs/Al_2O_3 interfaces in VCSELs are also found to degrade over the time of laser operation. The authors cite a reduction in strain due to smaller contraction of the $Al_{0.98}Ga_{.02}As$ layer as a possible explanation for the stability of the Ga-containing oxide. The strain field in the AlAs layer is found primarily at the oxide terminus and is not present for the Ga-containing oxide layer. The authors do not, however, report any delamination during the oxidation process itself, as is the case for the SBRs. In a conflicting argument, however, local stress measurements on a GaAs surface layer by shifts in the Raman spectra, reveal no difference between regions with an underlying $(Al_{1-x}Ga_x)_2O_3$ layer as compared to an underlying Al_2O_3 layer [114]. The authors report the same instabilities to thermal cycling as in [65] and [85], but conclude instead that delamination must be due to the chemical nature of the GaAs/oxide interfaces rather than the difference in strain due to volume contraction. As pointed out in [65] and [85], though, the strain is concentrated primarily around the oxide terminus rather than at the GaAs/$(Al_{1-x}Ga_x)_2O_3$ interfaces. Indeed in [99], delamination is found to originate at the oxide terminus itself. Therefore, one is led to believe that the delamination of the SBRs originates at the oxide terminus. However, because the layers delaminate during the oxidation process itself, it is difficult to immediately conclude the location

that the semiconductor/Al_2O_3 interfaces begin to delaminate. This issue will be further investigated in Section 3.5.1.

In [86], oxidation is performed on a GaAs/AlAs mirror structure for 30 mins at 425°C followed by a 10 min. oxidation to determine the resilience of the structure to repeated oxidations. The structure is found to delaminate during the second (10 min.) step of oxidation. Weak Ga_2O_3 formed at the GaAs/Al_2O_3 interface is discussed as the source of delamination. A graded AlGaAs layer introduced between the GaAs and the AlAs stabilized the structure by slowing the formation of Ga_2O_3 (i.e. slowing the progression of oxidation in the orthogonal direction to the oxidizing AlAs layer).

Multiple oxidations is also reported to cause delamination in GaAs/$(Al_{1-x}Ga_x)_2O_3$ mirror structures in [87]. The authors find that low (x<0.96) Al-containing oxides are more stable than higher Al-containing oxides. Thinner oxidation layers in mirror structures containing less total numbers of layers are also found to be more stable. Buffer layers of various Al compositions, placed between the high Al content oxidizing $Al_{1-x}Ga_xAs$ layer and the surrounding GaAs layers, are used to help stabilize structures during annealing and secondary oxidations. Contraction of the oxide layer due to crystallization during thermal cycling, and separation from the weak Ga_2O_3 layer, is concluded to be the primary mechanism of delamination. It is interesting to note that structures that have oxidized to completion are reported to be stable under further annealing and secondary oxidations, although no explanation is provided. The stability of a completed oxide in contrast to an unstable partially oxidized GaAs/AlAs structure is, however, discussed in some detail in [88]. The authors speculate that delamination during post-oxidation annealing is due to interfacial strain arising from the presence of by-products of the oxidation reaction. Raman spectroscopy was used to detect As and As_2O_3 in partially oxidized samples, completely oxidized samples, and over-oxidized samples. The over-oxidized structures contained less As and As_2O_3 and displayed improved thermal stability. However, an explanation of the relation between the reaction by-products to strain is not provided. On the other hand, according to previous results [86], extended oxidations should weaken the structure (increased Ga_2O_3 growth and crystallization/contraction of Al_2O_3).

3.3.9 Delamination of the SBR

It is somewhat surprising that literature was not found that describes delamination during the oxidation process itself, partly because large scale oxidations of structures similar to the SBR are not routinely performed (see Section 3.3.3). As detailed in Section 3.3.8, the delamination of GaAs/Al_2O_3 mirror structures typically occurs for multiple oxidation or oxidation/annealing processing sequences. It is therefore worthwhile to test the thermal stability of the SBR material itself prior to oxidation. The same SBR material as shown in Figure 3-8 was annealed in the oxidation furnace at 435°C while exposed to a constant flow of dry N_2. No structural changes were observed optically when comparing the annealed sample to an as-grown reference sample. To test the effect of thermal cycling, oxidations were attempted under the same conditions as those used for the delaminated structure shown in Figure 3-8, except with a cool-down step inserted. During the cool-down step the oxidation furnace is allowed to ramp down to a temperature of 200°C over the time period of 1 hr., before removing the SBR samples from the furnace. No significant reduction in delamination was observed by inserting the cool down step into the SBR oxidation process. Oxidations with and without a heating step, in which the furnace temperature is allowed to stabilize prior to flowing steam, also both produced delaminated structures. It is therefore concluded that thermal cycling is not the primary source of the observed delamination in the SBR structures

Oxidizing the PC LED structure discussed in chapter 2 was performed with no delamination. The difference between the Bragg mirror used in the PC LED and the SBR helps shed light on the nature of the delamination process. The AlAs layers in the SBR are almost 100 nm thicker (240 nm) than the AlAs layers in the PC LED (152 nm). Thicker AlAs layers suffer more volume contraction than thinner layers upon oxidation, so that the entire stack is under greater strain for the SBR as compared to the PC LED.

It is therefore hypothesized that the primary cause of the delamination observed in Figure 3-8 is stress induced during volume contraction at the oxide terminus. It is believed that the delamination originates at the oxide terminus [65,85,99], a hypothesis that will be supported by the results presented Section 3.5.1. Once the delaminated interface is incubated due to the

stress in the direction perpendicular to the oxidizing direction upon contraction at the oxide terminus, it propagates causing entire layers to buckle. The report that the stress in a GaAs surface layer on top of $(Al_{1-x}Ga_x)_2O_3$ is independent of the Al concentration also supports this theory [114], since the measurement may not have been able to detect stress in the plane of the oxide terminus. The dense As_2O_3-containing intermediate species, in addition to slowing the oxidation process, may be noncompliant at the oxide terminus causing layers to buckle as supported by the results in [88].

3.3.10 Oxidation Rate Dependencies

The highest oxidation rate is desired that does not degrade or delaminate the layers in the SBR structure. The rate of oxidation depends on various conditions during the steam oxidation process including: temperature [65,102,116], water temperature [115], composition [65,73], layer thickness [65,116,117,118], geometry [116, 119], and surrounding layers [120]. In addition, the oxidation rate itself is not constant and depends on the length of oxidation as discussed in Section 3.3.5. Detailing the rate dependencies of oxidizing the SBR structure is outside the scope of this work. Rather, the goal is to maximize the (stable) oxidation rate given the constraints of the SBR design.

Higher temperatures and increased Al content increase the rate of oxidation in the SBR structure. The temperature of the oxidation, however, must lie below the growth temperature of InP (~470°C). In addition, although less total number of layers should produce a more stable SBR structure for oxidation, at least 7 periods in the Bragg mirror are required for sufficiently high reflectivity (Figure 3-3). Lengthy oxidations also translate to a greater number of refills of the bubbler depicted in Figure 2-20. During each refill the water temperature varies (by ~ +/-5°C) leading to a slight variation in the oxidation rate. The effect on the oxide is noticeable under an optical microscope; therefore, the water is routinely heated on an external hotplate to reduce this effect and help ensure mirror uniformity.

3.4 Stabilizing the SBR Structure

As discussed in Section 3.3.3, stabilizing the SBR structure may be accomplished by oxidizing $Al_{1-x}Ga_xAs$ to form $(Al_{1-x}Ga_x)_2O_3$ which undergoes less volume contraction than Al_2O_3 formed from binary AlAs. The oxidation rate, however, drops dramatically with the addition of even small percentages of Ga [66]. In [66], the oxidation rate drops by more than 75% at 440°C, with the addition of only 2% Ga. It is possible to oxidize at higher temperatures to increase the oxidation rate. The InP growth temperature, however, is only 470°C, and oxidation well below that temperature is required to avoid degradation of the absorber region. Since for the SBR mirror, large-scale oxidation in a reasonable time period is required, the oxidation of $Al_{1-x}Ga_xAs$ is less attractive. Grading the Ga concentration at the interface between AlAs and GaAs is another method used to stabilize the $GaAs/Al_2O_3$ interface [86,91]. Compositional control of the grading is difficult though during the epitaxial growth and may lead to insufficient reflectivity of the Bragg mirror.

3.4.1 Stabilization of SBR at Reduced Oxidation Temperature

Higher temperatures will help activate the delamination process at the oxide terminus. Stress introduced upon contraction of the Al_2O_3 layers commences the delamination process. Oxidation at a lower temperature, however, may reduce the propagation of the delaminated AlAs layer and should help stabilize the entire SBR structure. In addition, as discussed in Section 3.3.3, lower temperature oxidized Bragg mirror structures have appeared in the literature, albeit of much lesser area, without report of delamination. The disadvantage of oxidizing at reduced temperatures is of course a slower oxidation rate.

Figure 3-11a is an SEM cross-sectional micrograph of the unoxidized/as-grown SBR structure that previously delaminated when oxidized at the elevated temperature of 435°C (Figure 3-8). The SEM-measured thickness of the AlAs layer (290 nm) is larger than the intended design (240 nm), indicating an approximately 17% higher than expected AlAs MBE growth rate. The GaAs thickness, which is more easily calibrated than the AlAs growth rate, is measured to be 105 nm and taken as the standard in the SEM measurement.

Figure 3-11b is an optical micrograph showing partial oxidation of a 500 μm diameter SBR mesa. A cylindrical geometry is used because of the increased oxidation rate [119]. The oxidation is performed at 400°C for 2 hrs. during which the oxidation front progresses isotropically 115 μm from the mesa edge. The oxidation is stopped short of completion to illustrate termination of the oxidation fronts. The material system is stable and delamination is not observed (compare to Figure 3-8a oxidized at 435°C). Oxidations were also attempted at the intermediate temperature of 415°C but severe delamination of the SBR layers, similar to that shown in Figure 3-8a, was still observed. Even at 400°C, some regions of delamination are observed at the edges of the SBR mesa shown in Figure 3-11b. SEM is used to verify that the delamination is occurring only at the top $GaAs/Al_2O_3$ interface, while other interfaces in the SBR remain intact. The layers surrounding the interior $GaAs/Al_2O_3$ pairs help stabilize the inner-most interfaces in the mirror stack. The top $GaAs/Al_2O_3$ interface may be stabilized by oxidizing at even lower temperatures, although the linear oxidation time decreases exponentially. Figure 3-11c is an SEM showing the oxidized layers of the SBR structure. From the SEM, the measured thickness of the Al_2O_3 layer is 230 nm (an AlAs contraction of ~14%).

To measure the reflectivity of the mirror structures in Figure 3-11a and Figure 3-11c, the top active layer is removed using the acid wet etch described in Section 3.3.1. The reflectivity of each mirror is measured using Fourier-transform infrared (FTIR) spectroscopy with a 150 μm diameter spot size on the mesa. Even though a gold mirror serves as a 100% reflective reference in the measurement, it still remains difficult to quantify the absolute reflectivity. For this reason, it is helpful to normalize each measured spectrum to its own reflectivity peak. The magnitude of the measured reflectivity peak is then scaled to the magnitude of the calculated peak for a direct comparison between the two. In addition, it should be noted that the accuracy of the FTIR system is limited for longer wavelengths above approximately 1900 nm, as indicated in the figure. The roll-off in the measured broadband reflectivity on the longer wavelength side of the stopband is also an artifact of the measurement. The same roll-off occurs when using gold and silver mirror standards, and other mirrors calibrated for absolute reflectivity.

The measured reflectivity is shown in Figure 3-11d and is compared to simulation for both the oxidized and unoxidized SBR structure. There is excellent agreement between the measured spectrum for the unoxidized mirror and the spectrum calculated using the layer thicknesses in Figure 3-11b. The FTIR measured oxidized mirror also matches well with the calculated mirror using the thickness measured in the SEM in Figure 3-11c. An extremely broadband SBR mirror is measured from 1200-2000 nm covering the entire Cr^{4+}:YAG power spectrum.

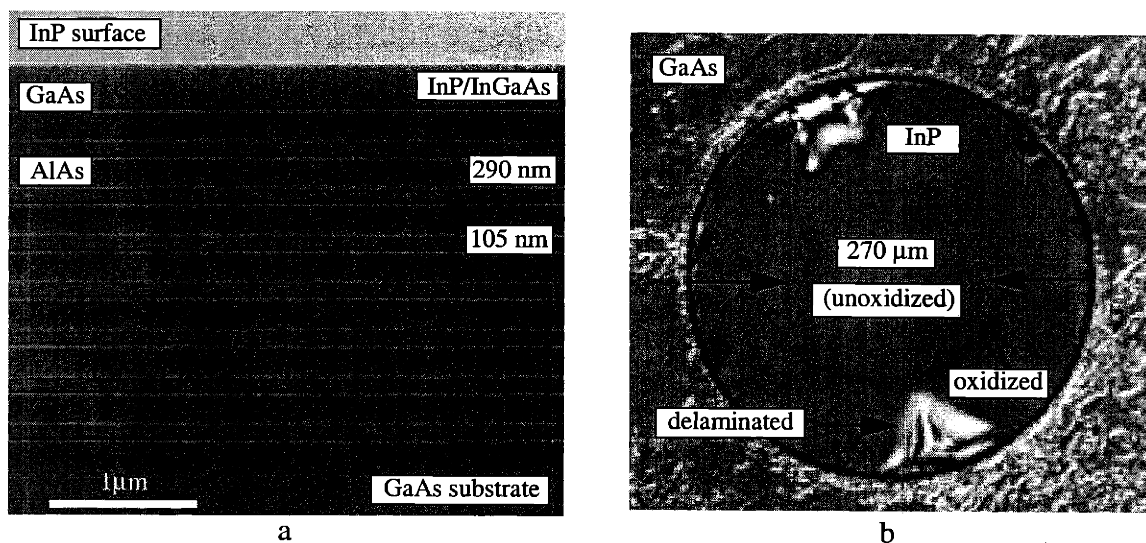

Figure 3-11. a) Cross-sectional SEM of unoxidized/as-grown layers in SBR. b) Optical micrograph of oxidation front progressing in SBR mesa oxidized at 400°C c) Cross-sectional SEM of SBR with oxidized low-index layers. d) Comparison between measured (solid-line) and simulated (dotted line) reflectivity.

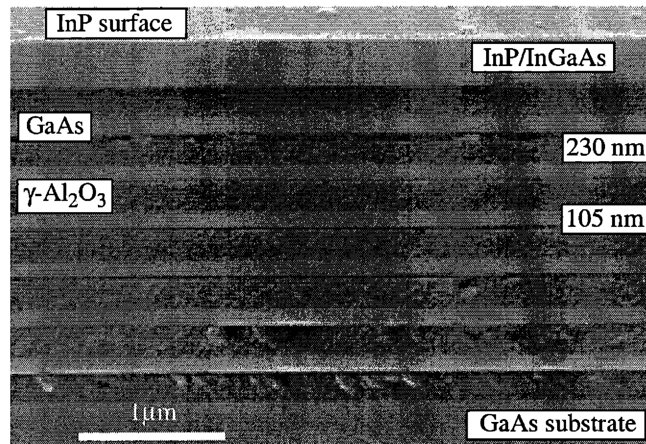

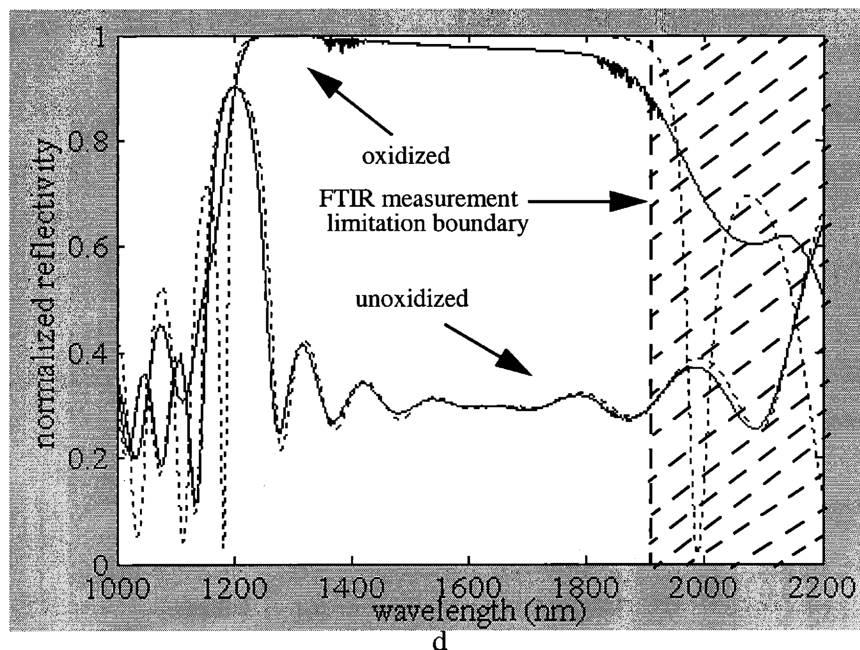

Figure 3-11. a) Cross-sectional SEM of unoxidized/as-grown layers in SBR. b) Optical micrograph of oxidation front progressing in SBR mesa oxidized at 400°C c) Cross-sectional SEM of SBR with oxidized low-index layers. d) Comparison between measured (solid-line) and simulated (dotted line) reflectivity.

An additional contribution to the stabilization of the SBR structure at lower temperatures is the slower oxidation of the GaAs. In [84], an AlAs surface layer is oxidized and the AlAs/GaAs interface is examined using Auger spectroscopy. At 430°C Ga_2O_3 is detected at the AlAs/GaAs interface and layer delamination occurs. It is reported that Ga_2O_3 does not form, however, at the interface at 400°C. Indeed, the GaAs substrate of each sample was examined fol-

lowing each oxidation at different temperatures. Discoloring of the GaAs surface indicating oxide formation was only observed above 400°C. Therefore, the formation of Ga_2O_3 is most likely reduced in the SBR structures when oxidizing at 400°C and below, strengthening the interface at the oxide terminus.

Although the quarter-wave SBR may be mechanically stabilized by oxidizing at lower temperatures, the oxidation rate is low, making it a less attractive solution for large-scale SBR structures. Alternative mirror designs are therefore pursued to stabilize the SBR material system at high-temperatures.

3.4.2 Alternative High-Reflectivity GaAs/Al_2O_3 Mirror

The successful oxidation of Bragg mirrors in mesas for the PC LED of diameters up to 250 μm encourages investigation into an alternative high-reflectivity GaAs/Al_2O_3 mirror that contains thinner Al_2O_3 layers. The Al_2O_3 layers of the PC LED (152 nm) are thinner than the Al_2O_3 layers of the SBR (217 nm) and therefore induce less strain in the heterostructure upon contraction during oxidation. In addition, as discussed in Section 3.3.3, thinner layer Bragg mirror structures (of much lesser area) have appeared in the literature without report of delamination.

The Al_2O_3 layer in the SBR may be made thinner by a corresponding increase in the thickness of the high-index GaAs layer such that the total phase-shift in propagating through the GaAs/Al_2O_3 period remains constant:

$$\Delta\phi = k_{GaAs}t_{GaAs} + k_{oxide}t_{oxide} \qquad \text{(EQ 76)}$$

where $k_{GaAs} = \frac{2\pi n_{GaAs}}{\lambda}$ and $k_{oxide} = \frac{2\pi n_{oxide}}{\lambda}$. For a quarter-wave stack, as depicted in Figure 3-5, the total propagation phase shift is π so that reflections from the dielectric interfaces add up in phase. The same condition is required for a broadband mirror consisting of thinner Al_2O_3 layers. For instance, if t_{oxide}=135 nm (~20 nm less than the thickness of the Al_2O_3 layers in the PC LED) then the thickness of the GaAs layer must satisfy:

$$t_{GaAs} = \frac{\pi - k_{oxide}t_{oxide}}{k_{GaAs}} \qquad \text{(EQ 77)}$$

Using EQ. 77, the thickness of the GaAs layer is calculated to be 145 nm for a 135 nm Al_2O_3 layer. Figure 3-12 shows the calculated reflectivity for a 7-period Bragg mirror consisting of 135 nm Al_2O_3 layers and 145 nm GaAs layers. The original 7-period quarter-wave stack is also included for comparison. Although the mirror bandwidth (1300-1700 nm for a >99.5% reflectivity threshold) is slightly less than for the quarter-wave stack, most of the 1250-1700 nm power spectrum of the Cr^{4+}:YAG laser (Figure 3-2) is still included.

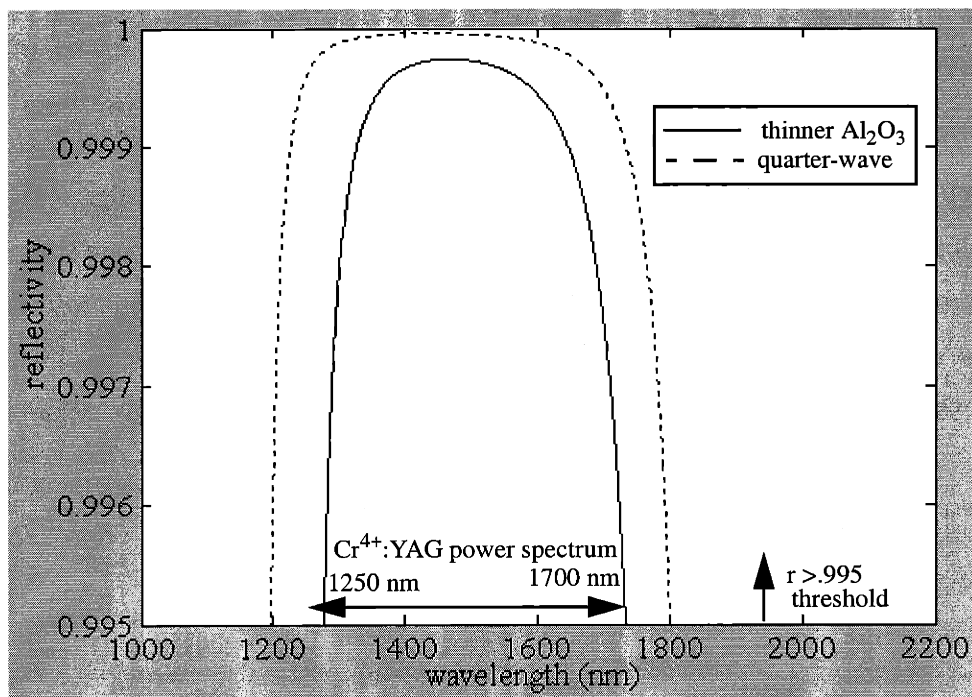

Figure 3-12. Reflectivity of a 7 period quarter-wave Bragg mirror (dashed line) and thinner oxide Bragg mirror (solid line). The thinner oxide mirror has a >99.5% reflectivity from 1280 to 1730 nm.

Figure 3-13a is a cross-sectional SEM of the as-grown/unoxidized SBR material system. Although in this particular structure only 6 periods are included in the Bragg mirror, the stopband of the oxidized structure should still be sufficiently wide. The GaAs thickness is ~145 nm, but the AlAs layers appear to be too thick as verified below using FTIR. Figure 3-13b is an optical micrograph showing partial oxidation of a 500 μm diameter SBR mesa containing the material system in Figure 3-13a. The oxidation was performed for 2 hrs. at 435°C and the oxida-

tion front progresses isotropically approximately 150 μm from the mesa edge. The oxidation is stopped short of completion to illustrate the progression of the oxidation fronts. Complete oxidation of the SBR mesa takes approximately 3.5 hrs. The SBR mesa is mechanically stable with the thinner Al_2O_3 layers, and no delamination is observed. The uneven oxidation fronts in Figure 3-13b arise from the slowing of the oxidation rate due to the growth of the dense As_2O_3-containing section at the oxidation front and the transition to a diffusion limited oxidation process as described in Figure 3-9. As the dense As_2O_3-containing section grows, oxidizing reactants can diffuse through neighboring GaAs layers and continue the oxidation process, leaving a portion of the AlAs layer unoxidized (Figure 3-13c). The oxidation rate in each AlAs layer depends as well on the progression of the oxidation front in neighboring AlAs layers that provide an alternative fast-diffusion pathway. Slow diffusion through the dense As_2O_3-containing oxidizing layer may force reactants to an alternative faster diffusion pathway through the neighboring porous γ-Al_2O_3 or AlO_xH_y layers in the mirror stack.

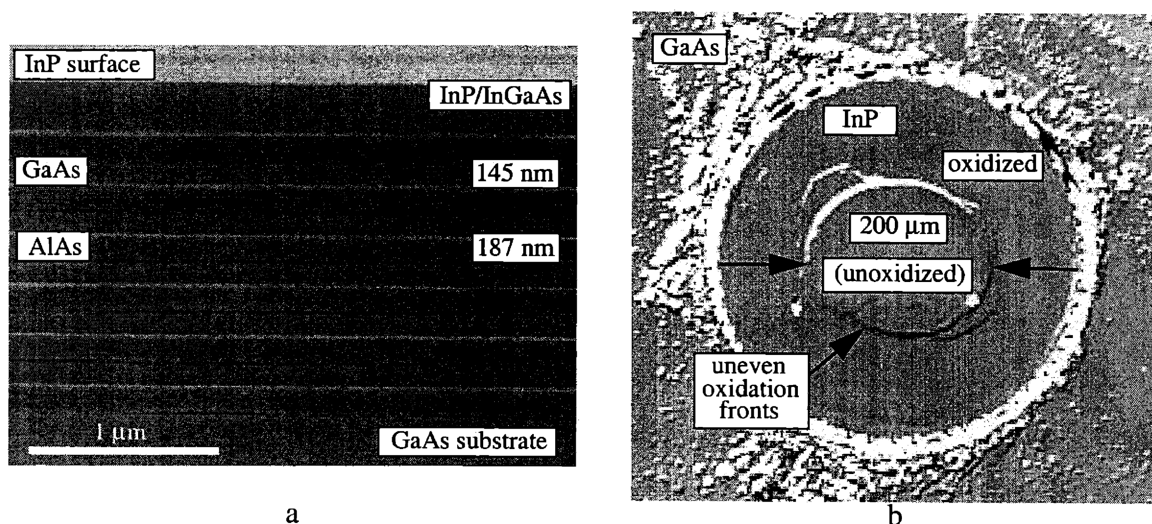

Figure 3-13. a) Cross-sectional SEM of unoxidized/as-grown layers in SBR. b) Optical micrograph of oxidation of SBR material containing thinner Al_2O_3 layers in the Bragg mirror. c) Obstructed oxidation due to dense As_2O_3-containing layer at oxide terminus causes uneven oxidation fronts to develop. d) Cross-sectional SEM of SBR structure with oxidized low-index layers and the top absorber layer removed. e) Comparison between FTIR measured reflectivity from the mesa edge and unoxidized mesa (solid lines), the mesa center (dashed-dotted line), and calculated (dotted line) reflectivities

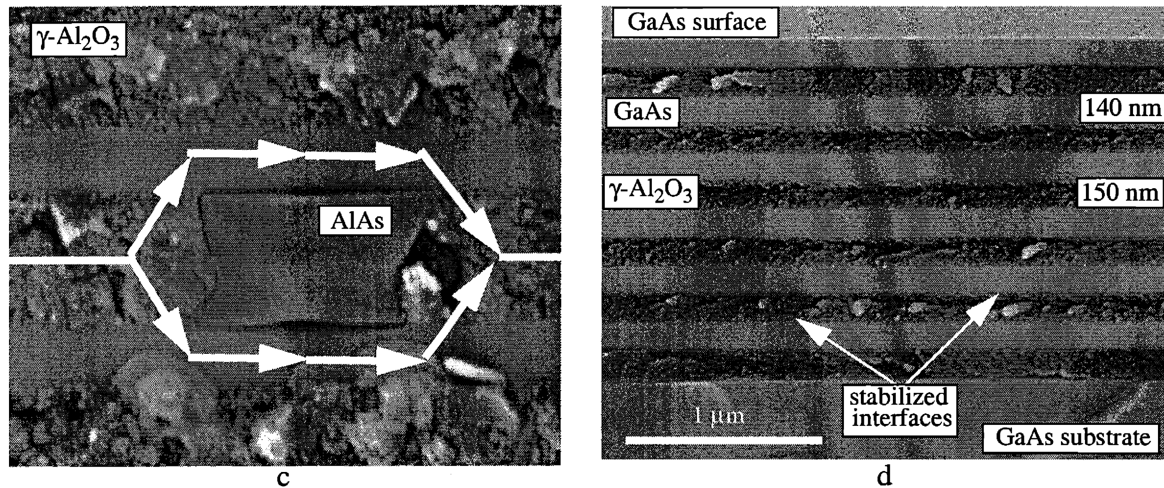

Figure 3-13. a) Cross-sectional SEM of unoxidized/as-grown layers in SBR. b) Optical micrograph of oxidation of SBR material containing thinner Al_2O_3 layers in the Bragg mirror. c) Obstructed oxidation due to dense As_2O_3-containing layer at oxide terminus causes uneven oxidation fronts to develop. d) Cross-sectional SEM of SBR structure with oxidized low-index layers and the top absorber layer removed. e) Comparison between FTIR measured reflectivity from the mesa edge and unoxidized mesa (solid lines), the mesa center (dashed-dotted line), and calculated (dotted line) reflectivities

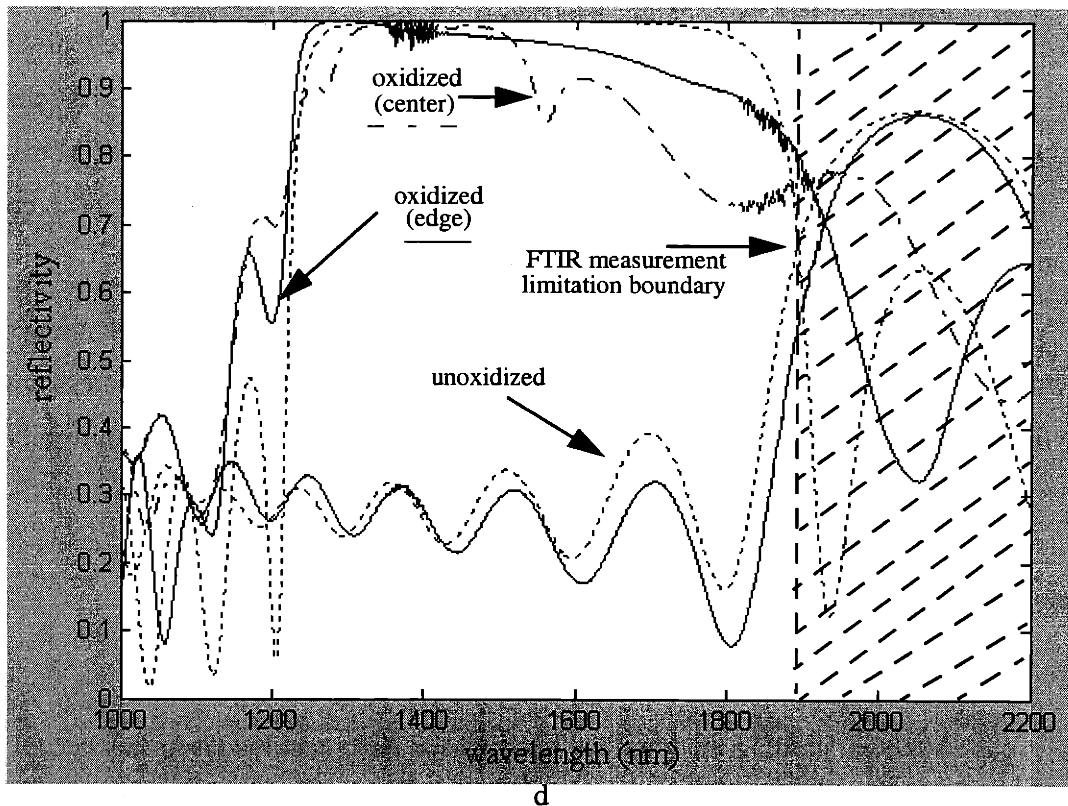

Figure 3-13. a) Cross-sectional SEM of unoxidized/as-grown layers in SBR. b) Optical micrograph of oxidation of SBR material containing thinner Al_2O_3 layers in the Bragg mirror. c) Obstructed oxidation due to dense As_2O_3-containing layer at oxide terminus causes uneven oxidation fronts to develop. d) Cross-sectional SEM of SBR structure with oxidized low-index layers and the top absorber layer removed. e) Comparison between FTIR measured reflectivity from the mesa edge and unoxidized mesa (solid lines), the mesa center (dashed-dotted line), and calculated (dotted line) reflectivities

Figure 3-13d is a cross-sectional SEM of the SBR in Figure 3-13b with the top layer removed for reflectivity measurements. No delamination has occurred at the interfaces of the Al_2O_3 and the GaAs layers. The GaAs thickness is measured to be 145 nm while the Al_2O_3 thickness is measured to be 140 nm, corresponding to a high measured volume contraction of almost 25%. The SEM-measured thicknesses are verified using FTIR-reflectivity.

To accurately measure the reflectivity of the mirror, the top absorber region is removed using the acid wet etch described in Section 3.3.1. The FTIR-measured reflectivity for both the oxidized and unoxidized mirror is shown in Figure 3-13d and is compared to simulation. The measurement was taken using the procedure described in Section 3.4.1. First, the simulated

reflectivity of the unoxidized structure is fit to the measured reflectivity and used to determine the exact unoxidized/as-grown layer thicknesses. While the measured thickness of the GaAs is 145 nm and matches that of the mirror design, the thickness of the AlAs is found to be ~187 nm, verifying the higher than expected AlAs MBE growth rate as initially suspected in the SEM measurement. The similar widths of each stopband indicates the accuracy to the choice of index contrast between AlAs and GaAs in the simulation.

The thicknesses measured by SEM are used to simulate the oxidized mirror reflectivity which agrees well with the measured reflectivity. The broad measured stopband shown with a solid line is from the outer portion of the mesa where the oxidation surfaces are uniform. Irregularities occur in the measured spectrum from the center of the oxidized mesa (dashed-dotted line), due to the slowing of the oxidation process from a reaction-limited to a diffusion-limited regime and the resulting uneven oxidation fronts (Figure 3-13c).

3.4.3 Buffer Layer at GaAs/Al_2O_3 Interface

Although grading the interface between the AlAs and the GaAs has been used to stabilize Bragg mirror structures [86,91], compositional control is difficult with MBE. The composition of a discrete buffer layer, however, is easily controllable and will not affect the optical properties of the SBR mirror provided the buffer layer is thin enough relative to the wavelengths that compose the Cr^{+4}:YAG laser pulse. The lower Al-content layers may buffer the contraction of the AlAs upon oxidation helping to stabilize the GaAs interface. The lower Al-content layers also help limit the formation of weak Ga_2O_3 bonds at the GaAs interfaces. To test these ideas, thin 15 nm $Al_{0.7}Ga_{0.3}As$ buffer layers are added to the SBR material system between the AlAs and the GaAs at each interface. Figure 3-14a is an optical micrograph of a partially oxidized mesa (435°C, 1 hr.) containing the SBR material in Figure 3-14a. The oxidation front has progressed 205 µm from the mesa edge. Complete oxidation of the SBR mesa is achieved in less than 2 hrs. Slight delamination has occurred near the mesa edges but overall the mechanical stability of the mesa is much improved over that of the same structure oxidized at 435°C but without the buffer layers (Figure 3-8a). The slight delamination appears to be an edge effect that occurs at the beginning of the oxidation process. The edge delamination may be removed by oxidizing at

slightly lower temperatures. It may be possible to further improve the mesa stability by increasing the thickness of the buffer layers. The ideal solution which complicates growth is grading the Al-content more gradually at the AlAs/GaAs interface. The oxidation rate of $Al_{0.7}Ga_{0.3}As$ at 435°C is ~3 nm/min.; it is therefore expected that the buffer layers completely oxidize as well. Figure 3-14b is a cleaved cross-section of the oxidized material where some of the interfaces have separated during sample preparation. A small (~15 nm) granular region is revealed at the bottom of the GaAs layer indicating that the buffer layers have oxidized as well.

Figure 3-14c is an SEM showing the oxidized layers in the SBR mesa in Figure 3-14b and the interfaces stabilized by the $(Al_{0.7}Ga_{0.3})_3O_2$ buffer layer. Since the $(Al_{0.7}Ga_{0.3})_3O_2$ buffer layers also oxidize, it is difficult to determine the exact layer thicknesses using only SEM. Instead, fitting to the measured reflectivity of the mirror structure (shown in Figure 3-13c) provides a more accurate determination of the layer thicknesses. The buffered-interface SBR structure is measured using FTIR after removing the top active region by wet-etching as described in Section 3.3.1. A completely oxidized 500 μm diameter SBR mesa is used for the FTIR measurement. The reflectivity spectra for both oxidized and unoxidized SBR mirrors are shown in Figure 3-14d and is compared to the calculated spectra. The unoxidized spectrum is calculated for the GaAs/AlAs quarter-wave mirror where the $Al_{0.7}Ga_{0.3}As$ buffer layers are included as part of the lower index AlAs layer. The best-fit of the unoxidized spectrum is for a 105 nm thick high-index layer and a 240 nm thick AlAs (combined with $Al_{0.7}Ga_{0.3}As$) layer. The calculated spectrum fits reasonably well while any inaccuracy is associated with the buffer layers. The measured stop-band of the oxidized structure is broad ranging from 1100-1800 nm. The best-fit calculation of the measured spectrum is for an Al_2O_3 layer thickness of 195 nm corresponding to ~19% total volume contraction of the oxidized AlAs and $Al_{0.7}Ga_{0.3}As$ material. The reduced total volume contraction (relative to that measured in the thinner-oxide SBR structure) may be due in part to the buffered interfacial $(Al_{0.7}Ga_{0.3})_2O_3$ layers.

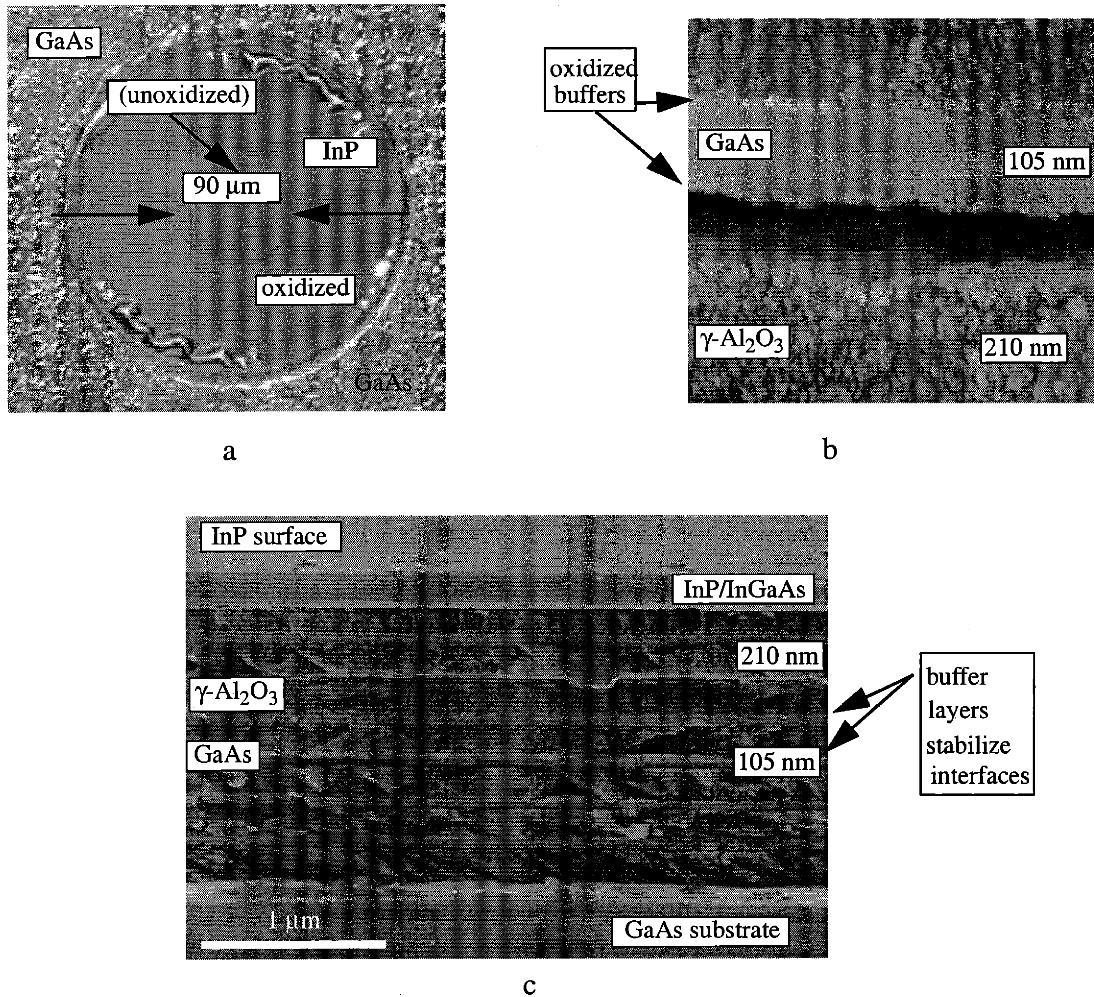

Figure 3-14. Optical micrograph of a partially oxidized SBR mesa containing SBR material (1 hr. at 435°C). b) Close-up SEM of interface separated during sample preparation revealing an oxidized interfacial buffer layer. b) Cross-sectional SEM of SBR with oxidized low-index layers. d) Comparison between measured (solid line) and calculated (dotted line) reflectivity.

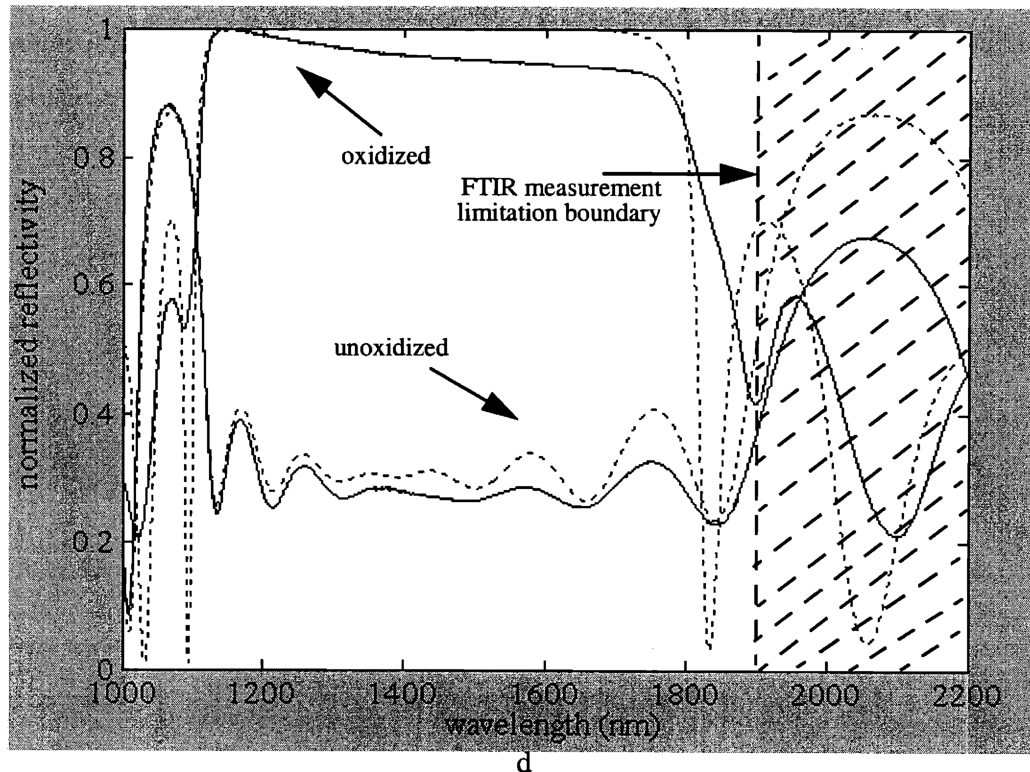

Figure 3-14. Optical micrograph of a partially oxidized SBR mesa containing SBR material (1 hr. at 435°C). b) Close-up SEM of interface separated during sample preparation revealing an oxidized interfacial buffer layer. b) Cross-sectional SEM of SBR with oxidized low-index layers. d) Comparison between measured (solid line) and calculated (dotted line) reflectivity.

Error is introduced in the measurement of the buffered-interface SBR structure because the buffered layers may not be completely oxidized at the center of the SBR mesa. To check the amount of error, a comparison is made between the FTIR-measured reflectivity using a 150 μm spot positioned at the edge of the 500 μm mesa. The stopband measured towards the edge of the mesa is red-shifted by approximately 10 nm from the stopband at the center of the mesa. A red-shift is indicative of a thicker total oxide layer in the SBR mirror on the edges of the mesa due to the extended exposure time to oxidizing reactants relative to the mesa center.

3.4.4 AlGaAs/Al_2O_3 SBR Structure

It is also found that $Al_{1-x}Ga_xAs/Al_2O_3$ mirrors are more stable than their GaAs/ Al_2O_3 counterparts [92-95]. Although the index of refraction decreases with Al content, the

index contrast with Al_2O_3 is still large enough for the mirror to be broadband. Figure 3-15 shows the calculated reflectivity spectrum for a 7 period $Al_{0.7}Ga_{0.3}As/Al_2O_3$ mirror and compares it to the $GaAs/Al_2O_3$ stopband. The index of refraction of refraction for $Al_{0.7}Ga_{0.3}As$ at 1440 nm is 3.08 so that the quarter-wave thickness of the $Al_{0.7}Ga_{0.3}As$ layer is 117 nm. Although the stopband (>99.5% reflectivity) has decreased because of the lower index contrast for the AlGaAs/ Al_2O_3 mirror, it still covers the majority of the Cr^{4+}:YAG gain spectrum in Figure 3-2.

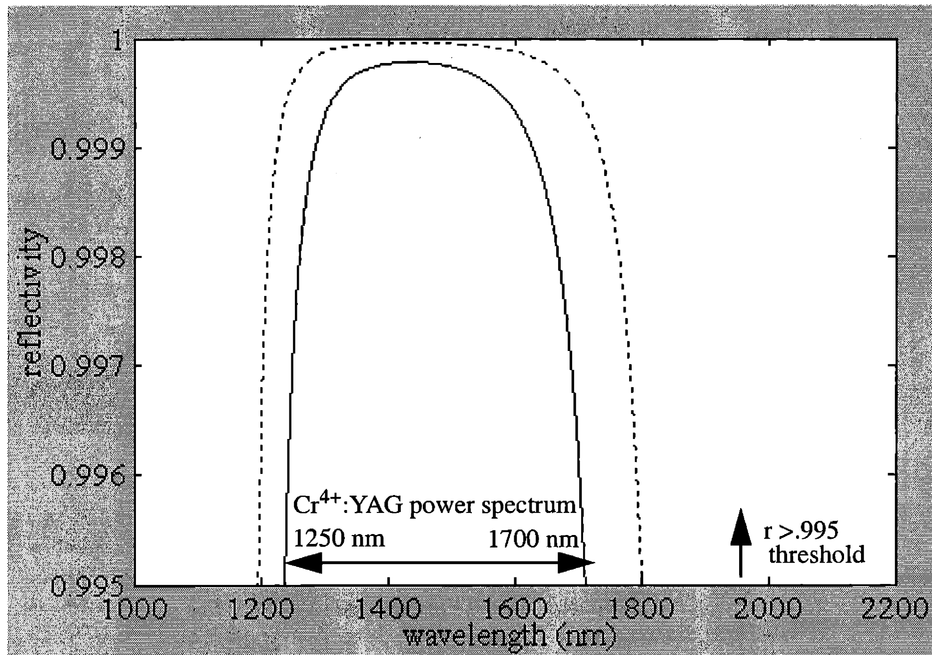

Figure 3-15. Reflectivity of a 7 period $GaAs/Al_2O_3$ Bragg mirror (dashed line) and a 7 period $Al_{0.7}Ga_{0.3}As/Al_2O_3$ Bragg mirror (solid line). The $Al_{0.7}Ga_{0.3}As/Al_2O_3$ mirror has a >99.5% reflectivity from 1260 to 1680 nm.

Figure 3-16a is a cross-sectional SEM of the unoxidized/as-grown $Al_{0.7}Ga_{0.3}As$/ AlAs SBR structure. Notice the low contrast between the high and low index layers of the mirror stack due to the higher Al-content in the low-index layers. Figure 3-16b is an optical micrograph of a partially oxidized 500 μm diameter SBR mesa containing the $Al_{0.7}Ga_{0.3}As$/AlAs mirror structure. The oxidation is performed at 435°C for 1 hour during which the oxidation front progresses 190 μm from the mesa edge. Complete oxidation of the SBR mesa is achieved in less than 2 hrs. All layers in the structure are intact with only small amounts of delamination occurring near the edges of the mesa. Since $Al_{0.7}Ga_{0.3}As$ oxidizes slowly at 435°C, the oxidation

extent into the high-index layer of the periods in the mirror should be a function of distance from the mesa edge. The initial thickness of the $Al_{0.7}Ga_{0.3}As$ layer and the AlAs layer are determined to be 150 nm and 270 nm, respectively, by a combination of SEM and by fitting to the FTIR reflectivity spectrum of the unoxidized structure. Figure 3-16c shows the $Al_{0.7}Ga_{0.3}As/Al_2O_3$ multi-layer mirror stack following 2 hrs.of oxidation taken from the center of a 500 μm mesa; the thicknesses are relatively unchanged. Figure 3-16d is an SEM of the same mesa now 50 μm in from the mesa edge. Only ~40 nm of the high-index layer remains, the rest of the material having been converted to oxide. Close to the edge of the mesa, the high-index $Al_{0.7}Ga_{0.3}As$ layer had completely oxidized. As a result of the oxidizing high-index layer, the measured reflectivity of the completely oxidized SBR mesa was poor, demonstrating that a lower Al-content layer is needed as the high-index layer.

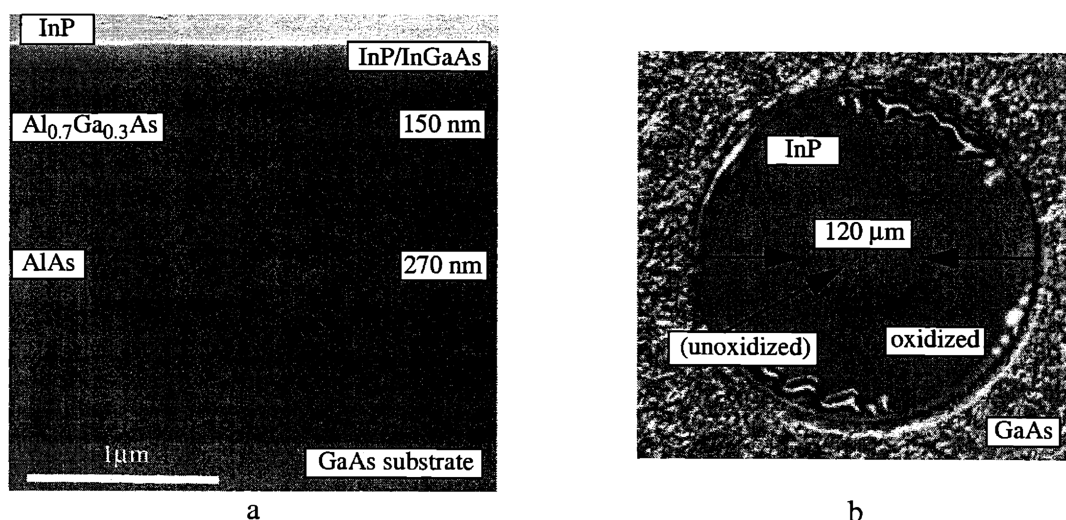

Figure 3-16. a) Cross-sectional SEM of unoxidized/as-grown layers in SBR containing $GaAs/Al_{0.7}Ga_{0.3}As$ layers. b) Optical micrograph of partially-oxidized SBR mesa (1 hr. at 435°C) containing SBR material in (a). An oxidation time of 2 hrs. completes the mesa oxidation. c) Cross-sectional SEM of SBR with oxidized low-index layers taken from the center of a 500 μm mesa and 50 μm from the edge (d).

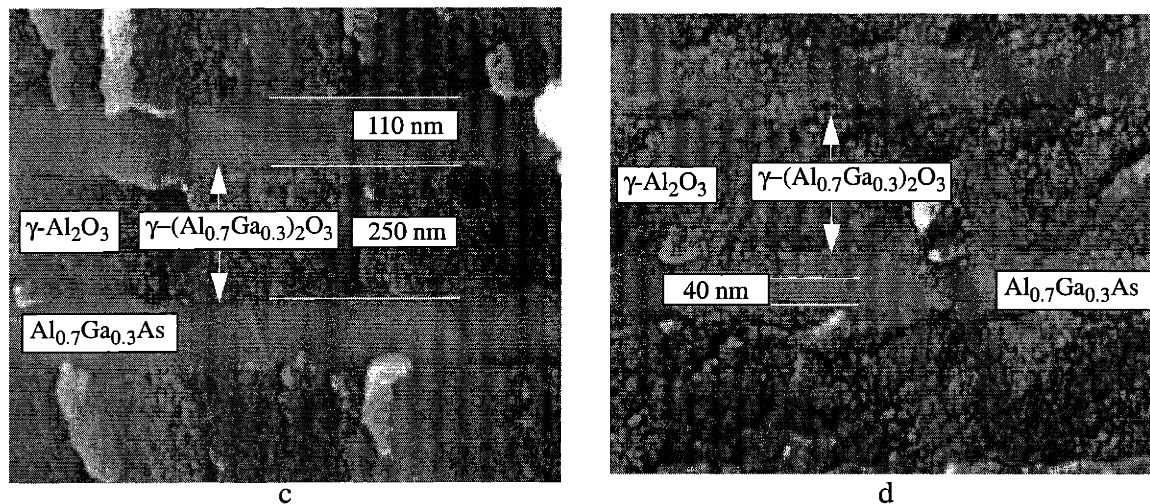

Figure 3-16. a) Cross-sectional SEM of unoxidized/as-grown layers in SBR containing GaAs/$Al_{0.7}Ga_{0.3}As$ layers. b) Optical micrograph of partially-oxidized SBR mesa (1 hr. at 435°C) containing SBR material in (a). An oxidation time of 2 hrs. completes the mesa oxidation. c) Cross-sectional SEM of SBR with oxidized low-index layers taken from the center of a 500 μm mesa and 50 μm from the edge (d).

It is important to note here that the absorber quality of the SBR mirror structures fabricated from the $Al_{0.7}Ga_{0.3}As/Al_2O_3$ mirrors was poor as determined by PL. A close examination of Figure 3-15b reveals oscillations at the GaAs interfaces, the amplitude of which increases until the interface with the absorbing region. Such oscillations at the interfaces do not appear in GaAs/AlAs mirror structures (Figure 3-11a and Figure 3-13a). It is therefore speculated that immobility of Al adatoms on the growth surface cause the interface oscillations and the corresponding poor quantum well efficiency. In addition, RHEED oscillations show improved surface reconstruction when growing GaAs in the mirror structures as opposed to $Al_{0.7}Ga_{0.3}As$. It is therefore believed that the lower Al content AlGaAs high-index layer will also allow growth of a high-quality active region. Such an oxidized structure should demonstrate improved stability over even the buffer-interface structure discussed in Section 3.4.3.

3.5 Self-Starting Cr^{4+}:YAG Laser

The SBR materials system is grown epitaxially and characterized using pump-probe spectroscopy, PL, and SEM to determine the quality of the growth. Although suitable mirrors were designed and oxidized using the various techniques described in this chapter, the quality

of the absorbing region was not always sufficient to modelock the Cr^{4+}:YAG laser, due mainly to the heavy lattice-mismatch discussed in Section 3.2.3.

Growth R885, however, self-started modelocking of the Cr^{4+}:YAG laser. The R885 structure contains the same original quarter-wave mirror design that delaminated in Figure 3-8 at 435°C, but stabilized at the reduced temperature of 400°C as described in Section 3.4.1. The higher quality of the absorbing region on R885 relative to other growths is likely due to the phosphine overpressure applied before the growth of the absorbing region. The temperature, and therefore the emission wavelength, vary radially across each as-grown wafer. Therefore, to probe the performance of the Cr^{4+}:YAG laser versus wavelength of the absorber region in the SBR, a strip of material 1 inch in length is cleaved from the R885 wafer and oxidized. The high-reflectivity portions of the SBR used to initially modelock the laser are located near the cleaved edge. An oxidation time of 9.5 hours produced oxidation fronts terminating at depths between 200 and 300 μm as determined by SEM and optical microscopy. Although some localized delamination of the upper-most $GaAs/Al_2O_3$ interface occurred near the cleaved edge (the same as that shown in Figure 3-11b), self-started modelocking of the Cr^{4+}:YAG laser was achieved by narrowing the beam spot size.

To self start modelocking, an end mirror in the Cr^{4+}:YAG laser cavity is replaced by the broadband oxidized SBR. The position and orientation of the SBR are optimized by maximizing the feedback from the laser cavity. Further details about modelocking the Cr^{4+}:YAG laser are reported elsewhere [75]. Figure 3-17 shows the results of self-starting modelocking using the broadband SBR from growth R885 in combination with KLM. The wide tunability range of the laser (Figure 3-17a) is evidence of the high-quality of the broadband $GaAs/Al_2O_3$ mirror. The peak of the pulse spectrum is at 1490 nm (Figure 3-17b). A fringe-resolved auto-correlator was used to measure the pulse-width that fits a 32 fs sech-shaped pulse (the true bandwidth limited pulse would have a pulse-width of 35 fs). To the best of our knowledge, these are the shortest self-started pulses in a Cr^{4+}:YAG laser cavity due to the high-quality large-scale Bragg mirrors in the SBR [75].

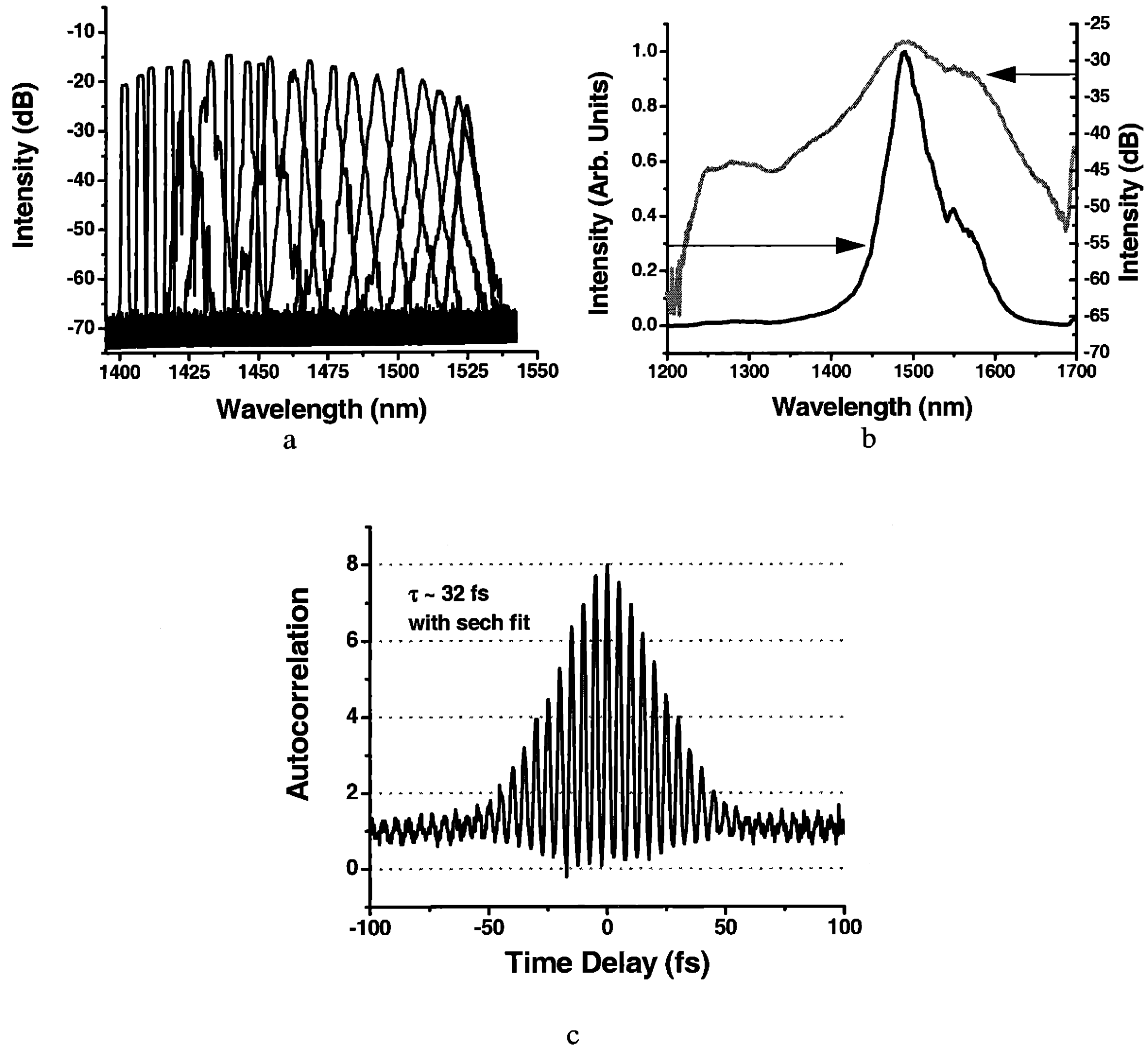

Figure 3-17. Measured data from the Cr^{4+}:YAG laser cavity modelocked using the oxidized SBR from growth R885 in combination with KLM. Results show a) Tunability from 1400 to 1525 nm. b) Pulse spectrum c) Interferometric auto-correlation.

3.5.1 Reducing Two-Photon Absorption

To reduce two-photon absorption, a larger (500 μm)^2 high-quality surface area of SBR material is desired so that a broader spot size may be used in the Cr^{4+}:YAG laser cavity. SBR mesas having a cylindrical geometry oxidize faster than a cleaved edge because the total surface area at the oxidation front decreases with time [119]. In addition, a mesa geometry simplifies alignment in the Cr^{4+}:YAG laser cavity. To probe the performance of the laser versus wavelength of the absorber region in the SBR, an array of 500 μm mesas are fabricated on a strip of material 1 inch in length from the center of the as-grown wafer. Oxidation at 400°C produces a small amount of delaminated material near the mesa edges as shown in Figure 3-11b. Since the performance of the Cr^{4+}:YAG laser is extremely sensitive to nonuniformities in the SBR, 500 μm mesas were oxidized at the reduced temperature of 375°C in an attempt to obtain a larger surface area with no delaminated material. Figure 3-18a is an optical micrograph of a 500 μm diameter SBR mesa from growth R885 oxidized for 2 hours at 375°C. The oxide extends 60 μm from the mesa edge with little evidence of delamination. An oxidation of 10 hours (Figure 3-18b), however, produced an oxidation extent of only 140 μm indicating that the oxidation rate has slowed. The reason the oxidation rate has slowed is that the process has become diffusion-limited, as described in Section 3.3.5, due to growth of a dense As_2O_3-containing region at the oxidation front. It is believed that the region of highest stress in the $GaAs/Al_2O_3$ layers, that causes delamination at higher temperatures, is at the oxidation terminus. To verify the assumption, Figure 3-18c shows the result of reintroducing the SBR structure in Figure 3-18b to the oxidation furnace for an additional 2 hrs.of oxidation at 375°C. Since localized layer delamination occurs only at the oxidation terminus, it is concluded that delamination can originate from the oxide terminus when oxidizing at higher tempertures. As further evidence, the SBR material is oxidized at 435°C and the oxidation front is examined using SEM. Figure 3-18d shows that delamination is occurring at the oxi-

dation front due to stress in the plane of the oxide terminus. A delaminated layer then propagates (especially at high temperatures) yielding the structure originally shown in Figure 3-8.

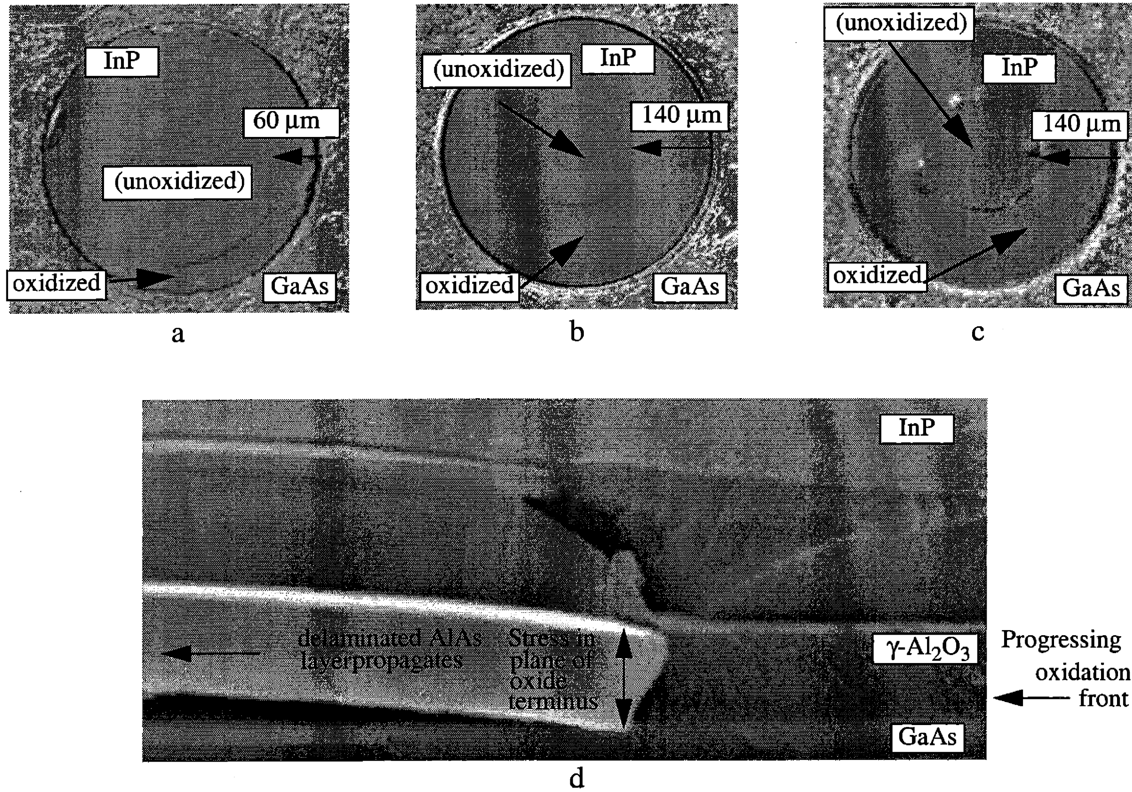

Figure 3-18. a) Original SBR structure oxidized at 375°C for 2 hrs. b) Original SBR structure oxidized at 375°C for 10 hrs. c) Continued oxidation of structure in (b) at 375°C for 2 hrs. causes delamination at the oxide terminus. d) Cross-sectional SEM of delaminated layer originating at oxide terminus in SBR structure oxidized at 435°C for 45 mins.

From the experiments detailed in Figure 3-18, it is clear that a large (500 μm diameter) mesa required for the Cr^{4+}:YAG laser cannot be fabricated from the same materials system used to generate the ~200 μm SBRs and the 35 fs pulses in Figure 3-17. Clearly, a higher temperature oxidation process is desired so that oxidation may be completed prior to the onset of a diffusion-limited regime. The alternative thinner-oxide SBR mirror design (Section 3.4.2), the buffered-interface SBR (Section 3.4.3), and the $Al_{0.7}Ga_{0.3}As/Al_2O_3$ (Section 3.4.4) all may be oxidized at higher temperatures (435°C) with little delamination.

Figure 3-19 shows optical micrographs of 500 μm mesas containing the alternative SBR mirror design (a), the buffered-interface SBR (b), and the $Al_{0.7}Ga_{0.3}As/Al_2O_3$ SBR design (c), each with the top absorber layer removed. The original SBR materials system that delaminates at high oxidation temperatures is included for completion (d). For comparison, all four structures are oxidized to completion at 435°C for 3.5 hrs; structures (b) and (c) are over-oxidized based on the rates reported in Section 3.4.3 and Section 3.4.4. The corresponding FTIR reflectivity spectra, each normalized to its respective peak reflectivity, taken from the center of each mesa are compared in Figure 3-19e.[1]

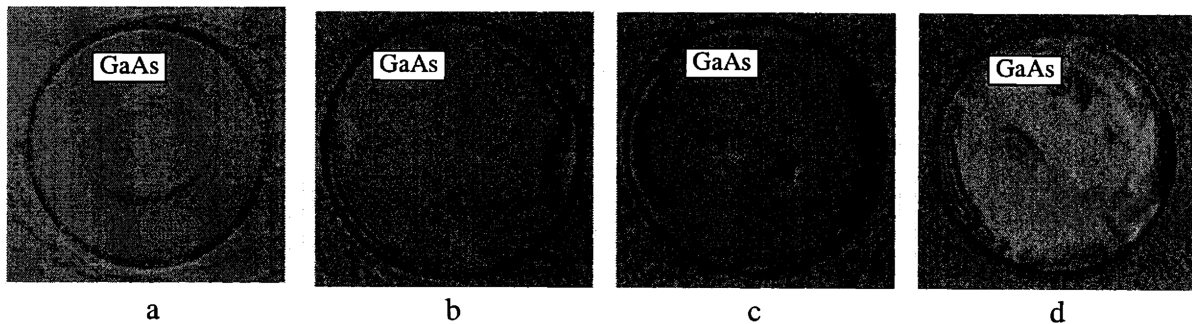

Figure 3-19. 500 μm SBR mesas with top absorbing layer removed, each oxidized for 3.5 hrs.at 435°C: Thinner-oxide (a), buffered-interface (b) $AlGaAs/Al_2O_3$ (c) and standard quarter-wave stack (d). e) FTIR-measured reflectivity for structures (a)-(c).

1.Reflectivity from the original quarter-wave stack structure in (d) is nonuniform and therefore omitted because of the delaminated layers throughout the mesa.

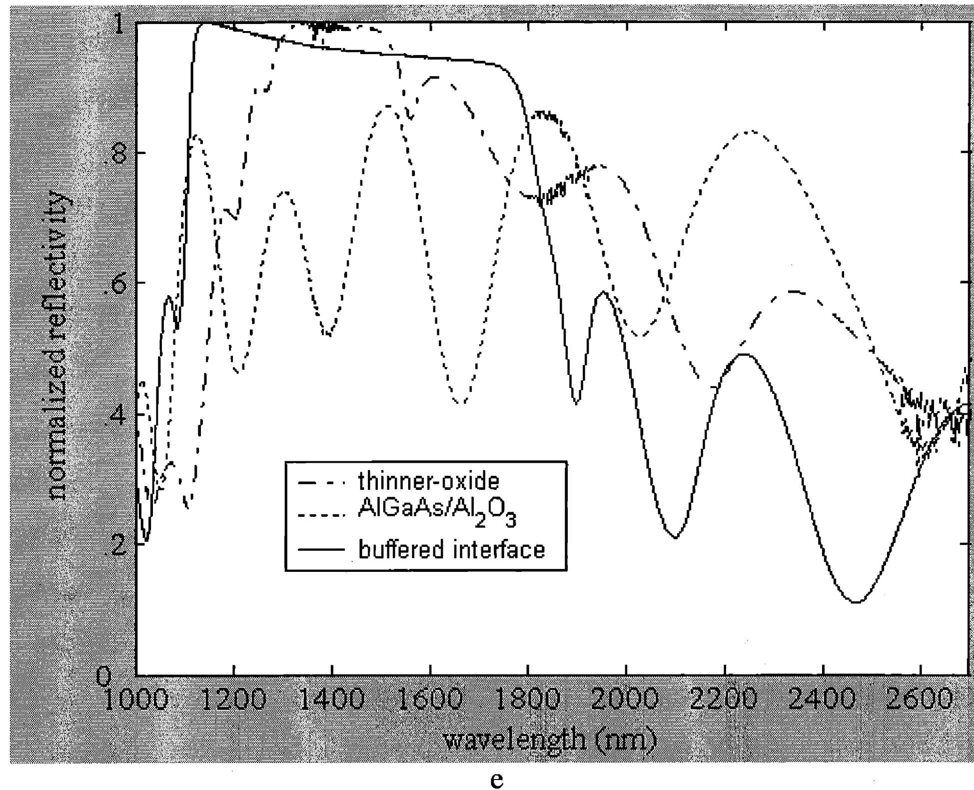

Figure 3-19. 500 μm SBR mesas with top absorbing layer removed, each oxidized for 3.5 hrs.at 435°C: Thinner-oxide (a), buffered-interface (b) $AlGaAs/Al_2O_3$ (c) and standard quarter-wave stack (d). e) FTIR-measured reflectivity for structures (a)-(c).

The high-index layers of the $Al_{0.7}Ga_{0.3}As/Al_2O_3$ SBR have oxidized vertically in the mirror stack as described in Section 3.4.4, leading to the poor reflectivity of the structure in Figure 3-19b. The alternative thinner-oxide mirror SBR has a relatively wide stopband, but is irregular because of nonuniformities in the mirror as shown in Figure 3-19a. The nonuniformities develop because of the onset of the diffusion-limited oxidation regime (as discussed in Section 3.4.2) for the slower oxidizing thin AlAs layers. The buffered-interface SBR materials system shows a widest-stop band, due to the high-quality of the oxidized mesa shown in Figure 3-19b.

The buffer-interface SBR therefore shows the most promise for modelocking the Cr^{4+}:YAG laser with reduced two-photon absorption. Unfortunately, the absorber region of the buffered-interface SBR structure was not of high-enough quality for use in the Cr^{4+}:YAG laser.

However, there is no reason to expect that a sufficiently high-quality absorber region, like that grown on the structure used to generate the 35 fs pulses, cannot be grown as well on the buffered-interface SBR structure in the future.

The $Al_{0.7}Ga_{0.3}As/Al_2O_3$ SBR is another potentially well-suited structure. However, the Al-content must first be reduced to eliminate the possibility of vertical oxidation of the high-index layers and to improve the quality of the absorber region as discussed in Section 3.4.4. The alternative mirror design structure, although nonuniform for 500 μm diameter mesas because of the slower oxidation rate of the thinner AlAs layers, is also well-suited for smaller [$(150\ \mu m)^2$] SBRs.

3.6 Conclusions

SBRs using quarter-wave stack $GaAs/Al_2O_3$ mirrors ~200 μm wide were fabricated in a III-V materials system and used to self-start mode-locking of an ultrafast Cr^{4+}:YAG laser, tunable over a range of 1425-1500 nm, and able to generate 35 fs pulse-widths, the shortest pulses to date for a Cr^{4+}:YAG laser with a SBR. The $GaAs/Al_2O_3$ Bragg mirror may be interpreted as a one-dimensional PC because of the high-index contrast and wide stopband (or PBG). Using FTIR, the stopband was measured and extends from 1200-2000 nm covering the entire Cr^{4+}:YAG laser power spectrum. The InP/InGaAs absorbing quantum well is heavily lattice-mismatched to the GaAs substrate, but may be made of sufficient quality for the SBR by applying a phosphine overpressure that induces the growth of a thin GaP layer just before beginning the growth of the lower InP layer. The $Al_xGa_{1-x}As/Al_2O_3$ materials system provides high index contrast so that the Bragg mirror stopband (>99.5% reflectivity) covers the entire Cr^{4+}:YAG laser gain spectrum. Fabrication of large-scale Bragg mirrors in the $Al_xGa_{1-x}As/Al_2O_3$ materials system is feasible provided particular care is taken in the design of the broadband mirror to avoid delamination during the steam oxidation process.

Even larger SBR structures ($\sim(500\ \mu m)^2$) are desired to reduce the limiting effects of two-photon absorption. Therefore, three separate alternative Bragg mirrors to the standard $GaAs/Al_2O_3$ quarter-wave stack that may be oxidized at higher temperatures were designed and fabricated. A thinner oxide $GaAs/Al_2O_3$ mirror, a $GaAs/Al_2O_3$ Bragg mirror with interfaces buff-

ered with a thin AlGaAs layer, and an $AlGaAs/Al_2O_3$ Bragg mirror were all explored with the steam oxidation process. A 500 μm diameter buffered-interface SBR mesa was successfully fabricated and identified as the most promising structure to be used in the future for reducing two-photon absorption in the Cr^{4+}:YAG laser cavity. The thinner oxide $GaAs/Al_2O_3$ mirror is entirely stable for smaller (~150-200 μm) diameter SBR mesas. The $AlGaAs/Al_2O_3$ mirror was also shown to be stable, but requires further investigation using lower Al-content high-index layers to avoid vertical oxidation of the entire mirror stack and improve the quality of the absorber region.

Overall, the mechanical stability of large-scale oxidized $Al_{1-x}Ga_xAs/(Al_{1-x}Ga_x)_2O_3$ Bragg mirrors has been thoroughly investigated. The work presented in this chapter lays the foundation for the design and fabrication of large-scale mirrors in the $Al_{1-x}Ga_xAs/Al_2O_3$ materials system for SBRs and various other optical applications.

Chapter 4. The Monorail Microcavity Laser

4.1 Optical Sources for Integrated Optoelectronics

Driving the integration (and miniaturization) of electronic devices is the dramatic reduction in manufacturing cost resulting from decreasing the length of interconnects (Figure 4-1) involved in a system all the way from the global network to the chip level. By 2010, it is believed that ultra-fast electronic systems will consist of multiple interconnected microprocessor chips that process in parallel with >500 MHz off-chip clock speeds [123]. As more functionality is condensed onto each chip, electrical interconnection at both the board and the chip level is compressed and high-frequency transmission becomes difficult due to crosstalk (interaction between the charged electrons carrying current in adjacent interconnects). An additional problem of densely-packed electronic interconnects is breakdown due to atomic motion of the metal, or electromigration [124], as more and more current is forced down each small wire.

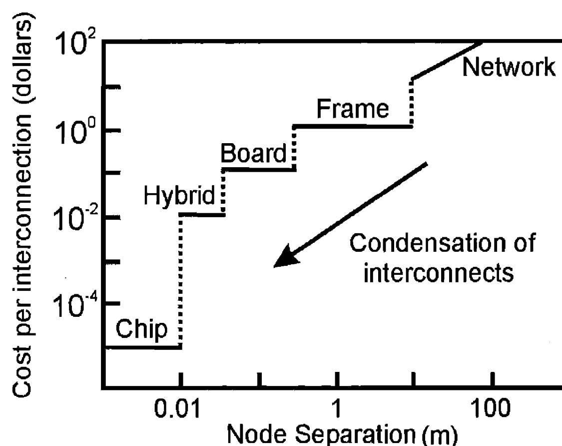

Figure 4-1 (from [123]) The cost per interconnection decreases dramatically as optical networking becomes more integrated.

A potential solution is to utilize optical interconnects that do not suffer the same crosstalk and breakdown problems as electrical interconnects [125]. The generation of the optical signal to be transmitted is a major concern for future integrated electrooptical systems. For instance, LEDs typically have poor external efficiency, although as shown in Chapter 2, PCs offer promising results for enhancing the external efficiency. The poor external efficiency results in unnecessary power dissipation and a maximum of 1000 LEDs/cm^2, operated under normal mW conditions, before the chip melts; a larger packing density than this is required, however, for future integrated optoelectronic systems. Although optical sources (lasers and LEDs) with typical mW power consumption may be appropriate for such applications as optical clock distribution at the board level, faster low-power emitters are needed at the chip level. Indeed, buried deep within a chip where the packing density is at its greatest, even nW optical sources may need to be considered [123].

The lowest levels of a chip require the highest operation speeds (>500 MHz) for an optical interconnection system. The spontaneous emission in a semiconductor is limited to the order of nanoseconds making high-speed operation of an LED difficult for such applications. Operation speeds at more than a few gigahertz bandwidth are possible, however, through stimulated emission above threshold in a laser cavity. In addition, the high-speed laser signal may or

may not need to be waveguided depending on the specific level of integration and application desired. Although wireless broadcast of a signal may be appropriate at the board level and the less-densely packed upper regions of a chip, guided wave interconnects are more appropriate for the interconnections at the highly-integrated levels buried deep within an optoelectronic chip. To avoid coupling losses, a laser integrated into a waveguide is ideal.

It is concluded that an ultra-low threshold/low power, high-speed, integrated waveguide laser is desirable for interconnection in future optoelectronic systems. The purpose of this chapter is to explore the use of PCs in achieving such a design.

4.2 Literature Review: Low-Threshold Semiconductor Lasers

In a semiconductor laser, the fraction of light coupling into the lasing mode relative to the total spontaneous emission is called the spontaneous emission factor β. In the context of laser device physics it is helpful to define β as [125]:

$$\beta = \frac{A\Gamma_{cav}}{(1-A)\Gamma_{free} + A\Gamma_{cav}} \quad \text{(EQ 78)}$$

where A is the fraction of solid angle subtended by the lasing mode and Γ_{cav} and Γ_{free} are the emission rates into the cavity mode and into free space respectively.

Low-threshold, low power laser operation therefore requires designs that maximize β. A value of β=1 indicates that all of the emitted light is coupled into a single lasing mode creating a thresholdless laser. In fact, if all spontaneous emission could be collected from a laser it would also appear thresholdless regardless of the value of β, and the laser output would resemble that of an LED. However, stimulated emission is faster than spontaneous emission, so that laser oscillation is typically more useful for high-speed operation. In addition, nonradiative

recombination pathways will increase the lasing threshold. Therefore, high-speed low-threshold semiconductor lasers are designed for high radiative efficiency directly into the lasing mode.

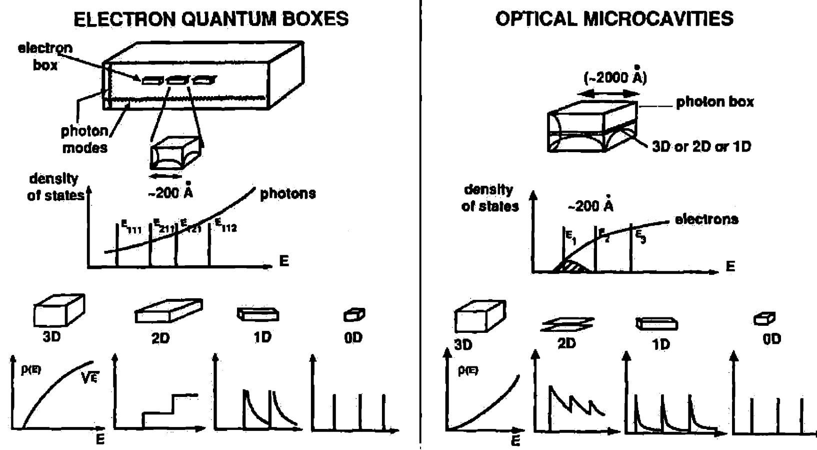

Figure 4-2 (from [126]) Low-threshold lasing is obtainable by limiting the available optical and electrical density of states in a semiconductor laser.

The value of β may be increased by limiting the degrees of freedom in the available optical and electrical density of states as summarized in Figure 4-2. The optical density of states may be limited by reducing the dimensionality of the system, the limit being a single mode optical microcavity of volume $V = \left(\frac{\lambda}{2n}\right)^3$. Reducing the electrical density of states narrows the emission linewidth leading to Purcell enhancement according to Fermi's golden rule (EQ. 30).[1] For instance, quantum dots or quantum boxes create a 0-D density of electrical states that increases the emission rate into the lasing mode at the expense of other competing processes such as nonradiative recombination. Therefore, as a general rule of thumb, a low-threshold semiconductor laser is achieved by reducing the volume of the optical cavity to limit the density of available optical states, and narrowing the emission linewidth (low-temperature or quantum confinement) to increase the emission rate into the lasing mode.

As the dimensionality of the laser is reduced, the reflectivity of the mirrors surrounding the cavity must be correspondingly increased. That is, since the total gain on each pass of the optical mode is reduced for smaller optical microcavities, the number of passes must be

1. A weak-coupling regime where irreversible radiative processes dominate is assumed in this discussion so that Fermi's golden rule applies.

increased before energy leaks out of the optical mode. The number of cycles before the energy in the cavity is reduced by a factor of $e^{-2\pi}$ is equivalent to the cavity Q. Therefore, high Q microcavities are required for low-threshold laser oscillation. A maximum overlap Γ between the active region and the lasing mode also increases the gain on each pass, possibly enabling lower Q cavities to exhibit low threshold. Another important parameter to consider when reducing the volume of the laser cavity is the nonradiative recombination lifetime that is likely to be reduced due to an increase in the ratio (~1/r) of surface area ($\sim r^2$) to volume ($\sim r^3$).

In conventional in-plane cleaved facet lasers, the spontaneous emission factor is low ($\sim 10^{-5}$). The most straightforward method of increasing β is to reduce the cavity length along the axial direction of a laser diode. By reducing the cavity length and introducing high-reflectivity facets, submilliampere threshold currents in short-stripe laser diodes have been demonstrated [127]. A different method of increasing the value of β is a vertical cavity surface emitting laser (VCSEL). A VCSEL consists of a 1D PBG created by quarter-wave Bragg mirrors surrounding an active region with thickness equal to λ/n [128-130]. The value of β for a VCSEL (10^{-3}-10^{-5}) depends on the width in the directions perpendicular to the Bragg mirrors where other optical modes may exist. By also reducing the width in the perpendicular directions to the order of a wavelength, lasing in "micropost" cavities has been demonstrated [131-133] with threshold currents below 40 μA [133].

Microdisk [134-137], microsphere [138], and microcylinder [139] lasers rely on total internal reflection to create "whispering gallery" mode operation. Various values of β for such structures, as high as 0.1 for a microdisk [136], have been calculated or demonstrated depending on the temperature of operation and the emission linewidth of the active medium. A record low threshold current of 40 μA has been reported for a microdisk laser [137]. The main problem, however, for such microcavity laser structures lies in integration and coupling of light from the lasing mode into a waveguide for interconnection purposes. One approach to output coupling from the lasing mode is to place an output waveguide next to the microcavity, as was done for the "photonic wire" microlaser reported to have a value of β=0.3 [140-142]. Typical

values of important properties for low-threshold operation are summarized for several microcavity lasers in Figure 4-3.

Microcavity	Active Volume (μm^3)	Mode Volume (μm^3)	Cavity Q	Nonradiative Lifetime (ns)
Airpost VCSEL	10^{-1}	10	2,000 - 20,000	1
Microdisk	10^{-1}	1	100-1,000	1
Microcylinder	10^{-1}	10	100-1,000	1
Short Cavity Diode	1	100	10,000-20,000	10

Figure 4-3 (from [126]) Properties of several microcavity lasers

Low-threshold semiconductor lasers using PCs have also recently been explored. A PC surrounding an active medium with a PBG that overlaps the material gain creates a high Q optical cavity enabling lasing at low powers. The first such laser was presented in 1999 [143], by introducing a defect in a hexagonal lattice PC; the PBG that overlaps the material emission creates a high Q microcavity. A modal volume of $2.5\left(\frac{\lambda}{2n}\right)^3$, a cavity Q of 250, and a threshold optical pump power of 500 μW are reported [144]. A similar electrically-pumped PC microcavity laser reported in [145] showed a threshold current of 300 μA and a cavity Q of ~1164, but was limited by poor radiative efficiency due to heat generation through nonradiative recombination pathways. The radiative efficiency may be improved by cooling the lasers, a bulky and expensive solution, however, for optical interconnection.

Clearly, a low-threshold integrated microlaser is desirable for high-speed optical interconnection. Low-threshold is obtained by designing high Q, low-volume microcavities. An important design consideration is minimizing nonradiative recombination such as Auger recombination and surface recombination, which limit radiative efficiency. Poor radiative efficiency caused by nonradiative recombination generates heat instead of light. Nearby edges of the microcavity enable high rates of surface recombination increasing the threshold carrier density. The high carrier densities in small volume optical microcavities then increases the Auger recombination rate which further increases the laser threshold.

4.3 Integrated Waveguide Microcavities

A low-threshold microlaser integrated with a waveguide is useful for optical interconnection. Before choosing an appropriate generic microcavity laser design, it is important to first consider some previous experimental and theoretical work that has been performed on waveguide microcavity structures [146-156]. As discussed in Section 4.2, low-threshold operation of a laser requires a high-Q, low modal volume microcavity. The modal volume is here defined as:

$$V_m = \frac{\int \varepsilon \mathbf{E}^* \cdot \mathbf{E} d^3 \mathbf{r}}{(\varepsilon \mathbf{E}^* \cdot \mathbf{E})_{max}} \tag{EQ 79}$$

where ε is the dielectric constant, $\varepsilon \mathbf{E}^* \cdot \mathbf{E}$ is the energy density in the electric field, and $(\varepsilon \mathbf{E}^* \cdot \mathbf{E})_{max}$ is the peak value of the energy density. Various loss mechanisms determine the cavity Q. The total cavity Q for a waveguide microcavity primarily consists of a radiation Q, Q_{rad}, and a waveguide Q, Q_{wg}. Q_{rad} represents light lost to free-space modes while Q_{wg} represents useful light extracted into the waveguide surrounding the microcavity. The total cavity Q, is therefore written as the sum

$$\frac{1}{Q} = \frac{1}{Q_{rad}} + \frac{1}{Q_{wg}}. \tag{EQ 80}$$

Perhaps the most intuitive structure for a waveguide microcavity is a structure that resembles an in-plane DBR laser, as reported in [148]. Deep gratings are etched into a channel waveguide with a quarter-wave phase shift introduced to form a high measured total cavity Q (~2500) of the microcavity. The high reported Q is actually Q_{wg}, however, since the structures were measured in transmission. The poor transmission indicates that although Q_{wg} is high, Q_{rad} is correspondingly low, making the structures less attractive for use as an integrated microlaser. The index contrast between the core of the cladding and the waveguide is the most likely source of low Q_{rad} and subsequent loss in the structure.

To provide a high-Q cavity with improved coupling to waveguide modes instead of radiation modes, a novel geometry (Figure 4-4a inset) was proposed in [146]. A high-dielectric waveguide (surrounded by air) is modified by a periodic set of air holes of lattice constant *a*, creating a 1D PC. Figure 4-4a plots the photonic band diagram along the waveguide direction for the parameters given in the caption. A PBG in the guided modes is created that separates the upper-most state in the dielectric band and the lower-most state in the air band. Figure 4-4b is a vector plot of the in-plane electric field for each band and for a defect state. The fundamental defect state for the system is created by separating two of the holes, causing more of the electric field lines for the lower-most air band state to intersect the high-dielectric region. Therefore, as discussed in Section 1.2.9, the energy of the lower-most air band state is reduced and a defect state is pulled down into the PBG. The defect state sweeps across the PBG as the hole separation is further increased. For the example given in Figure 4-4b, the defect width is 1.5a.

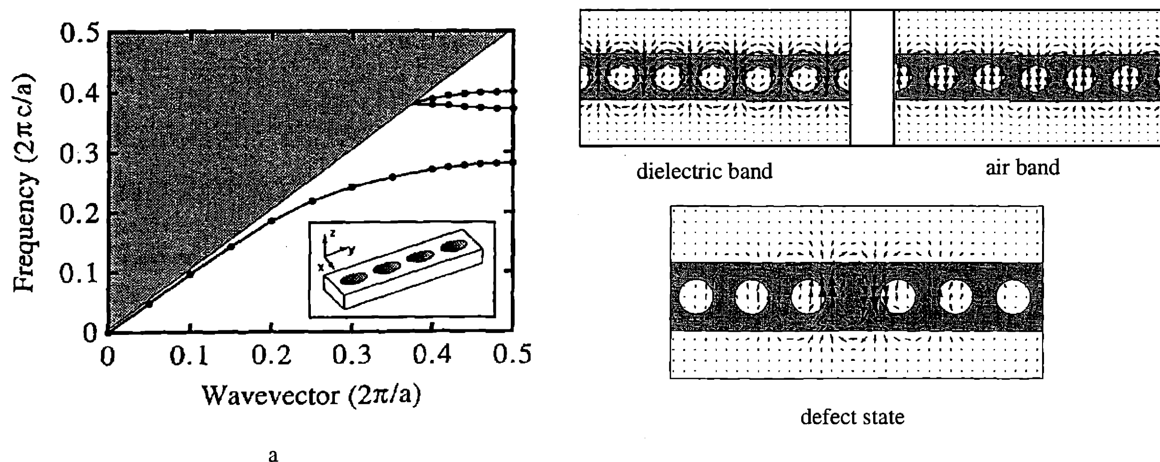

Figure 4-4. a) (from [147]) Photonic band diagram along the x-direction for a waveguide (n=3.37) surrounded by air (n=1) containing air holes separated by a lattice constant a, with a waveguide width 1.2a, waveguide thickness 0.4a, and hole diameter 0.6a. b) Vector plot of electric field distributions for air-band, dielectric band, and a defect state with hole separation of 1.5a.

Since the defect state derives from the guided state at the edge of the air band it can be expanded primarily in terms guided modes. Therefore, its projection onto the radiation continuum is small so that even a well-confined (high Q) mode leaks most of its energy into the channel waveguide and less into radiation modes, giving the device more potential for an inte-

grated low-threshold laser as compared to the deep-grating etched structure. A similar microcavity waveguide structure containing notches in the edges of the air-bridge, instead of holes, is presented in [149]. The PBG along the waveguide for the notch structures is much lower, however, than for holes. An examination of Figure 4-4b shows that the difference in filling factors of the air and dielectric bands for the hole structure must be higher than for any notch structure, yielding a larger PBG. Therefore, the air-bridge microcavity structure containing holes and detailed in Figure 4-4 is identified as a potential candidate for a low-theshold microlaser.

Air-bridge microcavity structures were successfully fabricated in the InGaAsP materials system for operation at 1.55 μm [150]. At MIT, monorail microcavity structures similar to the air-bridge have been fabricated in the Si/SiO_2 materials system with a measured cavity Q of ~265 and a modal volume of .055 μm^3 [151]. Most importantly, monorail and air-bridge microcavities using the $GaAs/Al_2O_3$ materials systems have been successfully fabricated and measured at MIT [152-156]. The monorail microcavity structures have a low-dielectric supporting layer underneath the waveguide (Figure 4-5a) which reduces the cavity Q relative to the corresponding air-bridge structures where the underlying low-dielectric is completely removed. A monorail structure is more practical to consider than an air-bridge for a microlaser design, however, because of the improved thermal dissipation through the underlying layers. In addition to being able to lattice-match high-quality active material to GaAs, the $GaAs/Al_2O_3$ materials system is particularly attractive for a low-threshold microlaser because of the excellent thermal properties of Al_2O_3 [157]. As described in Section 4.2, the poor radiative efficiency of microcavity lasers makes heating of the laser a significant problem that may become a fundamental limitation in performance.

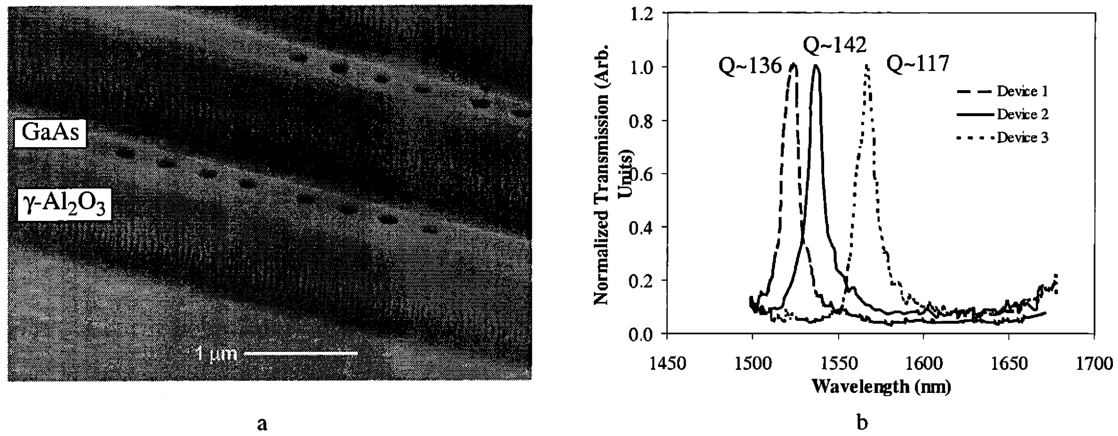

Figure 4-5. (from [155]) a) SEM of several passive monorail microcavity structures in the $GaAs/Al_2O_3$ materials system b) Measured transmission spectra for several different monorail microcavity structures.

The measured transmission spectra for several $GaAs/Al_2O_3$ monorail structures with different defect widths is given in Figure 4-5b. The resonant modal volume associated with the microcavities is ~.056 μm^3. The small modal volume and suitable thermal properties make monorail microcavities in the $GaAs/Al_2O_3$ materials system an attractive candidate for a low-threshold integrated microlaser. Indeed, with a sufficiently narrow bandwidth emitter (such as a quantum dot) a spontaneous emission enhancement of η, given by [158]

$$\eta = \frac{Q}{4\pi V_m}\left(\frac{\lambda}{n}\right)^3, \qquad \text{(EQ 81)}$$

becomes possible. Using a modal volume of .056 μm^3, an index of refraction of 3.37 for GaAs, the highest measured modal volume of 142, at 1.55 μm an enhancement of 20 is calculated. For a wide-bandwidth emitter (such as a quantum well) the enhancement must be calculated directly from Fermi's golden rule (EQ. 30).

4.4 The Monorail Microcavity Laser

A monorail microcavity laser is proposed for high-speed optical interconnection. The monorail microcavity laser is initially designed for activation through optical pumping (Fig-

ure 4-6). It consists of the original monorail structure, but now contains an active medium. In addition to the potential for low-threshold, low-power operation, the primary benefit of the monorail microcavity, as compared to the other microcavity lasers discussed in Section 4.2, is that light is easily extracted from the lasing cavity into the channel waveguide. Light leaks out of the lasing mode along the direction in the channel waveguide. A preferred direction may be chosen by slightly reducing the size of one of the holes at the output, as shown in Figure 4-6. Therefore, the emitter and waveguide are fully integrated reducing coupling losses.

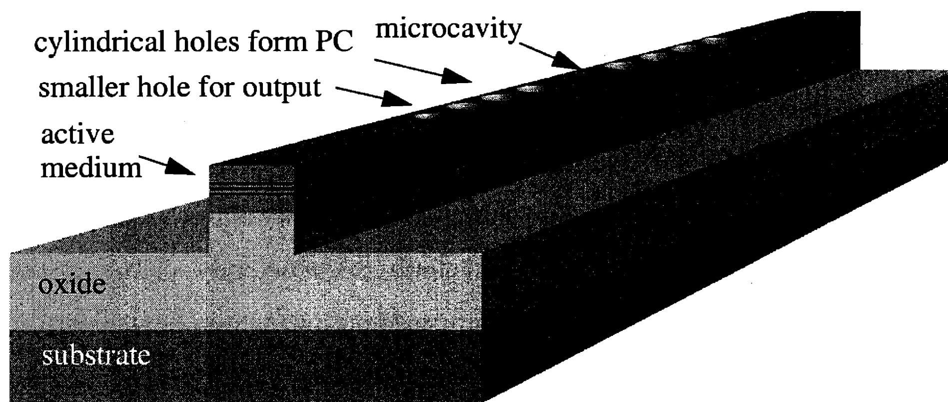

Figure 4-6. Generic monorail microcavity laser

4.4.1 Materials System

The choice of materials system is crucial in designing the monorail microcavity laser because of the high surface area to volume ratio which leads to high nonradiative surface recombination rates. As shown in Figure 4-4b, the electric field energy is concentrated around the hole surfaces that border the cavity due to the symmetry of the defect state, so that there is a direct competition between emission into the lasing mode and nonradiative recombination at the hole surfaces. To minimize nonradiative recombination at the nearby surfaces, the active medium needs to provide carrier confinement. Therefore, quantum wells are used. In addition, the symmetry of the defect state is TE-like which matches well with the emission from the InGaAs quantum well [146]. Quantum wells are used instead of quantum dots because of the present higher quality of their epitaxial growth using the Riber 32P system (Figure 2-9). Quantum dots, how-

ever, may prove useful in the future because of their narrower emission bandwidth and potential Purcell enhancement.

The choice of active material should contain the minimum possible surface recombination velocity. The surface recombination velocity of GaAs and AlGaAs is typically around 10^6 cm/s, an order of magnitude faster than that of InGaP (~10^5 cm/s) [159]. Although it may be possible to passivate the AlGaAs and GaAs surfaces with a $(NH_4)_2S_x$ treatment, to reduce the surface recombination velocity to ~10^6 cm/s, the reported values are still not as good as that for InGaP. It has also been reported that reactive-ion etching of InGaAs with a CH_4:H_2 plasma (a readily available etchant gas) can reduce the surface recombination velocity of InGaAs/InP quantum well structure to $1.2*10^4$ [160]. The reduction is attributed to H_2 surface passivation. For the microlaser then, an InGaAs/InGaP quantum well structure is chosen for the active region. The emission wavelength is chosen to be 980 nm so that in addition to application as an optical interconnect, the monorail microcavity laser could find use efficiently pumping erbium-doped waveguides. It should be emphasized that a significant improvement in device performance may be realized with a further investigation of surface passivation techniques.

Figure 4-7 details the materials system for the monorail microlaser. Since the Q of the structures is not as high as some of the other microcavity lasers described in previous sections, three quantum wells are used in the active region instead of a single quantum well, to provide the necessary gain for laser oscillation. The distance from the quantum wells to the oxide interface and the air interface are large enough to prevent carrier tunneling out of the quantum well. Since $In_{0.51}Ga_{0.49}P$ is lattice-matched to a GaAs substrate, an AlGaAs layer (also lattice-matched) may be grown beneath the active region and later converted to Al_2O_3 to provide the required index confinement in the active region, in the same manner as for the passive monorail structure. 90% Al content is chosen for the AlGaAs layer and graded to 80% Al at the InGaP interface to help stabilize the structure during the steam oxidation process; problems with mechanical stability during the oxidation process are discussed in detail in Chapter 3.

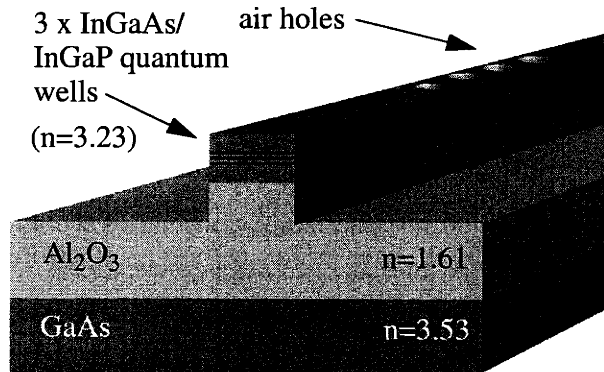

Figure 4-7. Monorail microcavity laser materials system

4.4.2 Design of the Lasing Cavity

Figure 4-8 is a plot of the simulated transmission through a monorail microcavity containing four holes on either side of the defect cavity. The simulation was performed using a 2D finite-difference time-domain scheme [161]. The fundamental mode is excited at one end of the waveguide while the transmission is measured at a monitor point on the opposite end of the structure. The dimensions of the structure are shown in the inset schematic in the arbitrary units of the lattice constant, since the entire structure can be scaled to any wavelength as discussed in Section 1.2.6. The given structure is separated from the substrate by a 1.5 μm thick $(Al_{0.9}Ga_{0.1})_2O_3$ spacer layer. The peak transmission through the cavity is given by [154]:

$$T_{max} = \frac{Q^2}{Q_{wg}^2} \qquad \text{(EQ 82)}$$

The transmission is close to 95% through the structure which according to EQ. 80 indicates that $Q_{rad} \gg Q_{wg}$, as required for efficient coupling between the lasing cavity and the output waveguide. The high-transmission is obtained at the expense of a slight increase in the modal volume and slight-reduction of the overall cavity Q~130. As seen in Figure 4-8, the peak trans-

mission is even as high as the transmission lower-frequency light outside the bandgap that couples to guided modes in the dielectric band of the 1D PC.

An index of refraction of n=3.37 for GaAs was used in the calculation. However, to first order the device dimensions may be scaled to account for the lower index of refraction of InGaP (n=3.23 at 980 nm), used for its lower surface recombination velocity as discussed in Section 4.4.1.[1] For operation at 980 nm, the lattice constant of the structure is calculated to be 256 nm; the rest of the parameters for 980 nm are listed in Figure 4-8.

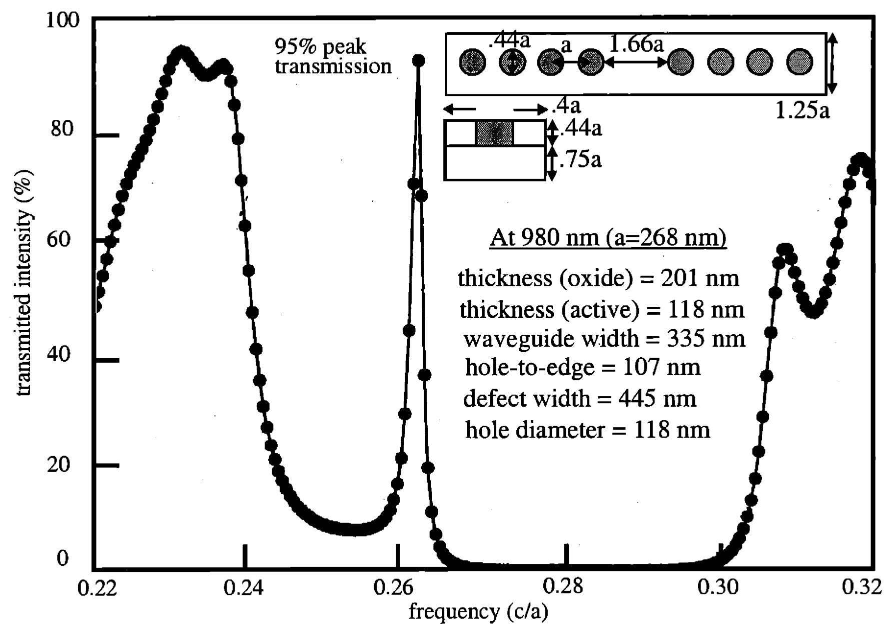

Figure 4-8. Simulated transmission through a monorail microcavity (schematic of simulated structure is inset).

4.5 Rate Equation Analysis

Optical pumping is used to test the monorail microcavity structure; the results are analogous to dc-bias operation of an electrically activated monorail microcavity laser. The semiconductor rate equations in the weak-coupling regime are therefore written with a generation term, g, that represents the number of excited carriers created per second from pumping. The carrier and photon number rate equations are written:

1. Since the InGaAs quantum wells (8 nm thick) constitutes only about 17% of the total active region thickness, the index of refraction is taken to be that of pure InGaP.

$$\dot{n} = g - (1-\beta)\Gamma n - \beta\Gamma(n-n_o)s - \Gamma_{surf}n - \Gamma_{auger}n^3 \quad \text{(EQ 83)}$$

$$\dot{s} = \beta\Gamma[n + s(n-n_o)] - \gamma s \quad \text{(EQ 84)}$$

where n is the *number* of free carriers in the cavity, s is the *number* of photons in the lasing mode, n_o is carrier number required for transparency in the total active medium, Γ_{surf} is the surface recombination coefficient, Γ_{auger} is the Auger recombination coefficient, and γ is the photon loss rate from the lasing mode. In writing EQ. 83 and EQ. 84, it is assumed that the spontaneous emission rate, Γ, is equal for all modes and in particular for free space modes and the lasing cavity mode; this is a reasonable assumption because of the broad InGaAs quantum well emission linewidth at room-temperature that limits Purcell enhancement. It is also assumed that the gain follows a linear dependence on carrier number as is commonly done for microcavity lasers [6,162]. The form of EQ. 83 is particularly useful because of the explicit dependence of spontaneous emission and stimulated emission on β.

Threshold in a microcavity laser occurs when the photon loss rate from the lasing mode is equal to the gain:

$$n_{th} = \frac{\gamma}{\beta\Gamma} - n_o. \quad \text{(EQ 85)}$$

EQ. 85 demonstrates that for a given value of β, threshold is reduced by increasing the radiative emission rate (Γ) relative to the photon loss rate(γ). For the monorail microcavity laser Γ is fixed since Purcell enhancement is limited by the broad InGaAs emission bandwidth. γ is determined by the *total* cavity Q as described by EQ. 80. The cavity Q is 130 in Figure 4-8 and matches well with the average value of Q for the experimental transmission spectra in Figure 4-5. Therefore, Q=130 is used as an approximation to the cavity Q for the microlaser in the following calculations. A typical transparency carrier density for an InGaAs quantum well of $2.1\times10^{18}\ cm^{-3}$ is also used which is easily converted to carrier number by multiplying by the total active volume. Three quantum wells are chosen to provide sufficient gain in the active medium.

A MATLAB code is written (Appendix A.1) and used to numerically solve EQ. 83 and EQ. 84 for the monorail microcavity laser. The injection current is calculated by estimating the total amount of pump-light absorbed by the quantum wells in the monorail microcavity. A $\lambda = 810\,\text{nm}$ pump laser source focused to a reasonable 5 μm spot size is assumed. A $Ti{:}Al_2O_3$ laser source readily generates $\lambda = 810$ nm pump light, and the energy of the input photons lies below the bandgap of the InGaP barrier layers so that carriers are only generated in the quantum wells. The only unknown in solving the microcavity laser equations is the value of β. The power leaking out of the monorail microcavity is plotted as a function of both pump power and the corresponding injection current in Figure 4-9 for several different values of β. Important parameters in the calculation are listed in the inset. The power is measured directly at the lower reflectivity side of the monorail microcavity. To isolate the dependence of threshold on β, all nonradiative recombination (surface and Auger) are set to zero.

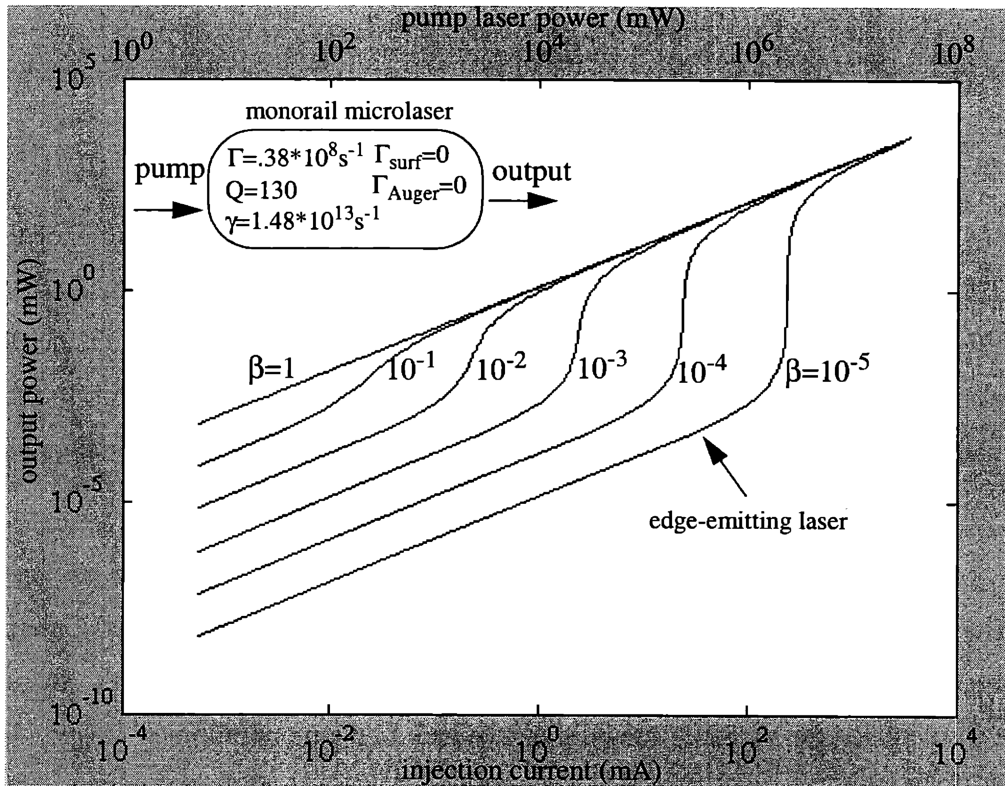

Figure 4-9. Calculated power output from monorail microcavity laser with simulated transmission from Figure 4-8 for a wide range of β values.

Even for β=1 only a maximum power output on the order of 100 μW is expected for 200 mW of pump power (the damage threshold for optical testing of the devices).

4.5.1 Estimation of Spontaneous Emission Factor

β is less than one for the monorail microcavity lasers because of the broad emission linewidth of the InGaAs quantum well relative to the microcavity and spontaneous emission into both radiation modes and guided modes. The bandgap provided by the holes along the monorail waveguide extends from approximately 860 nm to 1120 nm and should forbid propagation of guided modes across the entire emission bandwidth. The calculation of β begins with Fermi's golden rule (EQ. 30) and depends on the active volume, the material and cavity quality factors,

and the detuning between the material and cavity resonance peaks. For equal emission rate into all modes (no Purcell enhancement) the following expression for β may be derived [125,163]:

$$\beta = \frac{f\lambda^4}{4\pi n_{eff}^3 V\Delta\lambda} \quad \text{(EQ 86)}$$

where f is the confinement factor of the lasing mode, n_{eff} is the effective index of the lasing mode, λ is the peak wavelength of the emission, $\Delta\lambda$ is the FWHM, and V is the modal volume. For $V \sim .056\ \mu m^3$, $f = \frac{V_{active}}{V} = .076$, $\lambda = 980$ nm, $\Delta\lambda \sim 60$ nm, and $n_{eff} = 3.23$ (since the mode is largely confined in the dielectric in Figure 4-4), a value of $\beta = .005$ is calculated. Notice that in this estimation, the value of Q is irrelevant since it is much larger than the material quality factor ($Q_m \sim 16$ for FWHM=60 at 980 nm).

Extensive calculations of β for VCSELs of various sizes have been performed [163]. The monorail microcavity is similar to a VCSEL in that both structures consist of a 1D PBG along the axial direction with index confinement in the two lateral directions. Therefore, the values of β calculated for VCSELs should translate well to the monorail microcavity. Indeed, it is shown in [163] that EQ. 86 is an accurate calculation of β for VCSELs containing active material with a large FWHM, as is the case for the InGaAs quantum wells. Therefore, a value of $\beta = .005$ is assumed for the monorail microcavity laser. According to Figure 4-9, with $\beta = .005$, for 200 mW pump power the maximum power output is < 1 μW (below threshold). Threshold for the structure occurs at approximately 300 μA of injected current.

The low output power may be increased by increasing the cavity Q, for instance, by adding more holes to the monorail on the higher-reflectivity side of the microcavity. An increase in the reflectivity by adding more holes, while decreasing the photon loss rate γ, also decreases the radiation Q leading to more loss to radiation modes. Physically, increasing the reflectivity by adding more holes increases the confinement of the cavity mode along the waveguide, and correspondingly spreads out the defect state in reciprocal space, enabling phase-matching to radiation states above the light cone.

4.5.2 The Effects of Nonradiative Recombination

Nonradiative effects are extremely important in the monorail microcavity laser because of the small volume and high-carrier densities required in the laser design. The small volume of the microcavity relative to the diffusion length of a carrier in the quantum well (>1 μm) enables any carrier to recombine nonradiatively at an exposed surface. The total surface recombination rate is therefore given by the ratio of the exposed surface area to active volume and the surface recombination velocity (v_s) as $\Gamma_{surf} = \frac{A_s}{V} v_s$. Figure 4-10a details the output characteristics of the monorail microcavity laser as a function of surface recombination velocity (v_s). The effect of surface recombination is to increase the threshold injection current (and pump power) and to sharpen the threshold transition. A surface recombination velocity of 1.2×10^4 (H_2-passivated InGaAs as discussed in Section 4.4.1) is used in the calculations for the monorail microcavity laser.

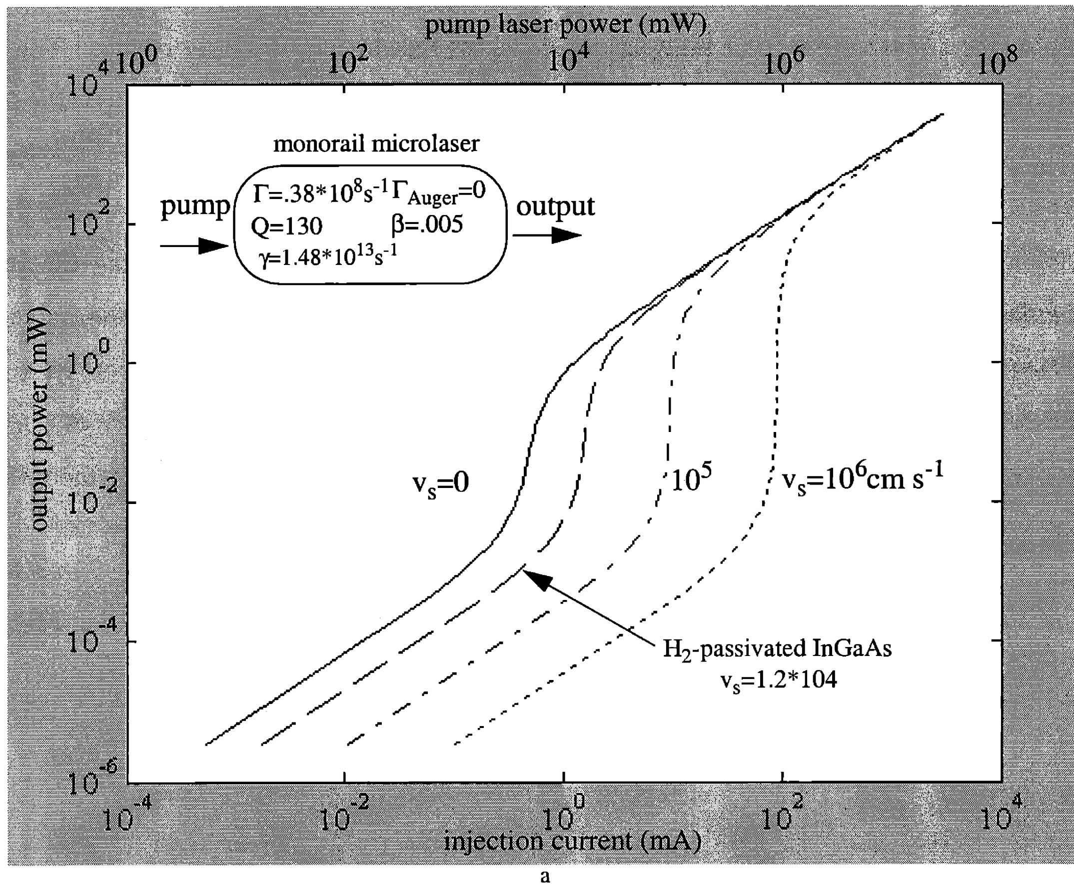

Figure 4-10. The effects of surface recombination on the power output from a monorail microcavity laser (parameters are inset).

The value Γ_{auger} is calculated using parameters similar to an InGaAs quantum well reported in [6]. Further details of the calculation may be found in Appendix A.1. The effect of Auger recombination is stronger than that of surface recombination. Indeed, according to Figure 4-10b, reasonable values of the Auger recombination coefficient for InGaAs quantum wells lead to unreasonable optical pump powers and injection currents at threshold. Clearly, Auger recombination is a critical problem for the monorail microcavity laser and for all low-threshold microcavity lasers.[1]

1. Interestingly, an Auger term is omitted in much of the microcavity laser literature cited in the previous sections.

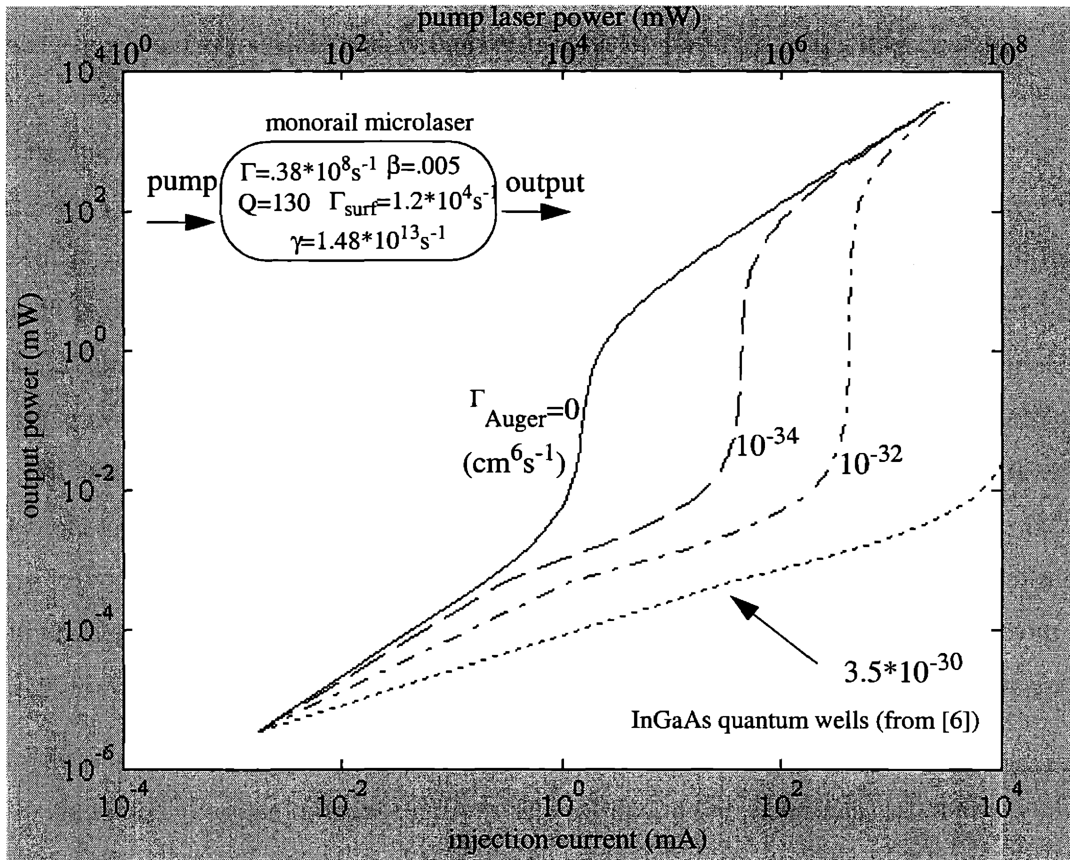

Figure 4-11. The effects of Auger recombination on the power output from a monorail microcavity laser (parameters are inset).

4.5.3 Alternative Model of Monorail Microcavity Laser

The standard density rate equations for a semiconductor laser are [6]:

$$\dot{N} = G - BN^2 - f v_g g N_p - \Gamma_{surf} N - \Gamma_{auger} N^3 \quad \text{(EQ 87)}$$

$$\dot{N}_p = f v_g g N_p + \beta B N^2 - \gamma N_p \quad \text{(EQ 88)}$$

where N is the carrier *density*, G is the generation rate per unit volume, N_p is the photon density relative to the modal volume, g is the gain (assumed to have a logarithmic dependence on carrier density [6]), $f = \frac{V_{active}}{V}$ is the confinement factor of the lasing mode, and B is the bimolecular recombination coefficient. EQ. 87 and EQ. 88 are numerically solved for comparison purposes to

the results in Section 4.5.1 and Section 4.5.2, using similar assumptions for the optical pumping rate. The threshold gain is determined by maximizing the transmission through a standard VCSEL structure with a phase-shifted defect region sandwiched between two quarter-wave stack DBR mirrors. The index contrast in the mirrors and the phase-shift of the cavity region are adjusted to produce a similar transmission spectra to that of the monorail microcavity laser structure in Figure 4-8. The VCSEL structure is a 1D analog of the monorail microcavity laser and can be used to determine the threshold gain. Gain is incrementally added to the phase-shift region until the transmission is maximized. In the calculation it is assumed that gain is only added to the microcavity even though the lasing mode may overlap active material in the monorail outside the cavity. As a check of the assumption, when gain is also added to all high-index layers of the test VCSEL structure, only a small sub-nanometer shift in the transmission peak at 980 nm is observed. The MATLAB code used in the calculations is found in Appendix A.3. The value of the gain for maximum transmission through the VCSEL structure provides a reasonable estimate of the threshold gain for the monorail microlaser. A threshold gain of $2*10^3$ cm^{-1} is found for the structure and is comparable to typical a semiconductor edge-emitting and surface-emitting lasers.

Figure 4-12 is a comparison between the two models of the monorail microcavity laser (key parameters are inset). Although for clarity Auger recombination is not included in the calculation, the effect on both models is the same as the trend shown in Figure 4-11. The two

microcavity laser models agree well and support the accuracy of the calculations. The threshold injection current is similar for the two models although the threshold is not as sharp for model 2.

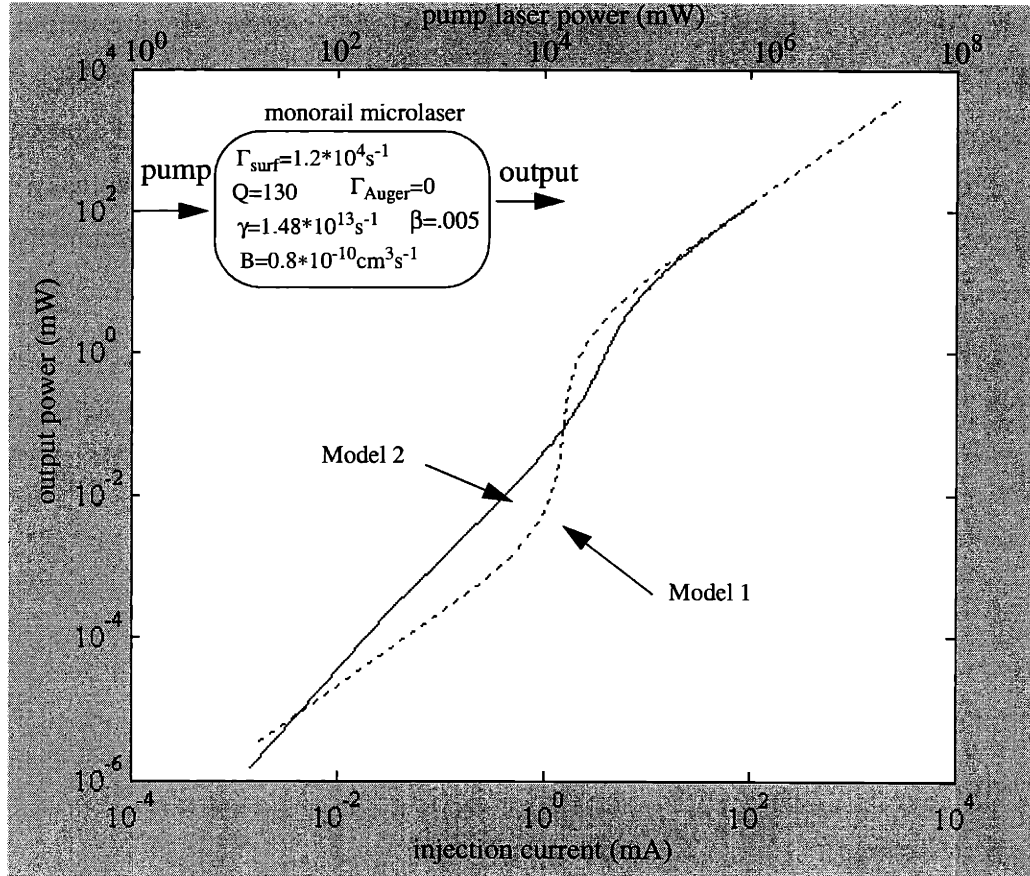

Figure 4-12. Comparison between monorail microcavity laser models. The first model (dotted line) uses the rate-equations in EQ. 83 and EQ. 84 and defines threshold as the stimulated emission rate equaling the cavity loss rate. The second mode (solid line) uses EQ. 87 and EQ. 88 and determines the threshold gain by maximizing transmission through a VCSEL structure analogous to the monorail microcavity.

4.6 Device Fabrication

The microcavity laser fabrication involves MBE, electron beam evaporation, electron-beam lithography, RIE, and steam oxidation processes. The process steps are summarized in Figure 4-13. Each monorail microcavity laser sample contains many different devices. The lattice constant is fixed on each sample so that the frequency position of the PBG along the axial direction of the monorail is fixed. The defect width is the most sensitive parameter that will determine the position of the cavity resonance. The defect width is varied by 25% around the design parameters in Figure 4-8. The number of holes at the output facet is also varied from 3 to 5 to adjust the balance between Q_{rad} and Q_{wg} as described in Section 4.4.2.

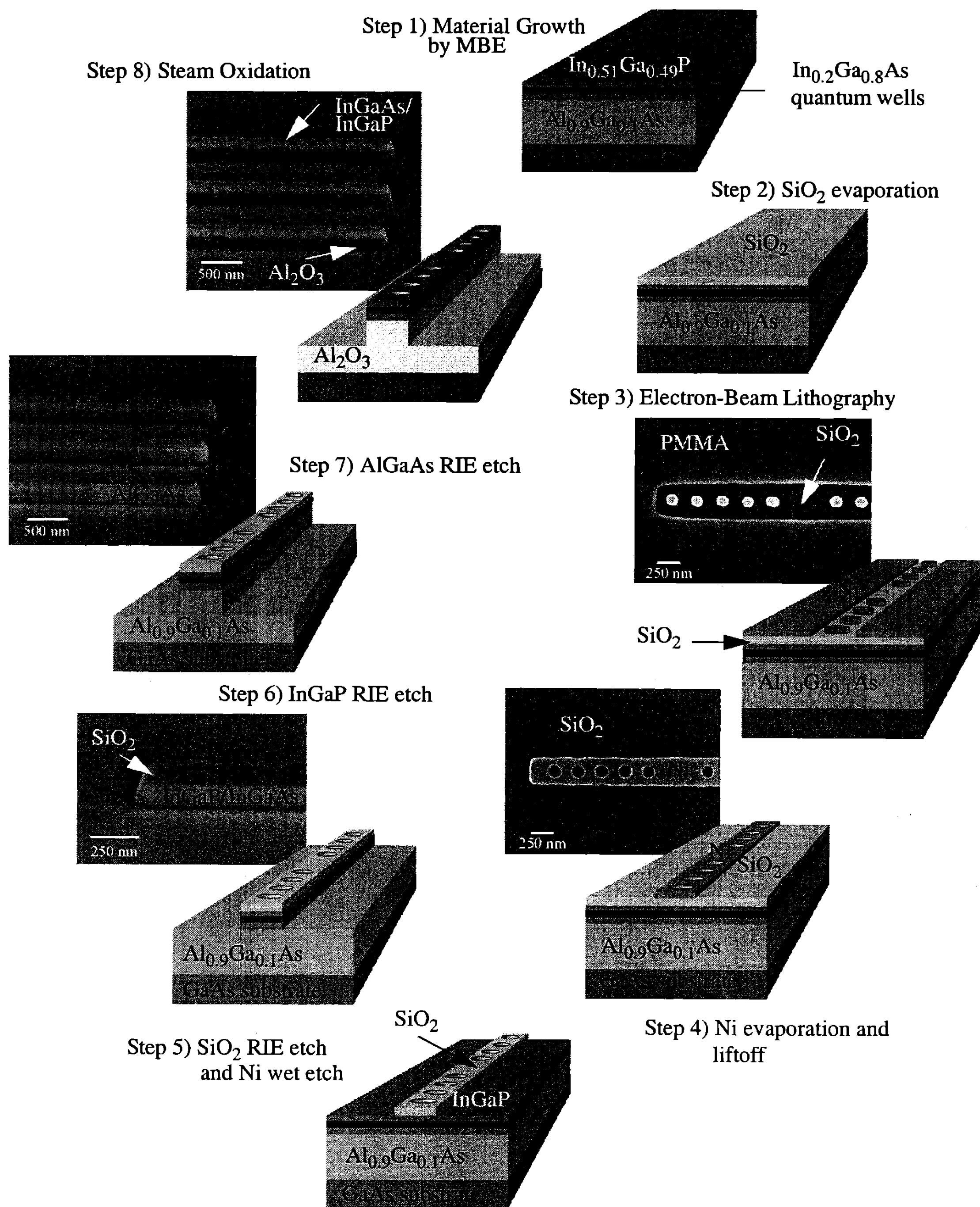

Figure 4-13. Monorail microlaser fabrication process.

4.6.1 Materials Growth and Characterization

The fabrication process begins with the materials system growth by MBE using the Riber 32P system (Figure 2-9). The material composition and thicknesses are determined using x-ray diffraction (Figure 4-14a) as described in further detail in Section 2.4.7. The quantum well quality is determined using room-temperature PL (Figure 4-14b) taken with the measurement setup in Figure 2-11.

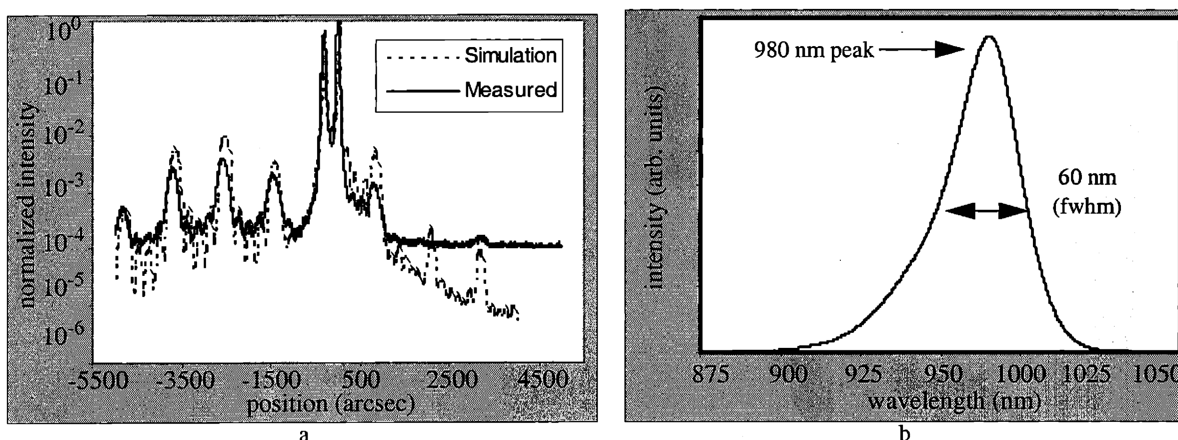

Figure 4-14. Monorail microlaser materials system characterization. a) Comparison between simulated and measured x-ray diffraction spectra. b) Room-temperature PL spectra.

Following the material growth, a 100 nm layer of SiO_2 is evaporated onto the sample using the electron beam evaporation system in NSL. Evaporated SiO_2 can be used as an etch mask through both the In-containing and Al,Ga-containing layers of the monorail material system.

4.6.2 Device Patterning

The monorail microcavity structures are patterned using electron beam lithography. The resist coating and development use the same process parameters as described in detail in Section 2.6.4. Patterns are exposed using a base dose of 50 pA, a field size of 100 μm, and a clock speed of 237 kHz. An SEM of the patterned monorail microlaser structure is shown in Figure 4-13. Following development, 30 nm of Ni is evaporated onto each sample using the electron

beam evaporator in NSL. A liftoff process is then used to reverse the pattern. In the liftoff process, each sample is sprayed with a sequence of 1-methyl 2-pyrolidinone, acetone, and isopropanol until the PMMA has been removed leaving a Ni mask of the monorail structure. An SEM of the Ni mask is given in Figure 4-13. The Ni pattern is then transferred to the SiO_2 layer using RIE with a CHF_3 etch gas at 10 mT pressure and 300 V DC bias. The etch rate is calibrated before each etch using a profileometer; the etch rate is stable at ~26 nm/min. for evaporated SiO_2. Finally, the Ni is etched using a standard Transene Co. Ni etchant and rinsed with DI H_2O. Residual Ni is removed using a brief O_2 RIE step.

4.6.3 Reactive-Ion Etching and Oxidation

The SiO_2 etch mask is used to transfer the monorail microlaser pattern to both active layer and the AlGaAs underlayer. Etching of the active region uses a CH_4:H_2:O_2 etch gas in the ratio 20:20:2.5 sccm., 5 mT pressure, and 100 W input power, in a converted sputtering system RIE in NSL. Etching is continued using a BCl_3:$SiCl_4$ etch at 8 mT pressure and 380 V DC bias. Further details of the BCl_3:$SiCl_4$ etch may be found in [67]. Figure 4-13 shows SEMs of each etch step. The remaining SiO_2 mask is them removed using the CHF_3 etch described in Section 4.6.2. The device fabrication is completed using the steam oxidation process described in detail in Chapter 3. The oxidation is performed at 435°C for 1 hr. An SEM of several completed device structures is shown in Figure 4-13.

4.7 Device Characterization

The monorail microcavity lasers were tested by optically pumping with a tunable Ti:Al_2O_3 (730-950 nm) laser using a similar measurement setup to that shown in Figure 2-28; the same setup used for testing the PC LED structures in Chapter 2. The PL is observed from the top of the monorail microcavity devices so that only scattered light from the lasing mode and spontaneous emission will be detected. Therefore, the measured light scattered from the lasing mode should only be a percentage of the power output simulated in Section 4.5. However, the nanowatt sensitivity of the measurement set-up should suffice to test the monorail microcavities. Unfortunately, initial investigation into the monorail microlaser structures produced no observable PL

from the monorail microcavity laser structures. Based on the previous discussions in the chapter, however, this may not be a surprising result.

A potential reason for unobservable PL from the microlaser structures is nonradiative recombination that increases the threshold carrier density and may derive from a combination of several potential sources: 1) Auger recombination, 2) surface recombination, or 3) another non-radiative recombination process, such as quantum well damage from oxidation, as was explored in detail in Section 2.9.2.

To first separate out the effects of nonradiative surface recombination, test structures that consist of various size boxes and parallelpiped structures are fabricated from the monorail microlaser materials sytem. Figure 4-15a shows an SEM of a test structure fabricated using the same process as the microlaser described in Section 4.6, but with the process terminating after the active region etch step (step 6 in Figure 4-13). The various size structures enable measurement of the effects of surface recombination as a function of active volume, and in particular a measurement of the surface recombination velocity. The surface recombination velocity is measured by comparing the PL from 10 parallelpiped structures each 10 μm long with widths varying from 1 to 10 μm. The PL from each structure is normalized to the largest structure that has a limited surface recombination component. The measurement was performed at low enough powers that Auger recombination should be negligible.

A plot of the normalized PL versus parallelpiped width is shown in Figure 4-15b along with a curve fitted to the measured data. The effect of surface recombination appears to become important for test structures with widths below ~ 5 μm. From the fitted curve the surface recombination velocity is determined to be ~$5.0*10^5$ cm/s, a larger value than $1.2*10^4$ cm/s previously assumed from the literature The measured value, however, is an overestimate of the exact surface recombination velocity since even the largest structure has a finite nonradiative surface recombination component. In addition, the H_2-passivation of the InGaAs sidewalls may be incomplete due to the brief etch time (~10 mins) at low pressures (5 mT) [160]. An examination

of Figure 4-10 shows that a slight overestimation of the surface recombination velocity should only lead to minor discrepancies in the measured output PL.

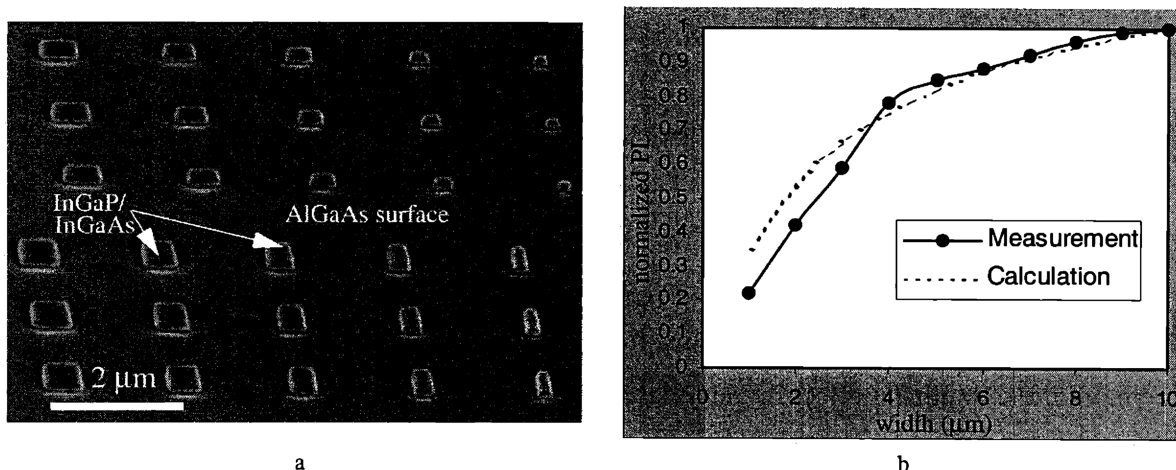

a b

Figure 4-15. a) A sample consisting of various size structures is used to measure the effects of surface recombination. b) Normalized PL as a function of sample size

A brief oxidation is the final step performed in the fabrication process of the monorail microlasers (Figure 4-13). The exposed sidewalls of the InGaAs quantum wells may provide a pathway for the quantum well damage suggested in Section 2.9.2 leading to an additional nonradiative component. Indeed, detectable PL was measured from test sample structures similar to those shown in Figure 4-15a, but with smaller active volumes comparable to that of the monorail microcavity. Like surface recombination, the effect of quantum well damage is also linear in carrier density and therefore will exhibit a similar effect on the laser properties as that shown in Figure 4-10.

The simulations presented in Section 4.5.2 identify Auger recombination as the primary candidate for limiting output power from the monorail microcavity laser. The problem of Auger recombination is complicated by surface recombination and quantum well damage effects that increase the threshold carrier density of the monorail microlasers. Cooling to lower temperatures reduces the threshold carrier density by reducing nonradiative recombination and will there-

fore reduce the effect of Auger recombination. It may therefore be necessary to test the monorail microcavity lasers at low-temperatures as other authors investigating PC microlasers have been forced to do [143]. Precise measurement at low-temperatures, however, was not currently available at MIT.

4.8 Conclusions

A detailed investigation into transforming the monorail microcavity filter into a microlaser device has been performed. The performance of the monorail microlaser under uniform optical pumping (dc-bias) was modelled using the semiconductor laser rate equations in combination with previously measured and calculated values of transmission through a corresponding monorail microcavity filter. The effects of nonradiative recombination are identified as severe, with the dominant effect on microlaser performance being a combination of surface and Auger recombination. These effects have limited the testing of successfully fabricated monorail microcavity lasers.

The analysis described in this chapter provides the information necessary to improve upon the monorail microlaser design. The generic models developed and the MATLAB code provided in Appendices A.2-A.4 may be used, with only slight modifications, to simulate the output power from any future microcavity laser designs. There are several advantages of the monorail microlaser that warrant further investigation of the structure including: low modal volume, low noise due to strong reabsorption of spontaneous emission, direct integration with a waveguide, and suitable thermal properties. The primary disadvantage of the monorail microcavity laser design identified in this chapter is nonradiative recombination, the most severe of which is Auger recombination. The effect of Auger recombination is further magnified by surface recombination which increases the threshold carrier density. Since the effect of Auger depends on N^3 where N is the carrier *density*, one way to lessen the effect is to increase the total volume of active material so that the threshold carrier number remains the same but the carrier density in the quantum wells is reduced. In addition, increasing the volume of active material provides a greater overlap with the lasing mode which increases the value of β (EQ. 86) and reduces the

threshold carrier number. Of course, as the gain is increased the transmission spectra of the monorail will change as well due to the large imaginary component of the index of refraction.

Another method of reducing the effects of Auger recombination is to reduce the threshold carrier density by decreasing the cavity photon loss rate by increasing Q_{wg}. However, because photons are only trapped by index-confinement in lateral directions along the monorail, increasing Q_{wg} leads to a corresponding decrease in Q_{rad} and loss to radiation modes. Since the transmission through the monorail microcavity (~95%) has already been optimized, increasing Q_{wg} further is limited without further increasing the confinement in the directions lateral to the waveguide. Another method of reducing the threshold carrier density is to enhance the radiative recombination rate by using a narrow bandwidth emitter (such as quantum dots) and taking advantage of EQ. 81. The relatively low value of Q (~130), however, will limit the achievable Purcell enhancement to about an order of magnitude (see Section 4.3). An increase in the radiative emission rate though Purcell enhancement will, however, also increase the value of β (~.005) through EQ. 78.

Even with a larger active volume containing a narrow bandwidth emitter that increases both the radiative emission rate and β, optical pumping of the monorail microlasers at pump powers below the damage threshold makes observation of a lasing threshold difficult. As mentioned in Section 4.5.2, even in the ideal scenario (β=1 with no nonradiative recombination components), only ~100 μW is expected to leak out of the lasing cavity when pumping at the damage threshold of 200 mW. In addition, only a small percentage of that light is scattered into radiation modes that may then be collected using the current PL measurement setup. Therefore, future measurements of an optically-pumped monorail microlaser structure may benefit from directly collecting light at the output edge of the waveguide or else coherently scattering output light into radiation modes using a grating at the output facet. Clearly, however, an electrically-pumped design is more attractive for future monorail microlaser structures and should simplify the testing process significantly.

Future monorail microcavity laser designs should also include larger defect microcavities that are less limited by nonradiative recombination. Even though the value of β is reduced and the cavity becomes multimode, the large cavity structures provide higher-power output and may be appropriate for some optical interconnect applications. In addition, they provide an attractive means of studying the lasing threshold as a function of total active volume. Several such structures have already been fabricated and underwent optical testing. The pumping efficiency of the structures was extremely low, however, so that lasing was not observed. An increase in pumping efficiency in the larger defect cavity structures may be achieved by electrical pumping.

In summary, future monorail microlaser designs need to optimize the value β and reduce the threshold carrier density by increasing the amount of active volume of narrow bandwidth emitters (such as quantum dots). For ease of testing and to be more attractive for application to optical interconnects, an electrically-pumped monorail microlaser is desirable. Quantum-well disordering should be explored to provide a means of reducing reabsorption of laser light along the output waveguide. Furthermore, additional surface passivation may help reduce the surface recombination velocity, thereby reducing the theshold carrier density and limiting Auger recombination effects. Methods of further relieving the effects of Auger through strain [6] may also warrant investigation. Further improvements in the monorail microlaser design require changes to the generic monorail design. For instance, an increase in Q_{wg} may be achieved through suppression of emission into radiation modes by embedding the monorail within a higher-dimensionality PC.

Chapter V. Conclusions and Future Directions

5.1 Introduction

The design, fabrication, and testing of several important III-V optical sources that benefit from the unique properties of PCs has been explored. It has been shown that PCs demonstrate the ability to greatly enhance the performance of optical sources in III-V materials. Conversely, it has also been shown that the III-V materials system provides the high-index contrast necessary for using PCs. Hopefully, the work presented here will provide a basis for continuing research on the benefits of PCs for III-V optical sources at MIT and beyond.

5.2 Future Work: The High-Efficiency Semiconductor PC LED

Enhancement in external efficiency in a semiconductor LED was demonstrated in Chapter 2 using a PC. The device was carefully tested optically to isolate the effects of the PC on external efficiency. A lower limit on the external efficiency of 17.2% was carefully identified and demonstrated. The same structure is capable of 28.3% external efficiency when nonradiative recombination introduced by the device processing is eliminated. A method of reducing the quantum well damage introduced during the device processing is suggested in Section 2.9.4 and should be pursued in the future. In addition, the external efficiency may be optimized by using

structures with higher overlap between the material emission and the PC resonances; these structures have been fabricated and are currently being tested at MIT.

From a display application point of view, an electrically-pumped device is more attractive. Therefore, a useful next step is to demonstrate the total "wall plug efficiency" of the design by electrically pumping the active region. Figure 5-1 is a schematic of a proposed electrically-pumped semiconductor LED that utilizes the PC designs explored in Chapter 2 to enhance device performance. The generic device design is similar to that presented in Section 2.4.1, consisting of an asymmetric active region containing a quantum well, an Al_2O_3 spacer layer, and a Al_2O_3/GaAs DBR, all grown epitaxially on a GaAs substrate. Metal contacts are made to the top p-type layer (InGaP:Be) and bottom n-type (AlGaAs:Si) barrier layers surrounding the quantum well, and are isolated from each other by an insulating SiO_2 layer. The metal contacts may take various shapes; in particular, a ring geometry may help inject carriers more uniformly in the quantum well beneath the PC. One potential problem with the device shown that must be addressed is nonradiative surface recombination at the hole surfaces. It may be possible to passivate the hole surfaces or directly inject carriers into the quantum well (as was done "artificially" by pumping at wavelengths longer than the InGaP barrier layers in Chapter 2). A hemispherical glass dome that

both protects the active region from the environment and helps further increase the brightness of the LED by widening the escape cone may be used to optimize the design.

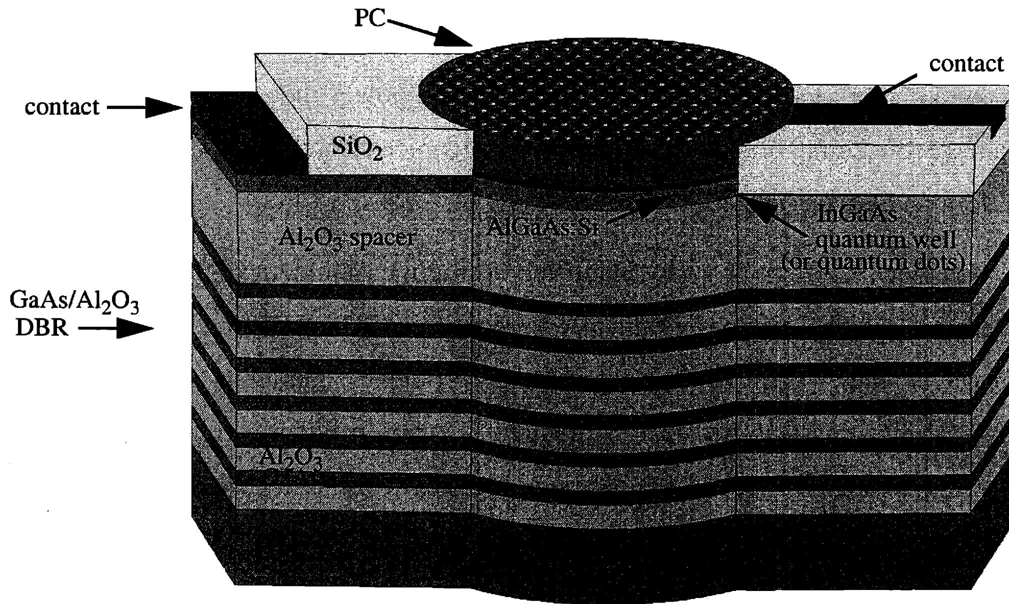

Figure 5-1. Generic design for electrically activated high-efficiency PC LED structure.

Further optimization of the PC LED should use narrow bandwidth emitters such a quantum dots that may experience Purcell enhancement from the leaky resonance modes available from the 2D PCs used in the LEDs. Quantum dots may also improve carrier confinement reducing the effects of nonradiative surface recombination. The optimal high-efficiency semiconductor PC LED design will match the resonant state linewidth to the material bandwidth by chirping the hole size to produce an optimal rate enhancement. To this end, electron beam lithography is particularly useful because it automatically chirps the PC hole size due to proximity effects. It may also be possible to further increase rate-enhancement by using quasicrystalline PC structures that maximizing the available density of states of the PC resonances at the Γ-point. The high-emission rate may prove useful for faster modulation of the electrically-pumped structure in Figure 5-1.

The PC LED structures fabricated have opened the door to a wealth of information. Many additional measurements may be performed on the high-efficiency PC LED struc-

tures that have already been presented in this thesis. For instance, lifetime measurements of PBG or resonance-enhanced LED structures may provide a direct determination of rate suppression or enhancement. Low-temperature measurements will suppress nonradiative recombination effects and enable a more accurate estimate of the external efficiency. An alternative method of reducing the effects of nonradiative recombination is to perform high-power measurements without surpassing the damage threshold of the structures by using picosecond pulses so that radiative recombination dominates even further.

Another important property identified during measurement of the PC LED structures is enhanced injection efficiency by optically pumping the PC LED structures at resonance with the pump wavelength. In measuring the external efficiency, pumping on resonance was avoided for comparison to unpatterned LED structures. However, when pumping on resonance over an order of magnitude increase in optical pumping was measured. Sharp resonances that provide enhanced optical pumping are easily identified from white-light reflectivity spectra of the PC LED structures.

The large measured enhancements of injection efficiency also encourage further exploration into applications of input-coupling using 2D PC structures. Potential applications include input-coupling a signal from low-index materials such as an optical fiber or free-space into higher-index optical components such as a waveguide, a resonator, or a detector. Another potential application is separate input and output coupling regions using 2D PCs to further enhance the total PL emitted from a given LED structure. Such structures have already been fabricated (SEMs are shown in Figure 5-2) and should be measured in the near future. Using such designs it may be possible to generate a white LED by cascading several different PC LED structures. The shortest wavelength ("blue") PC LED may be used to pump a longer wavelength ("yellow") LED which subsequently efficiently pumps the longest wavelength ("red") LED. The PCs are designed such that input resonances overlap the pumping color while output resonances over-

lap the corresponding emission color. White-light is generated from the sum of the various emission colors.

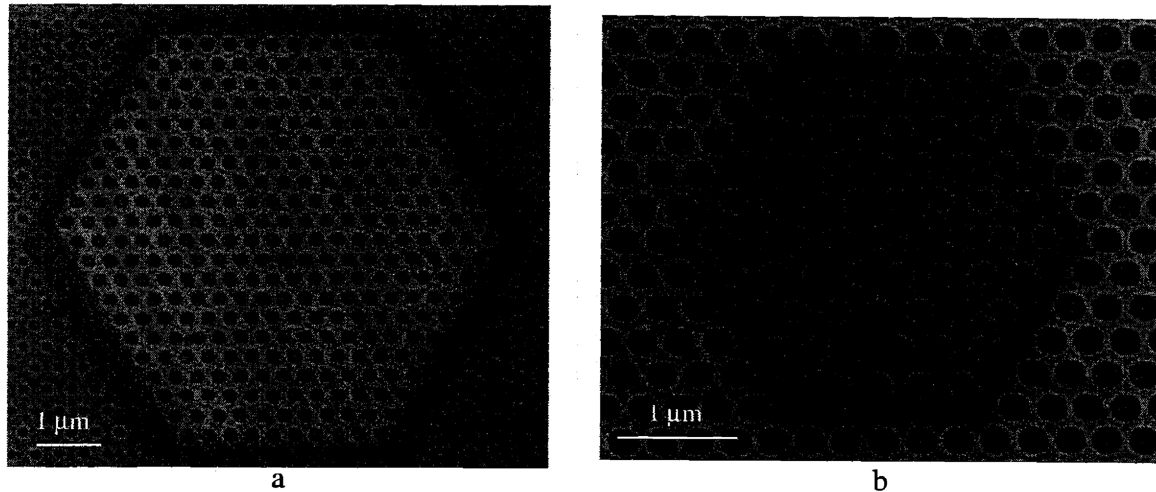

Figure 5-2. SEMs of LED structures consisting of two separate PC regions. a) The center PC region contains a resonance that overlaps the pump wavelength at 810 nm and therefore provides enhanced optical pumping of the surrounding PC region. The surrounding PC contains a resonance that overlaps the emission linewidth. b) The inverse of the structure shown in (a) at higher magnification.

Lasing action has also been observed on the LED structures and derives from the 2D feedback provided by the PC. The 2D lasing action is fundamentally different than 1D distributed feedback lasing and has previously been explored in [164-166]. LED enhancement and lasing action are measured on the same structure. Lasing occurs when the high-efficiency PC LED is pumped above threshold. Figure 5-3 shows the lasing peak for a particular PC LED structure pumped above threshold. The higher-frequency resonances that lead to higher external efficiencies are observed on the same structure. The position of the lasing peak was calculated by considering a small periodic perturbation to the index of refraction of the dielectric slab; the result matches well with the observed emission peak. The exact nature of the lasing mechanism in the PC LED structures warrants further study. By pumping on resonance, PC LED structures may be

excited above threshold without using high-input powers because of the corresponding high-injection efficiency.

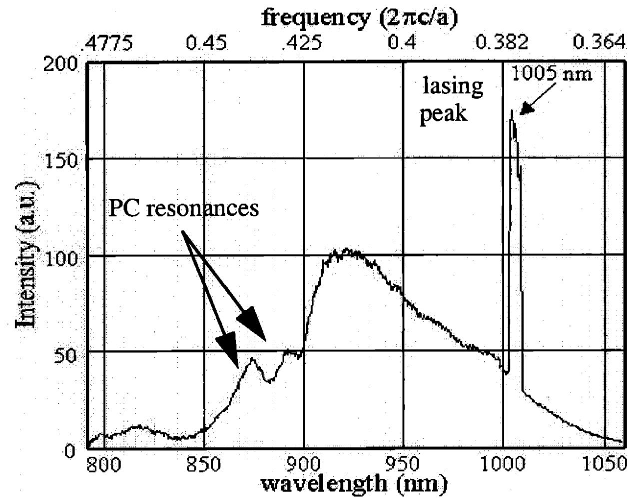

Figure 5-3. A PC LED structure that contains resonances used to enhance external efficiency is pumped above threshold. A lasing peak is observed at 1005 nm.

5.3 Future Work: Saturable Bragg Reflectors

The design and fabrication of wide-stopband SBRs fabricated over a large area for use in generating ultra-fast optical pulses in a Cr^{4+}:YAG laser cavity was presented in Chapter 3. A low-temperature method of oxidizing large-area SBRs was demonstrated and used to generate record 35 fs pulses with a mechanically stable 200 μm wide mirror. The limit in pulse-width is believed to be TPA therefore warranting further investigation into even larger area SBRs. Several alternative mirror designs were explored that may be oxidized at high temperatures to provide the necessary $(\sim 500\ \mu m)^2$ area necessary for a broader laser spot size and reduced TPA. A buffered-interface approach was identified as the most stable. A higher-quality absorber region needs to be grown on the structure in the future so that it may be tested in the Cr^{4+}:YAG laser cavity. $AlGaAs/As_2O_3$ Bragg mirrors should be pursued as the most stable structure in the future since it is an extension of the buffered interface into the entire high-index layer. However, a sufficiently low Al-content (<50%) is necessary to ensure negligible oxidation rate in the normal direction to the mirror stack.

The dense As_2O_3 intermediate species has been identified as slowing the oxidation process from a linear to a diffusion-limited regime. In addition, it has been shown that the primary source of stress and delamination occurs at the oxidation terminus. Further characterization of the delamination process is needed. For instance, the role of the dense As_2O_3 in the mechanical stability of the Bragg mirrors needs to be investigated further. Clearly, a model is suggested that characterizes the exact nature of the strain and stress at the oxide interface.

5.4 Future Work: The Microcavity Laser

The design and fabrication of a monorail microcavity laser was discussed in detail in Chapter 4. The threshold for the monorail microlaser under uniform optical pumping (dc-bias) was explored and guiding principles put in place for future designs of microlasers embedded in waveguides using PCs for optical interconnect applications. An electrical design, such as that proposed in Figure 5-4, is more attractive for testing purposes and for optical interconnects. The generic monorail design is the same although the lateral index contrast is reduced because of the barrier layers used for carrier injection. Carriers are injected laterally into the monorail microcavity through a p-type InGaP:Be layer and an n-type AlGaAs:Si layer surrounding the quantum well (or quantum dot) active region. A similar structure could also be fabricated in Si using narrow linewidth Er^{3+} emitters enabling an on-chip Si-based optical interconnect.

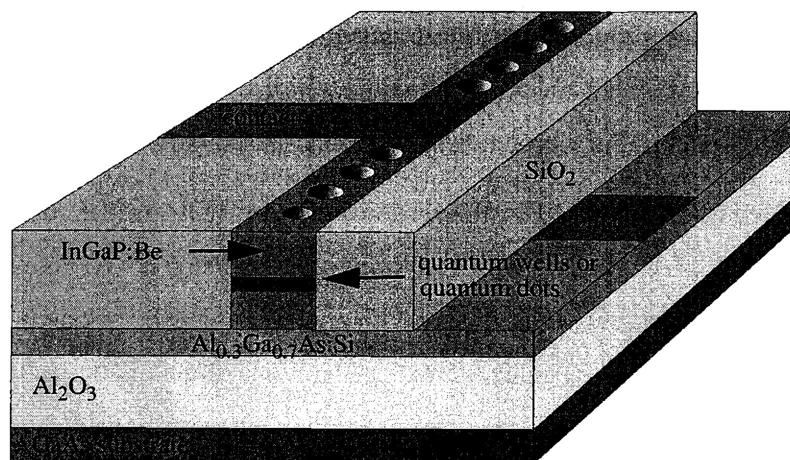

Figure 5-4. Generic design for electrically activated low-threshold monorail microcavity laser.

The monorail microlaser is limited at room-temperature by nonradiative recombination effects which are particularly detrimental because of the relatively low Q of the microcavity. Surface recombination raises the threshold carrier density to a level at which auger recombination becomes important. To operate at low threshold, quantum dot emitters with a narrow linewidth may be used to enhance the emission rate and increase the spontaneous emission factor β. Additional photon confinement (perhaps with PCs) along the lateral directions of the monorail may be necessary to raise the cavity Q and enable radiative emission processes to dominate nonradiative effects. The analysis presented in Chapter 4 shall hopefully provide a guideline for such future designs.

5.5 The Potential of Photonic Crystal Optical Sources

Enhanced performance of several optical sources in a III-V materials system has been demonstrated using PCs. Enhanced LED external efficiency, 2D PC lasing action, and enhanced input coupling/injection efficiencies were all demonstrated on a PC LED structures. A large area PC was carefully designed and fabricated as a mirror in an integrated SBR design. Finally, an integrated monorail microcavity laser was fabricated and modeled, and the guiding principles were identified for future monorail microlaser devices using PCs. The importance of the competition between radiative and nonradiative processes has been identified and characterized in detail. Quantum wells are used as the primary emitter material in this thesis, while narrow linewidth quantum dots are proposed for future designs that may further benefit from enhanced spontaneous emission (Purcell enhancement). Finally, oxidized $Al_xGa_{1-x}As$ has been shown to be a useful low-dielectric material in a broad diversity of PC-based optical sources.

The designs presented in the thesis hopefully will lay the foundation for future designs of optical sources using PCs at MIT. An important next step is to demonstrate the integration of a device such as the monorail microlaser with another optical component such a splitter, an add/drop multiplexer, or a PC waveguide. The final step envisioned is the full-integration of an emitter, waveguide, and detector. PCs may be used to enhance some or all of the components in the complete optical link.

Appendix A: MATLAB Scripts

The MATLAB code presented in this Appendix is for use in performing several of the calculations in Chapters 2-4. Comments are given in *italic font* while functions and input parameters are given in SMALL CAPS. The code is included for reference for future researchers and may require slight modifications when applied to other contexts. Although functions take several input parameters, some variables are changed directly within the MATLAB scripts. In some situations, several possible choices of materials parameters are given as comments.

A.1 SBR Transmission Matrix Reflectivity Calculation

```
FUNCTION ETALON=ETALON(NS,GAINS,L,LAMBDA)

%This function returns a T-matrix that represents the propagation through a medium of index
ns(2) and gain gains(2) and surrounded by media with indices of refraction n(1) and n(3) and
gain gains(1) and gains(3).  All units are taken to be in nanometers.%

% define imaginary component of index of refraction
kappa_left=-gains(1)*(lambda/(4*pi));
kappa_middle=-gains(2)*(lambda/(4*pi));
kappa_right=-gains(3)*(lambda/(4*pi));

% Define reflectivity and transmission values for each interface 1-2 and 2-3
```

```
r_left_middle=( (i*kappa_middle+ns(2)) - (i*kappa_left+ns(1)))/
((i*kappa_middle+ns(2))+(i*kappa_left+ns(1)));
t_left_middle=2*sqrt((i*kappa_middle+ns(2))*(ns(1)+i*kappa_left))/
((i*kappa_middle+ns(2))+(i*kappa_left+ns(1)));

r_middle_right=-((i*kappa_right+ns(3))-(i*kappa_middle+ns(2)))/
((i*kappa_right+ns(3))+(i*kappa_middle+ns(2)));
t_middle_right=2*sqrt((i*kappa_right+ns(3))*(ns(2)+i*kappa_middle))/
((i*kappa_right+ns(3))+(i*kappa_middle+ns(2)));

% Propagation constant in "middle" medium
beta_prop=2*pi*ns(2)/lambda + i*gains(2)/2;

% Calculate transmission matrices
T11=(1/(t_left_middle*t_middle_right))*(exp(i*beta_prop*L) -
(r_left_middle*r_middle_right)*exp(-i*beta_prop*L));
T21=(-1/(t_left_middle*t_middle_right))*(r_left_middle*exp(i*beta_prop*L) -
r_middle_right*exp(-i*beta_prop*L));
T12=(-1/(t_left_middle*t_middle_right))*(r_left_middle*exp(-i*beta_prop*L) -
r_middle_right*exp(i*beta_prop*L));
T22=(1/(t_left_middle*t_middle_right))*(exp(-i*beta_prop*L) -
(r_left_middle*r_middle_right)*exp(i*beta_prop*L));

etalon=[T11 T12;T21 T22];

%----Script for calculating sbr mirror reflectivity: parameters are directly input in .m file----%
% The function ALGAASINDEXADACHI returns the index of refraction for an input photon
energy for a given AlGaAs compound and takes the fraction of Al and the photon energy as inputs.
It is omitted here since the indices may simply be replaced by the best known values of ns for the
chosen materials system.%

resonance=1440;
gains=[0,0,0];                      % No gain assumed in mirror so all set to zero
contraction=0;                      % fractional contraction from oxidation
L1=resonance/(4*ns(1)) - contraction*resonance/(4*ns(1))
L2=resonance/(4*ns(2))              % quarter-wave stack
L1=135;
L2=145:                             % thinner oxide mirror


lambdas=[1000:1:3000];'             % broad wavelength range to fit to measured reflectivity
                                    both with and without oxidized layer
rgs=zeros(size(lambdas));
```

```
for index=1:length(lambdas)          % Calculate transmission matrix for each.
  ns=[1.66,algaasindexadachi(0,1.24/(lambdas(index)*10^(-3))),1.66];
                                     % The index of refraction of Al2O3 is assumed constant
                                     over the wavelength range of interest
  %ns=[algaasindexadachi(1,1.24/(lambdas(index)*10^(-3))),algaasindexadachi(0,1.24/(lamb
  das(index)*10^(-3))),algaasindexadachi(1,1.24/(lambdas(index)*10^(-3)))];
                                     % For unoxidized mirror
  %ns=[algaasindexadachi(1,1.24/(lambdas(index)*10^(-3))),algaasindexadachi(0.7,1.24/(lam-
  das(index)*10^(-3))),algaasindexadachi(1,1.24/(lambdas(index)*10^(-3)))];
                                     % For 70% Al low-index layer mirror
  nhigh=ns(2);
  nlow=ns(1);
  beta=2*pi*nhigh/lambdas(index);
  T_prop=[exp(i*beta*L2), 0;0, exp(-i*beta*L2)];
  T=(T_prop*etalon([nhigh,nlow,nhigh],gains,L1,lambdas(index)))^num_periods;
  T=etalon([1,1,nhigh],gains,resonance,lambdas(index))*T; %with air interface added
  rgs(index)=((abs(T(2,1))/abs(T(1,1)))^2)*100;
  det(T);                            % Check of reversibility: determinant must equal 1
end;

figure(1);                           % Plot results internal to function
plot(lambdas, rgs,'b');
axis([1000,3000,0,100]);
[X,Y]=max(rgs);                      % Determine peak reflectivity value
Maximum_R=X
Wavelength=lambdas(Y)
[X,Y]=min(abs(lambdas-1440));
R_1440=rgs(Y)
title('Reflectivity');
```

A.2 Monorail Microlaser Rate Equations Model 1

```
% SI_FUNDCONST script lists fundamental constants in SI units

q = 1.602176462e-19;
h = 6.62606876e-34;
mo = 9.10938188e-31;
c = 299792458;
eo = 8.854187817e-12;
uo = 4*pi*1e-7;
k = 1.3806503e-23;
h_bar = h./2./pi;
```

FUNCTION [PLS, POUTS2]=DC1(RESONANCE, QWTHICKNESS, NUMBEROFWELLS, DIAMETER, WIDTH, DEFECT, RECOMB, THRESHGAIN)

%This function calculates the input-output characteristics for the monorail microcavity laser. Several of the input parameters derive from previous functions. Lasertransmit.m calculates the resonant wavelength for the laser as approximated by a 1D DBR laser. g_{th} is then determined by using lasergains.m. A logarithmic dependence of gain on carrier density is then assumed. A more accurate dependence may be achieved by determining g_{max} from material properties and the form of (fc(N)-fv(N)) for the first quantum well transition.%

```
SI_FUNDCONST                          %fundamental constants function

%------------------------------Structural properties of microcavity laser------------------------------%

def=defect*10^(-3);
d=diameter*10^(-3);
t=qwthickness*10^(-3);
w=width*10^(-3);
res=resonance*10^(-3);
num_wells=numberofwells;
vs=recomb;
activethickness=.118;

%----------------------------------------Assumed material values----------------------------------------%

alpha=10^(4);                         % typical loss in waveguide
As=19.6;                              % 5 micron pump beam spot size in square microns
N_o=2.1*10^(18);                      % Typical transparency carrier density for InGaAs qw (in
                                      cm^-3) (See C&C pp 167)
Q=130;                                % Cavity Q: low Q value accounts for radiation loss
nu=(2*pi*3*10^(10))/(res*Q*10^(-4));% Depends on Q and resonant wavelength
A=1/(2.63*10^(-9));                   % Typical radiative lifetime in InGaAs qw (See [6] pp 167)
%A_c=2.5*A;                           % Maximum Purcell enhancement for semiconductor
                                      microcavity with quantum well emitter
wg=10*10^(-4);                        % output length of waveguide in cm

%-------------------------------Calculated values from input parameters------------------------------%

as=d*pi*t + 2*def*t;                  % surface area
vac=t*(def*w+(d*w-pi*(d/2)^2));       % volume of total active material
vac_total=vac*num_wells                 % total active volume
gammaconf=(.0043/.056);               % confinement factor in quantum well
```

```
As=19.6;                          % 5 micron pump beam spot size in square microns
Ac=vac/t;                         % cross-sectional area of single quantum well in square
                                  microns
A_c=A;                            % Assume qw bandwidth too wide for Purcell enhancement
%C=(beta*A_c)/((1-beta)*A +beta*A_c)*.01
                                  % C-factor, equivalent to β for equal emission rate into all
                                  modes
C=.005;                           % Input directly from calculation in Chapter 4

%----------Microcavity Laser Model #1: Based on maximizing cavity transmission using laser-
transmit.m and lasergains.m------------%

%C_auger=4.5*10^(-6)              % See [6] pp. 158-160 units of microns^6 s-1
C_auger=0;
a=0.15;
auger=C_auger*(sqrt(.025/(a*(1.24/.98))));
                                  % See [6] pp. 160
B=0.8*10^(2)                      % Bimolecular recombination coefficient for InGaAs qw
                                  model: pp 170 [6] micron^3 s-1
gamma=as*vs*10^(4)/vac            % surface recombination rate based on geometry of micro-
                                  cavity
%auger=3.5*10^(-6)
g_th=(threshgain)/gammaconf       % Threshold gain necessary in total active material from
                                  simulations (cm-1)
g_th_qw=g_th/num_wells;           % Threshold gain necessary per well
g_o=1.8*10^(3);                   % InGaAs qw model: pp 167 [6] (cm-1)
n_o=N_o*(10^(-12))*vac            % InGaAs qw model: pp 167 [6](number for transparency
                                  of an individual well)
n_th_qw=n_o*exp(g_th_qw/g_o)      % Threshold carrier number per well
n_th=num_wells*n_th_qw            % Threshold carrier number in total active material
x=linspace(0,7,100);              % sample set for generating carrier numbers
ns=n_o+(1-exp(-x)).*(n_th_qw-n_o); % sample set of carrier numbers designed to asymptoti-
                                  cally approach n_th_qw in each qw
gs=num_wells*(g_o.*log(ns./n_o)); % logarithmic approximation to gain (pp 167 [6]).
ns=num_wells.*ns                  %Redefine ns to represent total carrier number

tau_p=Q*res/(2*pi*3*10^14)        % Optical losses from cavity
tau_p_wg=Q*res/(2*pi*3*10^14)     % All loss assumed to be down waveguide for lasing mode
                                  since transmission is high
tau_p_rad=(tau_p_wg).*tau_p./(tau_p_wg-tau_p)
vg=1/(tau_p*threshgain)           % Gamma_conf*g_th*vg=loss
ss=C.*vac_total.*B.*((ns./vac_total).^2)./(1/tau_p - gammaconf.*vg.*gs)
                                  % photon number in lasing mode
```

```
ps=vac_total.*B.*((ns./vac_total).^2) + gammaconf.*vg.*gs.*ss + gamma.*ns +
vac_total.*auger.*((ns./vac_total).^3);  % carrier generation rate
pouts1=(1/tau_p_wg).*ss.*(1.24/res).*q.*(exp(-gammaconf*alpha*wg));
                                        % power out waveguide of length wg
pouts2=(1/tau_p_wg).*ss.*(1.24/res).*q;
                                        % power out waveguide
pouts3=(1/tau_p_rad).*ss.*(1.24/res).*q;
                                        % power lost to radiation modes
pls=(ps.*As)./(Ac*(1-exp(-t*num_wells))).*(1.24/.81).*q;
                                        % pump laser power


%------------------------------------------------Plot Results--------------------------------------------%

figure(1);                              % pump laser power versus carrier number
loglog(pls.*10^(3), ns);
xlabel('Input Laser Power (mW)');
ylabel('carrier number');

figure(2);                              % power out waveguide of length wg versus pump laser
                                        power with and without waveguide loss. (loss assumed into
                                        one waveguide direction: otherwise divide power by 2)
loglog(pls.*10^(3),pouts1*10^(6),pls.*10^(3),pouts2*10^(6));
plot(pls.*10^(3),pouts1*10^(6),pls.*10^(3),pouts2*10^(6));
title('Input Laser Power versus Power at end of 10 micron waveguide');
xlabel('Input Laser Power (mW)');
ylabel('Power Out Waveguide(microwatts)');
legend('waveguide loss','no waveguide loss');

figure(3)                               % pump laser power versus power leaking into radiation
loglog(pls.*10^(3),pouts3*10^(6));
title('Input Laser Power versus Power Out etched Facet');
xlabel('Input Laser Power (mW)');
ylabel('Radiation Power (microwatts)');

figure(5)                               % Injected current versus power leaking into waveguide
loglog(ps.*q.*10^(3),pouts2*10^(3));
title('Injection Current versus Power Out etched Facet');
xlabel('Injection Current (mA)');
ylabel('Power Out Output Facet (mW)');
```

A.3 VCSEL Transmission Model for Monorail Microlaser

FUNCTION LASERTRANSMITNEW=LASERTRANSMITNEW(N1,N2,DEF,L1,L2, NUM1, NUM2,GAIN)

%This function calculate the transmission through a one-dimensional periodic cavity structure. The purpose of this function is for use in calcuating transmission properties of one-dimensional (or higher-dimensional analogous) structures.%

```
Lcav=def;
ncav=n2;
num_holes_1=num1;
num_holes_2=num2;
lambdas=[800:.1:1300];
trans=zeros(size(lambdas));

for index=1:length(lambdas);            % Calculate using transmissiom matrices
  beta_2=2*pi*n2/lambdas(index);
  T_prop_2=[exp(i*beta_2*L2), 0;0, exp(-i*beta_2*L2)];
  T=(etalon([n2,n1,n2],[gain,0,gain],L1,lambdas(index))*T_prop_2)^(num_holes_2);
  beta_cav=2*pi*ncav/lambdas(index)+i*gain/2;
  T_prop_cav=[exp(i*beta_cav*Lcav), 0;0, exp(-i*beta_cav*Lcav)];
  T=T_prop_cav*T;
  T=((T_prop_2*etalon([n2,n1,n2],[gain,0,gain],L1,lambdas(index)))^(num_holes_1))*T;
  trans(index)=(1/abs(T(1,1)))^2;
  det(T);                               % Check of reversibility: determinant must equal 1
end

plot(lambdas, trans*100);               % Plot transmission versus wavelength
axis([800,1300,0,100]);
[x,y]=max(trans)
```

FUNCTION [GS, TRANS, GMAX]=LASERGAINSNEW(N1,N2,DEF,L1,L2, NUM1, NUM2,RES)

%This function calculates the transmission through a one-dimensional periodic cavity structure as a function of gain. The purpose of this function is for use in calcuating threshold gain in one-dimensional (or higher-dimensional analogous) cavity structures.%

```
Lcav=def;
num_holes_1=num1;
num_holes_2=num2;
ncav=n2;
resonance=res;
gs=[0:.001:.5]*10^(-3);                 % Typical range of gains
trans=zeros(size(gs));
```

```
for index=1:length(gs)
  beta_2=2*pi*n2/resonance;
  T_prop_2=[exp(i*beta_2*L2), 0;0, exp(-i*beta_2*L2)];
  T=(etalon([n2,n1,n2],[0,0,0],L1,resonance)*T_prop_2)^(num_holes_2);
  beta_cav=2*pi*ncav/resonance + i*gs(index)/2;
  T_prop_cav=[exp(i*beta_cav*Lcav), 0;0, exp(-i*beta_cav*Lcav)];
  T=T_prop_cav*T;
  T=((T_prop_2*etalon([n2,n1,n2],[0,0,0],L1,resonance))^(num_holes_1))*T;
  trans(index)=(1/abs(T(1,1)))^2;
  det(T);
end;

[x,y]=max(trans);
gmax=gs(y);
plot(gs,trans);
```

A.4 Monorail Microlaser Rate Equations Model 2

```
FUNCTION [PLS, POUTS2]=DC2(RESONANCE, QWTHICKNESS, NUMBEROFWELLS, DIAMETER, WIDTH,
DEFECT, CONF, RECOMB)
%This function calculates the input-output characteristics for the monorail microcavity laser and
returns vectors containing the input and output powers during optical testing. The threshold in
this function is determined by letting the stimulated emission rate equal the optical loss from the
cavity to determine n_th.%

SI_FUNDCONST                          % simple fundamental constants function

%--------------------------------Structural properties of microcavity laser---------------------------%

def=defect*10^(-3);
d=diameter*10^(-3);
t=qwthickness*10^(-3)
w=width*10^(-3);
res=resonance*10^(-3);
num_wells=numberofwells;
vs=recomb;
activethickness=.118;
as=d*pi*t + 2*def*t;
vac=t*(def*w+(d*w-pi*(d/2)^2));        % volume of single quantum well
vac_total=vac*num_wells                % volume of total active material
As=19.6;                               % 5 micron pump beam spot size in square microns
Ac=vac/t;                              % cross-sectional area of single quantum well in microns^2
```

```
gammaconf=num_wells*(t/activethickness)*conf
                                    % confinement factor in quantum well

%---------------------------------------Assumed material values---------------------------------------%

alpha=10^(4);                       % typical loss in waveguide
As=19.6;                            % 5 micron pump beam spot size in square microns
N_o=2.1*10^(18);                    % Typical transparency carrier density for InGaAs qw (in
cm^-3)
Q=130;                              % Cavity Q
nu=(2*pi*3*10^(14))/(res*Q)         % Depends on Q_wg (assumed to be ~Q for high-transmis
                                    sion structure and resonant wavelength
A=1/(2.63*10^(-9));                 % Typical radiative lifetime in InGaAs qw (See [6] pp 167)
%A_c=2.5*A;                         % Typical enhancement for semiconductor microcavity
wg=10*10^(-4);                      % output length of waveguide in cm

%-------------------------------------------Calculation of β-------------------------------------------%

%A_c=A;                             % Assume qw bandwidth too wide for Purcell enhancement
%C=(beta*A_c)/((1-beta)*A +beta*A_c)*.01
                                    % C-factor, equivalent to β for equal emission rate into all
                                    modes
C=.005;                             % Input directly from calculation in Chapter 4

%---Microcavity Laser Model #2: Based on threshold when stimulated emission rate equals opti-
cal loss rate---------------------------------%

gamma=as*vs*10^(4)/vac              % surface recombination rate based on microcavity geome-
                                    try
C_auger=10^(-6)                     % S ee [6] pp. 158-160
%C_auger=0;
a=0.15;
auger=C_auger*(sqrt(.0235/(a*(1.24/.98))))
%auger=3.5*10^(-6)
B=0.8*10^(2)                        %Bimolecular recombination coefficient for InGaAs
                                    qunatum well model: pp 167 [6] microns^3 s-1
n_o=N_o*(10^(-12))*vac              % Transparency carrier number for given quantum well
n_th=nu/(C*A) + n_o*num_wells       % Threshold carrier number in total active material com-
                                    bined
x=linspace(0,14,100);               % sample set for generating carrier numbers
ns=n_o*num_wells+(1-exp(-x))*(n_th-n_o*num_wells)
                                    % sample set of carrier numbers
ss=C.*A.*ns./(nu-C.*A.*(ns-n_o*num_wells))
```

```
                                    % photon number in lasing cavity mode
ps=A.*ns + C*A.*ss.*(ns-n_o*num_wells)+gamma.*ns+vac_total*auger.*((ns./vac_total).^3);
                                    % generation rate of carriers
pouts1=nu*ss.*(1.24/res).*q.*(exp(-gammaconf*alpha*wg));
                                    % power out waveguide of length wg
pouts2=nu*ss.*(1.24/res).*q;        % power out waveguide


%-----------------------------------------------Plot Results--------------------------------------------%
% Same as in Appendix A.2
```

References

1. N.W. Ashcroft, N. David Mermin, *Solid State Physics.* Saunders College Publishing. New York, New York, **1976.**

2. J.D. Joannopoulos, R.D. Meade, J.N. Winn, *Photonic Crystals: Molding the Flow of Light.* Princeton University Press. Princeton, New Jersey, **1995.**

3. J.D. Joannopoulos, *8.511: Theory of Solids*, Course Notes, Fall Semester, **1999.**

4. R.D Meade, A.M. Rappe, K.D. Brommer, J.D. Joannopoulos, *Phys. Rev. B.,* **1996,** *48*, 8434-37.

5. S. Fan, *Photonic Crystals: Theory and Device Applications,* **1997,** Doctor of Philosphy Thesis, Massachusetts Institute of Technology.

6. L.A. Coldren, S.W. Corzine, *Diode Lasers and Photonic Integrated Circuits,* John Wiley & Sons Inc., New York, **1995.**

7. P.R. Villeneuve, S. Fan, J.D. Joannopoulos, *Phys. Rev. B.,* **1996,** *54*, 7837-42.

8. E. Yablonovitch, T.J. Gmitter, R.D. Meade, A.M. Rappe, K.D. Brommer, J.D. Joannopoulos, *Phys. Rev. Lett.,* **1991,** *67*, 3380-83.

9. E. Yablonovitch, *Phys. Rev. Lett.,* **1987,** *58*, 2059-62.

10. S. John, *Phys. Rev. Lett.,* **1987,** *58*, 2486-89.

11. E.M. Purcell, *Phys. Rev.,* **1946,** *69*, 681-84.

12. R.G. Hulet, E.S. Hilfer, D. Kleppner, *Phys. Rev. Lett.,* **1985,** *55*, 67-70.

13. E. Yablonovitch, T.J. Gmitter, *Phys. Rev. Lett.,* **1989,** *63*, 1950-53.

14. K.M. Leung, Y.F. Liu, *Phys. Rev. Lett.,* **1990,** *65*, 2646-49.

15. Z. Zhang, S. Satpathy, *Phys. Rev. Lett.,* **1990,** *65*, 2650-53.

16. K.M. Ho, C.T. Chan, C.M. Soukoulis, *Phys. Rev. Lett.,* **1990,** *65*, 3152-55.

17. A. Mekis, J.C. Chen, I. Kurland, S. Fan, P.R. Villeneuve, J.D.Joannopoulos, *Phys. Rev. Lett.,* **1996,** *77*, 3787-90.

18. S.G. Johnson, S. Fan, P.R. Villeneuve, J.D.Joannopoulos, *Phys. Rev. B,* **1999,** *60*, 5751-58.

19. I. El-Kady, M.M. Sigalas, R. Biswas, K.M. Ho. *J. Lightwave Technol.,* **1999,** *17*, 2042-48.

20. T. Baba, N. Fukaya, in *Photonic Crystals and Light Localization in the 21st Century,* edited by C.M. Soukoulis, Kluwer, Dordrecht, **2001**.

21. M. Meier, A. Mekis, A. Dodabalapur, A. Timko, R.E. Slusher, J.D. Joannopoulos, O. Nalamasu, *Appl. Phys. Lett.,* **1999,** *74*, 7-9.

22. M. Imada, S. Noda, A. Chutinan, T. Tokuda, M. Murata, G. Sasaki, *Appl. Phys. Lett.,* **1999,** *75*, 316-18.

23. K.Y. Lim, D.J. Ripin, G.S. Petrich, L.A. Kolodziejski, E.P. Ippen, M. Mondol, H.I. Smith, P.R. Villeneuve, S. Fan, J.D. Joannopoulos, *J. Vac. Sci. Technol. B,* **1999,** *17,* 1171-74.

24. A. Ferrando, E. Silvestre, J.J. Miret, J.A. Monsoriu, M.V. Andres, P.S. Russell, *Electron. Lett.,* **1999,** *35*, 325-27.

25. T.M. Monro, D.J. Richardson, N.G.R. Broderick, P.J. Bennett, *J. Lightwave Technol.,***1999,** *17*, 1093-1102.

26. Y. Fink, D.J. Ripin, S. Fan, C. Chen, J.D. Joannopoulos, E.L. Thomas. *J. Lightwave Technol.,***1999,** *17*, 2039-41.

27. S. Fan, P.R. Villeneuve, J.D. Joannopoulos, H.A. Haus, *to appear Phys. Rev. B*.

28. S.Y. Lin, J.G. Fleming, E. Chow, in *Photonic Crystals and Light Localization in the 21st Century,* edited by C.M. Soukoulis, Kluwer, Dordrecht, **1995**.

29. S. Noda, M. Imada, A. Chutinan, and N. Yamamoto, in *Photonic Crystals and Light Localization in the 21st Century,* edited by C.M. Soukoulis, Kluwer, Dordrecht, **1995**.

30. A. van Blaaderen, K.P.Velikov, J.P.Hoogenboom, D.L.J. Vossen, A. Yethiraj, R. Dullens, T. van Dillen, A. Polman, in *Photonic Crystals and Light*

Localization in the 21st Century, edited by C.M. Soukoulis, Kluwer, Dordrecht, **1995**.

31. A. Mekis, J. Joannopoulos. *J. Lightwave Technol.,* **2001,** *19*, 861-5.

32. M.G. Craford, *IEEE Circuits and Devices Mag.,* **1992,** *8*, 24-9.

33. A. Forchel, P. Malinverni, *Compound Semiconductor,* **2000,** *6*, 74.

34. S. Fan, P.R. Villeneuve, J.D. Joannopoulos, *Phys. Rev. Lett.,* **1997,** *78*, 3294-7.

35. H. Yokoyama, K. Ujihara, *Spontaneous Emission and Laser Oscillation in Microcavities,* CRC Press Inc., New York, **1995.**

36. M. Boroditsky, R. Vrijen, T.F. Krauss, R. Coccioli, R. Bhat, E. Yablonovitch. *J. Lightwave Technol.,* **1999,** *17*, 2096-112.

37. M. Boroditsky, R. Coccioli, E. Yablonovitch, *Proc. Photon. West '98,* **1998,** *3283,* 184-190.

38. I. Schintzer, E. Yablonovitch, C. Caneau, T.J. Gmitter, *Appl. Phys. Lett.,* **1993,** *62*, 131-3.

39. S.H. Fan, P.R. Villeneuve, J.D. Joannopoulos, *IEEE J. Quantum Electron.,* **2000,** *36*, 1123-30.

40. M. Lipson, L.C. Kimerling, *Appl. Phys. Lett.,* **2000,** *77*, 1150-2.

41. N. Holonynak, Jr., S.F. Bevaqua, *Appl. Phys. Lett.,* **1962,** *1*, 82-4.

42. J.J. Wierer, D.A. Kellogg, N. Holonyak, Jr., *Appl. Phys. Lett.,* **1999,** *74*, 926-8.

43. H. Benisty, H. De Neve, C. Weisbuch. *IEEE J. Quant. Electron.,* **1998,** *34*, 1612-31.

44. N.F. Gardner, H.C. Chui, E.I. Chen, M.R. Krames, J.-W. Huang, F.A. Kish, S.A. Stockman, C.P. Kocot, T.S. Tan, N. Moll. *Appl. Phys. Lett.,* **1999,** *74*, 2230-33.

45. I. Schintzer, E. Yablonovitch, C. Caneau, T.J. Gmitter, A. Scherer, *Appl. Phys. Lett.,* **1993,** *63*, 2174-77.

46. W.N. Carr, G.E. Pittman, *Appl. Phys. Lett.,* **1963,** *3*, 173-5.

47. K.H. Huang, J.G. Yu, C.P. Kuo, R.M. Fletcher, T.D. Osentowski, L.J. Stinson, M.G. Craford, A.S.H. Liao, *Appl. Phys. Lett.,* **1992,** *61*, 1045-7.

48. E.E. Loebner, *Proc. IEEE,* **1973,** *61,* 837-61.

49. M.R. Krames, M. Ochiai-Holcmb, G.E. Hofler, C. Carter-Coman, E.I. Chen, I.-H. Tan, P. Grillot, N.F. Gardner, H.C. Chui, J.-W. Huang, S.A. Stockman, F.A. Kish, M.G. Craford, T.S. Tan, C.P. Kocot, M. Hueschen, J. Posselt, B. Loh, G. Sasser, and D. Collins. *Appl. Phys. Lett.,* **1999,** *75*, 2365-68.

50. W.L. Barnes, *J. Lightwave Technol.,* **1999,** *17*, 2170-82.

51. J. Vuckovic, M. Loncar, A. Scherer, *IEEE J. Quantum Electron.,* **2000,** *36*, 1131-44.

52. T. Baba, K. Inoshita, H. Tanaka, J. Yonekura, M. Ariga, A. Matsutani, T. Miyamoto, F. Koyama, K. Iga, *J. Lightwave Technol.,* **1999,** *17*, 2113-20.

53. M. Boroditsky, T.F. Krauss, R. Coccioli, R. Vrijen, R. Bhat, E. Yablonovitch. *Appl. Phys. Lett.,* **1999,** *75*, 1036-38.

54. H.-Y. Ryu, J.-K. Hwang, D.-S. Song, I.-Y. Han, Y.-H. Lee, D.-H. Jang, *Appl. Phys. Lett.,* **2001,** *78*, 1174-76.

55. H.-Y. Ryu, Y.-H. Lee, R.L. Sellin, D. Bimberg, *Appl. Phys. Lett.,* **2001,** *79*, 3573-5.

56. J.D. Jackson, *Classical Electrodynamics.* John Wiley & Sons, New York, New York, **1962.**

57. T. Ochiai, K. Sakoda. *Phys. Rev. B,* **2001,** *63*, 125107(1)-(7).

58. S. Fan, J.D. Joannopoulos, *Analysis of Guided Resonances in Photonic Crystal Slabs* (to be published).

59. A.A. Erchak, D.J. Ripin, S. Fan, P. Rakich, J.D. Joannopoulos, E.P. Ippen, G.S. Petrich, L.A. Kolodziejski. *Appl. Phys. Lett.,* **2001,** *78*, 563-65.

60. E. Desurvire, *Erbium-Doped Fiber Amplifiers: Principles and Applications.* John Wiley & Sons, New York, New York, **1994.**

61. S.G. Patterson, *Bipolar Cascade Lasers,* **2000,** Doctor of Philosphy Thesis, Massachusetts Institute of Technology.

62. K. Tai, T.R. Hayes, S.L. McCall, W.T. Tsang. *Appl. Phys. Lett.,* **1988,** *53,* 302-4.

63. S.J. Pearton, F. Ren, W.S. Hobson, C.R. Abernathy, U.K. Chakrabarti. *J. Vac. Sci. Technol. B.,* **1994,** *12*, 142-6.

64. M. Boroditsky, I. Gontijo, M. Jackson, R. Vrijen, E. Yablonovitch, T. Krauss, Chuan-Cheng Cheng, A. Scherer, M. Krames. *J. Appl. Phys.,* **2000,** *87*, 3497-504.

65. K.D. Choquette, K.M. Geib, C.I.H. Ashby, R.D.

66. O. Blum, H.Q. Hou, D.M. Follstaedt, B.E. Hammons, D. Mathes, R. Hull. *IEEE J. Sel. Topics Quantum Electron.,* **1997,** *3*, 916-24.

67. A.A. Erchak, *Design and Fabrication of a Light-Emitting Diode Using a Two-Dimensional Photonic Crystal,* **1999,** Masters of Engineering Thesis, Massachusetts Institute of Technology.

68. B.E.A. Saleh, M.C. Teich, *Fundamentals of Photonics.* John Wiley & Sons. New York, New York, **1991.**

69. A. Bek, A. Aydinli, J.G. Champlain, R. Naone, N. Dagli. *IEEE Photonics Technol. Lett.,* **1999,** *11*, 436-8.

70. L.A. Graham, D.L. Huffaker, T.H. Oh, D.G. Deppe, *Proceedings of the SPIE,* **1997,** *3003,* 63-68.

71. J.M. Dallesasse, N. Holonyak Jr., A.R. Sugg, T.A. Richard, N. El-Zein. *Appl. Phys. Lett.,* **1990,** *57*, 2844-6.

72. H. Nickel. *J. Appl. Phys.,* **1995,** *78*, 5201-3.

73. J.-H. Kim, D.H. Lim, K.S. Kim, G.M. Yang, K.Y. Lim, H.J. Lee. *Appl. Phys. Lett.,* **1996,** *69*, 3357-9.

74. R.A. Barry, V.W.S. Chan, K.L. Hall, E.S. Kintzer, J.D. Moores, K.A. Rauschenbach, E.A. Swanson, L.E. Adams, C.R. Doerr, S.G. Finn, H.A. Haus, E.P Ippen, W.S. Wong, M. Haner. *IEEE J. Sel. Areas Comm.,* **1996,** *14,* 999-1013.

75. D.J. Ripin, *A Few-Cycle Cr4+:YAG Laser and Optical Studies of Photonic Crystals,* **2002,** Doctor of Philosphy Thesis, Massachusetts Institute of Technology.

76. Erik R. Thoen, *Development of Ultrashort Pulse Fiber Lasers for Optical Communication Utilizing Semiconductor Devices,* **2000,** Doctor of Philosphy Thesis, Massachusetts Institute of Technology.

77. B.C. Collings, J.B. Stark, S. Tsuda, W.H. Knox, J.E. Cunningham, W.Y. Jan, R. Pathak, K. Bergman. *Opt. Lett.,* **1996,** *21,* 1171-73.

78. M.J. Hayduk, S.T. Johns, M.F. Krol, C. R. Pollock, R.P Leavitt. *Opt. Comm.,* **1997,** *137,* 55-58.

79. S. Spälter, M. Böhm, M. Burk, B. Mikulla, R. Fluck, I.D. Jung, G. Zhang, U. Keller, A. Sizmann, and G. Leuchs. *Appl. Phys. B.,* **1997,** *65,* 335-8.

80. Y. Chang, R. Maciejko, R. Leonelli, A.S. Thorpe. *Appl. Phys. Lett.,* **1998,** *73*, 2098-2100.

81. J.W. Matthews, A.E. Blakeslee. *J. Crystal Growth,* **1974,** *27,* 118-25.

82. E.R. Thoen, E.M. Koontz, M. Joschko, P. Langlois, T.R. Schibli, F.X. Kärtner, E.P. Ippen, L.A. Kolodziejski. *Appl. Phys. Lett.,* **1999,** *74*, 3927-3929.

83. D.J. Ripin, J.T. Gopinath, H. Shen, A.A. Erchak, G.S. Petrich, L.A. Kolodziejski, F.X. Kärtner, E.P. Ippen, *Appl. Phys. Lett.,* (to be published).

84. Y.-S. Lee, Y.-H. Lee, J.-H. Lee. *Appl. Phys. Lett.,* **1994,** *65*, 2717-9.

85. K.D. Choquette, K.M. Geib, H.C. Chui, B.E. Hammons, H.Q. Hou, T.J. Drummond, R. Hull. *Appl. Phys. Lett.,* **1996,** *69*, 1385-7.

86. M.H. MacDougal, P.D. Dapkus. *IEEE Photonics Technol. Lett.,* **1997,** *9*, 884-6.

87. P.W. Evans, J.J. Wierer, N. Holonyak Jr. *J. Appl. Phys.,* **1998,** *84,* 5436-40.

88. H.Q. Jia, H. Chen, W.C. Wang, W.X. Wang, W. Li, Q. Huang, J. Zhou. *J. Crystal Growth.* **2001,** *223,* 484-8.

89. M.H. MacDougal, P.D. Dapkus, A.E. Bond, C.-K. Lin, J. Geske, *IEEE J. Sel. Topics Quantum Electron.,* **1997,** *3*, 905-15.

90. M.H. MacDougal, H. Zhao, P.D. Dapkus, M. Ziari, W.H. Steier. *Electron. Lett.,* **1994,** *30,* 1147-9.

91. W.T. Tsang, M. Olmstead, R.P.H. Chang. *Appl. Phys. Lett.,* **1979,** *34*, 408-10.

92. M.S. Wu, G.S. Li, W. Yuen, C.J. Chang-Hasnain. *Electron. Lett.,* **1997,** *33,* 1702-4.

93. H.-E. Shin, Y.-G. Ju, H.-W. Song, D.-S. Song, I.-Y. Han, J.-H. Ser, H.-Y. Ryu, Y.-H. Lee, H.-Y. Park. *Appl. Phys. Lett.,* **1998,** *72*, 2205-7.

94. H. Gebretsadik, K. Kamath, K.K. Linder, P. Bhattacharya, C. Caneau, R. Bhat. *J. Vac. Sci. Technol. B,* **1998,** *16,* 1417-21.

95. H. Gebretsadik, O. Qasaimeh, H. Jiang, P. Bhattacharya, C. Caneau, R. Bhat. *J. Lightwave Technol.,* **1999,** *17*, 2595-604.

96. O. Blum, J.F. Klem, K.L. LEar, G.A. Vawter, S.R. Kurtz, *Electron. Lett.,* **1997,** *33,* 1878-80.

97. M.H. MacDougal, S.G. Hummel, P.D. Dapkus, H. Zhao, Y. Cheng, *IEEE Photonics Technol. Lett.,* **1995,** *7*, 385-87.

98. B. Koley, F.G. Johnson, O. King, S.S. Saini, M. Dagenais, *Appl. Phys. Lett.,* **1999,** *75*, 1264-66.

99. G.W. Pickrell, J.H. Epple, K.L. Chang, K.C. Hsieh, K.Y. Cheng, *Appl. Phys. Lett.,* **2000,** *76*, 2544-46.

100. B.E. Deal, A.S. Grove, *J. Appl. Phys.,* **1965,** *36,* 3770.

101. F.A. Kish, S.J. Caracci, N. Holonyak Jr., K.C. Hsieh, J.E. Baker, S.A. Maranowski, A.R. Sugg, J.M. Dallesasse, R.M. Fletcher, C.P. Kuo, T.D. Osentowski, M.G. Craford. *J. Electron. Mater.,* **1992,** *21*, 1133-9.

102. T. Langenfelder, S. Schroder, H. Grothe, *J. Appl. Phys.,* **1997,** *82,* 3548-51.

103. M. Ochiai, G.E. Giudice, H. Temkin, J.W. Scott, T.M. Cockerill, *Appl. Phys. Lett.,* **1996,** *68*, 1898-900.

104. S.A. Feld, J.P. Loehr, R.E. Sherriff, J. Miemeri, R. Kaspi, *IEEE Photonics Technol. Lett.,* **1998,** *10*, 197-9.

105. W.J. Mitchell, C.-H. Chung, S.I. Yi, E.L. Hu, W.H. Weinberg, *J. Vac. Sci. Technol. B.,* **1997,** *15,* 1182-86.

106. C.I.H. Ashby, M.M. Bridges, A.A. Allerman, B.E. Hammons, H.Q. Hou, *Appl. Phys. Lett.,* **1999,** *75*, 73-5.

107. C.I.H. Ashby, J.P. Sullivan, P.P. Newcomer, N.A. Missert, H.Q. Hou, B.E. Hammons, M.J. Hafich, A.G. Baca, *Appl. Phys. Lett.,* **1999,** *70*, 2443-5.

108. R.D Twesten, D.M. Follstaedt, K.D. Choquette, *Proceedings of the SPIE,* **1997,** *3003,* 55-61.

109. C.I.H. Ashby, J.P. Sullivan, K.D. Choquette, K.M. Geib, H.Q. Hou, *J. Appl. Phys.,* **1997,** *82,* 3134-36.

110. R.S. Burton, T.E. Schlesinger, *J. Appl. Phys.,* **1994,** *76,* 5503-7.

111. M.J. Cich, R. Zhao, E.H. Anderson, E.R. Weber, *J. Appl. Phys.,* **2002,** *91,* 121-4.

112. R.D. Twesten, D.M. Follstaedt, K.D. Choquette, R.P. Schneider Jr., *Appl. Phys. Lett.,* **1996,** *69*, 19-21.

113. T. Takamori, K. Takemasa, T. Kamijoh, *Appl. Phys. Lett.,* **1996,** *69*, 659-61.

114. J.P. Landesman, A. Fiore, J. Nagle, V. Berger, E. Rosencher, P. Puech, *Appl. Phys. Lett.,* **1997,** *71*, 2520-22.

115. K.M. Geib, K.D. Choquette, H.Q. Hou, B.E. Hammons, *Proceedings of the SPIE,* **1997,** *3003,* 69-74.

116. M. Osiñski, T. Svimonishvili, G.A. Smolyakov, V.A. Smagley, P. Mackowiak, W. Nakwaski, *IEEE Photonics Technol. Lett.,* **2001,** *13*, 687-89.

117. R.L. Naone, L.A. Coldren. *J. Appl. Phys.,* **1997,** *82*, 2277-80.

118. B. Koley, M. Dagenais, R. Jin, G. Simonis, J. Pham, *J. Appl. Phys.,* **1998,** *84*, 600-5.

119. A.C. Alonzo, X.-C. Cheng, T.C. McGill, *J. Appl. Phys.,* **1998,** *84*, 6901-5.

120. O. Blum, C.I.H. Ashby, H.Q. Hou, *Appl. Phys. Lett.,* **1997,** *70*, 2870-2.

121. E.M. Koontz, *The Development of Components for Ultrafast All-Optical Communication Networks,* **2000,** Doctor of Philosphy Thesis, Massachusetts Institute of Technology.

122. R. Ramaswami, K.N. Sivarajan, *Optical Networks: A Practical Perspective.* Morgan Kaufmann Publishers. San Fransisco, **1998.**

123. E.A. Fitzgerald, L.C. Kimerling, *MRS Bull.,* **1998,** *23*, 39.

124. C.A. Warwick, R.-H. Yan, Y.-O. Kim, A. Ourmazd, *AT&T Technical Journal,* **1993,** *Sept./Oct.,* 50-8.

125. H. Yokoyama, in *Spontaneous Emission and Laser Oscillation in Microcavities,* edited by H. Yokoyama and K. Ujihara, CRC Press, Inc., **1995**.

126. C. Weisbuch, R. Houdre, R.P. Stanley, in *Spontaneous Emission and Laser Oscillation in Microcavities,* edited by H. Yokoyama and K. Ujihara, CRC Press, Inc., **1995**.

127. T.R. Chen, B. Zhao, L. Eng, Y.H. Zhuang, A. Yariv, J.E. Unger, S. Oh, *Appl. Phys. Lett.,* **1992,** *60,* 1782-4.

128. F. Koyama, S. Kinoshita, K. Iga, *Appl. Phys. Lett.,* **1988,** *55,* 1089-91.

129. J. L. Lewell, S. L. McCall, Y.H. Lee, A. Scherer, A.C. Gossard, J.H. English, *Appl. Phys. Lett.,* **1989,** *54,* 1400-02.

130. R.S. Geels, L.A. Coldren, *Appl. Phys. Lett.,* **1990,** *57,* 1605-7.

131. T. Numai, T. Kawakami, T. Yoshikawa, M. Sugimoto, Y. Sugimoto, H. Yokoyama, K. Kasahara, K. Asakawa, *Jpn. J. Appl. Phys.,* **1993,** *32,* L1533.

132. M. Pelton, J. Vuckovic, G.S. Solomon, A. Scherer, Y. Yamamoto, *IEEE J. Quantum Electron.,* **2002,** *38*, 170-7.

133. D.L. Huffaker, L.A. Graham, H. Deng, D.G. Deppe, *IEEE Photonics Technol. Lett.,* **1996,** *8*, 974-76.

134. S.L. McCall, A.F.J. Levi, R.E. Slusher, S.J. Pearton, R.A. Logan, *Appl. Phys. Lett.,* **1992,** *60,* 289-91.

135. B. Gayral, J.M. Gerard, A. Lemaitre, C. Dupuis, L. Manin, J.L Pelouard, *Appl. Phys. Lett.,* **1999,** *75,* 1908-10.

136. M. Fujita, R. Ushigome, T. Baba, *IEEE Photonics Technol. Lett.,* **2001,** *13*, 403-5.

137. M. Fujita, R. Ushigome, T. Baba, *Electron. Lett.,* **2000,** *36*, 790-1.

138. M. Cai, K. Vahala, *Optics Letters,* **2001,** *26,* 884-6.

139. A.F.J. Levi, R.E. Slusher, S.L. McCall, S.J. Pearton, W.S. Hobson, *Appl. Phys. Lett.,* **1993,** *62,* 2021-3.

140. J.-P. Zhang, D.Y. Chu, S.L. Wu, S.-T. Ho, W.G. Bi, C.W. Tu, R.C. Tiberio, *Phys. Rev. Lett., **1995,*** *75,* 2678-81.

141. J.-P. Zhang, D.Y. Chu, S.L. Wu, W.G. Bi, R.C. Tiberio, X.W. Tu, S.-T. Ho, *IEEE Photonics Technol. Lett.,* **1996,** *8*, 968-70.

142. S.-T. Ho, J.-P. Zhang, L. Wang, *Proceedings of the SPIE,* **1996,** *2891,* 18-27.

143. O.J. Painter, R.K. Lee, A. Scherer, A. Yariv, J.D. O'Brien, P.D. Dapkus, I. Kim, *Science,* **1999,** *284,* 1819-21.

144. O.J. Painter, A. Husain, A. Scherer, J.D. O'Brien, I. Kim, P.D. Dapkus, *J. Lightwave Technol.,* **1999,** *17*, 2042-48.

145. W.D. Zhou, J. Sabarinathan, B. Kochman, E. Berg, O. Qasaimeh, S. Pang, P. Bhattacharya, *Electronics Letters.* **2000,** *36,* 1541-2.

146. P.R. Villeneuve, S. Fan, J.D. Joannopoulos, K.-Y. Lim, J.C. Chen, G.S. Petrich, L.A. Kolodziejski, R. Reif, *Appl. Phys. Lett.,* **1995,** *67,* 167-9.

147. P.R. Villeneuve, S. Fan, J.D. Joannopoulos, K.-Y. Lim, J.C. Chen, G.S. Petrich, L.A. Kolodziejski, R. Reif, *Proceedings of NATO Advanced Studies Institute on Photonic Band Gap Materials*, Kluwer, Dordrecht, **1995**.

148. T.F. Krauss, B. Vogele, C.R. Stanley, R.M. De La Rue, *IEEE Photonics Technol. Lett.,* **1997,** *9*, 176-8.

149. J.C. Chen, H.A. Haus, S. Fan, P.R. Villeneuve, J.D. Joannopoulos, *J. Lightwave Technol.*, **1996,** *14*, 2575-80.

150. J.P. Zhang, D.Y. Chu, S.L. Wu, W.G. Bi, R.C. Tiberio, R.M. Joseph, A. Taflove, C.W. Tu, S.T. Ho, *IEEE Photonics Technol. Lett.*, **1996,** *8*, 491-3.

151. J.S. Foresi, P.R. Villeneuve, J. Ferrara, E.R. Thoen, G. Steinmeyer, S. Fan, J.D. Joannopoulos, L.C. Kimerling, H.I. Smith, E.P. Ippen, *Nature,* **1997,** *390,* 143-45.

152. K.-Y. Lim, D.J. Ripin, G.S. Petrich, L.A. Kolodziejski, E.P. Ippen, M. Mondol, H.I. Smith, *J. Vac. Sci, Technol. B.,* **1999,** *17,* 1171-74.

153. K.-Y. Lim, D.J. Ripin, G.S. Petrich, P.R. Villeneuve, S. Fan, J.D. Joannopoulos, E.P. Ippen, L.A. Kolodziejski, *Adv. Mat.,* **1999,** *11,* 501-5.

154. D.J. Ripin, K.-Y. Lim, G.S. Petrich, P.R. Villeneuve, S. Fan, E.R. Thoen, J.D. Joannopoulos, E.P. Ippen, L.A. Kolodziejski, *J. Lightwave Technol.,* **1999,** *17*, 2152-60.

155. K.-Y. Lim, *Design and Fabrication of One-Dimensional and Two-Dimensional Photonic Bandgap Devices,* **1999,** Doctor of Philosophy Thesis, Massachusetts Institute of Technology.

156. D.J. Ripin, K.-Y. Lim, G.S. Petrich, P.R. Villeneuve, S. Fan, E.R. Thoen, J.D. Joannopoulos, E.P. Ippen, L.A. Kolodziejski, *J. Appl. Phys.,* **2000,** *87,* 1578-80.

157. M.H. MacDougal, J. Geske, C.-K. Lin, A.-E. Bond, P.D. Dapkus, *IEEE Photonics Technol. Lett.,* **1998,** *10*, 15-17.

158. H. Yokoyama, S.D. Brorson, *J. Appl. Phys.,* **1989,** *66,* 4801-5.

159. S.J. Pearton, F. Ren, W.S. Hobson, C.R. Abernathy, U.K. Chakrabarti, *J. Vac. Sci, Technol. B.,* **1994,** *12,* 142-6.

160. K. Tai, T.R. Hayes, S.L. McCall, W.T. Tsang, *Appl. Phys. Lett.,* **1988,** *53,* 302-4.

161. P.R. Villeneuve, D.S. Abrams, S. Fan, J.D. Joannopoulos, *Optics Letters,* **1996,** *21,* 2017-19. (*Simulation was performed by Dr. Villeneuve while at MIT)*

162. G. Bjork, Y. Yamamoto, *IEEE J. Quantum Electron.,* **1991,** *27*, 2386-95.

163. T. Baba, T. Hamano, F. Koyama, K. Iga, *IEEE J. Quantum Electron.*, **1991,** *27*, 1347-57.

164. M. Meier, A. Mekis, A. Dodabalapur, A. Timko, R.E. Slusher, J.D. Joannopoulos, O. Nalamasu, *Appl. Phys. Lett.,* **1999,** *74,* 7-9.

165. M. Imada, S. Noda, A. Chutinan, T. Tokuda, M. Murata, G. Sasaki, *Appl. Phys. Lett.,* **1999,** *75,* 316-18.

166. N. Susa, *J. Appl. Phys.,* **2001,** *89,* 815-23.